DSE - Electric Helicopter

H2Copter

M.S.T. van den Aarssen	4223233	A.A.E. Naorniakowski	4229541
L.M.A. Declerck	4206622	J.M.F. van Neerven	4231899
M. Dirkzwager	4206223	E.A. Schouten	4104161
R.J. Everaert	4082354	K. Schreiber	4080017
M.W. Goedhart	4232445	K.F. Yip	4232976

Final Report

Design Synthesis Excercise

TU Delft Delft University of Technology

Aerospace Engineering

June 30, 2015

ELECTRIC HELICOPTER

FINAL REPORT

by

DSE Group 11

Aarssen, Marc van den
4223233

Declerck, Laurent
4206622

Dirkzwager, Mats
4206223

Everaert, Rick
4082354

Goedhart, Menno
4232445

Naorniakowski, Alexander
4229541

Neerven, Matthijs van
4231899

Schouten, Ewout
4104161

Schreiber, Kevin
4080017

Yip, Bryan
4232976

in partial fulfillment of the requirements for the degree of

Bachelor of Science
Aerospace Engineering

at the Delft University of Technology,

June 30, 2015

Tutor: Dr. M. D. Pavel
Coaches: Ir. Johan Carvajal Godínez
Ir. Tim Visser

TU Delft Delft University of Technology

PREFACE

This report is commissioned by a group of 10 students as part of their Design Synthesis Exercise and is intended for the managers of this project and potentially for engineers in this technical area. This report will elaborate on the process of designing a coaxial hydrogen helicopter for 2020. During the design phase, besides the technical aspects, among others the market, the risk management, the costs and the sustainable development will be analyzed or defined.

This report is divided into four parts, in which each includes another phase in the design process. Readers who are particularly interested in the project objective, which includes the mission and market analysis are referred to the first part of the report. Readers who want to know more about the detailed design of the subsystems are referred to part two. People who are interested in the analyses of the final design are referred to part 3 of the report. The further design and production process and the recommendations are discussed in part 4.

We would like to express our gratitude to Dr. M. D. Pavel who made this project possible. We would also like to thank Johan Carvajal Godínez and Tim Visser for their support and assistance.

Delft
22/06/2015
van den Aarssen, Marc
Declerck, Laurent
Dirkzwager, Mats
Everaert, Rick
Goedhart, Menno
Naorniakowski, Alexander
van Neerven, Matthijs
Schouten, Ewout
Schreiber, Kevin
Yip, Bryan

Contents

Design analysis

Recommendations

List of symbols

Symbol	Definition	Unit
A	Area	[m^2]
AR	Aspect ratio	[-]
C	Heat capacity rate	[W/(Ks)]
C^*	Heat capacity ratio	[-]
C_D	Drag coefficient	[-]
C_{fe}	Equivalent skin-friction coefficient	[-]
C_H	Rotor drag coefficient	[-]
C_L	Lift coefficient	[-]
C_M	Momemt coefficient	[-]
C_P	Power coefficient	[-]
C_Q	Torque coefficient	[-]
C_T	Thrust coefficient	[-]
c	Chord length	[m]
D	Diameter	[m]
d	Disk offset	[-]
DL	Disc loading	[kg/m^2]
E	Energy	[kWh]
f	Wake distance	[m]
f	Colburn factor	[-]
FM	Figure of Merit	[-]
g	Gravitational acceleration	[m/s^2]
H	Blade drag	[N]
h	Height	[m]
I	Mass moment of inertia	[kg m^2]
j	Colburn factor	[-]
K	Forward flight coefficient	[-]
k_{dl}	Download factor	[-]
L	Lift	[N]
L	Flow length	[m]
L_S	Stack volume	[m^3]
l	Length	[m]
M	Mach number	[-]
m	Weight per unit span	[kg/m]
$\dot{m}$	Mass flow	[kg/s]
N_{tu}	Thermal unit number	[-]
N_b	Number of blades	[-]
n	Load factor	[-]
n_c	Cell number	[-]
p	Pressure	[Pa]
P	Power	[W]
Pr	Prandtl number	[-]

Symbol	Definition	Unit
Q	Torque	[Nm]
R	Radius	[m]
r	Non-dimensional blade span	[-]
RC	Rate of climb	[m/s]
Re	Reynolds number	[-]
Rg	Range	[km]
S	Surface area	[m^2]
SFC	Specific fuel consumption	[N/(Ws)]
T	Thrust	[N]
T	Temperature	[K]
t	Thickness	[m]
t	Time	[s]
u	Non-dimensional blade element velocity	[-]
U	Blade element velocity	[m/s]
V	Airspeed	[m/s]
v	Induced velocity	[m/s]
$\dot{w}$	Mass flow	[kg/s]
W	Weight	[kg]
X	Propulsive force	[N]
y	Blade location from root	[m]
Z	Force in z-direction	[N]
α	Angle of attack	[rad]
β	Flapping angle	[rad]
γ	Flight path angle	[rad]
γ	Lock number	[-]
δ	Wake approximation angle	[rad]
ϵ	Effectiveness	[-]
η	Efficiency	[-]
θ	Pitch angle	[rad]
λ	Inflow factor	[-]
μ	Advance ratio	[-]
μ	Tip speed ratio	[-]
ξ	Porosity	[-]
ρ	Density	[kg/m^3]
σ	Rotor solidity	[-]
τ	Torque per current	[Nm/A]
ϕ	Inflow angle	[rad]
χ	Wake angle	[rad]
ψ	Azimuth angle	[rad]
Ω	Angular velocity	[rad/s]

NOMENCLATURE

Abbreviation	Definition
AC	Alternating current
AC	Air cooling
APU	Auxiliary power unit
BOP	Balance of plant
CC	Combined cooling
CE	Compressor expander
CF	Characterization factor
CFRP	Carbon fibre reinforced plastic
COD	Constraints on the development
CS	Certification specification
DALY	Disability adjusted life years
DC	Direct current
DSE	Design synthesis exercise
EASA	European aviation safety agency
E-Fan	Electric fan
EP	End point
FMEA	Failure mode effect analysis
HV	High voltage
IATA	International air transport association
IC	Internal combustion
ICAO	International civil aviation organisation
FAR	Federal aviation regulation
FR	Functional requirement
LC	Liquid cooling

Abbreviation	Definition
Li-air	Lithium-air
Li-S	Lithium-sulfur
LV	Low voltage
MP	Mid point
MR	Mission requirements
MTOW	Maximum take-off weight
MV	Medium voltage
NASA	National aeronautics and space administration
NF	Normalization factor
NFR	Non-functional requirement
NOTAR	No tail rotor
PEM	Proton exchange membrane
RAMS	Reliability, availability, maintainability and safety
RoI	Return on investment
RPM	Revolutions per minute
SS	Single score
SWOT	Strengths, weaknesses, opportunities and threats
TBD	To be determined
VTOL	Vertical take off and landing
US	United States
USD	United States dollar
YASA	Yokeless and segmented armature

SUMMARY

The goal of the project is to design an electric helicopter that is more efficient than conventional helicopters. This is to be achieved by using an electric powertrain. The helicopter is designed to fly 100 km and perform a surveillance mission of 30 minutes, followed by a 100 km return flight. The helicopter has a coaxial configuration and is powered by a hydrogen-driven fuel cell. The payload consists of two persons and an infra-red camera, weighing 183 kg in total.

The coaxial rotors both have two blades with a VR12 airfoil. The diameter of the rotor disk was set at 9.0 m. The structural integrity of the blades is ensured by using a carbon fiber skin with a foam core. Optimization with a blade-element model has led to a cruise power of 104 kW, where 122 kW was predicted. Climb performance was worse than predicted: the required climb rate of 900 fpm takes more than the predicted 140.6 kW. The estimated rotor weight is 49 kg.

A carbon fiber tank pressure tank was designed to store the hydrogen. The total tank weight of 164 kg is smaller than expected, due to the use of stronger materials, aerospace standard safety factor and its large volume. The hydrogen is converted to electric energy by a custom-designed proton exchange membrane fuel cell, with a commercially selected compressor. Cooling the fuel cell was more complicated than expected; this is achieved by radiators and fans, at a total weight of 79 kg. Two synchronous three-phase AC motors have been commercially selected. These are controlled by inverters, which are also available off-the-shelf. The varying fuel cell output can be handled by the controller without using a high-power DC/DC converter. The electric driveline provided the possibility for a non-conventional hub design. An aerodynamically shaped, non-rotating hub accommodates the electric motors. The rotors are driven separately by means of planetary gear boxes, made of aluminium. The helicopter is controlled by means of Piezo-actuated servo flaps, eliminating the need for a double swashplate.

The structure of the body is tubular and made of steel, which has favourable fatigue properties. The body was designed using Autodesk Inventor, which was validated with an analytical design of the landing gear. The simple design of skids is preferred. The poles and front ends of the skids are made of aluminum, while the ground skids are made of heavier but more durable steel. The large size has caused the structure to weigh 128 kg, while 90 kg was projected.

Seats, lighting and a fire extinguisher have been selected off-the-shelf. The servo flap controls require a fly-by-wire control system. A glass cockpit design was aimed for in the commercial selection of instrumentation and avionics. A 3 kg infrared camera was added as payload.

A stability analysis was performed in order to size the tail surfaces. Trim conditions were determined for both longitudinal and lateral motions. With this, stability derivatives were determined. The horizontal tail was designed with a tail surface of 0.41 m^2 to meet trim conditions, and a proportional-differential controller was implemented to ensure stability. A vertical tail surface area of 0.75 m^2 was required for lateral stability.

A Failure Mode and Effect Analysis was performed in order to determine the risks. The highest technical risks are the cockpit reinforcement and the controllability. Stability and cooling are also topics of high risk. The reduced amount of moving mechanical parts increases the reliability of the helicopter. It is expected that the achieved availability is 84% due to reduced maintenance. Overhaul is required after 2000 h because of the limited life of the fuel cell, while 2200 h was set as a requirement.

It was determined that the innovation of a hydrogen helicopter leads to a good market perspective. There currently is little competition, but large investments are required to design the helicopter. In order to break even after 30 years, a price of $381,490 is required, with a production price of $349,271. The helicopter will be introduced on the market with a high price and a high quality. The hydrogen infrastructure will need to be implemented, but can be combined with the infrastructure for other vehicles. Pilot training is similar to conventional helicopters. Due to the dual control, the H2Copter can be used for pilot training.

A life cycle assessment was performed. The largest emission is caused by hydrogen compression. Overall, the emission per passenger-kilometer is 65% lower than for a conventional helicopter. The coaxial configuration reduces the noise during overflight and take-off due to the absence of a tail rotor. A 3 dB margin on the certification requirements can not be met during approach.

The gross weight of the H2Copter as determined to be 1065 kg, which is close to the budget of 1064 kg. Only the first iteration was performed for this report. Performance can be increased in the future by integrating the design of the different subsystems. It is expected that the first models can be sold in 2020.

1

Introduction

The current helicopter aviation branch contributes to worldwide pollution on two fronts. First, greenhouse gases are emitted by the internal combustion engines or turbines, used to power the majority of helicopters. Second, the engines and the rotor-wake interaction produce significant noise. Although the helicopter community accounts for a small part of the transportation sector, the helicopter itself is more polluting than other aerial vehicles. At the moment, hydrogen powered fuel cells have proven to be the most effective powerplant to change the helicopter into a zero-emission vehicle. There will be no need for heavy transmission systems, simultaneously reducing vibrations throughout the helicopter and eliminating the need for frequent maintenance. The noise produced by the helicopter can be diminished significantly.

The purpose of this report is to present a two-seat helicopter design with commercial applications that is using a hydrogen based propulsion system. In the previous design phases, the goals of the project, the mission and the requirements were already identified. Furthermore, a trade-off has already been performed on the most suitable concept. This report is more focused on the detailed elaboration of the chosen concept. This includes the design of the rotor system, the propulsion system, the rotor hub, the body and the stabilizers. Thorough analyses will be performed on the design, which includes the stability, performance, risks and costs. Also, an extensive analysis will be on the sustainability of the design. This analysis shows to which extent the more silent fuel cell will open new possibilities and pose new opportunities for the rotorcraft industry.

The report is divided into four separate parts. In the first part of the report the project objective will be discussed, which includes the project statement, mission analysis, requirements, chosen concept and market analysis. These are discussed in chapters 2, 3, 4, 5 and 6 respectively. The second part presents the subsystem design process and the final design. In chapter 7 the rotor design will be discussed, which is based on the aerodynamics of the rotor. Chapter 8 provides an elaboration on the propulsion system design, which includes the electric motors, fuel cell, cooling and hydrogen tank. The rotor hub design is explained in chapter 9. The body, chassis and cockpit design will be shown in chapter 10. Chapter 11 deals with the stability analysis, which is needed to design the stabilizers. This is the only elaborate analysis shown in this part already, because it was needed for the stabilizers design. The final design is shown in chapter 12. The third part deals with the performed analyses. This includes the flight limits analysis in chapter 13, a discussion about the operation and logistics in chapter 14, a thorough analysis on the sustainability in chapter 15, the cost breakdown in chapter 16, a risk analysis in 17 and a RAMS analysis in chapter 18. Chapter 19 provides the compliance matrix, in which compliance with the requirements will be assessed. In the fourth part of the report the next phases of the design phases will be discussed and a recommendation will be given for future investigations. These are provided in chapters 21 and 22.

Part I

Project objective

2

PROJECT STATEMENTS

This chapter will give an overview of the project set up by Delft University of Technology. It includes the formal project objective and mission need statements.

2.1. PROJECT OBJECTIVE STATEMENT

This project, named "Electric Helicopter", is the final project of the bachelor of Aerospace Engineering for ten students. The project guide [1] provided the problem which had to be tackled by the group. It describes that an electric or hybrid electric helicopter should be designed for a surveillance mission. It was later decided that the helicopter was to be introduced in the near future for the commercial market. With all this information, a formal project objective statement was defined as given below.

*Present a two-seat helicopter design with **commercial applications** that has **lower emissions** than comparable conventional alternatives by using **electric or hybrid electric** propulsion, by ten students within ten working weeks.*

2.2. NEED STATEMENT

An increasing effort to design greener alternatives is seen in the transport sector. The helicopter market is also in need of a low-emission alternative. Although the helicopter market is relatively small, conventional helicopters are very polluting. Through several studies [2, 3], the possibility of an electric helicopter was assessed. As previously discussed, such a concept will be elaborated in this project.

Apart from environmental concerns, the opportunity to push the development of sustainable propulsion alternatives is a driver for this need. A functioning hybrid electric helicopter will be a breakthrough for the aerospace industry, and it will encourage many new technological developments. It is expected that this will accelerate the development in many fields, in particular for electrical energy storage capabilities.

In the need statement, it is important that successful implementation of this propulsion technology will lower the emissions of light rotorcraft, with a payload of two persons. The rotorcraft will aim at multiple markets, but the design mission will be a surveillance mission. The design will be based on current technology, and a prototype is to be introduced in the year 2020. At the moment of defining the mission need statement, it is not certain that a fully electric vehicle is feasible with the current state of batteries and fuel cells, so there is also the option to make a hybrid electric vehicle. In that case, it should be easily adaptable to a fully electric concept as soon as the improvement in technology is sufficient. With this in mind, the mission need statement was defined as follows.

*The **emission** of a typical helicopter **surveillance** mission should be lowered by using an **electric** or **hybrid-electric** two-seat rotorcraft by the year **2020**, that should be able to fly **fully electrically** in the future.*

3

MISSION ANALYSIS

In this chapter the mission is analyzed. The goal is to design a rotorcraft, which has lower emission and is capable to fly a certain range, as stated in chapter 2. In order to design this, the mission profile and functions should be defined. The general flight profile is discussed in section 3.1. The functions of the rotorcraft are described in section 3.2.

3.1. FLIGHT PROFILE

The mission of the rotorcraft can be described in a couple of phases, which are listed below. A graphical representation of the mission can be seen in figure 3.1. The numbers shown in figure 3.1 are the minimum required specifications. This implies that if the optimum cruise speed turns out to be higher, this optimum value will be used. However, if the optimum speed is lower than the minimum required cruise speed, either the minimum required cruise speed will be used or changes have to be made in the design. Several phases are described in more detail in this section.

3.1.1. TAKE-OFF

During take-off one should comply with the height velocity diagram. An example of the height-velocity diagram for the start is given in figure 3.2. There are two areas in this graph to avoid. The first is called the dead-man region, which indicates the zone where it is not possible to perform a safe landing after an engine failure. This is because the altitude of the helicopter has to be high enough to switch into autorotation. The second area is the area with high forward speed and should be avoided because the time for the pilot to perform a safe landing is too small.

The helicopter will first climb vertically to an altitude of around 10 ft. This altitude is the most ideal altitude [5]. In case surroundings require a higher altitude, due to limited space, the helicopter has to climb higher vertically. This altitude should not be too high, since it requires more power and has a higher risk, as can be seen in figure 3.2. Once this altitude is reached, the helicopter will accelerate forward to gain forward speed. The required climbing rate is 900 fpm or 4.57 m/s to an altitude of 1980 m.

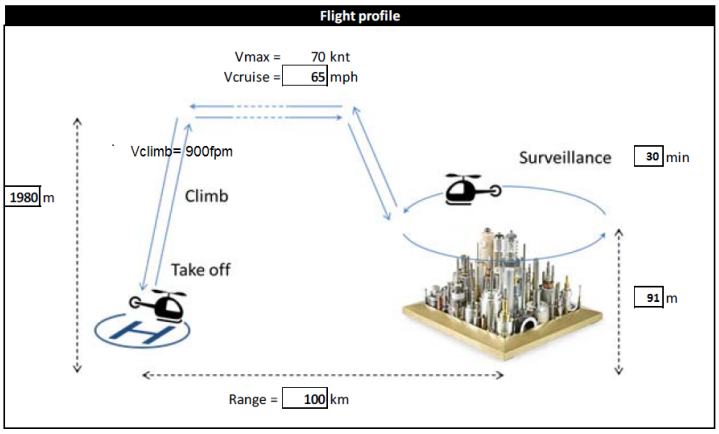

Figure 3.1: Graphical representation of the mission [1].

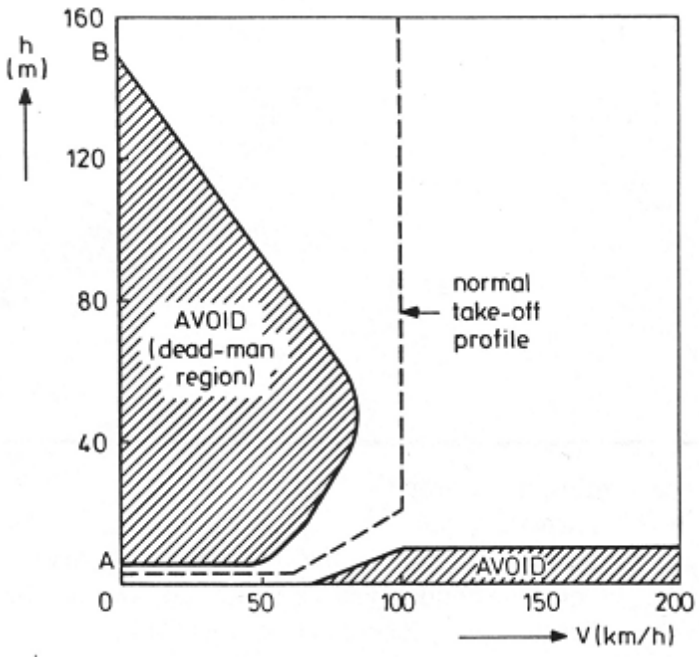

Figure 3.2: Example of a height-velocity diagram [4].

3.1.2. Cruise

During the cruise part of the mission, the rotorcraft is required to fly at an altitude of 1980 m for a range of 100 km approaching the surveillance and 100 km approaching the landing area. The cruise speed is required to be 57 kts, which is approximately 29 m/s. During the initial calculations, the optimum cruise speed was 39 m/s.

3.1.3. Surveillance

The rotorcraft should be able to carry out a surveillance routine. During this phase the rotorcraft will descend with an angle of 5 degrees to an altitude of 300 ft. This altitude is chosen, based on the minimum altitude for surveillance set by FAR [6]. The rotorcraft is designed for a flight motion at the endurance airspeed with a duration of 30 minutes. This flight motion depends on the type of goal of the rotorcraft. In case the rotorcraft has to circle around a building, for example, the rotorcraft will have different conditions then, for example, surveilling a larger area. The endurance airspeed, V_{ed}, is the most efficient airspeed for this phase. V_{ed} lies under the cruise speed and common flight speed for surveillance at 300 ft. The rotorcraft will be designed for the cruise speed and the actual endurance speed has to be calculated afterwards. This resulted in an endurance speed of 22 m/s as will be explained in chapter 13

For this mission, hover is not needed, but each helicopter is required to be able to hover. If a hover time needs to be implemented, this is part of the surveillance. However, hovering requires more power compared to forward flight. Thus, in order to meet the 30 minutes requirement of surveillance, a higher amount of energy at take-off is required.

After the surveillance phase, the rotorcraft will return to the original cruise altitude of 1980m. The velocity height curve, shown in figure 3.2, should be considered here as well. With an endurance speed of 22 m/s, it should first climb with a slope to a forward speed of 27 m/s before climbing vertically to an altitude of 1980 m.

3.1.4. Landing

During landing the slope of descent is 5 degrees[4]. The helicopter should descent according to the height-velocity diagram. An example height-velocity diagram is shown in figure 3.2. This means that the helicopter will descend with a forward velocity to a relatively low altitude. The forward velocity is reduced until the altitude is around 10 ft, if possible. This altitude can be higher, in case of high surroundings or limited space. Then the helicopter will descent vertically until landing.

3.2. FUNCTIONAL ANALYSIS

A design consists of many systems, which can be further subdivided into subsystems. Each subsystem is designed to perform a certain function. The function analysis is supported by two important tools. Those tools are the functional flow diagram and the functional breakdown structure. By analyzing the actions to be performed during the mission, the functional flow diagram can be designed. As can be seen in figure 3.3 the mission is divided in different action points in a horizontal line. Those points can be found restructured in vertical order including extra sub-actions. The logical order of the functional flow diagram helps to properly analyze and define all functions during the mission. The main mission functions can be defined as those from vertical take-off to vertical landing. Preparations and maintenance are important support functions and added to achieve the goal of designing a competitive market version. In the functional breakdown structure, shown in 3.4, the functions that the H2Copter must perform are displayed in a more technical fashion. The main functions per subsystem are listed in this breakdown structure.

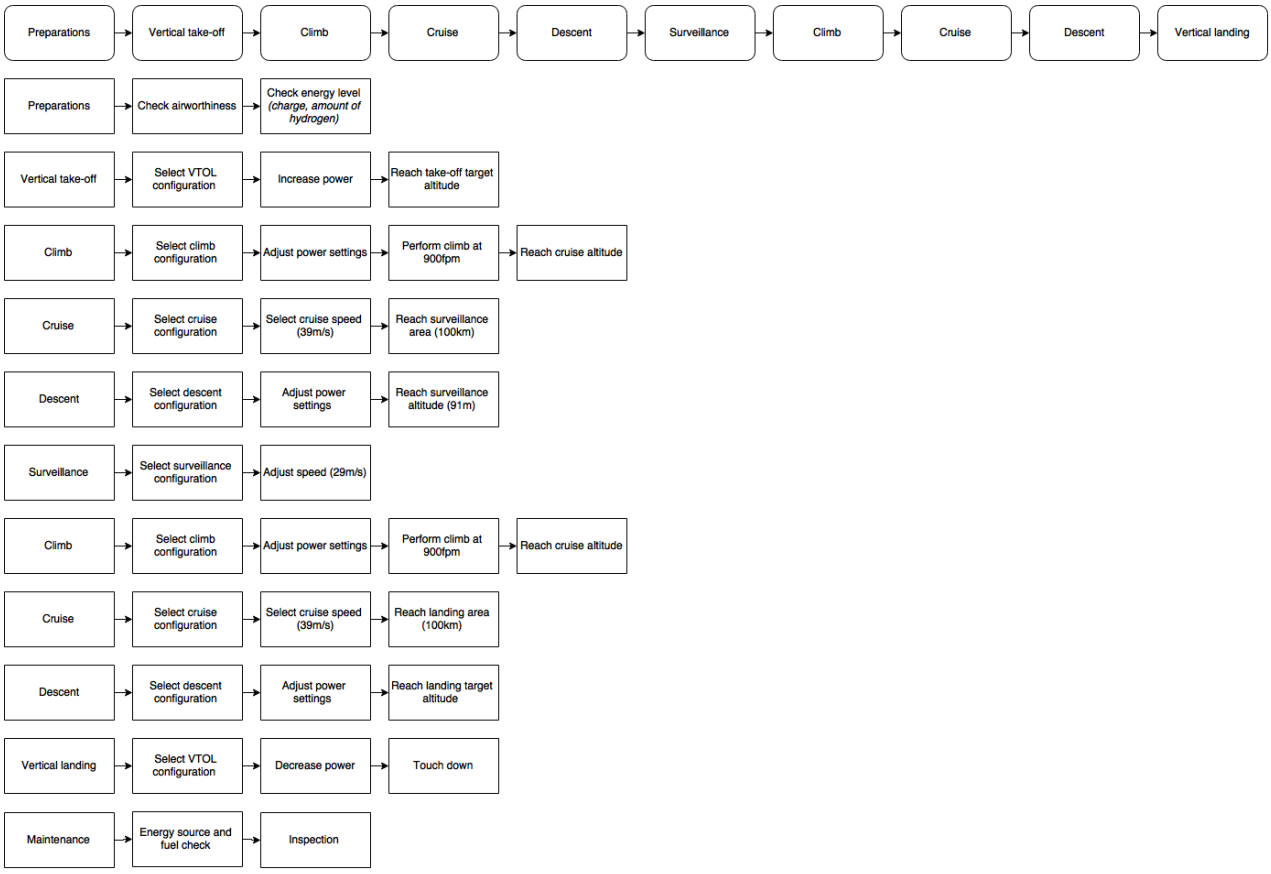

Figure 3.3: Functional flow diagram

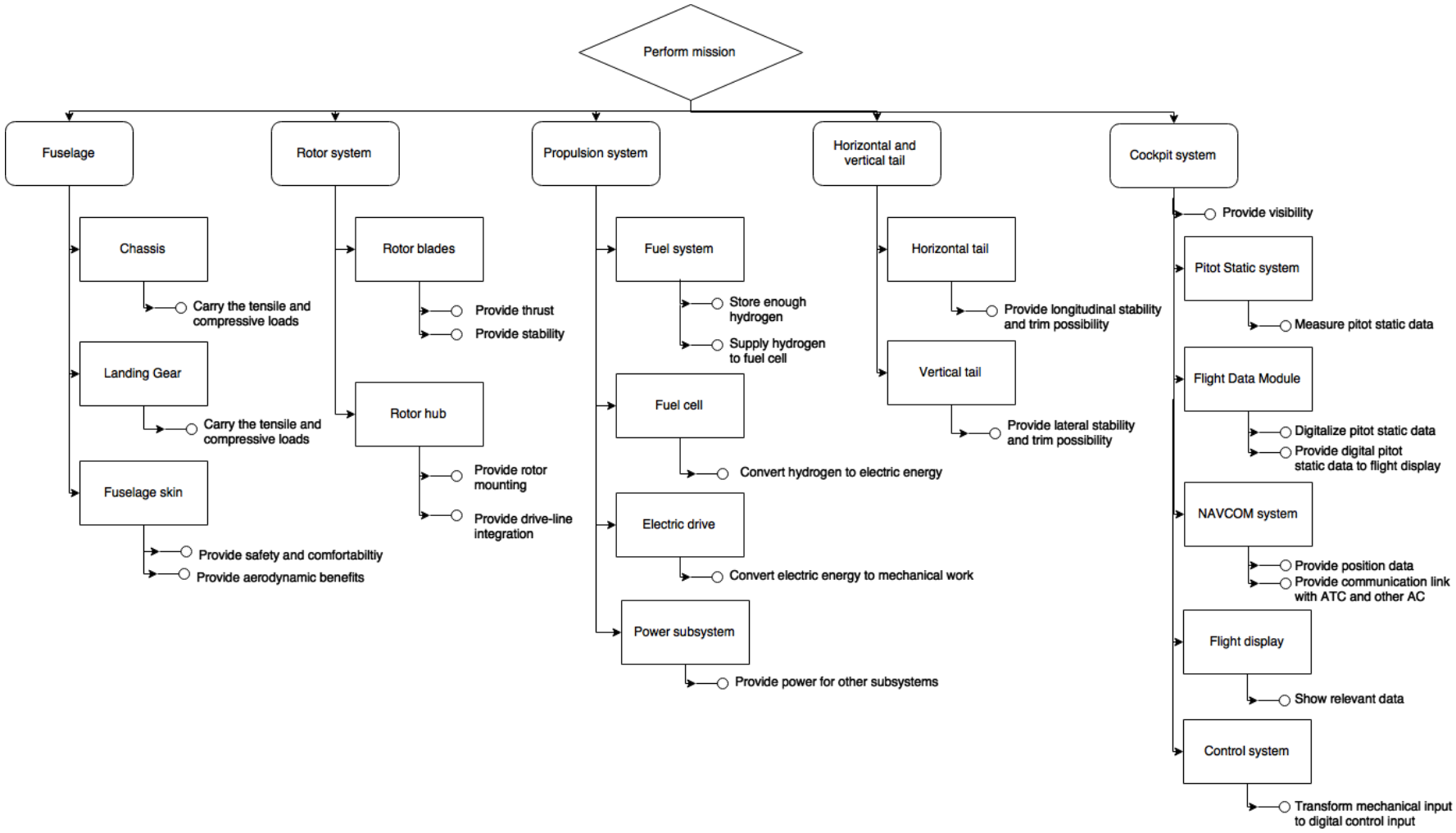

Figure 3.4: Functional breakdown structure

4

REQUIREMENTS

A successful product starts with the definition of the requirements which are considered during all design phases. In section 4.1 a complete list of all requirements is given, legislation is elaborated in section 4.3.

4.1. LIST OF REQUIREMENTS

Requirements are divided into 4 main groups: functional requirements, non-functional requirements, mission requirements and constrains on the development. All are listed in table 4.1 and 4.2. A crucial step in the design process is the verification of these requirements, to make sure the product is actually performing as desired. Applicable parts of this table will be given in a format of a compliance matrix after the design description of each component. This in order to verify if this specific component performs as intended.

4.2. KILLER REQUIREMENTS

The list of requirements is very long and detailed. first, the project was focused on meeting the most curial requirements, the killer requirements. These are listed below.

- The vehicle shall be able to perform vertical take-off and landing
- The vehicle shall have an electric or hybrid electric powertrain
- The vehicle shall be adaptable to fully electrically in the foreseeable future
- The vehicle shall be able to perform the specified mission.

4.3. CERTIFICATION BASIS

Rotorcraft are only allowed to fly in public airspace if certified. Certification requirements are determined by the state of registration and the state where the rotorcraft is flying. Globally, all flying vehicles need to be in compliance with the ICAO standards, but specific states ask for higher requirements. Bringing helicopter on the European market means one needs to be in compliance with the EASA regulations. A experimental certification will not be sufficient to sell the helicopter. This design should be certified according to CS27.

Table 4.1: Mission and constrains on the development requirements.

MISSION REQUIREMENT AND CONSTRAINS	
MR.1	The time before overhaul maintenance shall not be less than 2200 hours or 12 years (R22 specifications)
MR.2	The engine shall be accessible for maintenance
MR.3	The lifetime shall exceed 30 years
MR.4	The availability shall at least be 1 mission per day
MR.5	The reliability of the rotorcraft shall be **[TBD]** over the entire lifetime
MR.6	The engine shall emit no more than 15.1 g of hydrocarbons per kg of fuel burnt during any flight phase
MR.7	The engine shall emit no more than 37.0 g of nitrogen oxides per kg of fuel burnt during any flight phase
MR.8	A turboshaft engine shall have a smoke number of no more than 14.0 during any flight phase
MR.9	The engine shall emit no more than 243 g of hydrocarbons per hour of cruise
MR.10	The engine shall emit no more than 772 g of nitrogen oxides per hour of cruise
MR.11	The rotorcraft shall be in compliance with the ACARE goals [7]
MR.12	The noise levels of the vehicle shall be at least 3 EPNdB below the noise levels prescribed in CS-36
CONSTRAINS ON THE DEVELOPMENT	
COD. 1	The use of resources shall stay withing the predefined budget
COD. 2	The project shall be completed in 11 weeks
COD. 3	The project scale shall not exceed the workload of 10 engineers

Table 4.2: Functional and non-functional requirements.

FUNCTIONAL REQUIREMENTS		
FR.1	The rotorcraft shall be able to perform vertical take-off and landing	
FR.2	The rotorcraft shall be 3-axis controllable during the entire VTOL manoeuvres	
FR.3	The rotorcraft shall have a cruise flight configuration	
FR.4	The rotorcraft shall be 3-axis controllable during the entire cruise phase	
FR.5	The pilot accommodation shall provide a clear view to the ground	
NON-FUNCTIONAL REQUIREMENTS		
NFR.1	The rotorcraft shall have a maximum true airspeed of 70 kts	
NFR.2	The rotorcraft shall have a true airspeed in cruise of 57 kts	
NFR.3.a	The rotorcraft shall be able to carry a payload (crew) of 180 kg	
NFR.3.b	The rotorcraft shall accommodate two crew members	
NFR.4	The rotorcraft shall have an electric or hybrid-electric powertrain	
NFR.5	The rotorcraft shall be able to sustain a climb rate of 900 feet per minute	
NFR.6	The rotorcraft shall be able to cruise at an altitude of 1980 m	
NFR.7	The rotorcraft shall have a range of 200 km	
NFR.8	The rotorcraft shall be able to perform a 30 minute surveillance	
NFR.9	The rotorcraft shall provide a crash-safe energy storage, capable of withstanding **[TBD G's]**	
NFR.10	The rotorcraft shall be in compliance with EASA CS-27	
	NFR.10.1	The rotor craft shall have a MTOW of no more than 3175 kg
	NFR.10.2	The rotorcraft shall provide auto-rotational capabilities
	NFR.10.3	The rotorcraft shall provide a minimum climb ratio of 1/6
	NFR.10.4	The minimum ceiling height for hovering shall be 1219 m for a reciprocal engine setup
	NFR.10.5	The minimum ceiling height for hovering shall be 762 m for a turbine engine setup
	NFR.10.6	The rotorcraft shall be able to be landed without any excessive vertical acceleration
	NFR.10.7	The rotorcraft shall be able to be landed without bouncing and tip over tendency
	NFR.10.8	The rotorcraft shall be able to restart its engine in air during auto-rotation
	NFR.10.9	The rotorcraft shall provide near ground control-ability at a minimum wind-speed of 17 kts
	NFR.10.10	The rotorcraft shall have a structural safety factor of 1.5
	NFR.10.11	The rotorcraft shall be able to perform between the limiting maneuvering load factor of 3.5G and -1G
	NFR.10.12	The rotorcraft shall provide controllability and integrity during vertical gusts of 9.1 m/s in all flight phases
	NFR.10.13	The pilot control forces and torques shall be no more than • **NFR. 10.13a** 578 N for foot control • **NFR. 10.13b** 445 N for forwards, backwards stick control • **NFR. 10.13c** 298 N for lateral stick control • **NFR. 10.13d** (25.4+R)·2.919 N while using the flap tab stabilizer • **NFR. 10.13e** 357·R N-mm for twist control
	NFR.10.14	During emergency landing conditions the pilot shall experience loads no more than • **NFR. 10.14a** 4 G upwards • **NFR. 10.14b** 16 G forwards • **NFR. 10.14c** 8 G sidewards • **NFR. 10.14d** 20 G downwards • **NFR. 10.14e** 1.5 G rearwards
	NFR.10.15	During emergency landing conditions, items of mass shall be able to withstand loads of at least • **NFR. 10.15a** 1.5 G upwards • **NFR. 10.15b** 12 G forwards • **NFR. 10.15c** 6 G sidewards • **NFR. 10.15d** 12 G downwards • **NFR. 10.15e** 1.5 G rearwards
	NFR.10.16	During emergency landing conditions, the structures around tanks and pilot shall withstand loads of at least • **NFR. 10.16a** 1.5 G upwards • **NFR. 10.16b** 4 G forward • **NFR. 10.16c** 2 G sidewards • **NFR. 10.16d** 4 G downwards
NFR.11	The rotorcraft shall be adaptable to a fully electric power source	

5

CONCEPT

The purpose of this chapter is to summarize the research performed in the mid-term report [8] with respect to the feasibility of the selected aircraft design configuration, its propulsion system technology and the budget breakdown. This preliminary information will serve as a basis for a further multidisciplinary detail design phase of the project.

5.1. CONCEPT SELECTION

In chapter 2 the project and mission need statement have been defined. Vehicle flight characteristics belonging to the different mission flight phases have been presented in chapter 3. The requirements related to the vehicle and its mission have been defined in chapter 4. After carefully having defined these problem statements, feasible aircraft concepts need to be selected to perform the mission and meet all requirements. In the mid-term report [8], a design option tree has been established to generate an overview of all design possibilities for vehicle configurations as well as for important aircraft subsystems. From this design option tree, three feasible aircraft groups have been selected as main configuration design options by performing a trade-off using appropriate criteria. The group division outcomes are: powered rotor, non-powered rotor and tilt-wing aircraft concepts. A brief description of these aircraft groups is provided in sections 5.1.1 - 5.1.3. Another more detailed trade-off has been performed between the selected concepts from these groups to arrive at a single final feasible vehicle configuration, which is presented in section 5.1.4.

5.1.1. POWERED ROTOR

The concepts considered in the powered rotor concept group are most standard helicopter configurations, being the conventional, coaxial, flettner, tandem and side-by-side ones. From these configurations, advantages and disadvantages have been investigated in the mid-term report [8] resulting in the coaxial helicopter being selected as the most feasible powered rotor vehicle configuration, the most important reasons being the reduced yaw control system complexity by the use of independent rotor drive systems, low noise production, no tail rotor required, compactness and high manoeuvrability.

5.1.2. NON-POWERED ROTOR

Within this aircraft group, no separate configuration selection procedure has been applied; the considered configuration was the autogyro, an aircraft using a non-powered lift providing main rotor and a powered push propeller for thrust.

5.1.3. TILT-WING

A canard configuration has been selected as a feasible concept within the tilt-wing aircraft group. This configuration has benefits in efficient wing usage for providing lift. The engines are fixed to the wings, which can tilt with respect to the fuselage.

5.1.4. FINAL CONCEPT SELECTION

The result from a thorough trade-off process between these three aircraft groups is the selection of the coaxial helicopter concept originating from the powered rotor aircraft group. This concept will be analysed and worked out in detail to arrive at a final helicopter design. All its subsystems and components need to be designed in a multidisciplinary engineering environment. Chapters 7 to 12 will present the results from the detail design phase.

Table 5.1: Component masses of the coaxial helicopter.

Component	Mass [kg]	Component	Mass [kg]
Main rotor blades	73	Fuel tank	259
Main rotor hub and hinge	51	Cockpit controls	7.3
Stabilizers	8.6	Systems controls	9.7
Fuselage	90	Instruments	4.8
Landing gear	64	Avionics	10
Fuel cell	228	Furnishings and equipment	8.3
Electrical motors	54	Fuel	16.1

5.2. Powertrain concept

The powertrain of choice for the coaxial helicopter concept is a hydrogen electric drive. Due to the current state of battery technology, batteries cannot catch up with the energy density provided by the hydrogen fuel cell system over the range defined by the mission requirement. By designing a hydrogen electric drive, the drive-line can be designed fully electric, to make it a simple conversion to a fully battery driven design, once the performance of the batteries improves to an equal level in terms of energy density.

5.3. Budget breakdown

For the chosen helicopter concept a number of budgets are specified.

Mass is a driving factor in the design of the helicopter, thus a budget to keep it within limits has been made. The empty mass is estimated by means of the class II weight estimation method described by Raymond Prouty [9]. To the calculated empty mass the payload and fuel masses were added to get the gross take-off mass. This is specified at 1067 kg.

Because in later design phases components are designed separately, the previously calculated component masses are taken and established as a budget as well. The specified masses are shown in table 5.1.

The **power** required is another factor of importance. The power system, including the electrical motors and the fuel cell, is sized at a maximum peak power of 140.6 kW, which is used for climb and take-off. The maximum continuous power, used for cruise, is estimated to be 122 kW. As can be seen in table 5.1 the propulsion subsystem is a heavy part, meaning that violating the power budget can involve a considerable increase in weight.

The **energy** necessary to perform the mission will determine the amount of hydrogen that has to be carried along in the helicopter. The budget for energy is 982 MJ or 273 kWh for the complete mission, corresponding to 16.2 kg of hydrogen including a 15% margin for losses and the fact that a hydrogen tank cannot be emptied completely during flight.

6

MARKET ANALYSIS

In this chapter, the market for the H2Copter will be analyzed. In this final design phase, emphasis will lie on strategic market analysis, as opposed to the quantitative market analysis performed in the baseline report. This approach will be explained in section 6.1. In section 6.2, the long term goals and competitive advantage of the H2Copter are stated, after which, in section 6.3, the environment the helicopter is in will be evaluated, consisting of a PESTEL analysis and a competitor analysis. In chapter 6.4, a SWOT analysis will be provided and section 6.5 will conclude on the market strategy which is to be used for the H2Copter.

6.1. MARKET ANALYSIS APPROACH

In the baseline report [10], a preliminary market analysis was presented for an hybrid electric or all electric conventional helicopter. Now the concept is chosen, it is possible to analyse the market in further detail. In the baseline report, an estimation of the feasible retail price was already made. For this analysis, comparable aircraft were looked at and an added value for an electric aircraft as opposed to fossil fuel flying aircraft was obtained from the automotive industry. It should be noted that the added value was estimated for a concept with an all battery configuration while the chosen concept runs on a hydrogen fuel cell, which imposes higher operating cost due to the high price of hydrogen. However, since a system running on hydrogen also has benefits compared to batteries, such as reduced refueling time, and since the price of hydrogen is expected to decrease significantly in the coming years, the added value is expected to be the same for a battery powered and a hydrogen powered aircraft. Since the chosen concept is still comparable to the reference aircraft and since the added value is still applicable to it, the general estimation made in the baseline report is still seen as valid for the H2Copter. However, the uncertainty of this estimation is increased, thus the standard deviation is more likely to be exceeded.

Thus, it is expected to be able to sell the hydrogen helicopter for $333,000.00 USD ± 26%. This corresponds to a minimum of $246,400.00 USD and a maximum of $419,600.00 USD.

Since a selling price has already been estimated, this market analysis will focus on the strategic aspects of market analysis. Questions such as 'What will be the long term goals for the helicopter?' (section 6.2) 'What environmental factors and which competitors require the attention of the helicopter design team?'(section 6.3), 'What are the strengths, weaknesses, opportunities of and threats to the helicopter design?'(section 6.4) and 'What must be the market strategy for the helicopter design team?'(section 6.5) will be answered in this chapter. This will be done by comparing the helicopter to a reference. For the baseline report, the automotive industry was used as a reference. This will be done again, specifically, the company Tesla is looked at. Tesla was chosen for its resemblance to the helicopter; they build electric, high quality exclusive cars and their market strategy is very interesting. Two Tesla market analyses were found [11, 12] and the strategic market for the helicopter will be analysed using these analyses as guidelines.

6.2. LONG TERM GOALS AND COMPETITIVE ADVANTAGE

To be able to come up with a market strategy, the long term goals for the helicopter must be defined. The objective statement for this project is to 'Present a two-seat helicopter design with commercial applications that has lower emissions than comparable conventional alternatives by using electric or hybrid electric propulsion, by ten students within ten working weeks'. This is a goal on a rather short timespan, only ten weeks. What is it that is to be accomplished in the future? Tesla defined its long term strategic goal as 'To create affordable mass market electric vehicles (EV)' [11]. This long term goal is focused on mass market. For the Helicopter, the long term goal is less focused on mass market production, more on the reduction of emissions by helicopters. A long term goal could therefore be: 'To provide affordable and practical alternatives to fuel burning and polluting helicopters'. Copying the strategy of Tesla , this goal will be achieved by:

- Selling hydrogen helicopters, first this model, in the future possibly a newer, better model
- Selling patented innovative technology, developed for the helicopter. This is also a method Tesla uses
- Providing an example to the industry, showing that it is possible to build clean helicopters

The competitive advantage of the helicopter will be its innovative, electric, silent design and the knowledge that comes with it. For the helicopter that is designed, no big advantage is yet to be identified. However, at the time where other players enter the electric helicopter market, it is expected that a lot of knowledge has been gathered and thus the exceptional expertise of the company is an advantage over newer players. Another advantage of the helicopter is the use of the newest technology all in one helicopter, making it efficient and silent.

6.3. Environment analysis

For a good market analysis, the environment the helicopter is in must be analysed. This will be done in two ways; a Political, Economic, Social, Technological, Environmental and Legal (PESTEL) analysis will be given, along with a competitor analysis.

6.3.1. PESTEL analysis

A PESTEL analysis describes the Political, Economic, Social, Technological, Environmental and Legal environment of the market. Since this is very early to make a detailed PESTEL analysis, the categories Legal and Political, as well as Environmental and social will be joined.

Political and legal

- Certification. The political and legal environment determines if and when the helicopter is certified, which is of course very important, as without certification, the helicopter might be dangerous and will thus never fly.
- Support programs for green development might be available from the government. This will go hand in hand with the requirements set by the government concerning the reduction of emission of greenhouse gasses.

Environmental and social

- Climate change is increasingly becoming a problem. The designers are aware of this and so are the consumers. This might drive an increase in demand for green solutions
- The designers are aware that they have to have a low carbon footprint for the whole production process, otherwise the main point of building a green helicopter is gone. This might complicate the design and production process.
- Consumers realise that fossil fuel might not be available at some point in time. This might increase demand for vehicles which do not rely on fossil fuels.

Technological

- The helicopter has a large range compared to other electric aircraft. This might spike interest, seeing as electric helicopters with a big range were not available until now.
- There will be a need for a Hydrogen charging infrastructure for the helicopter to be a commercial success. This is one of the bigger problems that has to be tackled. A hydrogen distribution network is currently very limited, if not non existent. This is one of Tesla's strong points; Tesla has created a fast charging network where 80% of the US is already covered. This has to be done for hydrogen in order for the helicopter to be a success. Of course, the company must first asses the different sectors which show interest in the helicopter. If, for instance, only police forces are interested in the H2Copter, it might be a waste to set up a large infrastructure that is only used in some places.

Economic

- At the time of writing, an economic growth is taking place. This will increase customer confidence, increasing the chance that customers will pay large sums of money. This is also seen in the car and house industry as they flourish due to economic growth.

6.3.2. Competitor analysis

Three possible competitors for the helicopter are Agusta westland, Sikorsky, E-volo and Robinson. Per competitor, the threat and approach will be discussed.

Augusta Westland

By producing its concept plane Project Zero, Agusta Westland expressed its interest in entering the electric aircraft market. However, this model is a tilt rotor, ducted fan concept that is supposed to run on batteries. This concept is not considered a direct threat as the applications of a tilt rotor concept are different than for a helicopter. However, due to its capability to fly using fixed wings, the concept would possibly be able to beat the helicopter on range. Agusta Westland is also a well known company with much experience in helicopter building, which could make for a difficult competitor. Agusta Westland should therefore be closely monitored. Tesla's approach w.r.t. competitors which do not pose a direct threat consists of raising brand awareness and improving global expansion before the more serious threats from these companies enter the market [11]. This approach should also be used for the helicopter company, keeping in mind the different kind of customers.

Sikorsky

With the production of the Sikorsky Firefly concept, Sikorsky also showed interest in entering the electric helicopter market. Just like Augusta Westland, Sikorsky is a well known company with much expertise in helicopter building. The Firefly concept is more of a threat than Agusta's Project Zero in terms of its resemblance to a conventional helicopter. However, since this helicopter runs on batteries, its range and endurance are far out-rivaled by the hydrogen helicopter. The innovative design of the H2Copter also poses a benefit over the conventional, boring Firefly design. Sikorski could however pose a great threat in the near future. Tesla deals with great threats by differentiation, that is gaining superiority by technological advancement. The strategy for the hydrogen helicopter would be to gain technological superiority in the time it takes for Sikorsky to build a helicopter of equal value, thus staying a step ahead of Sikorsky by gaining knowledge and expertise regarding electric helicopter drive trains and the fly-by-wire control system. This could for instance be achieved by developing and patenting the drive train inside the hub.

E-Volo

E-Volo is a company entirely dedicated to electric rotorcraft. Its threat is substantial, the Volocopter is a working prototype. However, just like Sikorsky, the Volocopter flies on batteries and thus relies on the improvement of batteries to achieve a bigger range and longer endurance. However, when the batteries improve, E-Volo will be one of the bigger competitors due to their unique concept and their expertise in the field of electric rotorcraft. The same strategy as for Sikorsky will be used; develop the unique drive-train-in-hub concept along with knowledge concerning electric hydrogen helicopters.

Robinson

Robinson Helicopters has so far not shown interest in the electric helicopter market. It is therefore not a substantial threat. However, when Robinson decides to enter the electric helicopter market, the team must be weary of Robinson's expertise regarding conventional helicopters. Robinson poses no direct threat, but should be closely monitored nonetheless.

6.4. SWOT analysis

In a SWOT analysis, all Strengths, Weaknesses, Opportunities of and Threats to the design are analysed. Strengths and weaknesses are internal to the design; opportunities and threats are due to the environment. A SWOT analysis for the helicopter is given in table 6.1. For this analysis, the SWOT analysis from Tesla was looked at. While most components were the same, some varied and some elements, like the helicopter certification, were added.

6.5. Market strategy

Based on all these analyses, what should the market strategy be for the helicopter design team? Looking at Tesla and the analyses given in the previous chapters, there are some methods for a new, expensive, electric vehicle to be able to compete with all the competitors. These methods are:

Table 6.1: SWOT Analysis for the helicopter design.

	Helpful	**Harmful**
Internal	**Strengths:** -The helicopter has a long range for an electric aircraft -The helicopter flies green -The helicopter is innovative	**Weaknesses:** -Helicopter requires big initial financial investment -Design is dependant on other electric vehicle innovation
External	**Opportunities:** -The prices of oil keep rising -Public awareness of global warming raises demand for electric vehicles -Government is forced to embrace green solutions, support electric vehicles -The electric helicopter industry is a young one; small amount of competitors and room for improvement -By designing a refueling infrastructure, a large part of the market can be taken	**Threats:** -Other companies will eventually enter market -The design and the hub are not proven -Certification could become complicated -Efficiency of combustion engines increases -Refueling infrastructure has yet to be built

- Staying ahead of competition by developing innovative techniques before the competition does. For the helicopter this would for instance be done by developing and patenting the new hub design.
- Patenting and selling innovative ideas
- Partnering up with companies that have expertise in fields that the design team could use
- Develop a refueling structure before competitors do so

As a final consideration, Bowman's strategic clock is looked at. This clock is shown in figure 6.1. Bowman's strategic clock has two axes, the horizontal axis represents the price of a product, the horizontal axis the perceived value to the customer. In the clock, 8 price/value strategies can be identified, in the form of a clock, hence the name. The strategies in the clock are:

1. Low price/Low added value. This is a strategy where one tries to make the product as cheap as possible, not taking the loss of value into consideration. An example of this strategy is the low pricing of c-brand products in supermarkets; they are cheap but not of high quality.
2. Low price. This strategy aims to achieve the lowest price for a product of reasonable quality. An example of this strategy is the low pricing of b-brand products in supermarkets; they are less cheap than c-brand products but of better quality.
3. Hybrid. This strategy aims to get good quality products for the least anoumt of money. This is a very good tactic but not feasible for small companies. To sell a product of value at a low price is only feasible for big companies who do not need a high profit margin to survive. An example for this tactic is the low pricing of a-brand high quality products by big super market chains.
4. Differentiation. This strategy aims to sell products of high value at a reasonable price. This strategy is for instance used by companies that sell normal use, normal quality cars.
5. Focused differentiation. This strategy sells high quality products at a high price. This strategy is mostly used by companies that sell exclusive products for a specific customer group, such as exclusive (sports) car companies (Tesla, Lamborghini etc.).
6. Risky, high margins. This strategy tries to sell medium value products for high pricing. This tactic is not feasible in the long run and thus doomed for failure.
7. Monopoly pricing. This tactic sells low value products for high prices. This tactic is only feasible without any competition present; thus only monopolists can use this tactic. An example is the pricing of legal documents that have to be bought from the government; an individual needs these documents but can not get them at another place and will thus buy these documents, regardless of the high price.

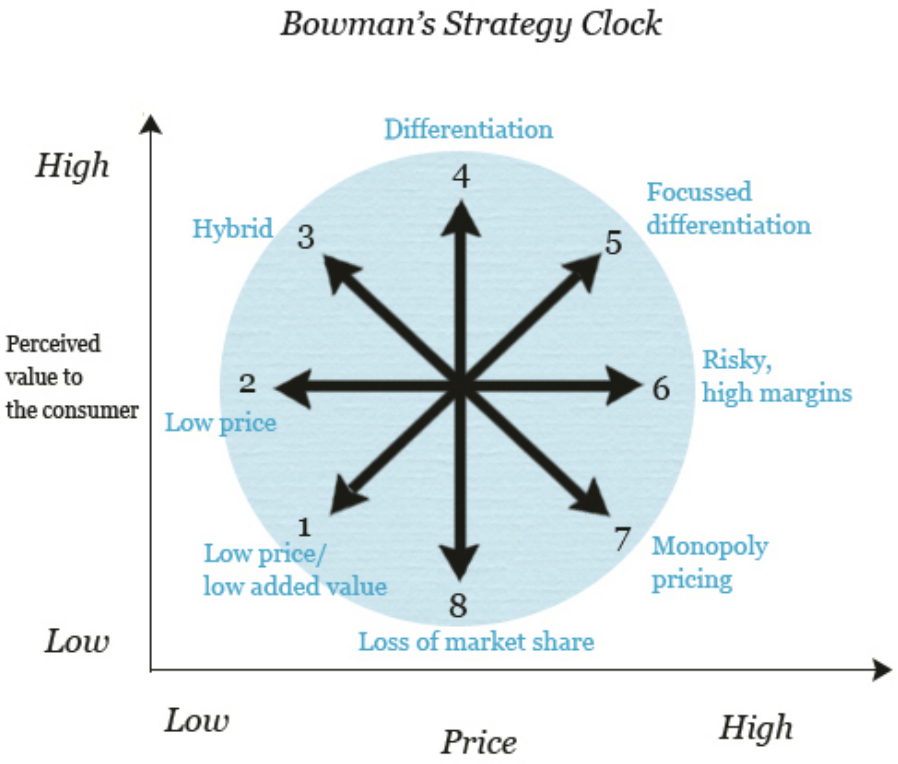

Figure 6.1: Bowman's Strategy Clock [13].

8. Loss of market share. This strategy sells products of no value for medium prices and will thus fail, since no customer will buy the product.

For new vehicle concepts, it is most frequently seen that the company begins with a tactic between 6 and 5. This is because the concept building costs a lot of money, selling for a low price is not yet feasible and the added value is not yet high enough for strategy 4. Thus, for the helicopter, rich customers with a drive to buy new innovative things will be targeted, just like Tesla. In the long run, cheaper helicopters should be built, moving the tactic more to strategy 4 in the clock. This is also the approach Tesla takes; with their model S they focused on rich males and now they are moving towards differentiation by introducing a more affordable car for the bigger public. Tesla can afford to do this because their production methods became cheaper due to their technical expertise and due to their brand name awareness, increasing interest amongst the general public.

Part II

Subsystem design

7

ROTOR

A coaxial rotor system is designed in the detail design phase of this project. In this chapter, the rotor system design process and corresponding results are presented. First the inputs and outputs are defined in section 7.1. The design process is explained in section 7.2, which contains a more elaborate description of the strategy to get from input to output. In section 7.3 the airfoil selection is discussed. The material selection and rotor blade structure follows in section 7.4. The next step is to look at the flow phenomena in the coaxial rotor system, which is done in section 7.5. In section 7.6 the aerodynamic coefficients are derived. When the analytical solution is known, the equations are numerically implemented in MATLAB, of which the procedure is explained in section 7.7. The final design results are presented in section 7.8. Finally, a sensitivity analysis is performed in section 7.9 and the verification and validation procedures and corresponding results are shown in section 7.10.

7.1. INPUT AND OUTPUT PARAMETERS

The input and output parameters are defined in an early stage of the design process. This is a first step to be performed in order to get a clear overview of which design output parameters are required from which input parameters. In tables 7.1 and 7.2 the input and the most important required output parameters are shown. Some outputs are solely relevant for the rotor design, while others (such as the Lock number γ) are also used for the design of other subsystems.

7.2. ROTOR DESIGN PROCESS

In order to get a clear overview of the strategy used to design the rotor system, the design process flowchart in figure 7.1 is made. This flowchart shows all the necessary design steps which are taken to arrive at the final rotor system design. The first step in the design process is the selection of an airfoil for the rotor, based on standard rotary wing airfoil criteria. From the airfoil specifications, C_{L_α} and C_{D_0} are found. These constants and the rotor mass per unit span m, found from the selected rotor material and structure, are needed for the calculation of the rotor aerodynamic coefficients. From the aerodynamic coefficients the thrust, power, H-force and torque are calculated for the upper and the lower rotor. If these results comply with the criteria indicated in figure 7.1, the output results are obtained. If not, iterations are necessary.

7.3. AIRFOIL SELECTION

The rotor blade airfoil is selected based on several important characteristics relevant for airfoils used in rotorcraft. For high lift generation, a high lift slope (C_{L_α}) is desired as well as a high maximum lift coefficient ($C_{L_{max}}$). A high stall angle is also important, so that lift can be generated for a larger range of angles of attack. For low drag, the lift to drag ratio, $\frac{C_L}{C_D}$, should be as high as possible. The drag divergence mach number, M_{DD}, should also be high in order to avoid the high drag that occurs beyond the M_{DD} airspeed.

Table 7.1: Input for the rotor design process.

Input	
W_0	Gross weight
RC	Climb rate
h	Mission altitude
V	Airspeed
N_b	Number of blades

Table 7.2: Output for the rotor design process.

Output			
R	Blade radius	Q	Rotor torque
θ	Blade pitch distribution	P	Rotor power
c	Blade chord	d	Rotor offset
Ω	Angular velocity	D	Rotor drag
W_r	Rotor weight	v_{ind}	Induced velocities
T	Rotor thrust	γ	Lock number

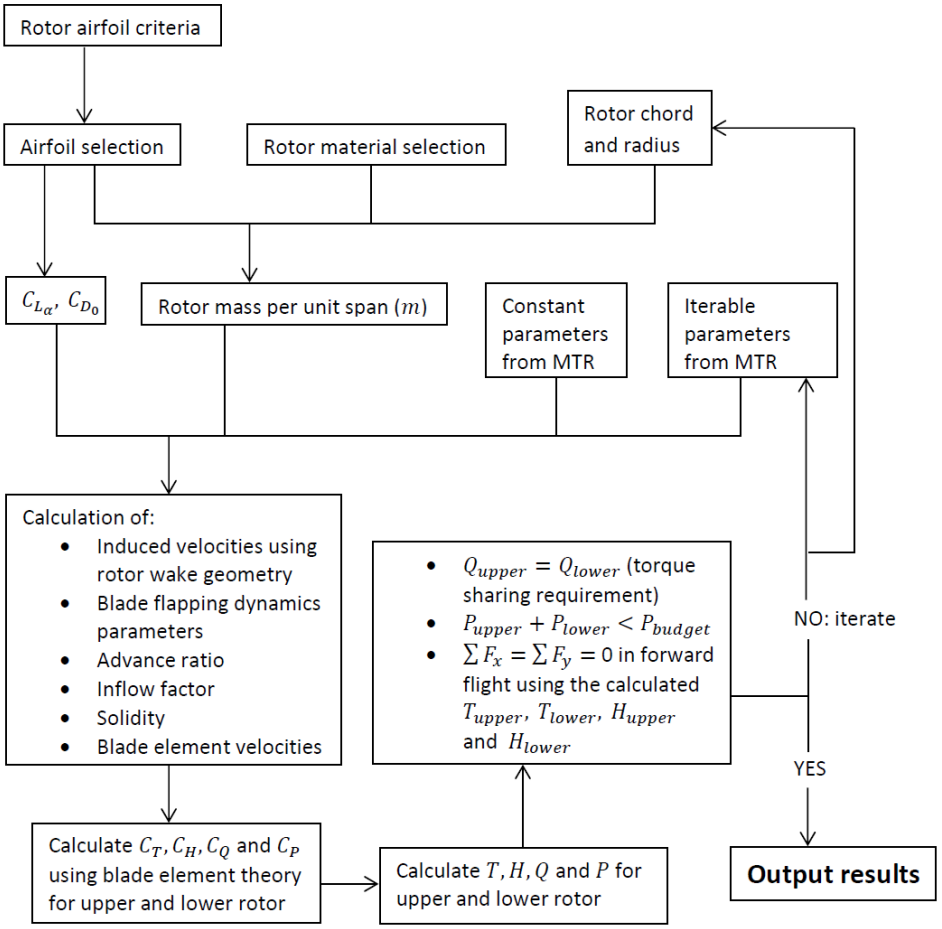

Figure 7.1: Rotor design process.

Airfoils that meet all these criteria are the VR12 - VR14, OA-3XX and DM-H3&4 families [14]. The VR12 airfoil is chosen for the design, because it has a particularly high stall angle and the data is easily accessible [15] as well. A sketch of the VR12 airfoil can be found in figure 7.2, and its important parameters are shown in table 7.3.

7.4. Rotor Materials and Structure

The first choice that has to be made is whether a metal or composite structure is more feasible for the design. Metal structures are easy to manufacture and relatively cheap. However, a composite structure is chosen as it is lighter and more resistant to corrosion, increasing its lifespan. Modern rotorcraft generally use composite rotor blade structures. A commonly used inner structure is shown in the rotor blade cross-section in figure 7.3 [16].

As can be seen, it consists of a skin with foam as core material. The leading cap, as indicated in the figure is often made of titanium for erosion protection. A non-structural mass can be added in order to shift the center

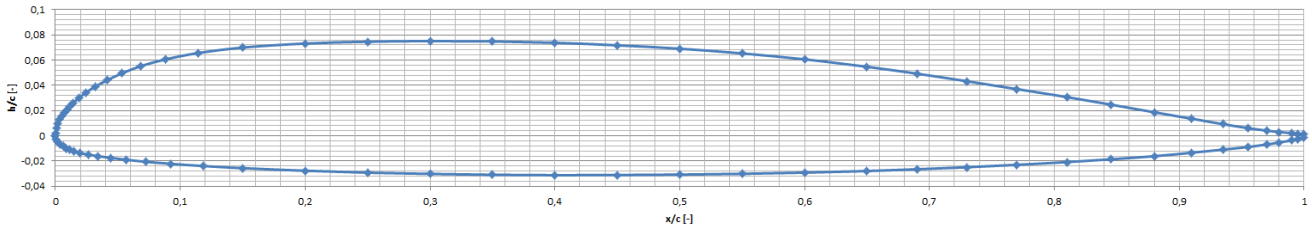

Figure 7.2: Schematic sketch of the VR12 rotor airfoil.

Table 7.3: Airfoil characteristics [15].

Parameter	Value	Unit	Parameter	Value	Unit
$C_{L_{max}}$	1.6	–	α at $\left(\frac{C_L}{C_D}\right)_{max}$	7	deg
$C_{L_{\alpha=0}}$	0.15	–	C_L at $\left(\frac{C_L}{C_D}\right)_{max}$	0.95	–
α_{stall}	19	deg	C_D at $\left(\frac{C_L}{C_D}\right)_{max}$	0.010	–
$C_{L_{alpha}}$	5.86	rad^{-1}	C_{m_0}	-0.004	–
$\left(\frac{C_L}{C_D}\right)_{max}$	94.4	–	$\left(\frac{t}{c}\right)_{max}$	0.08	–

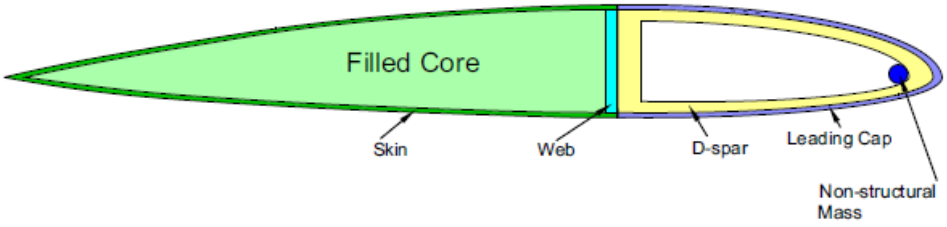

Figure 7.3: Sketch of the rotor structure [16].

of gravity of the structure. In order to make an estimation of the weight of the structure, several simplifying assumptions are made:

- The skin and leading cap are made of the same material.
- The D-spar is removed and the entire front chamber is filled with the same core material as the other chamber.
- The non-structural mass is removed, assuming the additional mass is low and is compensated somewhat with the additional core material.
- The web is made of the same material as the skin.
- The web is placed at the chord location with the highest thickness.

With these assumptions the only design variables are the skin thickness, web thickness and the material properties. The structure is placed in Autodesk Inventor as can be seen in figure 7.4. This is a program capable of calculating inner stresses in the structure from loading inputs applied on it, which can be implemented in the program. Using analytical calculations for inner stresses evaluations would be very challenging because of the airfoil shape which can not be defined as a function, since only separate airfoil coordinates are available.

Material selection

The materials chosen are carbon fibre reinforced plastic (CFRP) for the skin and web, and Compaxx 700-X foam for the core [17]. This foam is chosen because of its high strength and stiffness to weight ratio and is often used in wind turbine blades and rotors.

Implementation in Autodesk

The structure has to be able to withstand the forces on the rotor blade. As the stress in the root is the highest, the structure has to be sized so that it does not fail at this place. The rotor is made by extruding the structure

Figure 7.4: The structure implemented in Autodesk Inventor.

over the radius, not taking angle variations such as the manufactured blade twist into account. These angles are relatively small and it is assumed that they will not have a large impact on the stresses in the blade. The thrust force, which is estimated to be equal to the weight, is distributed equally over the radius, as a triangular force distribution is not possible to be implemented in the program. The program automatically takes the blade weight into account and an angular velocity (Ω = 45.2 rad/s [8]) is provided as an input to the program, out of which the program calculates the centrifugal force acting on the blade. The safety factor is set on 2.00 as a large number of assumptions are made. Using all these provided forces acting on the blade, the program calculates the inner stresses in the structure.

Structural design result

The skin thickness is set on 2 mm. This is an initial estimation in order to iterate for the thickness of the web, which is adjusted until the structure fails under the applied loading. The thickness for the web is then 7.8 mm and the weight is then 12.2 kg per blade. This means that the weight per unit span m is 2.71 kg/m, a parameter used for further calculations in section 7.6. After the final numerical design iterations resulting in the worst case scenario force distributions on the blade, these are implemented in Autodesk. The web thickness can be changed in Autodesk and the process is repeated until the calculated stress is beneath the maximum allowable material stress. The thickness of the skin has no significant effect on the resulting weight of the blade, thus no adjustments are made for it. Only the web thickness is therefore adjusted for iterations. The final weight is 48.8 kg for the complete coaxial rotor system.

7.5. Rotor wake geometry and aerodynamics

Before applying blade element theory for calculating the aerodynamic coefficients of the upper and lower rotor, it is important to understand the flow phenomena present in a coaxial rotor system during the different flight phases. The most important aerodynamic characteristic of this system is the interference between the wake generated by the upper rotor and the lower rotor. This causes the lower rotor to be subjected to a different average induced velocity compared to the upper rotor. The goal of the present section is to provide an analytical approach to describe the geometry of the wake interference of a coaxial rotor system in hover and forward flight, and to state a calculation procedure for the induced velocities on the upper and lower rotor in these flight phases.

7.5.1. Assumptions

The assumptions used to derive the analytical solution for the wake aerodynamic calculations of the coaxial rotor system are listed below.

- In hover, the lower rotor operates in the fully developed slipstream of the upper rotor.
- In hover, the area of the wake intersecting the lower rotor is half the disk area.
- In forward flight, the wake deflection is linear.
- In forward flight, the induced velocity across the lower rotor outside the wake is the same as the induced velocity across the upper rotor.
- In forward flight, the wake area intersecting the lower rotor can be approximated by a circular sector shape.
- The lower rotor does not aerodynamically affect the upper rotor in all flight phases.

7.5.2. Hover

Coaxial rotor momentum theory has been used to evaluate the induced velocities on the upper and lower rotors in hover. There exist four rotor system operating conditions in hover which are listed below [18]:

- Case 1: Rotors rotate in the same plane with thrust sharing, $T_l = T_u$.
- Case 2: Rotors rotate in the same plane with torque sharing, $Q_l = Q_u$.
- Case 3: $T_l = T_u$ with the lower rotor operating in the fully developed slipstream of the upper rotor.
- Case 4: $Q_l = Q_u$ with the lower rotor operating in the fully developed slipstream of the upper rotor.

Since rotor separation is needed for the rotors to safely operate without colliding and torque balance is needed to provide zero net torque to the fuselage, case 4 is of most interest. Therefore, for hover, induced velocity

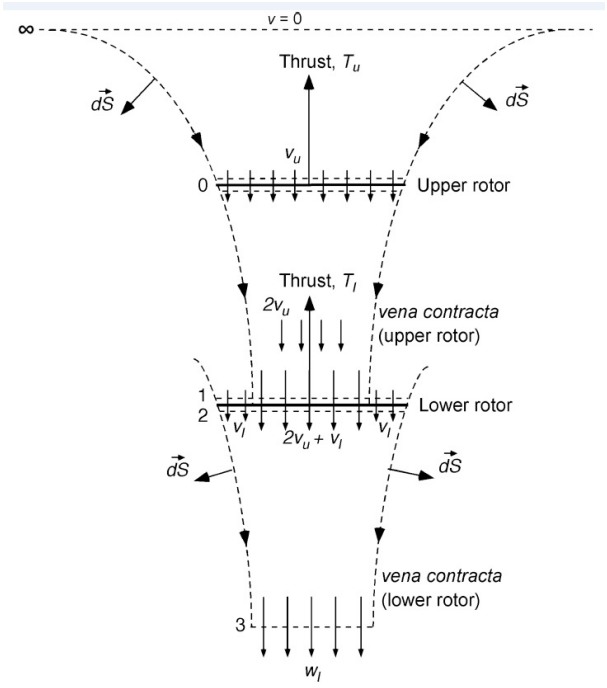

Figure 7.5: Induced velocities in hover [18].

calculations for the upper and lower rotor are performed using momentum theory which takes into account rotor torque sharing.

Upper rotor induced velocity

From standard momentum theory for coaxial rotors operating in a torque balanced condition in hover, equations 7.1 - 7.3 can be derived [19]. The parameters in these equations are illustrated in figure 7.5. Combining equations 7.2 - 7.4 results in the hover induced velocity of the upper rotor as a function of the maximum take off weight W, the density ρ and the rotor disk area A, given by equation 7.5.

$$v_{ind,l} = \frac{7}{16} v_{ind,u} \tag{7.1}$$

$$\frac{T_u}{T_l} = \frac{v_{ind,u} + v_{ind,l}}{v_{ind,u}} = 1 + \frac{v_{ind,l}}{v_{ind,u}} = \frac{23}{16} \tag{7.2}$$

$$v_{ind,u} = \sqrt{\frac{T_u}{2\rho A}} \tag{7.3}$$

$$T_u + T_l = W \tag{7.4}$$

$$v_{ind,u} = \sqrt{\frac{23W}{78\rho A}} \tag{7.5}$$

Equation 7.5 is the hover induced velocity of the upper rotor which is used for the derivation of the aerodynamic coefficients of the upper and lower rotor in both hover and forward flight conditions.

Lower rotor induced velocity

The induced velocity on the lower rotor in the area affected by the upper rotor wake is higher than the induced velocity across the area outside the wake. The area on the lower rotor affected by the upper rotor wake in hover conditions is illustrated in figure 7.6. It is assumed that the lower rotor operates in the fully developed slipstream of the upper rotor. The area of the lower rotor affected by the wake of the upper rotor is half the total disk area A. The induced velocity across this area is the sum of the upper rotor wake velocity when it is fully developed at the time it arrives at the lower rotor, $2v_u$, and the induced velocity on the lower rotor, v_l.

Combining this information with equation 7.1, the induced velocity across the area on the lower rotor affected by the wake of the upper rotor is derived in equation 7.6. The induced velocity on the lower rotor across the area outside the upper rotor wake is given by equation 7.7.

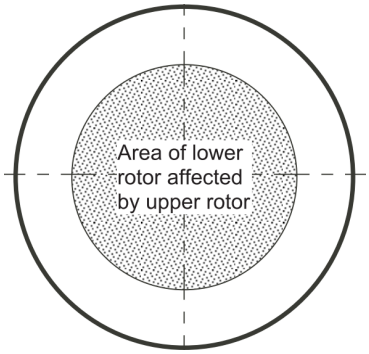

Figure 7.6: Area lower rotor affected by upper rotor in hover [19].

$$\left(v_{ind,l}\right)_{wake} = 2v_{ind,u} + v_{ind,l} = 2v_{ind,u} + \frac{7}{16}v_{ind,u} = \frac{39}{16}v_{ind,u} = \frac{39}{16}\sqrt{\frac{23W}{78\rho A}} \tag{7.6}$$

$$v_{ind,l} = \frac{7}{16}v_{ind,u} = \frac{7}{16}\sqrt{\frac{23W}{78\rho A}} \tag{7.7}$$

Equations 7.6 and 7.7 are therefore used in the numerical program in the end to calculate the induced velocity distribution across the lower rotor in hover. The induced velocities across the upper and lower rotor in forward flight depend on the upper rotor hover induced velocity and not on the lower rotor hover induced velocities, as is explained in section 7.5.3.

7.5.3. Forward Flight

Rotor Wake Skew Angle

A schematic of the side view of a coaxial rotor system in forward flight is presented in figure 7.7. The upper rotor generates a wake which intersects the lower rotor disk. The three areas 1,2 and 3 represent the upper rotor, the lower rotor outside the wake generated by the upper rotor and the lower rotor inside the wake, respectively. Since the cruise velocity is relatively high, it has been assumed that the wake deflection is of linear nature, since its linearity increases with forward flight velocity. The wake skew angle χ is defined as the angle between the plane perpendicular to the rotor disk and the wake line, and depends on μ_x and μ_y, the advance ratios parallel and perpendicular to the rotor disk, and $(\lambda_i)_{av}$, the average induced inflow factor [20]. The derivation of the skew angle is shown in equation 7.8.

$$\chi = \arctan\left(\frac{\mu_x}{\mu_y + (\lambda_i)_{av}}\right) = \arctan\left(\frac{\frac{V\cos(\alpha_r)}{\Omega R}}{\frac{V\sin(\alpha_r)}{\Omega R} + \frac{(v_{ind})_{av}}{\Omega R}}\right) = \arctan\left(\frac{V\cos(\alpha_r)}{V\sin(\alpha_r) + (v_{ind})_{av}}\right) \tag{7.8}$$

The wake skew angle increases with the flight velocity, since a larger horizontal velocity component causes a larger deflection of the upper rotor wake.

Wake Area on the Lower Rotor

As can be noted from figure 7.7, the magnitude of the wake skew angle determines the area of the lower rotor inside the wake from the upper rotor. This area decreases as the skew angle increases and is given by A in figure 7.8. This figure gives the top view of figure 7.7. The parameter f represents the distance between the centre points of the lower rotor and the upper rotor wake, and is indicated both in figure 7.7 and 7.8. It is given by equation 7.9, following from trigonometry in figure 7.7. The distance d is the rotor separation distance.
The induced velocities across the lower rotor in the regions inside and outside the wake from the upper rotor differ from each other. To be able to visualize the induced velocity variation over the lower rotor, the area of the lower rotor intersecting the wake from the upper rotor, A, needs to be expressed as a function of the rotor radius R, the rotor separation distance d and the skew angle χ. After performing some mathematical manipulations in a Cartesian $x-y$ coordinate system with the origin in the centre of the lower rotor in figure 7.8, the resulting area A is expressed in equation 7.10 with f given by equation 7.9.

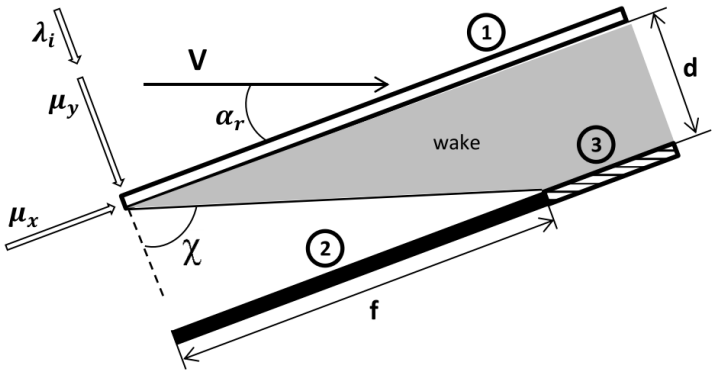

Figure 7.7: Coaxial rotor wake geometry in forward flight.

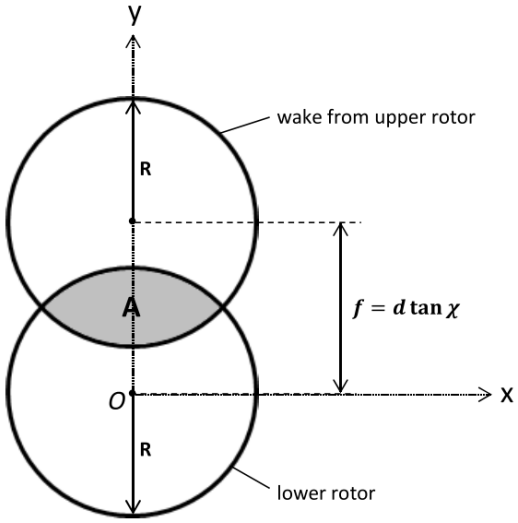

Figure 7.8: Intersection of wake from upper rotor with lower rotor.

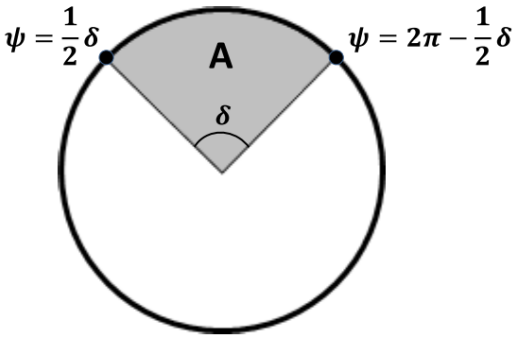

Figure 7.9: Wake area approximation on lower rotor.

$$f = d\tan(\chi) \tag{7.9}$$

$$A = \int_{-\sqrt{R^2-\frac{1}{4}f^2}}^{\sqrt{R^2-\frac{1}{4}f^2}} \left(2\sqrt{R^2-x^2} - f\right) dx \tag{7.10}$$

Equations 7.9 and 7.10 are used as inputs for approximating the lower rotor wake area in figure 7.8 for its numerical implementation as explained in section 7.5.3.

Lower rotor wake area approximation

Having evaluated the wake area A on the lower rotor given by equation 7.10 at this point, it remains to be determined from figure 7.8, per rotor revolution, what the percentage of the azimuth angle ψ is in which the lower rotor is inside the wake and which percentage of the rotor radius passes through the wake. This information is required for calculating the aerodynamic coefficients of the lower rotor at a later stage. As will be explained in section 7.6, this calculation uses a double integral to calculate the aerodynamic coefficients, averaged for the whole rotor per revolution. The first integral integrates over the azimuth angle ψ and is needed for azimuth averaging. The second integral integrates over the rotor radial position r, defined as $r = \frac{y}{R}$ (see figure 7.13). The wake area shown in figure 7.8, however, does not enable one to apply this method since the upper and lower boundaries representing the radial positions of the rotor inside the wake, in the integral integrating over the radial position, will constantly vary as the rotor passes through the wake. Therefore, a proposed approximation of the lower rotor wake area from figure 7.8 is shown in figure 7.9, which effectively enables one to determine the upper and lower boundaries for both the radial positions and azimuth angles in order to calculate the aerodynamic coefficients of the lower rotor. The aim is to find the angle δ in figure 7.9 such that the area A there is equal to the area A from figure 7.8. Equation 7.11 is used to calculate the angle δ for a given area

A from figure 7.8.

$$\delta = \frac{2A}{R^2} \tag{7.11}$$

The induced velocity variation on the lower rotor will therefore depend on the angle δ, representing the part of the rotor revolution over which the upper rotor wake is present on the lower rotor. The aerodynamic coefficients corresponding to the lower rotor depend on the induced velocity distribution as elaborated on in section 7.6.

General rotor induced velocity in forward flight

The general expression for the induced velocity across a rotor subjected to a forward flight velocity V and a rotor disk inclination angle with respect to the horizon α_r is expressed in equation 7.13 in which $(v_i)_0$ is given by equation 7.12 [21]. The parameter v_{ih} is the induced velocity across the particular rotor when it operates in hover. The term $(1 + Kr\cos(\psi))$ is a correction term for the forward flight induced velocity, which takes into account the fact that in practice the induced velocity is not constant over the entire rotor disk area, but varies as a function of the radial position r and the azimuth angle ψ. The parameter K is a constant, typically chosen to be equal to 1.2 [21]. As can be seen from equation 7.12, the term $(v_i)_0$ is present both at the left and right side of the equation. Therefore, this equation needs to be solved numerically for $(v_i)_0$ at the stage the other parameters in it are known, after which the induced velocity in forward flight can be expressed as a function of r and ψ using equation 7.13. In some calculations, it is more appropriate to have an average numerical value for the induced velocity, which can be calculated using equation 7.14.

$$(v_i)_0 = \sqrt{\frac{v_{ih}^2}{\left(\frac{V}{v_{ih}}\cos(\alpha_r)\right)^2 + \left(\frac{V}{v_{ih}}\sin(\alpha_r) + \frac{(v_i)_0}{v_{ih}}\right)^2}} \tag{7.12}$$

$$v_{ind} = (v_i)_0\left(1 + Kr\cos(\psi)\right) \tag{7.13}$$

$$(v_{ind})_{av} = \int_0^1 \int_0^{2\pi} \frac{1}{2\pi} v_{ind}\, d\psi\, dr \tag{7.14}$$

Equation 7.13 is used in section 7.6 to determine the aerodynamic coefficients of the upper and lower rotors in forward flight.

Upper rotor induced velocity

In figure 7.7, the **induced velocity on the upper rotor across area** (1) in forward flight is given by equation 7.13 with $(v_i)_0$ given by equation 7.12 in which v_{ih} in this case is the hover induced velocity of the upper rotor given by equation 7.5.

Lower rotor induced velocity

The induced velocity across the lower rotor in forward flight is higher in the part inside the wake from the upper rotor than in the part outside the wake. It is assumed that the lower rotor does not aerodynamically affect the upper rotor in any flight phase. It is known that for the lower rotor, the higher its forward flight velocity, the more it behaves like the upper rotor as an independent rotor from an aerodynamic perspective. In figure 7.7, it is therefore assumed that the **induced velocity across area** (2) is the same as the induced velocity across the upper rotor in forward flight, given by area 1. Since the upper rotor wake deflection in forward flight is linear, and therefore without contraction, it is assumed that the wake velocity arriving at the lower rotor at area 3 does not change with respect to the induced velocity across the upper rotor in area 1. The total **induced velocity across area** (3) consists of the sum of the upper rotor wake velocity arriving at area 3 and the induced velocity across the lower rotor in area 2. It is therefore equal to twice the induced velocity across area 2.

7.6. Analytical derivation of aerodynamic coefficients

In this section, the aerodynamic coefficients C_T, C_H, C_Q and C_P of the upper and lower rotor are derived for the forward flight phase. After each coefficient derivation, it will be explained which input parameters should be adjusted for them to be valid for the hover and climbing flight phases. The aerodynamic coefficients are then used to calculate the thrust, H-force, torque and power of the upper and lower rotor.

7.6.1. THRUST COEFFICIENT

The first step for calculating the thrust coefficient is to use given input parameters to calculate certain basic design parameters. From the given cruise altitude h, the density ρ is calculated using equation 7.15 from the ISA standard atmosphere.

$$\rho = \rho_0 \left(\frac{T_0 + a_h h}{T_0} \right)^{-\frac{g}{a_h R} - 1} \tag{7.15}$$

The cruise velocity V, the rotor disk inclination α_r, the rotational rotor speed Ω, the rotor radius R, the number of blades N_b, the chord c and the rotor induced velocity v_{ind} are used to calculate the advance ratio μ, the inflow factor λ, the solidity σ and the aspect ratio AR using equations 7.16 - 7.19 respectively [21].

$$\mu = \frac{V \cos(\alpha_r)}{\Omega R} \tag{7.16}$$

$$\lambda = \mu \tan(\alpha_r) + \frac{v_{ind}}{\Omega R} = \mu \tan(\alpha_r) + \lambda_i \tag{7.17}$$

$$\sigma = \frac{N_b c}{\pi R} \tag{7.18}$$

$$AR = \frac{R}{c} \tag{7.19}$$

The variables given by equations 7.16 - 7.18 are important design parameters, often returning in the derivation of the aerodynamic coefficients in this section.

BLADE FLAPPING DYNAMICS

The resultant velocities the blade element sees depend on the blade flapping dynamics. This can be seen in figure 7.10. A varying flapping angle β will result in varying velocities the blade element sees around one revolution. Therefore, expressions describing blade flapping dynamics need to be derived which is done in the present section.

The two main parameters representing blade flapping dynamics, which are useful for the derivation of the aerodynamic coefficients, are the blade flapping angle β shown in figure 7.10, and its derivative with respect to the azimuth angle ψ. These parameters are both expressed in Fourier series expansions in equations 7.20 and 7.21 [21]. The Fourier series are taken up to an accuracy of three terms, consisting of the coefficients a_0, a_1 and b_1. These coefficients, expressed in equations 7.22 - 7.24, depend on the mass moment of inertia of the blade I in equation 7.25, the Lock number γ in equation 7.26, an estimate for the average twist θ_{av}, the advance ratio μ, and the inflow factor λ [21].

$$\beta = a_0 - a_1 \cos(\psi) - b_1 \sin(\psi) \tag{7.20}$$

$$\frac{d\beta}{d\psi} = a_1 \sin(\psi) - b_1 \cos(\psi) \tag{7.21}$$

$$a_0 = \frac{1}{8}\gamma \left(\theta_{avg} \left(1 + \mu^2\right) - \frac{4\lambda}{3} \right) \tag{7.22}$$

$$a_1 = \frac{\mu \left(\frac{8}{3}\theta_{avg} - 2\lambda \right)}{1 - \frac{1}{2}\mu^2} \tag{7.23}$$

$$b_1 = \frac{4\mu a_1}{3\left(1 + \frac{1}{2}\mu^2\right)} \tag{7.24}$$

$$I = \frac{1}{3} m R^3 \tag{7.25}$$

$$\gamma = \frac{\rho C_{L_\alpha} c R^4}{I} \tag{7.26}$$

Equations 7.20 - 7.26 therefore represent the main blade flapping dynamics parameters, used in the next section to derive the velocities seen by a blade element in forward flight.

BLADE ELEMENT VELOCITIES

The constant inputs, the basic design parameters and the blade flapping dynamics calculations serve as inputs to determine the resultant velocities U_T, U_R and U_P seen by a blade element in forward flight. The expressions for these velocities are derived from trigonometric relationships using figures 7.10 - 7.13, which visualise all velocities and forces a rotor blade element is exposed to in forward flight condition, using different rotor viewing perspectives.

The velocity component U_T, visualized in figures 7.11 and 7.13, is parallel to the rotor rotational plane and perpendicular to the rotor blade. It is therefore the sum of the rotational rotor velocity V and the component of the forward flight velocity parallel to the rotor disk plane (depending on α_r) which is in turn made perpendicular to the rotor blade (depending on ψ). Equation 7.27 is therefore used to calculate U_T [21].

The velocity component U_R, visualized in figures 7.10 and 7.13, is the spanwise velocity component obtained from the forward flight velocity and the angles α_r and ψ, expressed in equation 7.28 [21].

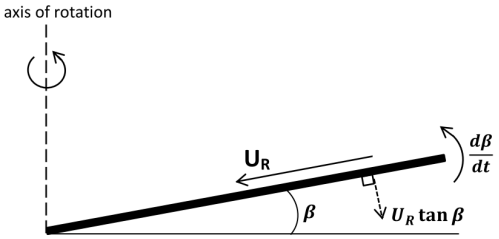

Figure 7.10: Rotor front view.

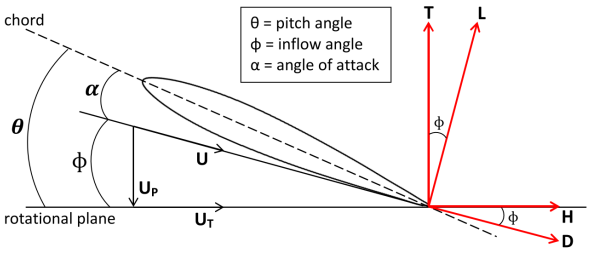

Figure 7.11: Blade element in forward flight.

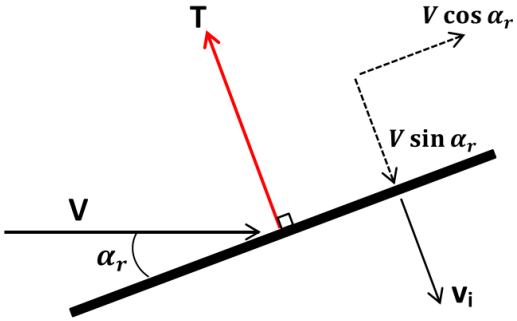

Figure 7.12: Rotor side view.

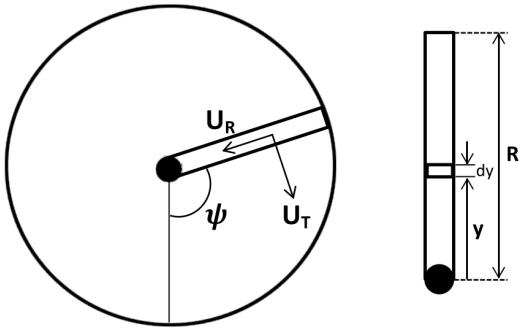

Figure 7.13: Rotor top view.

The velocity component U_P, visualized in figure 7.11, is the velocity component on the rotor blade perpendicular to the rotational plane. It is composed of the perpendicular rotor forward velocity component, the induced velocity, the component of U_R normal to the blade in case the blade has a nonzero flapping angle (as can be seen in figure 7.10) and a component resulting from the angular blade motion about the flapping hinge ($= y\frac{d\beta}{dt} = y\frac{d\beta}{d\psi}\cdot\frac{d\psi}{dt} = y\Omega\frac{d\beta}{d\psi} = rR\Omega\frac{d\beta}{d\psi}$) illustrated in figure 7.10. The resulting expression for U_P is given in equation 7.29 [21].
The resulting velocity seen by a blade element in forward flight U, illustrated in figure 7.11, is given by equation 7.30.

$$U_T = \Omega y + V\cos(\alpha_r)\sin(\psi) \tag{7.27}$$

$$U_R = V\cos(\alpha_r)\cos(\psi) \tag{7.28}$$

$$U_P = V\sin(\alpha_r) + v_{ind} + U_R\tan(\beta) + rR\Omega\frac{d\beta}{d\psi} \tag{7.29}$$

$$U = \sqrt{U_P^2 + U_T^2} \tag{7.30}$$

In some cases in the further aerodynamic coefficient derivation, it is useful to have a non-dimensionalized form of the velocities U_T, U_R and U_P. Dividing these velocities by the term ΩR results in expressions for u_T, u_R and u_P, given by equations 7.31 - 7.33 [21].

$$u_T = r + \mu\sin(\psi) \tag{7.31}$$

$$u_R = \mu\cos(\psi) \tag{7.32}$$

$$u_P = \mu\tan(\alpha_r) + \lambda_i + u_R\tan(\beta) + r\frac{d\beta}{d\psi} = \lambda + u_R\tan(\beta) + r\frac{d\beta}{d\psi} \tag{7.33}$$

Equations 7.31 - 7.33 are derived as these can often be used to simplify long equations to some extent by their substitution.

Derivation of the upper and lower rotor C_T

The thrust coefficient is derived starting from a calculation of the angles a blade element in forward flight is exposed to. These angles are the pitch angle θ, the inflow angle ϕ and the angle of attack α, illustrated in figure 7.11. The pitch angle θ is defined as the angle between the chord and the rotational plane, the inflow angle ϕ is the angle between the resultant velocity U seen by the blade element and the rotational plane, and the angle of attack α is the angle between the chord and the resultant velocity U. These angles are calculated using the blade element velocity results from section 7.6.1. The angle of attack given by equation 7.34 depends on the resultant pitch angle θ and the inflow angle ϕ. It follows from the definitions of α, θ and ϕ in figure

7.11. The total pitch angle θ in equation 7.35 in turn depends on the collective pitch angle θ_{col} applied by the pilot, the manufactured blade twist distribution $\theta(r)$ and the cyclic pitch $\theta(\psi)$. The cyclic pitch is given by a Fourier series expansion in equation 7.36 from which the coefficients $\theta_{c,r}$ and $\theta_{c,l}$ need to be determined at a later stage. The inflow angle ϕ given by equation 7.37 follows from trigonometry in figure 7.11. Substituting equations 7.35 - 7.37 into equation 7.34, the final equation for the angle of attack is found and expressed in equation 7.38 [21].

$$\alpha = \theta - \phi \tag{7.34}$$

$$\theta = \theta_{col} + \theta(r) + \theta_c(\psi) \tag{7.35}$$

$$\theta_c(\psi) = \theta_{c,r}\sin(\psi) + \theta_{c,l}\cos(\psi) \tag{7.36}$$

$$\phi = \arctan\left(\frac{U_P}{U_T}\right) \tag{7.37}$$

$$\alpha = \theta_{col} + \theta(r) + \theta_{c,r}\sin(\psi) + \theta_{c,l}\cos(\psi) - \arctan\left(\frac{U_P}{U_T}\right) \tag{7.38}$$

At this point, all information is available for determining the thrust coefficient in forward flight and hover for a given rotor. The incremental thrust coefficient of a blade element, following from geometry in figure 7.11, is defined in equation 7.39 [21].

$$dC_T = \frac{dT}{\rho A(\Omega R)^2} = \frac{dL\cos(\phi) - dD\sin(\phi)}{\rho A(\Omega R)^2} = \frac{\frac{1}{2}\rho U^2 c\,dy\left[C_l\cos(\phi) - C_d\sin(\phi)\right]}{\rho\pi R^2(\Omega R)^2} \tag{7.39}$$

From trigonometry in figure 7.11, equation 7.40 can be deduced.

$$U = \frac{U_T}{\cos(\phi)} \rightarrow \frac{U}{\Omega R} = \frac{U_T}{\Omega R\cos(\phi)} = \frac{u_T}{cos(\phi)} \tag{7.40}$$

If the number of rotor blades is N_b, the total incremental rotor blade element thrust coefficient becomes, after substituting equation 7.40 into equation 7.39, using the solidity σ defined by equation 7.18, and the equation $dy = Rdr$:

$$(dC_T)_{forw} = \frac{\frac{1}{2}\sigma {u_T}^2\left[C_L\cos(\phi) - C_D\sin(\phi)\right]}{\cos^2(\phi)}dr \tag{7.41}$$

To calculate the thrust coefficient of the upper rotor in forward flight $(C_{T_u})_{forw}$, which could be either climbing or cruise flight, the incremental blade element thrust coefficient needs to be integrated from the root to the tip of the blade, from $r = 0$ to 1. Furthermore, the incremental blade element thrust coefficient is indirectly a function of the azimuth angle ψ. Therefore, the rotor thrust coefficient will constantly vary around each revolution. This means that a second integral is needed for azimuth averaging, which is performed by integrating the expression for the incremental thrust coefficient from $\psi = 0$ to 2π and dividing the result by 2π [21]. The final result for the **upper rotor thrust coefficient in forward flight** is expressed in equation 7.42. The blade element lift coefficient C_L in equation 7.41 is assumed to vary linearly with the angle of attack, $C_L = C_{L_\alpha}\alpha + C_{L_{\alpha=0}}$, and the blade element drag coefficient C_D is assumed to be equal to its profile drag coefficient, C_{D_0}.

$$\left(C_{T_u}\right)_{forw} = \int_0^1\int_0^{2\pi}\frac{1}{2\pi}(dC_T)_{forw}\,d\psi\,dr = \int_0^1\int_0^{2\pi}\frac{1}{2\pi}\frac{\frac{1}{2}\sigma u_T^2\left[C_{L_\alpha}\alpha\cos(\phi) - C_{D_0}\sin(\phi)\right]}{\cos^2(\phi)}d\psi\,dr \tag{7.42}$$

The thrust coefficient of the upper rotor in equation 7.42 indirectly depends on the induced velocity across the upper rotor, for which a single expression exists which is derived in section 7.5.3. Since for the upper rotor there is only one expression for the induced velocity which is valid for the entire rotor disk in forward flight, the azimuth averaging for the integration for the thrust coefficient for the upper rotor is performed using the lower and upper boundaries of 0 and 2π for ψ. However, for the lower rotor, as can be seen in figure 7.9, the thrust coefficient needs to be calculated as the sum of the average thrust coefficients of the parts of the rotor disk inside and outside of the upper rotor wake. Therefore, the azimuth averaging for the calculation of the thrust coefficient of the lower rotor needs to be performed separately for these parts. The boundaries for the radial position r are still taken from 0 to 1 for both parts inside and outside of the wake, since for a given rotor blade position anywhere in its revolution the induced velocity does not vary from $r = 0$ to 1. Therefore, the resulting expression for the **lower rotor thrust coefficient in forward flight** is given by equation 7.43. For the evaluation of the first term in equation 7.43, the induced velocity across area 2 in figure 7.7 is used. For the second term, the induced velocity across area 3 in figure 7.7 is used.

$$
\begin{aligned}
(C_{T_l})_{forw} = &\int_0^1 \int_{\frac{1}{2}\delta}^{2\pi-\frac{1}{2}\delta} \frac{1}{2\pi} \frac{\frac{1}{2}\sigma u_T^2 \left[C_{L_\alpha}\alpha\cos(\phi) - C_{D_0}\sin(\phi)\right]}{\cos^2(\phi)} d\psi dr \\
&+ \int_0^1 \int_{2\pi-\frac{1}{2}\delta}^{\frac{1}{2}\delta} \frac{1}{2\pi} \frac{\frac{1}{2}\sigma u_T^2 \left[C_{L_\alpha}\alpha\cos(\phi) - C_{D_0}\sin(\phi)\right]}{\cos^2(\phi)} d\psi dr
\end{aligned}
\tag{7.43}
$$

For hover, the upper and lower rotor thrust coefficients are derived in the same way as for the forward flight phase. The difference is that for hover, different expressions for the induced velocities across the upper and lower rotor are used in the final equation for the thrust coefficient. Furthermore, $V = 0$ and $\alpha_r = 0$ in hover. Setting these parameters equal to zero, equation 7.40 is adapted to equation 7.44.

$$
U = \frac{U_T}{\cos(\phi)} = \frac{\Omega y}{\cos(\phi)} \rightarrow \frac{U}{\Omega R} = \frac{\Omega y}{\Omega R \cos(\phi)} = \frac{r}{\cos(\phi)} \tag{7.44}
$$

Using equation 7.44, equation 7.39 is adapted to equation 7.45 for hover.

$$
(dC_T)_{hov} = \frac{\frac{1}{2}\sigma r^2 \left[C_L\cos(\phi) - C_D\sin(\phi)\right]}{\cos^2(\phi)} dr \tag{7.45}
$$

The **thrust coefficient for the upper rotor in hover** is therefore given by equation 7.46. The induced velocity used to calculate it is given by equation 7.5.

$$
(C_{T_u})_{hov} = \int_0^1 \int_0^{2\pi} \frac{1}{2\pi} (dC_T)_{hov}\, d\psi dr = \int_0^1 \int_0^{2\pi} \frac{1}{2\pi} \frac{\frac{1}{2}\sigma r^2 \left[C_L\cos(\phi) - C_D\sin(\phi)\right]}{\cos^2(\phi)} d\psi dr \tag{7.46}
$$

For the lower rotor in hover, the induced velocities over the lower rotor per revolution are constant over the azimuth angle ψ but vary over the rotor radial position r as can be seen in figure 7.6. The opposite is true for the forward flight phase in which the induced velocities vary over the azimuth angle ψ and are constant over the radial position r per lower rotor revolution as can be seen in figure 7.9. Therefore, the **thrust coefficient of the lower rotor in hover** is given by equation 7.47. The boundaries containing the term $\frac{1}{2}\sqrt{2}$ in the integrals come from the fact that the wake on the lower rotor in hover ends at a radial position of $r = \frac{1}{2}\sqrt{2}$, since the lower rotor area affected by the wake is half the total disk area in hover [19].

$$
\begin{aligned}
(C_{T_l})_{hov} = &\int_0^{\frac{1}{2}\sqrt{2}} \int_0^{2\pi} \frac{1}{2\pi} \frac{\frac{1}{2}\sigma r^2 \left[C_{L_\alpha}\alpha\cos(\phi) - C_{D_0}\sin(\phi)\right]}{\cos^2(\phi)} d\psi dr \\
&+ \int_{\frac{1}{2}\sqrt{2}}^1 \int_0^{2\pi} \frac{1}{2\pi} \frac{\frac{1}{2}\sigma r^2 \left[C_{L_\alpha}\alpha\cos(\phi) - C_{D_0}\sin(\phi)\right]}{\cos^2(\phi)} d\psi dr
\end{aligned}
\tag{7.47}
$$

The induced velocities used to calculate the first and second terms of equation 7.47 are given by equations 7.6 and 7.7 respectively.

The thrust coefficients of both upper and lower rotors are now derived for the hover and forward flight conditions. These thrust coefficients are used to determine the thrust of the upper and lower rotor in these flight phases using equations 7.48 and 7.49 [21].

$$
T_u = C_{T_u}\rho\pi R^2(\Omega R)^2 \tag{7.48}
$$

$$
T_l = C_{T_l}\rho\pi R^2(\Omega R)^2 \tag{7.49}
$$

As can be noted, the rotor thrust follows directly from the thrust coefficient corresponding to the particular rotor, the air density ρ, the rotor radius R and the rotor rotational speed Ω. The latter three parameters are also used to calculate the thrust coefficients C_{T_u} and C_{T_l}. It now remains to determine expressions for the H-force, torque and power delivered by the rotors in sections 7.6.2 and 7.6.3.

7.6.2. H-FORCE COEFFICIENT

The H-force is the sum of the components of the lift and drag forces parallel to the rotor rotational plane, illustrated in figure 7.11. It is therefore a good representation of the aerodynamic rotor drag. The elementary H-force on a blade element resolved in rearward direction parallel to the flight velocity by the azimuth angle ψ is given by equation 7.50. It consists of the lift and drag dependent terms dH_0 and dH_i. The lift dependent term is, as can also be observed from figure 7.11, small as compared to the drag dependent term and can therefore be neglected. The resulting incremental H-force is therefore given by equation 7.51 [21].

$$dH = \left(dD\cos(\phi) + dL\sin(\phi)\right)\sin(\psi) = dH_0 + dH_i \tag{7.50}$$

$$dH_0 = dD\cos(\phi)\sin(\psi) = \frac{1}{2}\rho U^2 c C_{D_0}\cos(\phi)\sin(\psi)dy \tag{7.51}$$

The incremental H-force coefficient is given by equation 7.52, obtained by normalizing equation 7.51 [21]. Following the same reasoning as for the thrust coefficient, the **H-force coefficients in forward flight and hover of the upper and lower rotors** are given by equations 7.53 - 7.56. In hover, the forward flight velocity V is zero, resulting in an advance ratio of $\mu = 0$, reducing the term inside the integrals in equations 7.55 and 7.56.

$$dC_{H_0} = \frac{\frac{1}{2}N_b U^2 c C_{D_0}\cos(\phi)\sin(\psi)dy}{\pi R^2(\Omega R)^2} = \frac{\frac{1}{2}{u_T}^2 C_{D_0}\sigma\sin(\psi)}{\cos(\phi)}dr \tag{7.52}$$

$$\left(C_{H_u}\right)_{forw} = \frac{1}{2}\sigma C_{D_0}\int_0^1\int_0^{2\pi}\frac{1}{2\pi}\frac{\left(r+\mu\sin(\psi)\right)^2}{\cos(\phi)}\sin(\psi)d\psi dr \tag{7.53}$$

$$\begin{aligned}\left(C_{H_l}\right)_{forw} = &\frac{1}{2}\sigma C_{D_0}\int_0^1\int_{\frac{1}{2}\delta}^{2\pi-\frac{1}{2}\delta}\frac{1}{2\pi}\frac{\left(r+\mu\sin(\psi)\right)^2}{\cos(\phi)}\sin(\psi)d\psi dr\\ &+\frac{1}{2}\sigma C_{D_0}\int_0^1\int_{2\pi-\frac{1}{2}\delta}^{\frac{1}{2}\delta}\frac{1}{2\pi}\frac{\left(r+\mu\sin(\psi)\right)^2}{\cos(\phi)}\sin(\psi)d\psi dr\end{aligned} \tag{7.54}$$

$$\left(C_{H_u}\right)_{hov} = C_{H_0} = \frac{1}{2}\sigma C_{D_0}\int_0^1\int_0^{2\pi}\frac{1}{2\pi}\frac{r^2}{\cos(\phi)}\sin(\psi)d\psi dr \tag{7.55}$$

$$\begin{aligned}\left(C_{H_l}\right)_{hov} = &\frac{1}{2}\sigma C_{D_0}\int_0^{\frac{1}{2}\sqrt{2}}\int_0^{2\pi}\frac{1}{2\pi}\frac{r^2}{\cos(\phi)}\sin(\psi)d\psi dr\\ &+\frac{1}{2}\sigma C_{D_0}\int_{\frac{1}{2}\sqrt{2}}^1\int_0^{2\pi}\frac{1}{2\pi}\frac{r^2}{\cos(\phi)}\sin(\psi)d\psi dr\end{aligned} \tag{7.56}$$

Having calculated the H-force coefficients, the H-forces in hover and forward flight for the upper and lower rotors are calculated using equations 7.57 and 7.58 respectively [21].

$$H_u = C_{H_u}\rho\pi R^2(\Omega R)^2 \tag{7.57}$$

$$H_l = C_{H_l}\rho\pi R^2(\Omega R)^2 \tag{7.58}$$

The H-forces given by equations 7.57 and 7.58 are used in a later stage to determine whether forward flight iterations are necessary, as explained in section 7.7.

7.6.3. Torque and Power Coefficients

The torque on a rotor blade is defined as the force acting on it parallel to the rotational plane (consisting of a lift and drag dependent term) times the moment arm y, as given by equation 7.59 [21]. The drag dependent incremental blade element torque coefficient is given by equation 7.60 [21]. The torque coefficients for the upper and lower rotors in forward flight and hover are given in equations 7.61 - 7.64 and are derived based on the drag dependent term given in equation 7.60.

$$dQ = y\left(dD\cos(\phi) + dL\sin(\phi)\right) \approx y\left(dD\cos(\phi)\right) \tag{7.59}$$

$$dC_{Q_0} = \frac{N_b r R\left(\frac{1}{2}\rho U^2 c C_{D_0}\cos(\phi)dy\right)}{\rho\pi R^3(\Omega R)^2} = \frac{\frac{1}{2}r{u_T}^2\sigma C_{D_0}}{\cos(\phi)}dr \tag{7.60}$$

$$\left(C_{Q_u}\right)_{forw} = \frac{1}{2}\sigma C_{D_0}\int_0^1\int_0^{2\pi}\frac{1}{2\pi}\frac{\left(r+\mu\sin(\psi)\right)^2}{\cos(\phi)}r d\psi dr \tag{7.61}$$

$$\begin{aligned}\left(C_{Q_l}\right)_{forw} = &\frac{1}{2}\sigma C_{D_0}\int_0^1\int_{\frac{1}{2}\delta}^{2\pi-\frac{1}{2}\delta}\frac{1}{2\pi}\frac{\left(r+\mu\sin(\psi)\right)^2}{\cos(\phi)}r d\psi dr\\ &+\frac{1}{2}\sigma C_{D_0}\int_0^1\int_{2\pi-\frac{1}{2}\delta}^{\frac{1}{2}\delta}\frac{1}{2\pi}\frac{\left(r+\mu\sin(\psi)\right)^2}{\cos(\phi)}r d\psi dr\end{aligned} \tag{7.62}$$

$$\left(C_{Q_u}\right)_{hov} = C_{H_0} = \frac{1}{2}\sigma C_{D_0}\int_0^1\int_0^{2\pi}\frac{1}{2\pi}\frac{r^3}{\cos(\phi)}d\psi dr \tag{7.63}$$

$$\begin{aligned}\left(C_{Q_l}\right)_{hov} = &\frac{1}{2}\sigma C_{D_0}\int_0^{\frac{1}{2}\sqrt{2}}\int_0^{2\pi}\frac{1}{2\pi}\frac{r^3}{\cos(\phi)}d\psi dr\\ &+\frac{1}{2}\sigma C_{D_0}\int_{\frac{1}{2}\sqrt{2}}^1\int_0^{2\pi}\frac{1}{2\pi}\frac{r^3}{\cos(\phi)}d\psi dr\end{aligned} \tag{7.64}$$

The lift dependent term for the torque coefficient is given by equation 7.65 [21]. The **torque and power coefficients in hover and forward flight for the upper and lower rotors** are given by equation 7.66 in which C_{Q_0} is given by one out of equations 7.61 - 7.64 depending on the case of interest. The fact that the power coefficient is the same as the torque coefficient, as given in equation 7.66, can be verified by substituting equations 7.68 and 7.69 into equation 7.67. Equations 7.68 and 7.69 are used to calculate the rotor torque and power respectively when the torque and power coefficients for the upper and lower rotor in forward flight and hover are known [21].

$$C_{Q_i} = \lambda C_T + C_{H_i} \approx \lambda C_T \tag{7.65}$$

$$C_Q = C_P = C_{Q_0} + C_{Q_i} = C_{Q_0} + \lambda C_T \tag{7.66}$$

$$P = \Omega Q \tag{7.67}$$

$$Q = C_Q \rho \pi R^3 (\Omega R)^2 \tag{7.68}$$

$$P = C_P \rho \pi R^2 (\Omega R)^3 \tag{7.69}$$

The entire analytical solution of the rotor aerodynamic coefficients has now been derived. This solution needs to be numerically implemented to be able to effectively iterate parameters to arrive at an optimal rotor system design. These iterations are part of the rotor system design process, as can be seen in figure 7.1. The numerical implementation methodology and corresponding results will be discussed in section 7.7.

7.7. Numerical implementation methodology

In this section the numerical implementation of the calculations performed in sections 7.5 and 7.6 in MATLAB is described. First the rotor is divided into a matrix of segments, after which the equations can be used for each segment individually. A flowchart is provided for a clear overview of numerical procedures. A strategy for iterating is also included, to meet the requirements for each flight phase.

7.7.1. Numerical segments

In order to perform the calculations on individual segments, the rotor disk has to be split up into a number of segments. This is done by dividing the blade into n segments and the azimuth angle over which the blade will turn in m segments. These numbers can be adjusted down to reduce the calculation time, or adjusted up to increase the accuracy of the results. The location on the blade is represented by $0 \leq r \leq 1$ while the azimuth angle, ψ, is taken between 0 and 360 °. Initially, the blade is divided into 50 segments for each degree, thus n = 50 and m = 360. The points are distributed with a constant step size. These numbers should later be adjusted to check whether the accuracy is high enough.

7.7.2. Flowchart

To get from the input to the final output, several calculations have to be done. In figure 7.14 an overview is given of the flow of parameters from input to output. An important step is the iteration that follows from thrust and torque balance, and the power that has to stay within budget. As the rotor disk is divided into small segments, all the calculations from sections 7.5 and 7.6 can be performed on each individual point. The program is split up into several blocks. These are discussed in the following sections.

7.7.3. Preliminary calculations

In this first calculation block, which comes after the constants and iterable parameters, the calculations are performed that are not dependent on the location on the rotor disk. Here the atmospheric properties, advance ratio and Lock number are calculated.

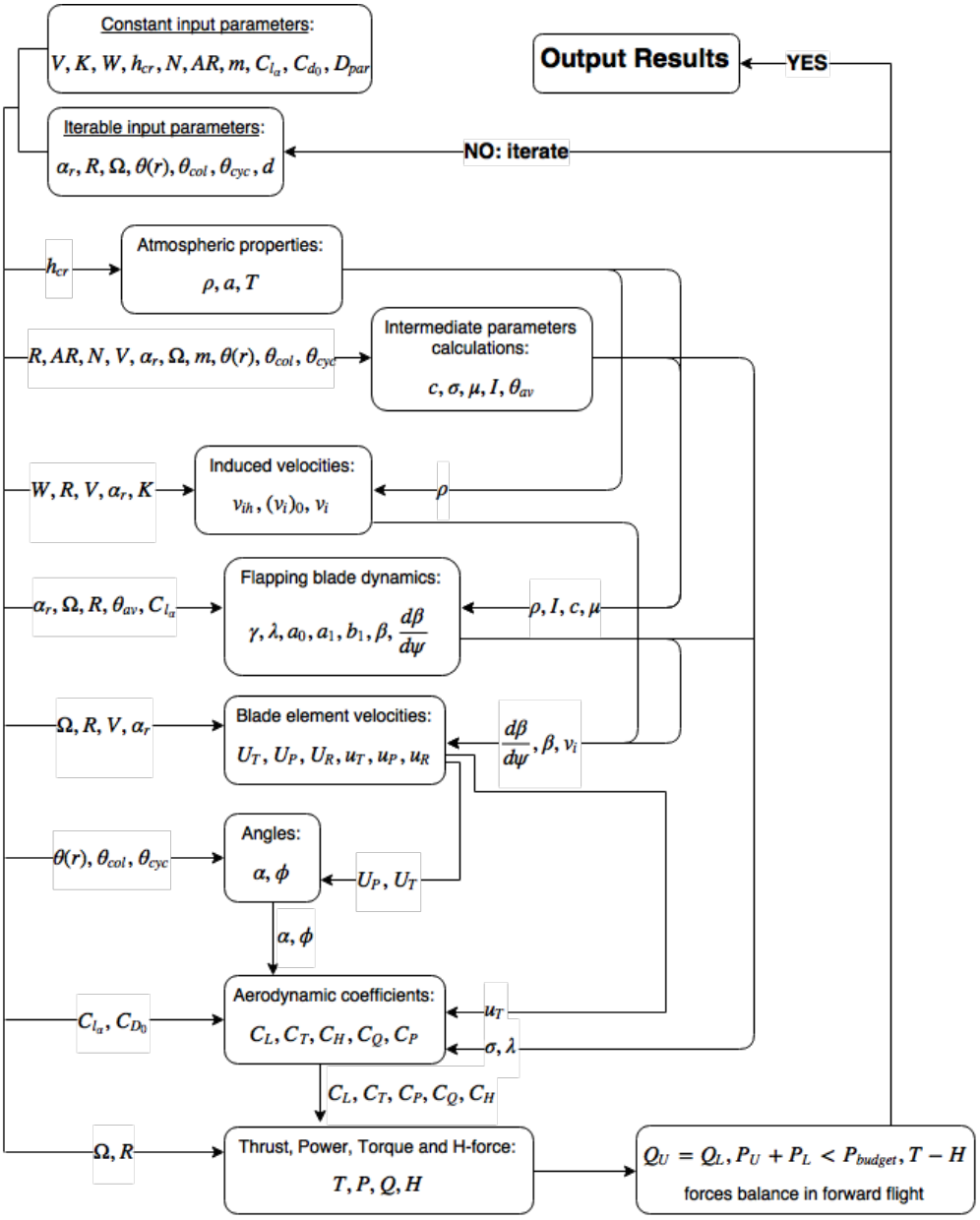

Figure 7.14: Flowchart of the numerical calculations.

7.7.4. Upper rotor

This block holds all the calculations on the upper rotor. Two loops are made, one for the segment location on the blade, r, and one for its angular location, ψ, on the disk. These two loops are nested, so that for each angle all the calculations on each blade segment are performed. The calculations are then performed according to sections 7.5 and 7.6. The integral and lift slope calculation have to be calculated differently.

Integrals

Integrals are solved numerically by the trapezoidal rule. This is a method that can be used for a set of individual points, and is an accurate enough function available in the program. First the integral is solved over the blade, r, on each azimuth angle, ψ. Then the double integral is solved by integrating a second time over the azimuth angle, ψ.

LIFT SLOPE

The airfoil that is chosen has a stalling angle of 19 degrees. However, on some points on the disk the angle of attack is higher than 19 degrees, indicating that this point is then in stalling conditions. The lift coefficient is taken as $C_{L_\alpha}\alpha + C_{L_{\alpha=0}}$. Thus for each point the angle of attack is checked. If the absolute value of the angle of attack is higher than 19 degrees, $C_{L_\alpha} + C_{L_{\alpha=0}}$ is set to zero. It is thus assumed that beyond this angle, the blade generates no lift.

7.7.5. LOWER ROTOR

This third calculations block holds all the calculations performed on the lower rotor. The main part is equal to the upper rotor calculations. The major difference is the different induced velocity due to the wake. A loop is added in order to check whether the wake hits the lower rotor. If the distance f is larger than $2R$ the wake does not hit the lower rotor, thus then the angle δ is set to zero.

7.7.6. ITERATIONS FOR ROTOR SYSTEM OPTIMIZATION

The final step is to iterate for an optimal design. As the helicopter is mostly cruising, the rotor is optimized for cruise. As there are many iterable parameters, some are first taken as constant. These are the radius, R, and rotational speed, Ω. These are taken constant as these are more difficult to iterate. Changing the radius changes the force distribution over the blade requiring an iteration in order to find a new optimal structure. The rotational speed has an impact on other subsystems, such as the gearbox design. This leaves the pitch angles (θ), the angle between the airspeed and rotor disk (α_r), and the rotor disk offset (d). In case it is not possible to iterate with only these parameters, the radius and rotational speed have to be adjusted.

STRATEGY

In order to meet the requirements, stated in section 7.2, the program is extended with a few extra commands:

- $\sum F_y = 0$: To have force balance in y-direction equation 7.70 is used. The forces can be seen in figure 7.16. Both sides of the equation are printed in the program, as can be seen in figure 7.15, which are the last two values on the first line (next to the first two values which are the upper and lower rotor thrust). When these two values are equal, this requirement is met. This balance is reached mostly dependent on the pitch angles, which increases mostly the thrust of the rotors.

$$(T_u + T_l)\cos(\alpha_r) + (H_u + H_l)\sin(\alpha_r) = W \tag{7.70}$$

- $\sum F_x = 0$: There also has to be force equilibrium in the x-direction. This is done by using equation 7.71. The parasite drag in this equation, D_{par}, is calculated using the $C_D S$ value from the Mid Term report [8]. Both sides of this equation are also printed and indicated by a 5 in figure 7.15. Both values have to be the same to meet this requirement. This equation is mostly dependent on the angle between the horizon and the rotor disk, α_r.

$$(T_u + T_l)\sin(\alpha_r) = D_{par} + (H_u + H_l)\cos(\alpha_r) \tag{7.71}$$

- $C_{Q_u} = C_{Q_l}$: The torque balance is necessary so that no yaw motion is present. The torque of both rotors are printed and have to be equal, as indicated by a 2 in figure 7.15.
- $C_{T_{left}} = C_{T_{right}}$: In forward flight, the moment on the left half of the rotor disk has to be equal to the right half in order to have equilibrium. This prevents that the helicopter will start to roll. This is approximated by assuming that when the thrust coefficient on both sides are equal, the moment is zero or small. This is mostly dependent on the cyclic pitch distribution. θ_{cyc1} and θ_{cyc2} from equation 7.36 are found by iterating them until the program prints an equal value for the left and right half of the rotor thrust coefficient. For the upper rotor these values are indicated by a 3, and with a 4 for the lower rotor in figure 7.15.
- $P_{req} \leq P_{budget}$: The power of the rotor system is printed (indicated by a 6 in figure 7.15) and has to be equal or less than the budget power.

After this iteration is completed, the twist angle distribution is a fixed parameter of the design and has a slope of -3 degrees. The radius and angular velocities remain the same and are 4.5 m and 432 rpm respectively. The twist and radius can no longer be changed for other flight phases and are thus no longer iterable parameters. A complete list of parameters can be found in section 7.8.

```
[T_u T_l W_possible W_aim] *10^4
1   0.5754    0.5747    1.1451    1.1448

[Q_u Q_l] *10^3
2   1.1957    1.1947

[UPPER ROTOR]
[Right C_T Left C_T]
3   0.0638    0.0638

[LOWER ROTOR]
[Right C_T Left C_T]
4   0.0636    0.0637

D_par (fixed - alpha_r) *10^3
5   1.0738    1.0768

Total power required [kW]
6 108.1356
```

Figure 7.15: Example output of the program.

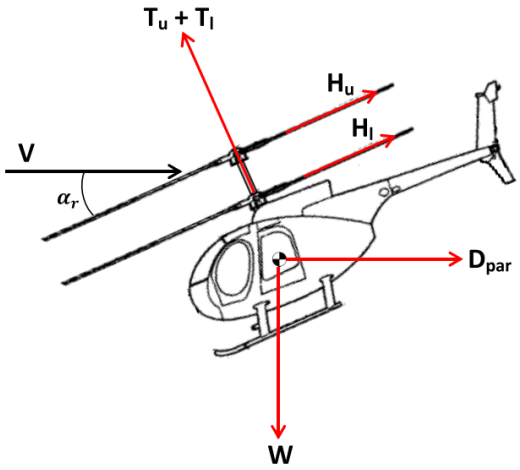

Figure 7.16: Forces acting on the helicopter in forward flight.

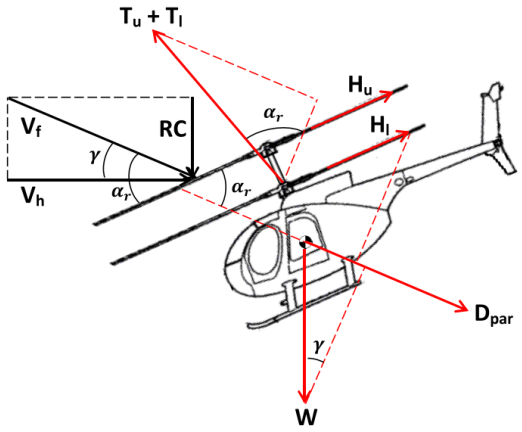

Figure 7.17: Forces acting on the helicopter in climbing flight.

Other flight phases

Besides cruise, there are more flight phases that has to be iterated for. There are several adjustments that have to be carried out for each flight phase. The iteration process is the same as for cruise, but with less iterable parameters. The radius and twist have to remain the same.

- Surveillance: In this phase the only change is the forward speed, which is 22 m/s.
- Hover: While hovering the forward speed is zero. The induced velocity is also different, as the assumption that the wake is linear is no longer valid. This is explained in section 7.5.
- Climb: This is the phase that requires the most adjustments. The rate of climb is a requirement and is 4.57 m/s [8]. This gives an additional angle, the flight path angle γ, shown in figure 7.17. The angle α_r is now the sum of the angle between the horizon and the rotor disk, and the flight path angle. The force equilibrium equation in y-direction has to be iterated according to equation 7.72.

$$(T_u + T_l)\sin(\alpha_r) = D_{par} + (H_u + H_l)\cos(\alpha_r) + W\sin(\gamma) \tag{7.72}$$

The iterations are performed for a range of velocities and are placed in Excel, as shown in figure 7.18. The purpose of this plot is to find the velocity for which minimum power is required for climb. A quadratic

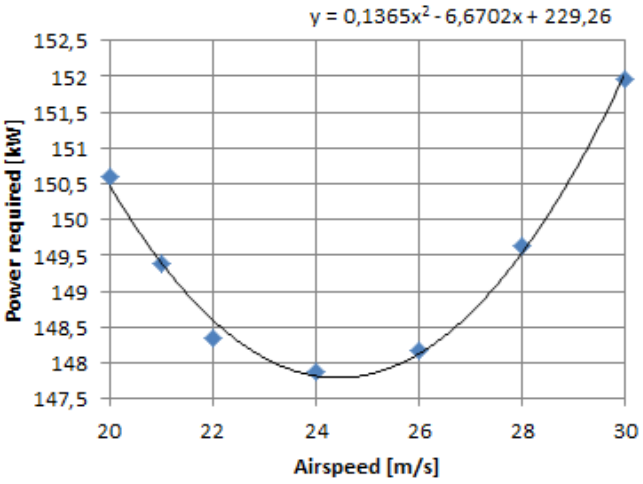

Figure 7.18: Power-velocity diagram for the climbing phase.

function is chosen to approximate the set of points resulting from the iterations as it returned the highest accuracy ($R^2 = 0.992$). As the power is a quadratic function of the velocity, this makes sense. The velocity with the lowest required power is chosen from the curve in figure 7.18 resulting in a forward climb velocity of 24.42 m/s. This velocity is used for the final iteration in the program for the climb phase to arrive at the final climb design results.

7.8. Results of rotor design iterations

In this section the results of the iterations for each flight phase are presented. For each phase, the requirements have to be met as described in the previous section. The parameters are given in tables, with the following definitions: T stands for the thrust and Q the torque. $C_{T_{left}}$ is the average thrust coefficient of the left half of the rotor and $C_{T_{right}}$ of the right half. θ_{tw} is the twist angle slope between the root and tip (starting on the root). θ_{cyc1} and θ_{cyc2} are the cyclic pitch coefficients (multiplied by $\sin(\psi)$ and $\cos(\psi)$ respectively). The maximum and minimum value of the pitch angle is also given, indicated by the subscripts max and min. The angle α_r is the angle between the airspeed and rotor disk. The advance ratio, μ, skew angle χ and required power P are also included in the tables. At last, the angle δ is added, which is a measure of how much wake hits the lower rotor. The Lock number, which is also an output, is not stated in the tables as it is constant for all flight phases. γ has a value of 6.7.

7.8.1. Cruise

The parameters that follow from the iterations for cruise are shown in table 7.4. This iteration is performed with a cruising speed of 39 m/s and height of 1980 m [8]. The induced velocities are not stated here as it depends everywhere on the rotor disk. The average induced velocity on the upper rotor (area 1 in figure 7.7) is 1.34 m/s. The lower rotor induced velocity outside the wake (area 2) is equal to this value, while the wake velocity on the lower disk (area 3) is 2.68 m/s.

The pitch angle is a combination of the collective, cyclic and twist angle. The total pitch angle distribution is shown in figure 7.19. The line at the top is the root of the blade, while the line at the bottom is at the tip. All other lines in between are linearly distributed over the blade span. Figure 7.20 shows the thrust coefficient distribution over the blade span for both rotors. This is averaged over the azimuth angle ψ. The twist angle slope is adjusted until this distribution is linear. The first thing to notice is that the thrust distribution for cruise is almost identical for both rotors. It can also be seen that the graph is not linear near the root, which can be explained by the fact that the blade stalls at some points on the azimuth angle. However it is more important that the distribution is linear near the tip, as here the most thrust is generated and a too high thrust at this element is not desired.

The induced velocities of both the upper and lower rotor are shown in figure 7.21 and 7.22 respectively. In these figures some elements are not shown, so that it is easier to follow the lines. The (almost) straight line

Table 7.4: Parameters of the rotor system for the cruising phase.

Parameter	**Upper rotor**	**Lower rotor**	Unit
T	5263	5259	[N]
Q	1150		[Nm]
$C_{T_{left}}$	0.0584	0.0583	[-]
$C_{T_{right}}$	0.0584	0.0583	[-]
H	32.92	32.92	[N]
θ_{tw}	-3	-3	[deg]
θ_{cyc1}	-0.26	-0.27	[deg]
θ_{cyc2}	0.25	0.25	[deg]
θ_{col}	7.83	7.93	[deg]
θ_{max}	8.13	8.24	[deg]
θ_{min}	4.47	4.56	[deg]
α_r	6.23		[deg]
μ	0.19		[-]
χ	82.0		[deg]
δ	40.6		[deg]
P_{req}	103.6		[kW]

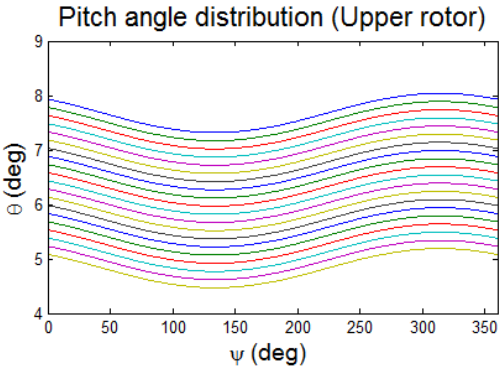

Figure 7.19: Pitch angle distribution of the upper rotor in cruise. The distribution for the lower rotor is almost identical.

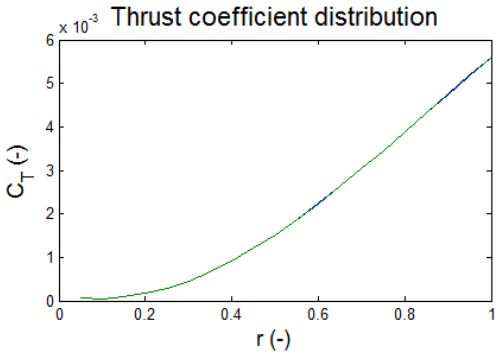

Figure 7.20: Thrust distribution of both rotors in cruise.

and the line with the most deviations stand for the root and tip location on the blade, respectively. As the extra term in the induced velocity (see equation 7.13) is a function of the blade location and the azimuth angle, it makes sense that the induced velocity at the root is constant for all angles. It can also be seen that the induced velocities at an angle of 90 and 270 degrees are equal for all blade locations. This also makes sense, as in equation 7.13 the term $\cos(\psi)$ is present. The difference between the two figures can clearly be seen and is around an azimuth angle of 0 or 360 degrees. The range of this angle is exactly the same as the angle δ as calculated earlier in section 7.5. This represents the wake that hits the lower rotor. It makes sense that the induced velocity in this area is higher compared to the upper rotor.

Disk offset

The disk offset can be determined with the flapping angle of the rotor blades. The maximum angle can be calculated by the program and is 5.0 degrees. Taking the worst case scenario, thus a positive angle for the upper rotor and negative angle for the lower rotor (or both the opposite), the distance so that the blades do not collide is simply calculated by equation 7.73. This gives a distance of 0.8 m. A safety factor of 1.25 is used to compensate for additional effects such as vibrations or gusts of wind causing the blades to flap more. Thus the disk offset is set on 1.0 m.

$$d = R\tan(\beta) \tag{7.73}$$

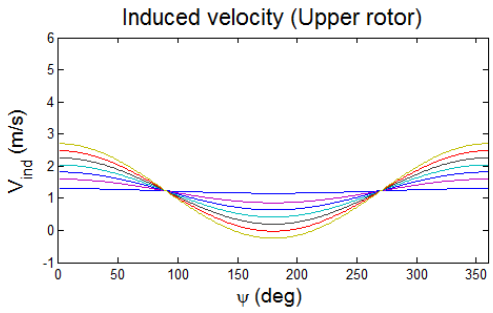

Figure 7.21: Induced velocity of the upper rotor in cruise.

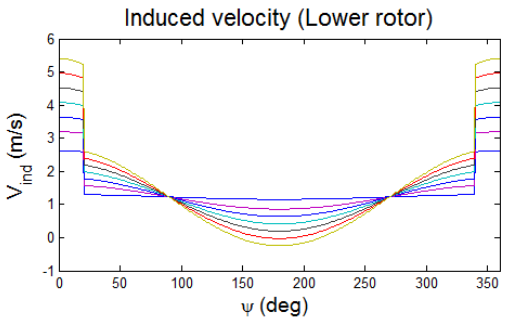

Figure 7.22: Induced velocity of the lower rotor in cruise.

Table 7.5: Parameters of the rotor system for the surveillance phase.

Parameter	**Upper rotor**	**Lower rotor**	Unit
T	5240	5239	[N]
Q	952		[Nm]
$C_{T_{left}}$	0.0481	0.0480	[-]
$C_{T_{right}}$	0.0481	0.0480	[-]
H	12.42	12.42	[N]
θ_{tw}	-3	-3	[deg]
θ_{cyc1}	-0.15	-0.16	[deg]
θ_{cyc2}	0.25	0.25	[deg]
θ_{col}	6.31	6.37	[deg]
θ_{max}	6.54	6.61	[deg]
θ_{min}	3.02	3.07	[deg]
α_r	2.50		[deg]
μ	0.11		[-]
χ	82.8		[deg]
δ	16.8		[deg]
P_{req}	86.1		[kW]

Table 7.6: Parameters of the rotor system in hover.

Parameter	**Upper rotor**	**Lower rotor**	Unit
T	3186	7277	[N]
Q	1254		[Nm]
$C_{T_{left}}$	0.0291	0.0674	[-]
$C_{T_{right}}$	0.0291	0.0674	[-]
θ_{tw}	-3	-3	[deg]
θ_{cyc1}	-0.02	-0.02	[deg]
θ_{cyc2}	0.25	0.25	[deg]
θ_{col}	6.68	10.05	[deg]
θ_{max}	6.87	10.24	[deg]
θ_{min}	3.43	6.80	[deg]
α_r	0		[deg]
μ	0		[-]
χ	0		[deg]
P_{req}	113.5		[kW]

7.8.2. SURVEILLANCE

The parameters that follow from the iteration for the surveillance phase are shown in table 7.5. This iteration is performed with a speed of 22 m/s and height of 91 m [8]. The results show indeed a lower power compared to the cruising phase, which is a sensible result. The skew angle χ is decreased as compared to cruise, causing a larger wake area intersecting the lower rotor disk, increasing the angle δ. The average induced velocity on the upper rotor (area 1 in figure 7.7) is 1.97 m/s. The lower rotor induced velocity outside the wake (area 2) is equal to this value, while the wake velocity on the lower disk (area 3) is 3.94 m/s.

7.8.3. HOVER

NUMERICAL RESULT

The parameters that follow from the iterations for hover are shown in table 7.6. For this iteration, the forward speed is 0 m/s and the height is assumed to be 0 m. The assumption that the wake is linear is no longer valid (as explained in section 7.5), thus no angle δ is shown. The resulting power makes sense, as it is higher for cruise. The thrust ratio of the rotors, however, are far apart. The lower rotor also produces more thrust than the upper rotor, which is expected to be the other way around. This can be explained by the assumptions made for the induced velocities, as there is a large deviation in velocity between the wake and outer part of the lower rotor. In section 7.10 it is verified that the calculations are correct, indicating that it is because of the strategy used. The induced velocity on the upper rotor is 6.29 m/s. Outside the wake on the lower rotor the average is 6.05 m/s, while inside the wake the average induced velocity is 15.7 m/s. The H-force in hover is 0 N, which is expected.

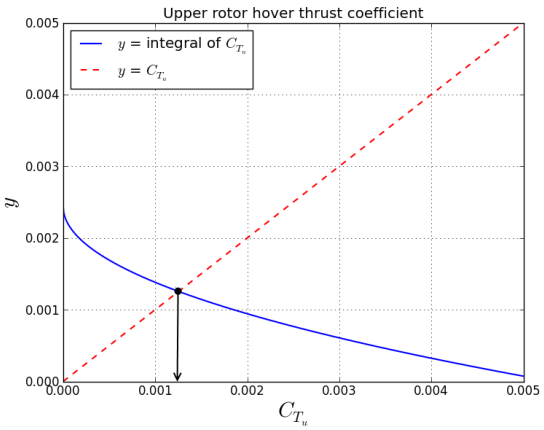

Figure 7.23: Graphical determination of the upper rotor hover thrust coefficient.

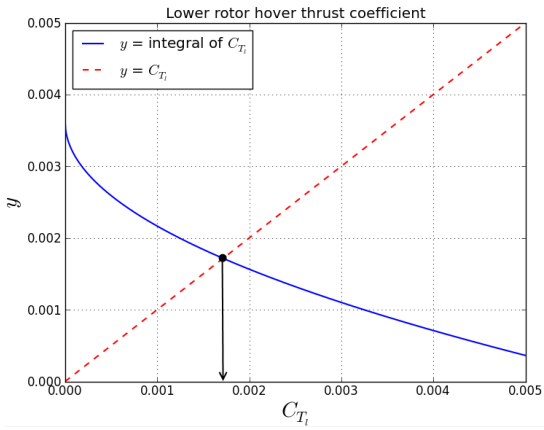

Figure 7.24: Graphical determination of the lower rotor hover thrust coefficient.

Graphical result

The hover thrust ratio is calculated with the use of the upper rotor induced velocity given by equation 7.6 and the lower rotor induced velocities given by equations 7.6 and 7.7. However, a graphical approach for determining the hover thrust coefficients of the rotors is also possible. Instead of using equation 7.6 representing the upper rotor induced velocity as a function of the maximum take-off weight, equation 7.3 is used. The first step is to write the induced velocity across the upper rotor as a function of the upper rotor thrust coefficient as shown in equation 7.74, starting from equation 7.3. From the upper rotor induced velocity as a function of C_{T_u} in equation 7.74, the induced velocities across the lower rotor inside and outside the upper rotor wake are found as a function of C_{T_u} by substituting equation 7.74 into equations 7.75 and 7.76.

$$v_{ind,u} = \sqrt{\frac{T_u}{2\rho A}} = \sqrt{\frac{C_{T_u}\rho\pi R^2(\Omega R)^2}{2\rho\pi R^2}} = \Omega R\sqrt{\frac{C_{T_u}}{2}} \tag{7.74}$$

$$\left(v_{ind,l}\right)_{wake} = \frac{39}{16}v_{ind,u} \tag{7.75}$$

$$v_{ind,l} = \frac{7}{16}v_{ind,u} \tag{7.76}$$

Since the upper and lower rotor thrust coefficients always depend on the induced velocity distribution across them, which in the present discussion is in turn a function of the upper rotor thrust coefficient, a graphical method is used to determine the solution of the set of equations given by 7.77 and 7.78 for the upper rotor and 7.79 and 7.80 for the lower rotor.

$$y = f(C_{T_u}) = C_{T_u} \tag{7.77}$$

$$y = f(C_{T_u}) = \int_0^1\int_0^{2\pi}\frac{1}{2\pi}\frac{\frac{1}{2}\sigma r^2\left[C_L\cos(\phi) - C_D\sin(\phi)\right]}{\cos^2(\phi)}d\psi dr \tag{7.78}$$

$$y = f(C_{T_l}) = C_{T_l} \tag{7.79}$$

$$\begin{aligned} y = f(C_{T_u}) = &\int_0^{\frac{1}{2}\sqrt{2}}\int_0^{2\pi}\frac{1}{2\pi}\frac{\frac{1}{2}\sigma r^2\left[C_{L_\alpha}\alpha\cos(\phi) - C_{D_0}\sin(\phi)\right]}{\cos^2(\phi)}d\psi dr \\ &+\int_{\frac{1}{2}\sqrt{2}}^1\int_0^{2\pi}\frac{1}{2\pi}\frac{\frac{1}{2}\sigma r^2\left[C_{L_\alpha}\alpha\cos(\phi) - C_{D_0}\sin(\phi)\right]}{\cos^2(\phi)}d\psi dr \end{aligned} \tag{7.80}$$

The graph in figure 7.23 plots the functions given by equations 7.77 and 7.78 to find their intersection. The coordinate of the intersection indicated by the arrow in figure 7.23 graphically represents the upper rotor thrust coefficient in hover. Likewise, the graph in figure 7.24 plots the functions given by equations 7.79 and 7.47 to determine the thrust coefficient of the lower rotor in hover. The integral functions given by equations 7.78 and 7.47 have been plotted numerically by evaluating them for 1000 values for C_{T_u} in the interval $[0 \rightarrow 0.005]$. From the intersection points in the graphs in figures 7.23 and 7.24, the thrust coefficients of the upper and lower rotors in hover have been found to be equal to 0.00125456 and 0.00171587 respectively. These have been found by zooming in to the intersection point several times after the graph was plotted in python. Therefore, it can be concluded that from the graphical method the thrust ratio $\frac{T_l}{T_u}$ is approximately equal to 1.368.

Coaxial rotor hover momentum theory predicts a thrust ratio of $\frac{T_l}{T_u} = 0.696$, according to equation 7.2. The numerical result for hover shown in table 7.6 gives a thrust ratio of $\frac{T_l}{T_u} = 2.284$. It is therefore evident that general

Table 7.7: Parameters of the rotor system in climb.

Parameter	**Upper rotor**	**Lower rotor**	Unit
T	6147	4604	[N]
Q	1634		[Nm]
$C_{T_{left}}$	0.0562	0.0421	[-]
$C_{T_{right}}$	0.0562	0.0421	[-]
H	39.03	33.85	[N]
θ_{tw}	-3	-3	[deg]
θ_{cyc1}	-0.12	-0.08	[deg]
θ_{cyc2}	0.25	0.25	[deg]
θ_{col}	8.65	8.32	[deg]
θ_{max}	8.87	8.52	[deg]
θ_{min}	5.37	5.06	[deg]
γ	10.8		[deg]
α_r	13.6		[deg]
μ	0.12		[-]
χ	72.8		[deg]
δ	198.4		[deg]
P_{req}	147.9		[kW]

Table 7.8: Parameters of the rotor system for maximum speed.

Parameter	**Upper rotor**	**Lower rotor**	Unit
T	5287	5286	[N]
Q	1512		[Nm]
$C_{T_{left}}$	0.0587	0.0588	[-]
$C_{T_{right}}$	0.0587	0.0588	[-]
H	55.42	55.41	[N]
θ_{tw}	-3	-3	[deg]
θ_{cyc1}	-0.30	-0.30	[deg]
θ_{cyc2}	0.25	0.25	[deg]
θ_{col}	8.97	9.16	[deg]
θ_{max}	9.30	9.49	[deg]
θ_{min}	5.57	5.77	[deg]
α_r	9.2		[deg]
μ	0.23		[-]
χ	79.7		[deg]
δ	99.0		[deg]
P_{req}	104.6		[kW]

coaxial momentum theory and the used blade element theory provide rather deviating results for hover, the alternative graphical result being closer to the momentum theory prediction than the main numerical blade element solution discussed throughout this chapter. However, it should be mentioned that the numerical and graphical solution methods for the evaluation of the hover thrust coefficients are based on input parameters being selected such that all iteration requirements mentioned in section 7.7.6 are met. This means that the inputs are iterated such that the results gained for T_u and T_l also meet for example the total rotor torque sharing and power budget requirements for hover. Apparently, to meet all requirements from section 7.7.6, it does not necessarily mean that the numerical and graphical rotor thrust sharing results originating from blade element theory match the momentum theory thrust sharing prediction in hover.

7.8.4. Vertical climb

The iteration for vertical climb is done with a forward speed of 24.42 m/s which is for the lowest power, as explained in section 7.7. The height is set on the point which will result in the highest power required. This is at 0 m. This is done because the rate of climb has to be achieved at every height in climb. The results are shown in table 7.7. There is a large difference between the thrust, which can be explained by the large influence of the wake. As the angle α_r is relatively large and the skew angle χ is low, the angle δ is high. The power required is also high. This could be due to the required rate of climb, pushing the design to its limits.

7.8.5. Maximum speed

The maximum speed can also be determined. At the point of this iteration it is known from the propulsion design, as explained in chapter 8, that the maximum power is 140.6 kW. Thus this power is taken in order to determine the maximum speed the helicopter can achieve. The height is taken as 1980 m, as a decrease in altitude lowers the maximum speed and this is the maximum height in the mission. This results in the parameters shown in table 7.8. The resulting maximum speed is then 48.3 m/s.

7.9. Sensitivity analysis

The script written in MATLAB has to be iterated manually until the requirements are met. If the weight of the helicopter is changed by 1 kg in the program, the output is almost the same. A more interesting analysis is to change the weight by a larger number. A change of 100 kg is chosen, after which a table is made to compare the results. The iteration is done with a weight of 1167 kg in cruising conditions. The results are shown in table 7.9. The average is taken if the upper and lower rotor have different parameter values. Several conclusions can be drawn from this comparison. An increase in weight increases the thrust, torque and pitch angles in order to compensate for the extra force required. The cyclic pitch is decreased as well as α_r. The skew angle is increased

Table 7.9: Sensitivity table compared to cruise with a change in weight of 100 kg.

Parameter	**Upper rotor**	**Lower rotor**	Unit	**Difference** [%]
T	5754	5747	[N]	9.3
Q	1195		[Nm]	4.3
$C_{T_{left}}$	0.0638	0.0637	[-]	8.5
$C_{T_{right}}$	0.0638	0.0637	[-]	8.5
θ_{tw}	-3	-3	[deg]	0
θ_{cyc1}	-0.29	-0.30	[deg]	-11.1
θ_{cyc2}	0.25	0.25	[deg]	0
θ_{col}	8.05	8.13	[deg]	2.7
θ_{max}	8.37	8.46	[deg]	2.8
θ_{min}	4.67	4.74	[deg]	4.0
α_r	5.7		[deg]	-9.3
μ	0.19		[-]	0
χ	82.3		[deg]	0.4
δ	30.4		[deg]	-25.1
P_{req}	108.1		[kW]	4.3

slightly, thus decreasing the wake effect on the lower rotor (and thus a lower δ). The power is increased by 4.3 %. Averaging over the 100 kg, the increase in power required for 1 kg of added mass is 0.043 % or 0.045 kW.

7.10. Verification and Validation

In this section the verification and validation procedure and corresponding results are explained. Verification is mostly aimed at debugging the numerical program, while validation compares the results to reference data.

7.10.1. Verification

The verification procedure is split up in two parts; code and calculation verification.

Code verification

Manually calculating every function is a difficult task and not always possible in order to verify the program. Thus the program is gone through step by step. At every block the functions are evaluated, usually by graphically plotting the resulting values. Some of these graphs are shown in the design results, in section 7.8. The pitch angle calculations can be checked, by looking at the graph in figure 7.19. The linear distance between the lines represent the twist angle distribution, while the cyclic pitch gives the periodic behavior that looks like a wave. The collective pitch is the average in this graph. By manually checking the values, such as the average of the pitch angle distribution (which gives the collective pitch plus half the twist distribution value), the code for these angles can be verified. The induced velocity graphs in figure 7.21 and 7.22 can also be used to verify the code. As the function for the induced velocity is dependent on the cosine of the azimuth angle, it is expected that all values are equal at 90 and 270 degrees. Also the average has to lie on the root of the blade, as there r = 0. For the lower rotor it is expected that the induced velocity is higher near an angle of 0 degrees, which is indeed the case. The range where the induced velocity is higher is exactly the angle δ, representing the angle where the wake hits the lower rotor. This strategy is used for almost all equations implemented in the program, checking whether the output makes sense and the values are as expected.

Calculation verification

The program is simplified in order to verify the calculations. The skew angle is set on 90 degrees, thus indicating that the wake has no influence anymore on the lower rotor. The program then returns results that are equal for both rotors, indicating that the calculations performed in both rotor blocks are correct. Then the velocity is set to zero. Iterating for this point gives an α_r angle of 0 degrees. This has to be true, as these are hover conditions. Thus after these steps are taken, the program is verified and is concluded to be correct.

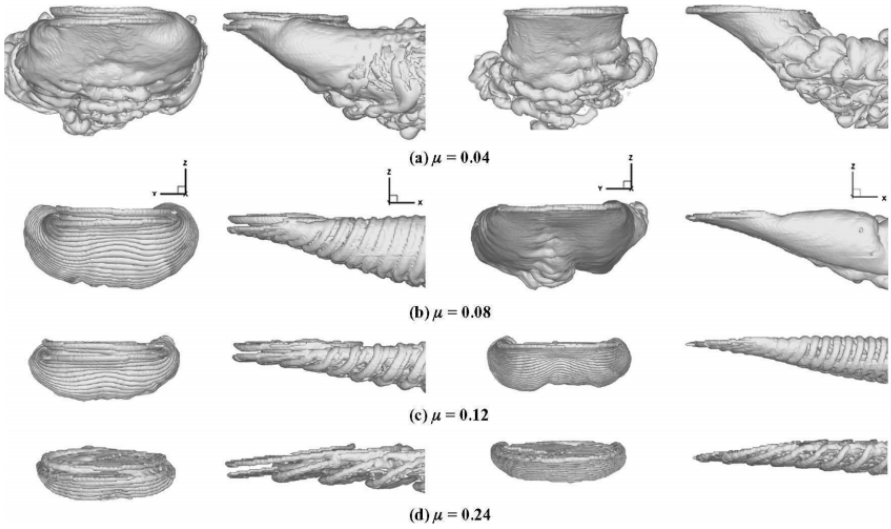

Figure 7.25: Experimental wake determination for coaxial (left) and single rotor (right) systems at different advance ratios. [23]

7.10.2. VALIDATION

After verification, reference data needs to be used to validate the code for its intended use. As in the present case no experiments are readily available for validation, reference parameters from similar coaxial rotorcraft need to be selected. To validate the program, the Kamov Ka-15 coaxial reference rotorcraft is chosen and its main design parameters are implemented as inputs in the program to investigate whether the program output required power is below the maximum given available power installed in the Kamov Ka-15. The parameters of the Kamov Ka-15 are: MTOW = 1410 kg, V_{max} = 42 m/s, R = 4.98, c = 0.24 m, Ω = 397 RPM, d = 1.13, N_b = 3 and h_{max} = 3000 m [22]. The result after some iterations in the program is a required power of 151 kW for the rotorcraft operating at its maximum altitude and maximum speed for which the required power is expected to be maximum. As the total installed power is given to be 190 kW [22], one can conclude that the estimate of 151 kW required is a decent approximation, as the installed power always needs to be higher than the required power because of safety factors applied in the design. A recommendation for a complete validation would be to repeat this process for many existing helicopter designs, and also to validate not only the power but many other parameters as well. However, most parameters (not being the most basic ones) are often hard to find from technical data sheets on the Internet and have therefore not been considered for the present validation.

The thrust ratio $\frac{T_u}{T_l}$ is an interesting second parameter to be validated. This ratio is nearly 1 for cruise and surveillance conditions, while for hover it reduces to a value below 1. Looking at reference coaxial rotor systems, this ratio is often above 1 for all conditions, as explained previously. Therefore, it can be concluded that the thrust ratio can not be validated at the moment. A proposed recommendation is that a more thorough code verification would need to be performed with respect to the calculation of the thrust ratio before its validation. In particular the wake approximations and corresponding assumptions would need to be verified in more detail. Wind tunnel experiments could also be performed for hovering coaxial rotors to determine the induced velocity variations for validation purposes.

Another interesting characteristic is the skew angle. In nearly all mission phases it is observed to be quite high: around 80 degrees. In figure 7.25 [23] experimental wake geometries of a coaxial rotor system in forward flight are shown for different advance ratios. The figure illustrates that a large skew angle already exists at an advance ratio of only 0.12. The surveillance and cruising mission phases of the H2Copter have advance ratios of 0.11 and 0.19 respectively, which means that the magnitude of the skew angle is reasonably validated. All other parameters, except the ones hard to find from experimental data, are well within reasonable values, such as the power for different flight phases (hover always requires more power than cruising conditions and the power for surveillance is lower than for cruise).

8

PROPULSION

In the following chapter, a description will be given of the design process of the propulsion subsystem of the helicopter. A schematic overview of the subsystem is given in figure 8.1. It consists of several parts that will be treated in their respective subsections. The main task of the propulsion subsystem is to provide adequate power to the rotors during all phases of flight. The chapter is structured as follows: the design of the components starts at the motors and follows the schematic in figure 8.1 towards the fuel tank.

8.1. ELECTRIC MOTOR

An electric motor is required to drive the rotors. In order to simplify control, it was decided that the rotors should be driven by a separate motor. It would be best to custom-design a motor that fits the needs exactly. There are methods to custom-design electric motors, but the group does not have the electrical engineering expertise to follow these methods. It was decided that this is outside the scope of the project. It is required to select a third-party motor.

8.1.1. MOTOR TYPE SELECTION

The motors that were considered are shown in table 8.1. For all motors, the highest-performing type was selected.

With the exception of the US hybrid motors, all commercially available motors that were found are synchronous AC motors. An attempt was made to find a trend of the specific power. Figure 8.2 shows the specific power of the motors, together with the maximum continuous power. It can be concluded from this figure that the spread in specific power is too large to make a useful prediction of this value, even if only motors of the same type are considered. When motors of the same manufacturer are compared, there is still a large spread. Therefore, it is decided that interpolating between existing motors would provide too little confidence that the design is feasible. An existing motor will be selected.

In figure 8.2, the required power is also shown. The lightest solution is to use two Enstroj EMRAX 207 motors per rotor. This would lead to a total motor weight of 18.6 kg per rotor. However, using two motors per rotor would complicate the design of the gearbox considerably. The second lightest solution is to use the Enstroj EMRAX 268 motor, with a weight of 20.3 kg. It was found that using this motor is more convenient than using the two EMRAX 207 motors, because of the simplification of the gearbox design. Compared to the third lightest

Table 8.1: Commercially available motors. Specific power is based on continuous power.

Manufacturer	**Model**	**Power** [kW]	**Efficiency** [%]	**Max. speed** [rpm]	**Mass** [kg]	**Spec. power** [kW/kg]
YASA	400 [24]	75	95	7500	24	3.13
YASA	750 [25]	75	95	3250	33	2.27
YASA	250 [26]	65	95	9000	18	3.61
US Hybrid	EDU200 [27]	85	93	7200	176	0.48
US Hybrid	GCU100 [28]	80	0.96	3000	65	1.23
Enstroj	EMRAX 207 [29]	40	93-98	6000	9.3	4.30
Enstroj	EMRAX 228 [29]	55	93-98	5500	12.3	4.47
Enstroj	EMRAX 268 [29]	90	93-98	4000	20.3	4.43
GKN/EVO	AF-130 [30]	64	95.1	8000	30.5	2.10
GKN/EVO	AF(M)-140 [30]	75	96.5	5000	40	1.88
GKN/EVO	AF-230 [30]	200	95.1	8000	57.5	3.48
GKN/EVO	AF-240 [30]	150	96.5	5000	80	1.88
Protean	Drive [31]	54	0	0	34	1.59

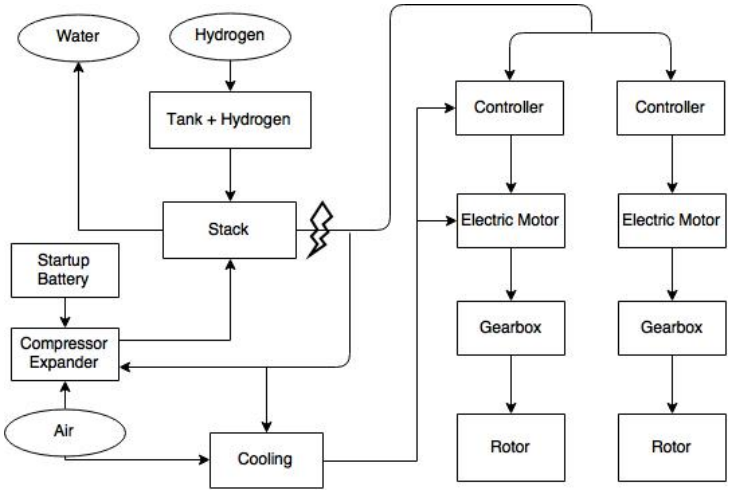

Figure 8.1: Schematic overview of the sizing of the power (Diamond blocks define loop inputs, trapezoidal blocks indicate converged outputs, the remaining blocks define calculation steps within the loop.

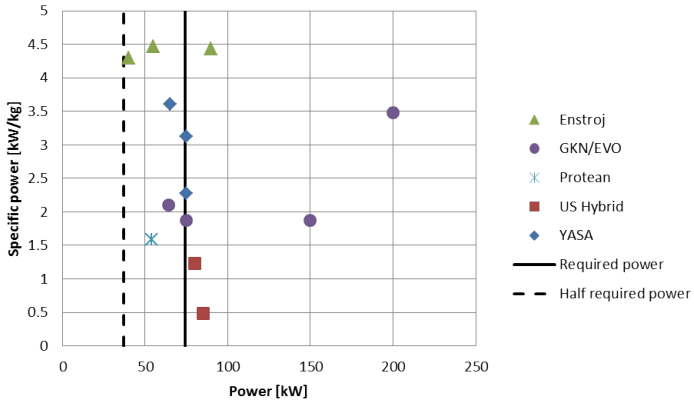

Figure 8.2: Specific power of commercially available motors.

motor option, the YASA 400, the EMRAX 268 has a lower rotational speed, which is also advantageous in terms of gearbox design. Therefore, the decision is made that the Enstroj EMRAX 268 motor will be used on the H2Copter.

The selected motor is a brushless synchronous three-phase AC motor. The working principle of an AC synchronous motor is shown in figure 8.3. There are three sinusoidal input currents, with a phase shift of 120 °. Each of the signals is connected to a fixed electromagnet on the stator, that causes a magnetic field along one axis. The magnetic field axes are also 120 ° apart. The magnetic fields of the three magnets can be added. Because the inputs are phase shifted, the resulting magnetic field will be rotating with a constant amplitude. The permanent magnet in the middle is locked to this magnetic field. This causes the middle part, the rotor, to rotate. In reality, the stator electromagnets are coils with a sinusoidal winding distribution, to make sure the magnetic field has constant amplitude. The selected motor is an axial flux motor, which is a variation to this concept. This concept still requires three sinusoidal inputs.

8.1.2. Motor capabilities

In order to clarify the behaviour of this motor type, figure 8.4 shows the performance curve of a similar type of motor. It can be seen that the torque that can be delivered by the motor is constant when the motor speed is not too low or high. This torque is known to depend on the root-mean-square (rms) current that is delivered to the windings. The amount of torque per current is a characteristic value for a motor. The output power is then linearly dependent on the motor speed. It should be noted that the maximum power cannot be delivered at every motor speed. The maximum torque cannot be delivered continuously; the maximum continuous torque

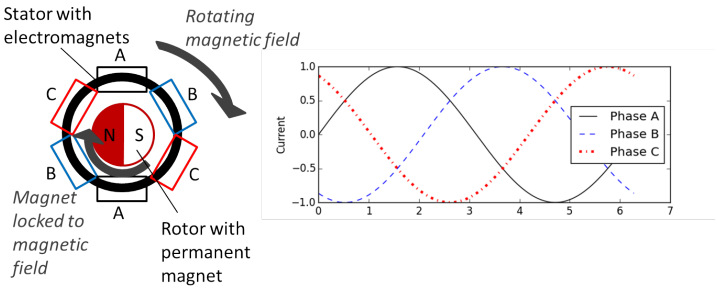

Figure 8.3: Working principle of a three-phase synchronous AC motor.

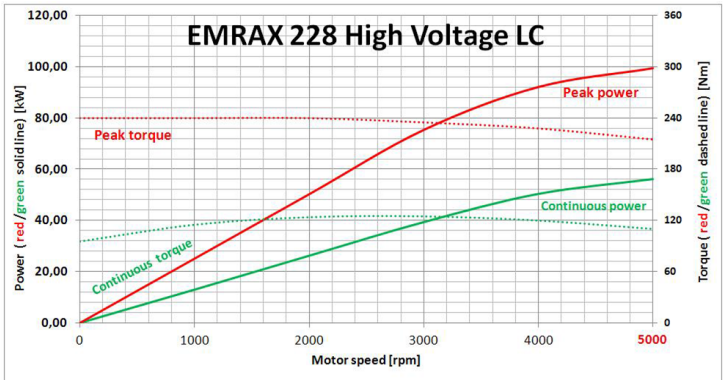

Figure 8.4: Power characteristic of the EMRAX 228 motor.

is lower.

Table 8.2 shows some data on the different types of EMRAX 268 motors. The motor types are characterized by their voltage level and cooling type (e.g. EMRAX 268 HV-CC). There are three cooling types for the motor: air cooling, liquid cooling and combined (air and liquid) cooling. The air and liquid cooling variants also exist for the MV and LV motors, but they are not shown. It can be seen that combined cooling leads to much higher continuous power, at the expense of 400 g compared to air cooling. Although this poses more stringent requirements on the cooling, it reduces the motor speed, so it makes the gearbox much lighter. It was decided that the air and liquid cooling variants are not suitable for the design. The low voltage variant was discarded due to the very high current (500 A) that was required to operate the motor. Higher currents inevitably lead to higher losses in the controller.

The efficiency can be obtained more accurately from figure 8.5. Enstroj does not provide such an efficiency plot for the EMRAX 268 motor, but it does provide plots for the similar EMRAX 207 and 228 motors. Figure 8.5 refers to the EMRAX 207 motor. It can be seen that it is possible to operate at an efficiency of 96% at maximum continuous torque between 1500 and 3500 RPM. The lowest efficiency is 86%. Because these plots are similar for the EMRAX 207 and 228 motors, it is assumed that these efficiencies are also obtained by the EMRAX 268 motor.

Table 8.2: Data on the different types of Enstroj EMRAX 268 motors [29].

	High voltage (HV)			**Medium voltage** (MV)	**Low voltage** (LV)
Cooling	Air (AC)	Liquid (LC)	Combined (CC)	Combined (CC)	Combined (CC)
Weight [kg]	19.9	20.3	20.3	20.3	20.3
Continuous power [kW] at 2000-4000 RPM	40-75	40-75	50-90	50-100	50-90
Continuous current [Aph RMS]	125	125	125	180	500
Maximum rotational speed [RPM]	4000	4000	4000	4000	4000
Torque per current [Nm/Aph RMS]	2	2	2	1.4	0.5
Motor efficiency [%]	93-98	93-98	93-98	93-98	93-98

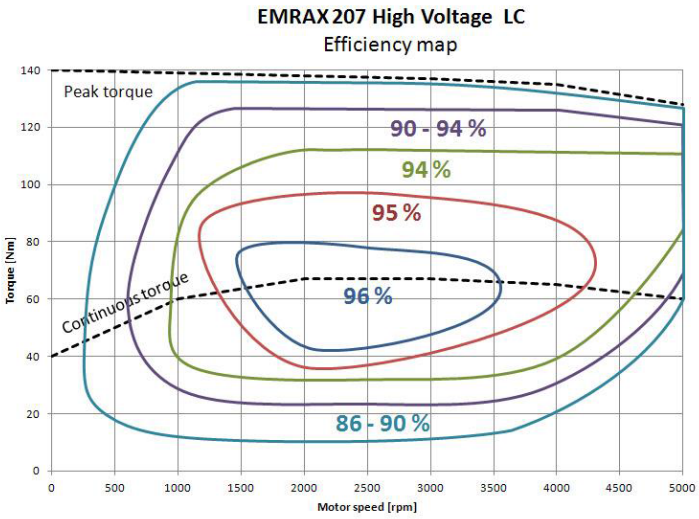

Figure 8.5: Efficiency map of the EMRAX 207 motor.

When looking at figure 8.4, it is clear that the required motor speed for a given continuous power can be obtained by means of linear interpolation between the points given in table 8.2. This is given in equation 8.1. When the power and the motor speed are known, the torque follows from equation 8.2 and the current follows from the torque per current τ according to equation 8.3. This current is given in Aph RMS, which represents the root-mean-square value of the current per phase. The voltage in a three-phase circuit can be defined as the line-to-line voltage or the line-to-neutral voltage. Equation 8.4 [32] is used to compute the line-to-neutral voltage. In this equation, I and V_{LN} are both RMS values. PF is the power factor caused by the phase shift between voltage and current. Synchronous AC motors generally have a high power factor [33], which is considered a good feature. The lowest power factor from [33] (0.72) is taken to be used in this equation. This is actually a relatively low value. A minimum efficiency of $\eta = 0.86$ is assumed to arrive at the power delivered to the motor, and an additional factor of 1.2 is used to make sure that the equipment is not destroyed at higher voltages.

$$\Omega = \frac{P_{out} - P_{low}}{P_{high} - P_{low}} \left(\Omega_{high} - \Omega_{low}\right) + \Omega_{low} \tag{8.1}$$

$$P_{out} = T\Omega \tag{8.2}$$

$$T = \tau I \tag{8.3}$$

$$P_{out} = 3 I V_{LN} \eta PF \tag{8.4}$$

Using these equations, It is calculated that the HV motor operates at a rotational speed of 3200 RPM, a phase RMS current of 110.4 A and has a maximum required line-to-neutral voltage of 432.9 V. The MV motor requires a motor speed of at least 2960 RPM and a phase RPM current of 170.5 A. The maximum line-to-neutral voltage of this motor is 280.3 V. Both motors are currently considered feasible. There is a slight preference for the HV motor due to the lower current required, but the selection will depend on the possibility of providing this voltage and current by the fuel cell and controller.

8.2. Motor controller

While the motor requires a three-phase alternating current, the fuel cell delivers only DC. A motor controller is used to convert the DC input to an AC output of the correct frequency and amplitude. The controller is essentially a controllable three-phase inverter. In order to demonstrate the working principle, figure 8.6 shows an example the output of a single-phase inverter.

On the input of the inverter, there is a DC voltage V_d. The inverter can invert this voltage by switching the poles. It does so at a regular switching frequency $f_s = \frac{1}{T_s}$. Within the switching interval, the output changes between positive and negative once, resulting in a pulse-width modulated (PWM) signal. The required AC signal is the first harmonic of the PWM signal. A three-phase inverter works slightly differently, but the principle of operation is the same. It is important to realize that the output voltage of an inverter has a maximum, which is regulated by (but not equal to) the input voltage. There is no minimum: bringing the input voltage down is possible without significant additional power losses. The motor controller is able to control the amplitude and

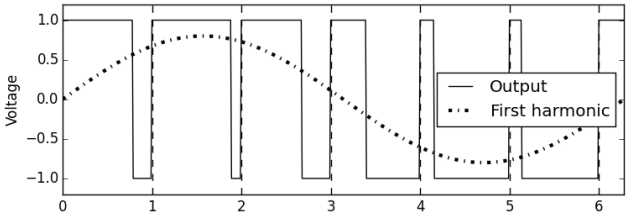

Figure 8.6: Example of the output of a single-phase inverter with bipolar switching.

Table 8.3: Different types of the motor controller [35].

	BAMOCAR-D3-			
Type	400-250	400-400	700-250	700-400
Input voltage [V]	24-400	24-400	24-700	24-700
Maximum output voltage [V]	260	260	450	450
Voltage ratio [-]	0.65	0.65	0.65	0.65
Maximum output current [Aph RMS]	125	200	125	200
Dissipation [kW]	2.0	3.0	2.6	4.0
Weight [kg]	5.8	6.8	5.8	6.8

frequency of the output signal.

The motor manufacturer Enstroj recommends to use the UNITEK BAMOCAR D3 controller. An alternative is the Gen4 Size 10 controller by Sevcon [34], but it has comparable performance at a higher weight. A constraint on the controller is that it must be able to deliver the line voltage and current that are required for the motor. It must be able to do so with a range of input voltages, since the fuel cell output is not constant.

As explained previously, the output voltage of the controller requires a minimum input voltage. This voltage is not equal to the output voltage, due to the three-phase topology and limits on the on-time of the switches of the inverter. The maximum ratio between input and output voltage was determined by looking at data on the controller. The different types of the recommended controller are given in table 8.3.

The controller comes in a high and medium voltage type, which both have a high and medium current variant. The higher current variants come at the price of 1 kg extra weight. The two possible motors have been matched with the possible controllers. For the HV motor, the maximum required line voltage is 432.9 V, as explained in section 8.1. Using the voltage ratio in table 8.3, this leads to a minimum input voltage of 666.0 V. The input voltage, however is limited by the maximum input voltage of the controller, which can be no more than 700 V. The fuel cell is not able to keep the voltage within such a small range, so the high voltage motor is not suitable. A DC/DC converter can solve this problem, but converters for this power level are very heavy. The MV motor requires at least 280.3 V, leading to a minimum controller input of 436.1 V. The high voltage controller can handle an input voltage of 700 V. The range of 436.1 to 700 V is large enough for the fuel cell. The current of 170.5 A can be delivered by the high current variant. This is a suitable combination. Summarizing, the selected motor is the **Enstroj EMRAX 268 HV with combined cooling** and the controller is the **UNITEK BAMOCAR-D3-700-400**.

8.3. Fuel Cell Stack

The fuel cell stack consists of multiple cells that are connected in series to provide the desired power output. The type of fuel cell that is going to be used is a Proton Exchange Membrane Fuel Cell (PEMFC). This fuel cell is most commonly used for transportation purposes because of his relatively low weight and operating temperature. Properties of the fuel cell used in the Honda Clarity have been used since this is a good example of contemporary fuel cell [36].

The behaviour of an individual cell with respect to current and voltage is shown in figure 8.7a. Every point on this curve corresponds to a certain combination of external load and fuel flow rate. The cell voltage at maximum gross power is a design choice, and it will be the main variable in the optimization of the fuel cell system. The second variable is the internal fuel cell pressure. Multiplying the cell current density with the cell voltage, gives the cell power density, as can be found in figure 8.7b. It can be seen that performance improves

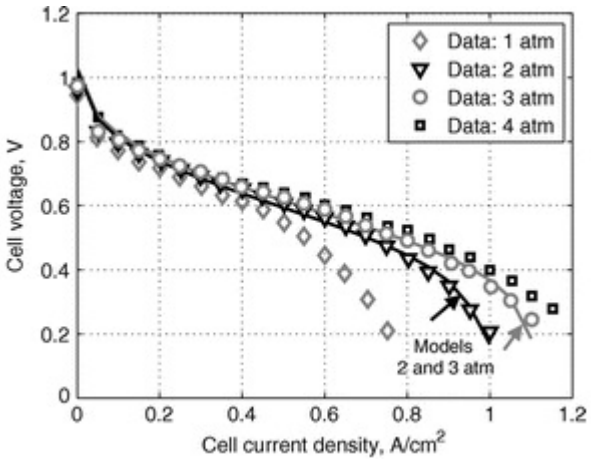

(a) Cell current density vs. cell voltage.

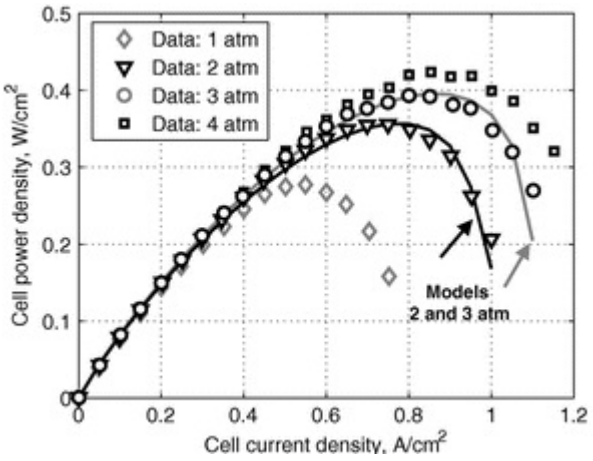

(b) Cell current density vs. cell power.

Figure 8.7: Properties of an individual fuel cell [36], based on the Honda Clarity.

with increasing operating pressure.

The fuel cell stack has been designed to minimize the overall fuel cell system weight. This system comprises of the stack, the fuel tank, the fuel, the cooling system and the balance of plant (BOP) for both the fuel cell stack and the fuel tank. As stated in the previous paragraph, the cell voltage at maximum gross power and the internal fuel cell pressure are the main design variables. Some other design variables were chosen to be held constant, as they had been shown to maximize the power output of a cell, without a penalty in parasitic power or weight [37]. For instance, the operating temperature of the fuel cell has been set to 80° Celsius.

The fuel cell stack has been sized using the approach described by Datta and Johnson in [36]. The stack needs to be capable of delivering a maximum net power (P_{net}) of 148 kW, as specified in the MTR [8]. This is the power required by the helicopter to maintain a climb rate of 900 ft/min, including 5% transmission and other losses. This means that a power of 140.6 kW will be delivered to the rotor. Afterwards, it is corrected for the achieved transmission loss, which was 8.32%. This results in a net design power of 153.4 kW. However, the fuel cell should also be able to keep itself and all necessary sub-components running. The total power required is defined as the the gross power P_{gross}. It includes the net power, the compressor power and additional losses. An overview is shown in equation 8.5. Because the fuel cell will operate at an elevated pressure, it requires a compressor to supply compressed air that is used in the electrochemical process. A small amount of power can be recovered from the compressed air by using an expander at the end of the cycle, which results in a reduction in gross power. Using the procedure Datta and Johnson propose, P_{others} is estimated to be 5% of P_{gross}.

$$P_{gross} = P_{net} + \left(P_{comp} - P_{exp}\right) + P_{others} \tag{8.5}$$

With P_{net} fixed and P_{others} being a function of P_{gross}, the gross power depends on the compressor and expander (CE) powers. Assuming isentropic compression and expansion, the power required by the CE is defined by equation 8.6. The equation presented here is an adaptation of the standard isentropic relations as found in [38].

$$\begin{aligned} P_{CE} = \left(\left(\frac{p_{stack}}{p_{ambient}}^{\frac{k-1}{k}}\right) - 1\right) \cdot \frac{T_{ambient} \cdot c_p \cdot \dot{w}_A}{\eta_{compressor}} - \\ \left(\left(\frac{p_{ambient}}{p_{stack} - P_{loss}}^{\frac{k-1}{k}}\right) + 1\right) \cdot T_{stack} \cdot c_p (\dot{w}_A - \dot{w}_O) \cdot \eta_{expander} \end{aligned} \tag{8.6}$$

P_{CE} equals the required compressor power minus the power retrieved from the expander. In the above equation $p_{ambient}$ is the ambient pressure, p_{stack} is the pressure in the stack and p_{loss} is the assumed pressure loss over the air flow cycle from the compressor to the expander. $T_{ambient}$ and T_{stack} denote the ambient and the stack temperatures respectively. The mass flow of air is denoted by $\dot{w}_A$ and the oxygen depletion rate is denoted by $\dot{w}_O$. Both are expressed in kg/s. The constants c_p and k, the specific heat and the specific heat ratio

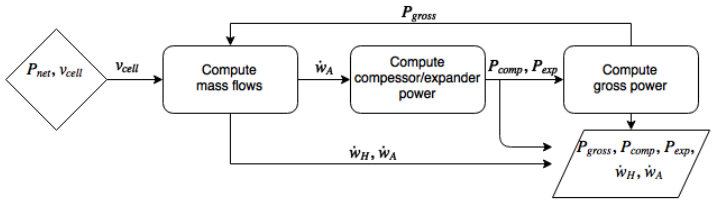

Figure 8.8: Schematic overview of the sizing of the power (Diamond blocks define loop inputs, trapezoidal blocks indicate converged outputs, the remaining blocks define calculation steps within the loop.

respectively, are those for dry air. Although the air in the expander will be moist because of the water vapor that is produced in the fuel cell, the dry air assumption does not imply large discrepancies. Because of the water vapor, the mass flow will increase slightly, and therefore the expander is believed to deliver more power than calculated.

Because of the interdependence of the gross power and the mass flow rate of air, and therefore the CE power, the following procedure has been used for power sizing. Following the scheme presented in figure 8.8, the cell voltage at max power and the maximum required net power are defined as input first. Secondly, using an estimate of the gross power, the relevant mass flows are computed as shown in [36]. Using those flows, the required CE power is obtained through equation 8.6. Then, the new gross power is calculated. Using the new gross power, the mass flows are calculated. This creates a loop that is repeated until convergence of gross power is obtained.

Using the cell voltage as input, at a predefined stack pressure, the gross power during climb can be obtained. The gross power and the cell power directly size the fuel cell mass according to equation 8.7. Here, n_c denotes the number of cells and A the cell area. These two variables can be kept undefined throughout the weight sizing routine, as they will only appear together as $n_c \cdot A$. Ls and W_s denote stack volume (m^3) and stack weight (kg) respectively. The parameters t_c (cell thickness), ρ_c (cell density)and ξ (porosity) are assumed to be constant 2.224 mm, 1988 kg/m^3 and 0.6 respectively [36]. The cell power p_c can be obtained from figure 8.7b. Now the stack size is known, the fuel flow can be obtained for all flight phases, given the required net power during these parts of the flight profile. Multiplying the fuel flow with the flight time per phase, produced a total fuel mass that needed to be stored on board. Using the relationship between tank weight and fuel weight, which is defined in section 8.6, the fuel tank weight can be calculated.

$$n_c A = \frac{P_{gross_{max}}}{p_c} \quad , \quad L_s = n_c A t_c \quad , \quad W_s = L_s \rho_c \xi \tag{8.7}$$

In figure 8.9 the variation of fuel cell system weight with design cell voltage at maximum power is shown. The weight of the individual components is shown in the lower part of the graph. In this optimization the weight of the radiators is also taken into account. An approximation is made on the weight by linearization about a reference point. Details of how the radiator weight is calculated can be found in section 8.5. The Now, only the fuel stack dimensions remain unknown and need to be defined. The individual cells are assumed to have a standard thickness, therefore only the number of cells and the frontal area of the cells can be altered. These parameters depend solely on the design voltage of the complete stack. It is required that at maximum power, when cell voltage is lowest, the stack voltage does not fall under 440 V and at low power, thus high cell voltage, the stack voltage will not rise above 700 V. This constraint stems from the converters and electric motors. Since the individual fuel cells in the stack are in series, the cell voltages add up to the stack voltage. With the number of cells the cell area is calculated and a square cell is assumed. This resulted in the fuel cell explained in table 8.4. For packaging purposes, the stack was divided in three parts and put next to each other, which made the final dimensions 630 x 750 x 250 mm. The fuel stack performance during the major flight phases is shown in table 8.5.

8.4. Fuel cell balance of plant

Apart from the fuel cell stack, described in section 8.3, other components are required to keep the fuel cell running. These components range from simple valves, to humidifiers and condensors. Although these will have to be designed in detail during further design stages, in this report only an estimation will be made. The compressor and expander (CE), sized in section 8.3, will be treated in more detail. Off-the-shelf parts will be

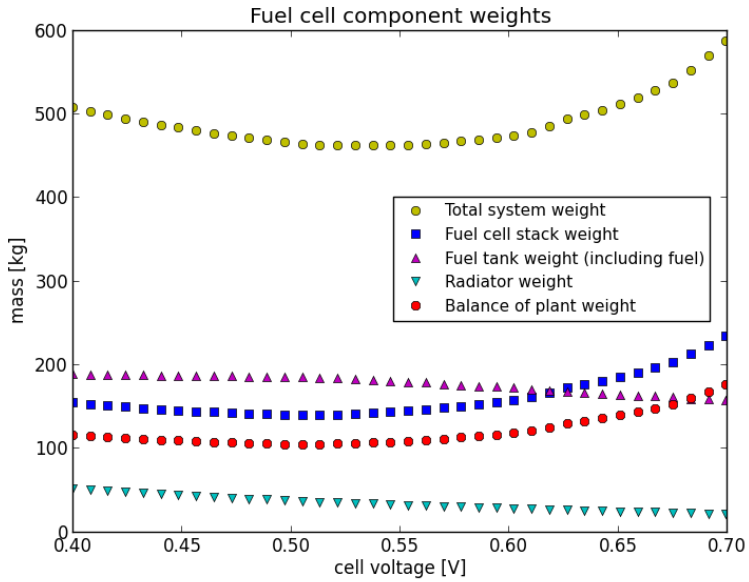

Figure 8.9: Optimization of the fuel cell, fuel tank and cooling system combined. Kinks in the graph is because of roughness of data.

Table 8.4: Specifics of the fuel cell stack at maximum power.

Parameter	**Value**	**Unit**
Number of cells	850	[-]
Cell Area	0.0625	[m^2]
Design cell voltage	0.53	[V]
Design cell current density	6600	[A/m^2]
Stack volume	118	[L]
Stack weight	140.9	[kg]
Fuel weight	17.4	[kg]

used for its design. These components are referred to as the balance of plant (BOP) of the fuel cell.

From [36] it had been identified that the CE is the heaviest component within the BOP. To maintain a high fidelity of design, the CE has been designed in more detail than the remaining components in the BOP. However, the design of turbomachinery is a complex and time consuming task. It has therefore been decided that the selection of off-the-shelf products would be the most efficient design procedure. The CE has to provide adequate pressurization at the required air flow rates. Furthermore, no contamination of the airflow is allowed, because the fuel cell stack is very sensitive to impurities. Opcon Autorotor has experience in the design of CE's for fuel cell applications, and they provide compressors that are adequate for application in the H2Copter [39]. It has been assumed that the expander is of the same weight as the compressor. The pressure difference between inlet and outlet, and the air flow rate are both very similar to those of the compressor, therefore justifying the assumption.

In climb, the CE requires 22 kW to compress the air flow. The required power will be provided by an electric

Table 8.5: Power and fuel flow during the four different flight phases.

Flight Phase	P_{net}	P_{CE}	P_{gross}	V	$\dot{w}_H$	$\dot{w}_A$	t_{phase}
	[kW]	[kW]	[kW]	[V]	[g/s]	[g/s]	[s]
Climb	153	21.9	185	451	3.65	313	846
Cruise	126	13.0	147	534	2.45	210	4194
Descent	51	4.21	58	655	0.793	68.0	846
Surveillance	106	8.77	122	577	1.87	160	1800

Table 8.6: Balance of plant components and their respective weights.

Component	**Subcomponents**	**Weight** [kg]
Compressor/Expander (CE)	Compressor [39]	15.0
	Expander	15.0
	Electric motor [40]	7.3
	Motor Controller [41]	6.8
	Driving belt	0.5
Remaining BOP		38.7
Total BOP		83.4

motor. For this purpose, the ES-LAK-M100 by LZ design [40] has been chosen. Its low weight and adequate power make it a suitable choice. Next, a compatible controller was chosen accordingly.

The remaining components of the BOP were assumed to size linearly with the fuel cell stack weight. For this procedure, the relative weight of the BOP from the fuel cell in [36] has been used as a baseline. It has been calculated that the BOP is 27.5% of the fuel cell stack weight. Table 8.6 provides an overview of the components and weights in the BOP, including the weight of the CE. It has to be mentioned that, contrary to Datta and Johnson, the cooling system is not considered a part of the BOP. It will be treated in section 8.5.

8.5. Cooling

The fuel cell has to be working at a temperature of 80 °C exactly to have an optimal performance. When the temperature only increases to 85 °C the delivered cell power will be less, while a temperature of 100 °C generally causes irreparable damage [37]. Not only the fuel cell, but also the electric motors as well as the controllers require active cooling to keep the temperature within acceptable range. The stated systems are being cooled by water in combination with a compact heat exchanger, which is a typical cooling system in both automotive and aviation. Water is pumped through the helicopter in order to heat up and move the heat to a heat exchanger, through which outside air will flow to cool down the water again. This type of heat exchangers is called a crossflow radiator.

Required heat rate

The inefficiency of the controllers and the electric motors cause a total heat rate of 23.6 kW [29, 35]. The DC/DC converters generates heat as well, but since this is only 53 W [42], it is assumed that it will cool itself. The rate for the self-designed fuel cell has to be calculated by hand. The efficiency of the fuel cell stack can be calculated by equation 8.8 [36].

$$\eta_{fc} = \frac{v_{c,design}}{v_{c,theoretical}} \tag{8.8}$$

The theoretically achievable cell voltage $v_{c,theoretical}$, according to the chemical reaction, is 1.47 V for a fuel cell that delivers liquid water as output. The cell voltage at maximum power is 0.53 V. The equation results in an efficiency of only 36%. When the fuel cell delivers 148 kW net power, or 185 kW gross power, the waste heat is 328 kW. Combining this result with the earlier mentioned rates, the cooling system will have to deal with 348 kW when the helicopter is flying at full power.

Heat exchanger sizing

To size the radiators that will be in contact with outside air, at first some conditions of the cooling system have to be specified. The specific heat capacity c_p of the chosen cooling fluids, air and water, are 1005 and 4190 J/kg-K respectively. When this value is multiplied by the mass flows $\dot{m}$ of the fluids, as in equation 8.9, the heat capacity rates are obtained in W/K. These are the rates at which the fluids are capable to store waste heat. The mass flows are design parameters for the radiator; higher flow rate results in easier heat removal but requires larger pumps or fans to move this amount. Now C^* can be calculated with equation 8.10, which is the ratio between both the lowest capacity rate and the highest.

$$C_{air,water} = \dot{m}_{air,water} c_{p_{air,water}} \tag{8.9}$$

$$C^* = \frac{C_{min}}{C_{max}} \tag{8.10}$$

The other environmental aspects are the radiator inlet temperatures. The water is assumed to completely heat

Table 8.7: Fluid and radiator parameters used during sizing [43].

Parameter	Unit	Value		Parameter	Unit	Value
		Water	Air			
Prandtl Number	Pr [-]	2.56	0.712	j/f	[-]	0.25
Pressure drop	Δp [Pa]	10000	500	Surface porosity	σ [-]	0.8
Colburn factor	j [-]	0.032	0.02	Hydraulic diameter	d_h [m]	0.0025
Density	ρ [kg/m^3]	992	0.92	Surface efficiency	η_{surf} [-]	0.8

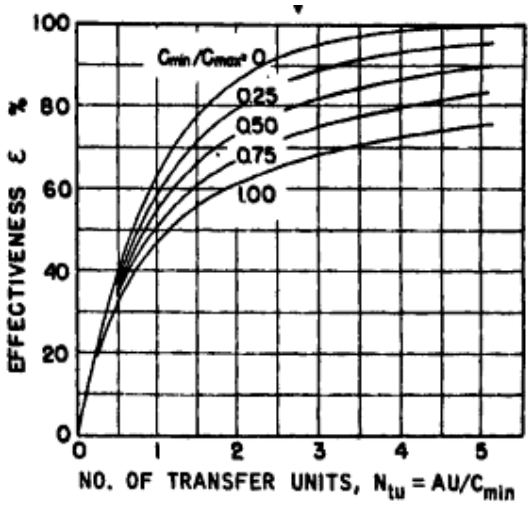

Figure 8.10: Graph of ϵ against number of thermal units (Ntu) for multiple C^* [43, p207].

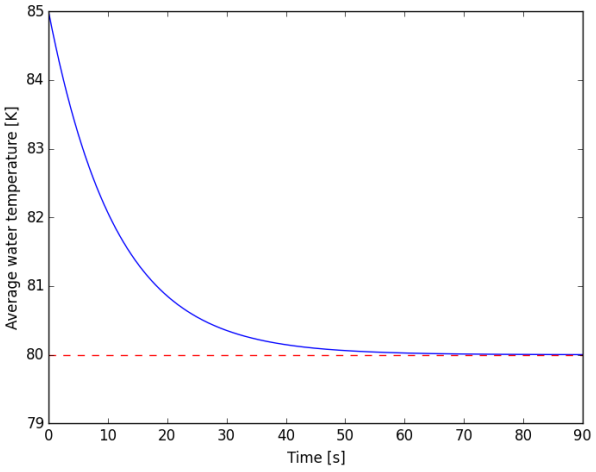

Figure 8.11: Progress of the water temperature after overheating

up in the fuel cell. Since it is working on 80 °C, the water inlet temperature is taken to be the same. The air inlet temperature is taken to be 35 °C. This is equivalent to a US military hot day. Although this temperature is high, the cooling system is designed to still be able to remove the amount of heat at maximum power. The maximum theoretical heat rate can now be found with equation 8.11. The effectiveness of the radiator necessary to remove all heat from the cooling water is calculated with equation 8.12.

$$Q_{max} = C_{min}\left(T_{water,in} - T_{air,in}\right) \quad (8.11)$$

$$\epsilon = \frac{Q}{Q_{max}} \quad (8.12)$$

At this point a first estimation on the dimensions of the heat exchanger has to be made. Two dimensions are chosen: the flow length of the air L_{air} and the flow length of the water L_{water}. These are the lengths both fluids have to travel through the heat exchanger. To calculate the number of thermal units for either fluid, a measure for the heat removal capability, equation 8.13 is used. The used parameters are stated in table 8.7. These are based on the fluid characteristics in the radiator environment as well as on typical values for radiators of this size and temperature [43]. With both the number of thermal units for both sides of the heat exchanger the total thermal units can be calculated using equation 8.14.

$$N = \frac{4Lj\eta_{surf}}{d_h Pr^{2/3}} \quad (8.13)$$

$$\frac{1}{Ntu} = \frac{1}{N_{air}\left(\frac{C_{air}}{C_{min}}\right)} + \frac{1}{N_{water}\left(\frac{C_{water}}{C_{min}}\right)} \quad (8.14)$$

Now the total number of thermal units is known, figure 8.10 can be used. Together with the ratio of heat capacities C^* the achievable effectiveness ϵ can be determined. Comparing this to the required efficiency as calculated earlier, it can be seen whether the chosen flow lengths are enough to remove the waste heat. If not, the lengths can be changed to meet the requirements, or the mass flows can be changed to lower either the effectiveness or the ratio of capacities.

When the number of thermal units turns out to be high enough, the frontal area for both fluids can be calculated using equation 8.15. The porosity is added because not all of the frontal can be used to flow fluid through, but also radiator material is present. The third dimension of the follows automatically from the combination of areas and flow lengths. With this the volume of the heat exchanger can be calculated, and with the volume

Table 8.8: Specifics of each of the four heat exchangers.

Parameter	Unit	Value		Parameter	Unit	Value
		Water	Air			
Heat capacity rate	C [W/K-s]	5028	3015	Ratio of heat capacities	C^* [-]	0.599
Flow length	L [m]	0.980	0.049	Effectiveness	ϵ [-]	0.64
Num. of therm. units	N [-]	15.3	1.83	Volume	V [L]	17.75
Frontal area	A_{fr} [m^2]	0.00376	0.299	Mass	m [kg]	8.88
Mass flow	$\dot{m}$ [kg/s]	1.20	3.0	Num. of therm. units	Ntu [-]	1.51

the mass. The density is assumed to be 0.5 kg/m^3 [36].

$$\frac{\dot{m}}{A_{fr}} = \sigma \sqrt{\frac{2(j/f)\rho\Delta p}{NPr^{2/3}}} \tag{8.15}$$

With the above stated approach, the cooling system has been sized iteratively, by changing the flow lengths mass flows of both the water and air. This resulted in a total of four radiators, since less would either not be capable of removing all heat, or become too big to fit properly into the fuselage. The final dimensions of one heat exchanger are 49 x 980 x 369 mm.

The machines to provide the mass flows for both fluids are electric pumps and electric fans for water and air respectively. To deliver four radiators 1.25 kg of water every second two electric pumps from Davies Craig are being used. Two EWP 150s will be installed in parallel to double the water flow. They can both deliver 150 L/min, which will result in a total mass flow of 4.96 kg/s, or 1.24 kg/s per radiator. Both pumps weigh 1.1 kg and use 120 W of power on 12 V [44]. A total amount of sixteen small fans will be used to create an airflow through the radiators. Four will be installed on top of each other at the back of a radiator, in order to suck the air through it, which is possible since the radius is only 8 inch, or 203 mm. Each fan requires a power supply of 54 W on 12 V, making a total of 864 W. The maximum air flow of these fans are 4000 m^3/h, sufficient for this system. The weight is increased a lot due to this solution: 19.2 kg since the weight per fan is 1.2 kg. However, this solution is preferred since no large area air inlets are needed in the outside air stream, therefore reducing the fuselage drag significantly. Another benefit is that it will be able to cool all of the systems during hover. Since in that flight phase no outside airflow is present and fans are the only way to cool the radiators[45].

To calculate the weight of the water inside the cooling system, the actual flow area of the water times the flow length is used, which means without correction of the porosity. This results in a water weight of approximately 4 kg per radiator. The weight per meter for silicon hoses of 1 inch diameter, typically used in these applications and fitting on the chosen pumps, have a weight of 0.30 lbs/ft or 0.45 kg/m [46]. Estimated is that 10 m of hose is needed which makes a total tube weight of 4.5 kg. The water continuously present in these tubes is 4.9 kg.

The robustness of the cooling system against unexpected overheating is analyzed as well. It can be noted that the system is stable, meaning that it will always return to its nominal state. When the water heats up due to overheating, Q_{max} will increase as stated in equation 8.11. Because the efficiency does not change, the heat removal Q will increase with Q_{max} (equation 8.12). Because the water cools down again, Q_{max} will decrease again, resulting in a slow approach to the nominal water temperature. It can be seen in figure 8.11, that if the system heats up to 85°C the water temperature will be back at 80°C in only 90 seconds. The best solutions remains to decrease the power for a moment and let the system cool down.

All weights added up the cooling system has a total mass of 79 kg. This is exceeds the budget for cooling, which assumed to be part of the fuel cell balance of plant in Datta's estimation [36]. In this approach the impact of fuel cell cooling turned out to be underestimated. The results in this section are verified and validated with example calculations and heat exchangers in [43].

8.6. Hydrogen tank

The hydrogen tank is a very heavy component of the H2Copter. This section explains the selection and sizing of the hydrogen tank. Three types of storage were considered: gaseous storage (in pressure tanks), liquid storage (in cryotanks) and solid storage (by physically or chemically attaching hydrogen to another substance.

8.6.1. Gaseous storage

Hydrogen has a very low density. In order to keep the size within reasonable bounds, very high pressures are required. There are currently two industry standards: 350 bar and 700 bar [47]. For pressures higher than 350 bar, hydrogen does not behave like an ideal gas anymore: the increase in pressure becomes higher than the increase in density. This causes the hydrogen mass fraction of the tank to decrease [47]. From preliminary analysis, it was determined that a 350 bar tank will fit in the design, so this industry standard was followed.

For mobile storage of hydrogen, there are two types of tanks of interest. Type 3 tanks have an outer shell made of composite, but contain a layer of metal on the inside (the liner) to prevent the hydrogen from escaping. In type 4 tanks, the liner is made of plastic, which is lighter, but more complicated to manufacture. Composites are very suitable for tank design, because the loads are very predictable, and always tensile.

The hydrogen weight fraction is limited by the strength of the material. Datta and Johnson [36] stated in 2014 that a tank containing 5.4% hydrogen in weight was possible, with a total density of 0.038 kg/L. Quantum Technologies [48] have designed a tank that contains 7.5% hydrogen. This tank only contains 1.55 kg of hydrogen, so a larger tank could have an even higher mass fraction. Furthermore, this tank was designed for automotive transport with a safety factor of 2.25. Aerospace structures usually have a lower safety factor. The tank contains 0.03875 kg of hydrogen per liter of (internal) volume.

8.6.2. Liquid storage

Hydrogen becomes liquid at 20.28 K when stored at 1 atm. It is possible to store hydrogen in its liquid state. This leads to increased densities of about 0.071 kg/m^3, but it requires adequate isolation. When hydrogen is stored in its liquid state, it slowly boils off, depending on the level of isolation. Another disadvantage is that cooling the hydrogen to cryogenic temperatures requires a lot of energy.

According to Datta and Johnson [49], 5 kg hydrogen can be stored cryogenically (in its liquid form) at a weight fraction of 5.5% and a total density of 4 kg/m^3. This is not much better than their prediction of compressed hydrogen. It was decided that this slight performance increase does not outweigh the complications in handling liquid hydrogen.

8.6.3. Solid storage

A different approach is to store hydrogen in a solid form by attaching the molecules to other substances. This increases the volumetric capacity dramatically. Solid storage can be preformed physically by physisorption (adsorption), or chemically.

Physisorption

There is a large interest in adsorption (attachment to a surface at a molecular level) of hydrogen to carbon nanotubes. The hydrogen molecules are attached to the surface of the adsorbent. There has been a large discussion about the capabilities of carbon structures; hydrogen weight fractions between 0.3% and 68% have been reported. Zhou [50] has compared 40 references and has tried to reproduce their results. He found that the maximum capacity is 0.44% at 77 K and 40 bar of pressure. this is too low to compete with the other technologies.

Adsorption on activated carbon provides better results, but tanks are required for the higher pressure. Bimbo [51] explains the idea of making a hybrid pressure tank internally covered with a layer of adsorbent material. This tank has increased density due to the physisorption, and the empty space can be used to store gaseous hydrogen. It was found that the adsorbents provide a hydrogen mass fraction that is too low. The most feasible materials are AX-21 with a weight fraction of 5.6% and MOF-177 with 7.4% hydrogen [52]. The pressure tank, which must also be cooled to the temperature of liquid nitrogen, is not included in this. It is therefore decided that physisorption is not feasible.

Chemical storage

A well-investigated way of storing hydrogen is by using metal hydrides. This increases the density, but the hydrogen weight fraction is limited to 3% [50]. Complex hydrides are more feasible. $LiBH_4$ is promising with a capacity of 18%, but it has several disadvantages. Only 13.5% of the weight is releasable hydrogen, high temperatures are required, the chemicals are dangerous and the tank is not included in the weight estimation [53]. With the additional disadvantage that it currently only works in laboratories, this option was discarded.

Another possibility is the use of $NaAlH_4$, but it only has a theoretical hydrogen capacity of 5.55%, excluding the

tank [54]. There is a flight-proven airplane design using $NaBH_4$ for storage [55], but this substance has an even lower capacity of 4% [56]. It is concluded that solid storage is not feasible for flight.

8.6.4. TANK DESIGN

The decision is made that compressed hydroge storage is the most feasible option. Commercially available tanks are usually designed for automotives, and do not contain enough hydrogen for the H2Copter. Land-based tanks, on the other hand, are much too large. Therefore, the tank is custom-designed to fit the needs of the helicopter. The tank will not be designed in detail. The goal is to find an accurate estimation of the weight and size of the tank.

The industry standard is to produce composite tanks using filament winding. This process is suitable for the normal shapes of pressure vessels, but it does not allow the production of any shape. The standard method is to design tanks with geodesic winding. This means that the fibers are loaded only in tension. With pure geodesic winding, there are no shear loads, so the fibers will not slip [57].

Pipkin and Rivlin [58] found that the ideal tank has an isotensoid design. This means that the stress is equal throughout the material. They derived equation 8.16 to compute the weight of the structural material of an isotensoid pressure vessel. This equation is not dependent on the shape of the tank; it is valid for any closed shape. The weight depends on the material density ρ, the pressure difference P, the internal volume V and the maximum stress $\bar{\sigma}$. Filament winding requires polar holes in the end caps to attach the vessel to an axial beam. The equation is only approximate when the hole radius r_0 is not zero, but it is still very accurate. When the hole radius is half of the maximum radius R, the error is only 1.7%. It is decided to disregard the hole, and to use the equation directly.

$$m = \frac{3\rho P V}{\bar{\sigma}} \tag{8.16}$$

Vasiliev [57] derived how the geodesic isotensoid design could be made using filament winding. The final shape is not a cylinder with spherical end caps: the end caps are much flatter. Away from the polar holes, the shape of the end caps is described by equation 8.17 [57]. The equation defines the axial coordinate of the end caps z in terms of the radius r, the hole radius r_0 and the maximum radius R. The integral was evaluated numerically by means of the trapezoid rule. With the assumption that there is no polar hole, the equation reduces to equation 8.18. It can be seen that this equation has a singularity for $r = 0$, but it does not diverge when approaching this value. The calculations were verified by comparing the shape to the shapes plotted by Vasiliev [57].

$$z = -\int_R^r \frac{r^3\sqrt{R^2 - r_0^2}\,dr}{\sqrt{R^6\left(r^2 - r_0^2\right) - r^6\left(R^2 - r_0^2\right)}} \tag{8.17}$$

$$z = -\int_R^r f(r)\,dr = -\int_R^r \frac{r^3 R\,dr}{\sqrt{R^6 r^2 - r^6 R^2}} \tag{8.18}$$

A suitable type of liner for a type 4 tank is 5 mm high-density polyethylene (HDPE) [47]. For a type 3 tank, 7 mm aluminium is said to be suitable, but this is much heavier than HDPE [47]. It is decided to design a type 4 tank. With the assumption that the tank is thin-walled, the liner weight is computed according to equation 8.19 by using the surface area S of the tank, the thickness of the liner t_l and the HDPE density ρ_l. The area of a surface in Cartesian coordinates is given by equation 8.20 [59]. This equation is converted to cylindrical coordinates to arrive at equation 8.21. In this equation, the function $f(r)$ from equation 8.18 can be reused. This integral was also evaluated numerically with the trapezoid rule. The final surface area was obtained by adding the cylindrical part with length L_{cyl} in equation 8.22.

$$m_l = \rho_l t_l S \tag{8.19}$$

$$S_{cap} = \iint_S \sqrt{1 + \left(\frac{\delta z}{\delta x}\right)^2 + \left(\frac{\delta z}{\delta y}\right)^2}\, dx dy \tag{8.20}$$

$$S_{cap} = \iint_S \sqrt{1 + \left(\frac{\delta z}{\delta r}\right)^2 + \frac{1}{r^2}\left(\frac{\delta z}{\delta \theta}\right)^2}\, r dr d\theta = 2\pi \int_0^R \sqrt{1 + \left(f(r)\right)^2}\, r dr \tag{8.21}$$

$$S = 2\pi R L_{cyl} + 2 S_{cap} \tag{8.22}$$

The calculations were validated by reproducing an existing design. The tank that was used is described in [47]. It is made of composite with tensile strength of 2550 MPa and a density of 1.800 kg/m^3 and it stores 5.6 kg of usable hydrogen at 350 bar. The safety factor on the tensile strength is 2.25, and a factor of 1.25 is used for overpressure during refill. Not all the hydrogen can be taken out: the 'empty' pressure is 20 bar, so some extra hydrogen is put into the tank. The non-ideal density of hydrogen was determined with the process described in [60]. The reference tank was designed for room temperature (25°C). It has a cylindrical length equal to three times the diameter. Table 8.9 shows the component weights of the reference tank, along with those of the reproduced tank.

The estimated carbon fiber and the liner mass are very close to the actual values. This indicates that the computed shape is close. Because the density of the glass fiber and the foam were unknown, the mass of those components could not be reproduced. They were simply copied, along with the balance of plant components.

With the validated model, a new tank could be designed. The estimation of the new tank is also shown in table 8.9. Some design inputs were changed for this. The reference tank was made of Torayca's T700S carbon composite. Torayca also produces a stronger composite: T1000G [61]. Hydrogen pressure vessels and aerospace are listed among the applications of this material, so it is suitable. It has a higher tensile strength of 3040 MPa, with the same density. The safety factor of 2.25 is reduced to the aerospace standard of 1.5. This factor is a standard for load-carrying components in aerospace products. It is also decided that the tank should not be limited to room temperature: it is designed to be operational at 50°C.

It is found that the glass fiber is only used for the logo imprint. Tank manufacturer Quantum states that the glass fiber layer has no structural function [47]. It was therefore removed from the final design. The reference tank has foam to protect the end caps. This is useful for automotive applications, because the tank can be attached firmly to the sturdy structure of the vehicle, ensuring proper load introduction. Only the end caps need additional protection against impact with other components. Due the size of the H2Copter tank, mounting in this way is not possible. This also removes the necessity of adding foam to the end caps.

Crash safety is ensured by the two pressure relief devices. When a crash occurs, they can rapidly empty the tank due to the high pressure. This can be done automatically by means of a shock sensor. An additional safety measure is implemented in the mounting: the end caps with the holes, which are the weakest spots in the design, are mounted on the left and right side of the helicopter. If the plugs breaks on impact, the pilots are not directly located in the hydrogen flow. Furthermore, the tank has the beneficial feature that it does not explode when a piece of the tank is pierced, because of the the filament wound fiber structure [62].

For safety, it was decided to make some changes in the balance of plant. There will be two pressure and temperature transducers, while the reference tank only has one of each. It is estimated that the valves and transducers do not have to be heavier than the ones on the reference tank: they are designed to withstand the pressure, and the mass flow has only a very small effect. The piping, boss, plug and vehicle interface brackets have to be larger for this tank: it was assumed that their weight scales with the volume.

The final tank has a hydrogen mass fraction of 9.57%. This value is higher than on the reference tank, due to the stronger material and reduced safety factor. The removal of the glass fiber and the foam has also caused an increase of the hydrogen weight fraction. It is also determined that some of the lighter components of the balance of plant do not increase in weight when the size of the tank increases. This causes larger tanks to have a larger hydrogen mass fraction.

Table 8.9: Properties and mass breakdown of the reference tank, the reproduced tank and the custom tank.

	Ref. tank	Validation	New tank	Comments
Recoverable H_2 mass [kg]	5.6	5.6	17.4	
Total H_2 mass [kg]	6.0	6.0	18.7	
Pressure [bar]	350.0	350.0	350	
Design temperature [°C]	25.0	25.0	50	
Internal volume [m^3]	0.258	0.258	0.857	
Safety factor [-]	2.25	2.25	1.50	
Material	T700S	T700S	T1000G	
Tensile strength [MPa]	2550	2550	3040	
Density [kg/m^3]	1800	1800	1800	
Component weights [kg]				
Structure				
Liner	11.4	11.7	20.8	
Carbon fiber	53.0	53.8	99.9	
Glass fiber	6.1	(6.1)	0	No structural function; removed
Foam	5.2	(5.2)	0	Other impact solution
Structure total	75.7	76.8	120.7	
Balance of plant				
Check valves (2)	0.4	0.4	0.4	
Manual Valve (1)	0.2	0.2	0.2	
Excess flow valve (1)	0.2	0.2	0.2	
Service vent valve (1)	0.2	0.2	0.2	
Shutoff valves (3)	1.8	1.8	1.8	
Relief valves (3)	0.6	0.6	0.6	
Pressure transducer (1)	0.1	0.1	0.2	Twice
Temp. transducer (1)	0.1	0.1	0.2	Twice
Pressure regulator (1)	2.1	2.1	2.1	
Pressure relief devices (2)	1.0	1.0	1.0	
Piping/fittings	4.0	4.0	13.3	Scaled with volume
Boss	0.4	0.4	1.3	Scaled with volume
Plug	0.2	0.2	0.7	Scaled with volume
Vehicle interface brakets	5.2	5.2	17.3	Scaled with volume
Fill system control module	1.0	1.0	1.0	
Misc	2.0	2.0	2.0	
BOP total	19.4	19.5	42.5	
Total tank + reserve fuel	95.5	96.7	164.5	
Total tank + fuel	101.1	102.3	181.9	
H_2 mass fraction [%]	5.54	5.47	9.57	

9

ROTOR HUB

The design of an electric driven helicopter brings new possibilities and freedoms to the design of the rotor hub. Conventional coaxial helicopters use two steel shafts to run the rotor discs in opposite direction, driven by a combined gear box. The shafts have to enter the fuselage to be able to be driven by the engine. Using the electric drive, electric motors can be placed more freely in contrast to their fossil fuel driven counter part. The main task of the hub is to connect the rotors to the fuselage and provide flight controls towards the blades. As discussed in section 9.3 a servo flap control is developed to decrease complexity and drag of the conventional swash plate assembly. With this in mind the only control task of the hub is to provide the space to guide control cables towards the rotors.

To shift the center of gravity closer to the rotor discs and decrease the amount and weight of drive-line components, the electric motors shall be placed close to the rotors. By doing so the hub needs to provide space to guide power and cooling lines towards the motors. Section 9.1 explains how this space will be given even though a gearbox will be placed in line with the shaft, of which the design is explained in section 9.2. Further steps are taken to display the structural design and material choice on the hub.

In figure 9.1 the work flow of the hub design, all sub assemblies included, can be seen. Split in the same manner as this chapter, the flow diagram shows the fields of structural hub, gearbox and servo flap design.

9.1. STRUCTURAL HUB DESIGN

The structural hub design concentrates on the design of the structure determining the disc spacing and providing the structure towards the fuselage. The main loads experienced by the hub are torque, induced by the counter-rotating rotors, axial loading due to weight carrying function and bending due to the pitch and roll induced forces. Different materials are taken into consideration: steel and aluminum. To keep the cost to an oversee-able level, titanium will not be included. The peak load factors for the hub design can be taken from the certification which include gust loads in maximum flight conditions. As verified in section 10 a FEM analysis is performed on the designed structure to validate the function of the chosen design and material.

Starting from the fuselage onwards the hub is connected via a load distributing surface.

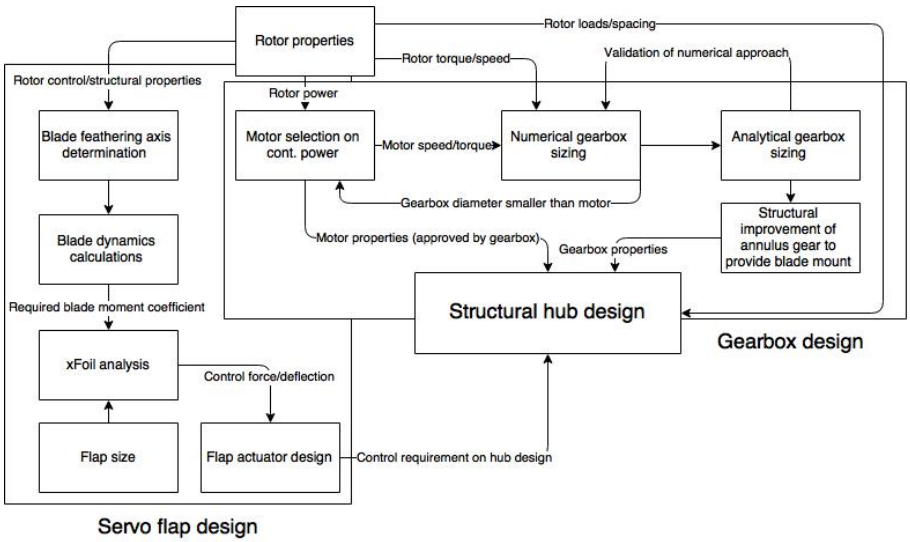

Figure 9.1: Flow diagram of the hub design.

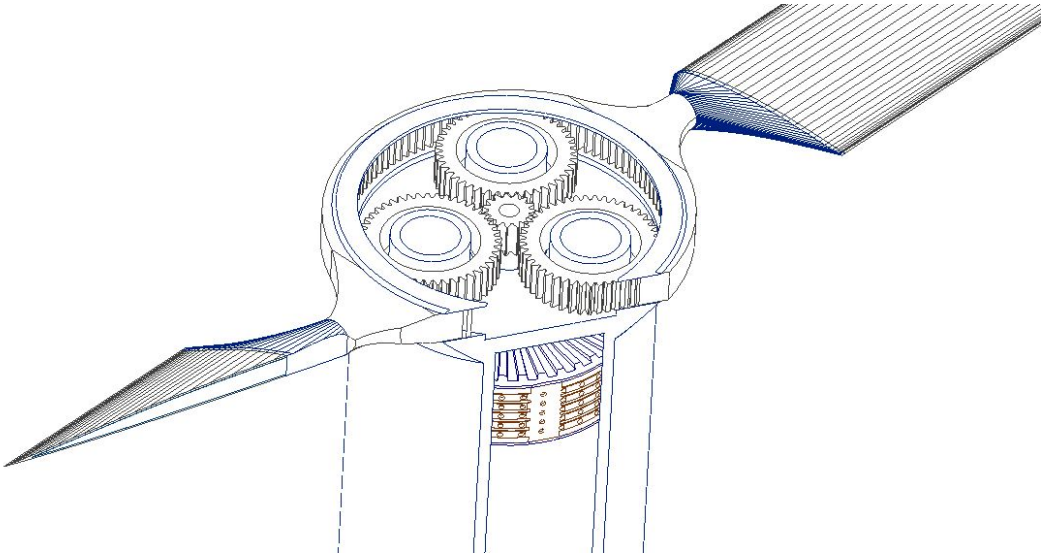

Figure 9.2: Drive-line hub integration.

By doing so the hub-rotor assembly can be re-positioned towards the center of gravity without having a huge impact on the assembly of components within the rotorcraft. This option makes it easy to improve the stability after all components have been assembled. Assuming the maximum bending loads in all directions to be equal, a round shape is the most efficient choice. Given the round shape, use of available extrusion material can be made, which can also decrease production time and cost. Load cycles are mainly induced by control changes.

To make sure everything is covered in the analysis, one rotor turn is considered to be a cycle. The requirement on hub loading is the certification load factor of 3.5 on gust loads. One of the main players when it comes to the material choice is the available room. Whereas a light weight design can be realized with aluminum when room is available, steel rather scores at limited space and high load applications. Since a motor and gearbox integration into the hub is planned, the minimum hub diameter is predefined. With the results of the motor-gearbox combination the hub can be sized and a material selection can be performed. With a wall thickness of 3 mm, for impact and buckling safety, the hub structure is checked for aluminum and steel. The maximum stress obtained in the hub, during a combined loading due to rotor torque, vertical load and bending exceeds 40 MPa, as numerically determined with the Autodesk Inventor. Aluminum 7075-T6 offers a fatigue strength of 159 MPa for 500,000,000 cycles. A safe use of 19000 hours can be guaranteed by using an aluminum hub. The weight saving over a steel design is with 34 kg versus 98 kg a factor of 2.88.

9.2. GEARBOX DESIGN

As given by the rotor design a rotational speed of 432 rpm is required. For electric motors this speed can be considered relatively slow, meaning that the specific power of state of the art motors cannot be achieved in the motor design. This has structural reasons since a motor requires high torque to deliver the power, which results in a large structural weight. A gearbox brings the ability to use state of the art motors, and convert the high speed and low torque to low speed and high torque. As discussed in section 9.1 the approach is to package the electric motor and gearbox inside the hub. To make the setup space efficient, a similar diameter of gearbox and motor is favourable. The motor selection as described in section 8.1 goes in line with the gearbox design. Since the motor selection is based on existing systems, a perfect match in size cannot be made. Different gearbox designs exist, yet not many are suitable for the intended use. Conventional spur gears would increase the required cross-sectional area since input and output shaft are present with an offset. To decrease the space required, a planetary gearbox is the best solution, figure 9.3. With a larger power and torque density than conventional spur gears, planetary systems find use in many applications. Due to complex lubrication and shifting properties, if a variation of gear-ratios is required, planetary gears show disadvantages for some applications. Since the gear ratio is fixed the planetary gearbox is the best choice for the rotor drive.

9.2.1. GEARBOX

A planetary gearbox can be driven in different ways. The most space efficient manner is to run the sun in combination with the planet gears and keep the annulus gear fixed. By doing so, a gear ratio of +1 in comparison to a planet fixed assembly can be achieved. To be able to guide cooling lines and electric cable through the hub towards the motors and blades, the gearbox needs to have fixed planets, to enable guidance of those elements through the center of each planet. With a spinning sun and annulus, the annulus can be used as mounting point of the rotor blades. Using thus the high strength gear steel to provide the load transfer between the two rotating blades.

With that in mind the gearbox can be sized. A first approach is a numerical calculation based on the maximum stress experienced on the gear circumference. With formula 9.1 the maximum contact stress between the sun and planet as well as planet and annulus can be calculated [63]. The formula includes several gear properties: F is the face width, r the gear diameter, E the youngs modulus, F the facewidth and ϕ the pressure angle. By keeping most variables fixed to standard values, material properties and pressure angle do vary. The main design iteration is based on the remaining properties the gear diameters and face widths. The tip speeds and loads follow from the chosen gear ratios and diameters. By calculating the stress factor with formula 9.2 an evaluation on the life cycle of the gears is made. Statistical data on stress cycle factor, temperature factor, reliability factor and a safety factor of 1.5 are chosen. Multiplying the maximum stress factor with the maximum yield strength of the gear material gives the allowed constant load to endure the lifetime. The requirement for the gear design is to keep the value of the maximum contact stress in formula 9.1 below the mentioned result.

$$\sigma = \sqrt{\frac{W\left(1+\frac{r_1}{r_2}\right)}{r_1 F\pi\left[(1-\nu_1^2)/E_1+(1-\nu_2^2)/E_2)\right] sin\phi}} \tag{9.1}$$

$$stressfactor_{max} = \frac{f_{stresscycle}}{f_{safety}\cdot f_{temperature}\cdot f_{reliability}} \tag{9.2}$$

The final sizing input can be seen in table 9.1. The iteration results in a gear ratio of 1:7 for the selected motor of section 8.1. This ratio does not require a second stage gearbox since the gearbox diameter lies close to the motor diameter. With the torque and speed of the rotor given, the main input variables are gear ratio, and gear dimensions. Each electric motor comes with a specific performance curve. To let the motor run at a high efficiency the gear ratio needs to be based on it. The resulting numerical values in table 9.2 show maximum allowed stress factor versus the maximum acting stress factor present between the gears. The sun being the most critical gear due to its small amount of teeth, shows a safety factor of 1.53 for its service.

Considering the analytical results, shown in table 9.3, obtained by designing the gearbox in the engineering software KISSsoft, one can see that the flank safety lies with 1.49 very close to the numerical value of 1.53. Since many simplifications on the numerical side are made, an offset is to be expected. With an offset of 2.6 %, the numerical value can be seen as validated.

A schematic overview of the final gearbox sizing can be seen in figure 9.3. The room for cooling line and electric cable guidance is marked by the gray areas. The integration of gearbox and rotor mounting into the hub can be seen in figure 9.2. It shows the mounting of the top disc.

Table 9.1: Numerical gearbox sizing.

Parameter	Value	Parameter	Value	Parameter	Value
Rotor torque [Nm]	1635	Pressure angle [deg]	20	Stress cycle factor	0.89
Rotor RPM	432	Face width [m]	0.036	Sun cycles	399168000
Gear ratio	7	Sun diameter [m]	0.0375	Yield strength [MPa]	1724
Input torque [Nm]	233.57	Sun radius [m]	0.01875	Safety factor	1.5
Motor RPM	3024	Planet diameter [m]	0.1125	Temperature factor	1
Face loads [N]	4152.38	Planet radius [m]	0.05625	Reliability factor	1.096
Amount of Planets	3	Anulus diameter [m]	0.2625	Youngs modulus [GPa]	200
Density [kg/m^3]	7750	Anulus radius [m]	0.13125		
Mass [kg]	14.89	Poisson ratio	0.3		

Table 9.2: Gear stress factors.

	Sun gear		Planet gears		Anulus gear
Max. allowed stress factor		0.541		0.541	
Max. acting stress factor		0.531		0.317	
Safety factor		**1.53**		2.56	

Table 9.3: Analytical gearbox results.

	Sun gear	Planets	Annulus gear
Actual tip circle [mm]	53.8	140.6	311.4
Root safety	5.53	3.19	5.2
Flank safety	**1.49**	1.65	3.98

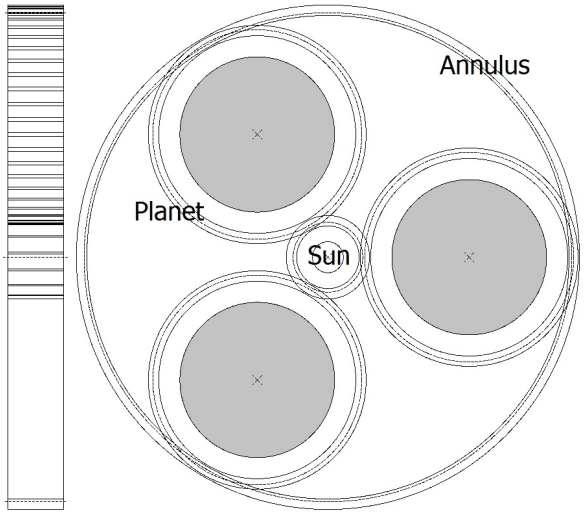

Figure 9.3: Schematic gearbox overview.

9.3. SERVO FLAP DESIGN

In the field of rotor control, the swash plate structure is the most used technique to control the rotor blades. Its structure provides a fully mechanical control system of large complexity, especially for a coaxial rotor assembly. With large complexity comes maintenance. The exposed control structure additionally tends to generate a large amount of drag during flight. Enclosing or even removing the structure will have a great effect on drag, weight and maintenance. During a rotation of the rotor disc, the blades get turned around the feathering axis by twisting the root of the blade. This pure mechanical process can be executed by an aerodynamic moment, too. Current flettner rotorcraft, like the Kaman K-Max, make use of so called servo flaps. Servo flaps are small control surfaces positioned at the trailing edge of the blade, to increase and change the aerodynamic moment on the blade. Those control surfaces get controlled by mechanical links reaching from the pilots control elements towards the surfaces in the blades. Having the control links purely enclosed brings aerodynamic advantages. Additionally the force required to pitch the blade via a control surface is noticeably smaller than required via a swash plate assembly. To decrease complexity, weight and maintenance it is possible to improve the servo flap control by means of electric actuation. The goal is to remove most of the mechanical links towards the control surfaces and implement an electric actuation. As tested by Eurocopter, this can be realized using piezo stack actuators [64]. Given the maximum rotor speed of 432 rpm, the required control frequency results in 7.14 Hz. The requirements on the sub-components are mentioned in the respective sections.

The following sections display a closer look onto the analysis of the servo flap and its requirements towards the electro-mechanic actuator. The design of the actuator is shown as well as its implementation into the blade structure.

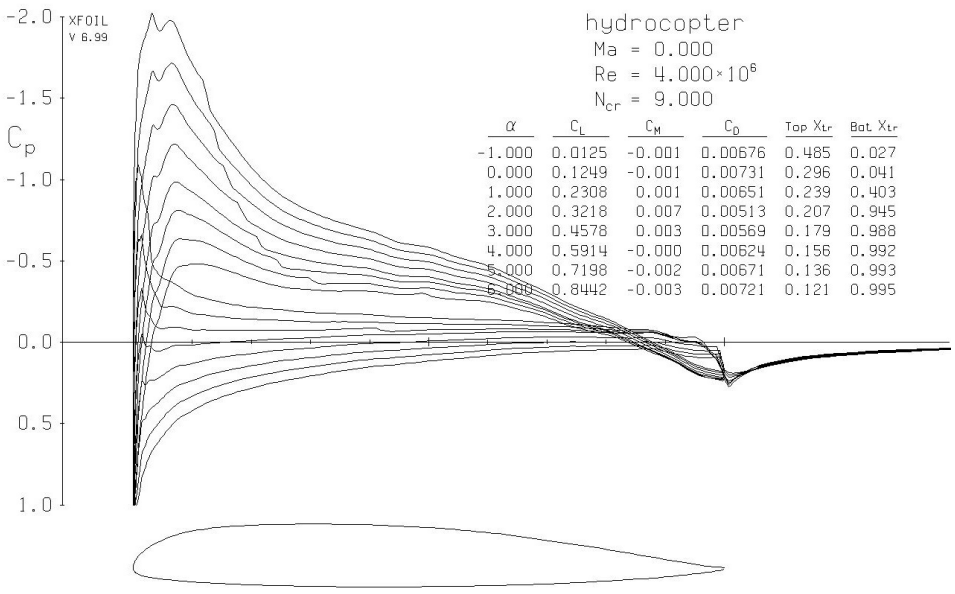

Figure 9.4: Blade moment coefficient analysis with final hinge position.

9.3.1. Flap analysis

The flap is an aerodynamic device of the servo flap assembly. To achieve quick blade responses and keep the required flap deflection to a minimum, the placement near the blade tip, in large air speeds, is favourable. At high cruise speeds, parts of the retreating blade span is under total stall. Mounting the flap in the stall region close to the disc center would cause loose of control for that part of the rotation. To keep the time intensity of the design to a responsible level, the span and chord length of the flap are set to 0.5 m and 0.2c respectively. For redundancy reasons, each blade will include a second full control unit, which is able to continue work in case of failure of the primary unit and therefore align with aerospace standards. Both flaps, inner and outer, are designed to operate on the minimum air speeds experienced by the inner flap. The distance of the primary flap to the tip is set to 0.2 m

Different from a conventional swash plate control, the blade is purely mounted on the feathering axis, without any pitch determining links. Striving for low required control forces and induced drag, the hinge should be placed as close to the center of pressure as possible. Since the chosen airfoil is unsymmetrical, the center of pressure moves with the angle of attack. In an iterative process, using xFoil, a hinge position is determined by entering different hinging points and analyzing the resulting moment coefficients as visualized in figure 9.4. The figure shows the xFoil results for the range of operational angle of attacks. The resulting position of the feathering axis is determined to be (0.258x, 0.05y), based on the low magnitude in moment coefficient changes.

To enable the blade control a moment around the blade needs to be generated. This moment will be generated by the deflection of the servo flap. Since the flap size and position is fixed, only the deflection angle can be varied. The required torque around the feathering axis is based on the angular acceleration needed to control the blade with the required frequency and given inertia, as listed in table 9.4. Using the resulting moment in combination with formula 9.3, the relation between moment coefficient, induced by the flap deflection, and resulting torque on the blade can be determined. The maximum and minimum blade pitch is given by the rotor design. The flap is to be designed for maximum blade pitch at minimum airspeed to ensure control in every flight situation.

$$T = \frac{1}{2} C_m \rho V^2 c^2 \tag{9.3}$$

In the figures 9.5 and 9.6 the two maximum angles in combination with the required flap deflection can be seen. Due to the offset of the center of gravity as well as the asymmetry of the airfoil, the upward and downward blade deflections require different flap inputs. As can be seen in figure 9.5 the upward deflection of the flap is shown. With the upward deflection a nose up moment around the blade gets generated. The upward deflection

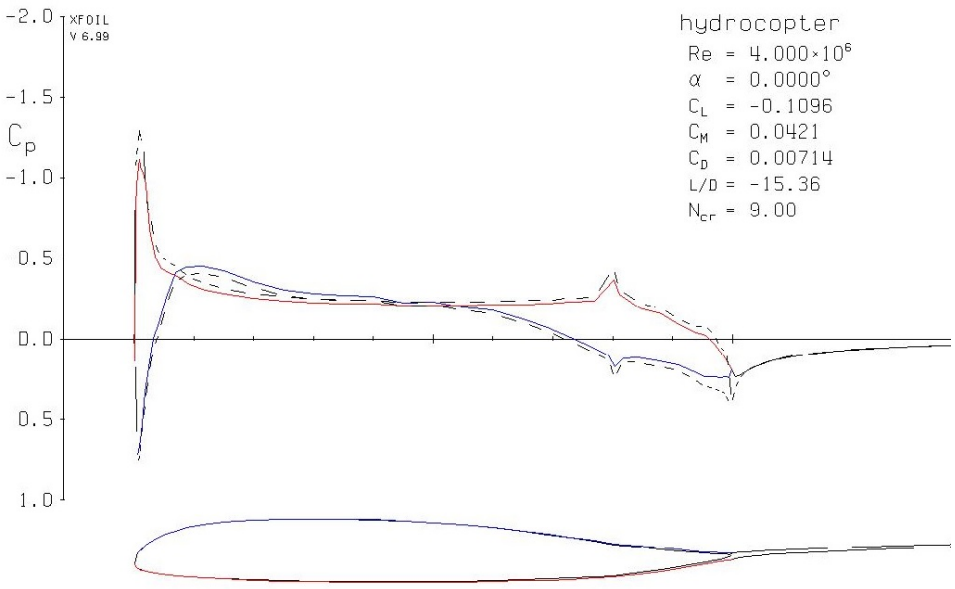

Figure 9.5: Servo flap upward deflection at minimum 0 degrees blade angle.

of 4 degrees results in an angular acceleration of 39.81 rad/s. The same angular acceleration is achieved in opposite direction by a downward flap deflection of 7 degrees as can be seen in figure 9.6.

The torque required to turn the flap around the flap hinging axis forms the requirement for the actuator design. Depending on the arm on the flap hinging axis the deflection and force required can be derived as shown in table 9.5.

9.3.2. SERVO ACTUATOR DESIGN

The flap mounted on the blade requires a control mechanism. Since the idea is to replace a fully mechanical linkage with an electric-mechanical assembly, an actuator needs to be designed. A possibility is the use of piezo stacks. Piezo stacks are small sandwich structured elements which change shape when a voltage is applied. With a large frequency range those elements can be used for high frequency applications. Piezo stacks in general deliver large forces but small deflections. Mounted in a bracket, the resulting deflection can be increased, which results in a reduced net-force. To reduce the amount of components, flexible brackets can be designed. Since the actuators have to be placed inside the blade, a low weight and complexity is very important, due to the large centrifugal forces acting. The forces required to control a single flap can be found in table 9.5.

Piezo stacks can be found in different sizes, due to the limited space inside the blade two reference stacks are chosen for comparison, as can be seen in table 9.6. Those two stacks are of the same kind but differ in frontal area, which brings a difference in weight and force. The bracket designed to increase the deflection performance of the stacks can be seen in figure 9.7. The maximum deflection ratio is set to be 10. Increasing this value leads to very high normal forces in the bracket structure and therefore a heavier design. As can be inspected in figure 9.7 the piezo stacks expand in x-direction and contract the height of the bracket in y-direction. This contraction is used to change the angle of flap via a rod as can be seen in figure 9.8. Since the piezo stacks are solely used in compression mode, zero deflection will result in a maximum flap deflection in one direction. To make sure the force acting on the flap via the bracket is large enough for the most critical flight situation, the bracket is designed to resist these loads without deflecting more than allowed. As mentioned two flaps are available per blade for redundancy reasons. To make sure the deflection of a flap with failed actuator can be corrected to a neutral position, two actuators are used per flap. Both sharing 50 % of the required maximum force.

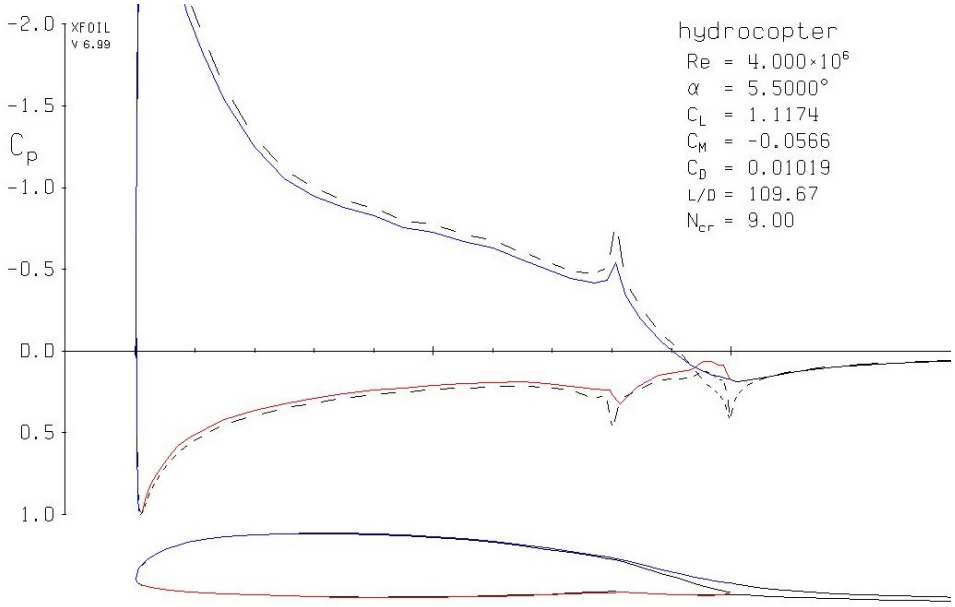

Figure 9.6: Servo flap downward deflection at maximum 5.5 degrees blade angle.

Table 9.4: Dynamics of the rotor blade.

Parameter	**Value**
Blade chord length [m]	0.23
Weight [kg]	12.5
C.o.G x	0.4
Hinge position x	0.258
Hinge position y	0.05
RPM	432
Max. up deflection [deg]	5.5
Max. down deflection [deg]	0
0.5T [s]	0.0694
Angular velocity [rad/s]	2.76
Angular acceleration [rad/s^2]	39.810
Blade moment of inertia [kg·m^2]	0.02067

Table 9.5: Properties of the control flap.

Parameter	**Value**
Required control force [N]	248
Required deflection [mm]	0.731
Control arm [mm]	3.795
Control frequency [Hz]	7.14

Table 9.6: Reference piezo stacks.

Parameter	**Value**	
	TS18 H5 104	TS18 H5 202
Mass [g]	4.5	16
Block force [N]	840	3388
Max. deflection [mm]	0.0145	0.0145
Stack length [mm]	18	18
Efficiency	0.35	0.35

Table 9.7: Actuator assembly.

Parameter	**Value**
Assemblies per flap	2
Stacks in series	8
Stacks in parallel	1
Stack deflection [mm]	0.009
Bracket deflection ratio	10
Bracket weight [g]	200
Actuator weight [g]	328
Total power required [W]	244

Different materials can be chosen for the design of the actuator bracket. Due to the large force applied by the piezo stack, the used material requires a large yield strength. Furthermore the large amount of cycles affects the fatigue life of the bracket. The considered materials are steel, aluminum and titanium. With the advantages of weight saving the aluminum and titanium structures are scoring with respect to a steel design. Concentrating

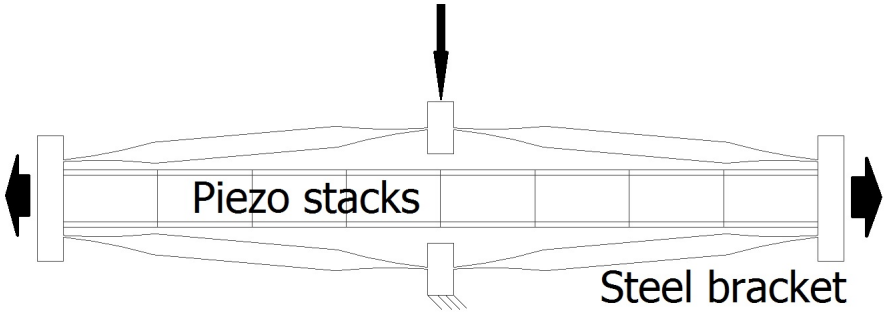

Figure 9.7: Piezo stacks and steel bracket forming the flap actuator.

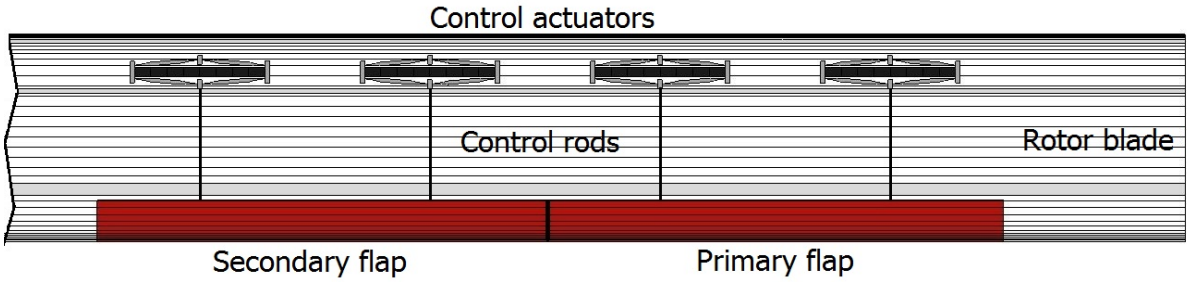

Figure 9.8: Piezo servo flap blade integration.

on the fatigue issue during the operation of the control element, the amount of cycles in combination with the all-time apparent high loads will cause the aluminum and titanium structure to fail. Steel on the other hand does have an endurance limit, a load limit from where the amount of cycles do not cause any fatigue. For conventional steel alloys the endurance limit ranges between 40 % and 50 % of the maximum yield strength. The main design requirement of the bracket is therefore to stay under the load of 300 MPa for standard carbon steel alloys. To maintain a safety factor of 1.5 the bracket is designed to experience a maximum stress of 200 MPa. To make an efficient use of the piezo stacks, the bracket needs to translate the small stack deflection to a large resulting deflection towards the control surface. The bracket in figure 9.7 is designed to enable a deflection ratio of 10, meaning the deflection of the stacks can be increased by a factor of ten. The resulting force decreases therefore with a similar ratio. The design shown is able to withstand two maintenance cycles which equals a flight time of 4000 hours. The first design iteration of the actuator results in an assembly weight of 0.328 kg and a maximum power consumption of 30.5 W per actuator.

9.3.3. Blade control

With the lack of a swash plate, no mechanical control input is given. To control the blades correctly, the pilot input gets translated by a flight computer to a required flap deflection. The angular position of the blade is known via the position sensors of the electric motors. By that a virtual swash plate can be generated. The fly by wire technology brings a major advantage over conventional controls being the possibility of filtering the pilot input to keep the rotorcraft in stable flight conditions. The implementation of a autopilot does not require any changes to the control hardware. Limiting factor to autonomous flight control and fly by wire is the certification. Fly by wire systems for small aircrafts are currently undergoing certification processes.

10

CHASSIS, BODY AND COCKPIT

In this chapter, the design of the aircraft chassis, body and cockpit will be elaborated upon. For the chassis, the general load carrying structure will be considered. This structure also contains the landing gear. For the body part, the hull will be considered. For the cockpit, the interior of the aircraft will be considered.

In section 10.1, the design approach for the structural elements will be explained. In section 10.2, the skid layout is chosen and the model that was made for this landing gear will be shown. In section 10.3, the structure of the chassis will be explained and designed. Finally, in section 10.4, the cockpit interior will be designed.

10.1. STRUCTURAL DESIGN STRATEGY

To design the body for the helicopter, a trade off is made between different body-chassis combinations. Once one of these configurations is chosen, the components that need to be in the helicopter are put in a computer aided design (CAD) program, Autodesk Inventor in this case, and closely packed together. This includes constraint boxes, which were designed to be big enough for the pilots to fit in. This way, the minimum required space for the cockpit is derived. Using the computer modelling program, a supporting structure layout is designed, making sure to accommodate every component. For this layout, the structure is then sized for the critical load cases. The first approach to size the structure was to write a MATLAB program which could derive the forces in each separate member. However, since this program needed to be extremely flexible and applicable to all possible structure configurations, it was decided that the construction of such a program would fall outside the scope of this project and therefore this procedure was not used. However, in order to still be able to calculate the loads in each load bearing member, and thus to be able to size the members appropriately, the CAD program Inventor is again used. To validate the calculations of Inventor, a simple structure is modelled in excel and the resulting forces are checked against the results from Inventor. When the structure is sized, a cockpit is fit as tightly as possible in the packaging in the modelling program, to minimize the fuselage drag. As a final step, the interior of the aircraft will be considered, selecting some essential items which need to be in the helicopter.

10.2. LANDING GEAR

In this section, different types of landing gear options will be traded off. After a type of landing gear has been selected, the sizing method will be explained and compared to the results obtained using Inventor. Afterwards, a first iteration sizing will be made for the landing gear.

10.2.1. LANDING GEAR TRADE-OFF

For the landing gear, three main options were available:

- Skid landing gear
- Fixed wheel landing gear
- Retractable wheel landing gear
- Fixed 3-point landing gear

Skids are often seen on lightweight, low speed helicopters. Skids are favorable due to their simplicity. Disadvantages of skids are added drag, which is why they are not used for high speed helicopters, and the inability to move the aircraft while on the ground. This last disadvantage is why skids are not favorable for heavy aircraft, as these would be too difficult to maneuver on the heliport. Another reason is that, for helicopters which need a lot of power to hover, take off is more efficient if the helicopter has a forward speed, which is easier to achieve using wheels.

Table 10.1: Landing gear advantages and disadvantages.

	Advantages	**Disadvantages**
Skids	simple, lightweight	fixed structure
Fixed Wheels	good ground handling	higher weight
Retractable Wheels	good ground handling, aerodynamic	highest weight
Tripod config.	lightweight	unstable on ground

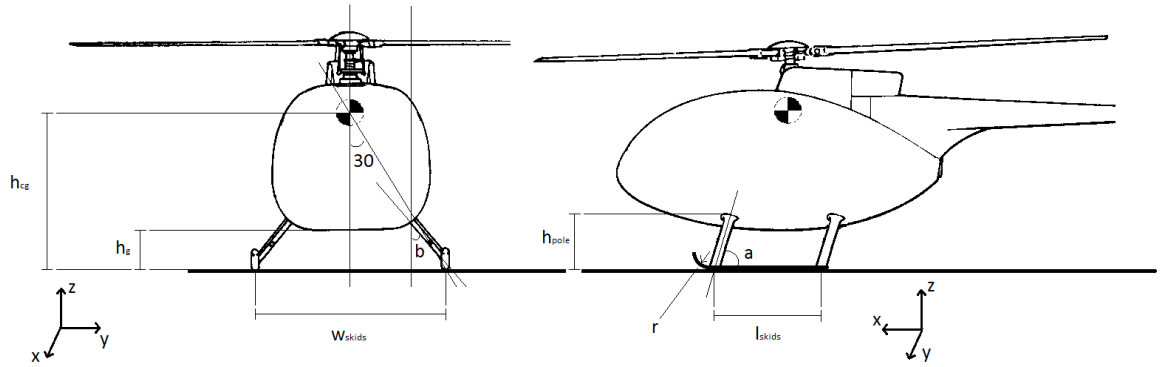

Figure 10.1: Helicopter parameters visualised, front and side view, axis systems included [66].

Fixed wheels are mostly used on heavy helicopters which fly at low speeds, due to the added ability to maneuver the aircraft when on the ground and the ability to take of and land on a runway. For fast flying helicopters, retractable landing gear can be used to reduce drag. However, this often comes with a weight penalty due to added complexity.

For the H2Copter, it was decided to use simple skids as landing gear. This is due to the fact that the helicopter is relatively light and the power to hover is no critical point of attention. These simple skids consist of three components: four poles connecting the fuselage to the skids, two skids connecting the poles on the ground and a front end to accommodate for a skewed landing.

10.2.2. Landing Gear Sizing

In order to size the skids, one must first know their layout. The layout of the skids is mostly dependant on helicopter geometry and some other requirements. A first requirement is that the skids should be designed in such a way that, when it is stationary on the ground and given an excitation, the aircraft does not topple. Toppling the aircraft is called static rollover. The maximum angle the aircraft vertical axis can make with respect to the azimuth is in general around 30° [65], and is shown, along with the other parameters, in figure 10.1. When this angle is exceeded, the center of gravity moves over the pivoting point, one of the skids in this case, and the aircraft will top over. Using this maximum angle and the position of the aircraft center of gravity, one can derive the minimum distance between the skids, w_{skids}. The equation for the horizontal distance between the two skids is given in equation 10.1

$$W_{skid} = 2h_{cg} \tan(30°) \tag{10.1}$$

In equation 10.1, h_{cg} is the height of the center of gravity measured from the ground, which was found to be 1.33 m from the computer modelling program. A ground clearance, h_g, of 35 cm was taken for the skid analysis. This estimation was made based on the ground clearance of both the Robinson R22 and the Mosquito XE helicopters, which were 34 and 36 cm, respectively. From helicopter geometry, it became clear that, to achieve both this ground clearance and the skid width, the poles reaching from the helicopter to the skids on the ground needed to be 70cm long. Thus, the angle b was 45°. The angle a, the angle between the poles and the vertical when looking at the aircraft from the side, was kept variable in the program in order to optimize skid weight. At the front of the skids, it was decided to place a beam in the form of a quarter of a circle with a radius of 10 cm. This front end is placed on the skids such that the aircraft could land on the front of its skids, when descending in a nose-down attitude.

Next, the ultimate load cases for the landing gear needed to be defined. These ultimate load cases were ob-

Table 10.2: Load case requirements for different aircraft components given in g.

	Load factor **Pilot**[g]	Load factor **Items of mass**[g]	Load factor **Structure**[g]
Upward	4	1.5	1.5
Forward	16	12	4
Sideward	8	6	2
Downward	20	12	4
Rearward	1.5	1.5	Not specified

tained from CS27 requirements as specified by EASA [67]. The requirements specify a few load cases which the rotorcraft must be able to withstand. These loads are given in g and can be found in table 10.2. The CS27 requirements specify load cases in five directions (up, down, front, rear and side) and for three systems. These 'systems' are: the pilot, items of mass in the aircraft, and structural components. For this chapter, only the latter is of interest; the other two categories are shown for comparative purposes.

To calculate actual loads from the maximum g-load the structure has to bear, it was chosen to multiply the g-load by the maximum take off weight (MTOW). In equation 10.2, the load on the skid is derived for a 4g situation.

$$F = 1068 \cdot 4 \cdot 9,81 = 40918N \tag{10.2}$$

One must note that the CS27 requirements specify one extra load case for the landing gear of a helicopter specifically; the landing gear of the helicopter shall be able to withstand a load of 1.33 times the MTOW at an angle of 45° at the front in upward direction. This load shall be carried by the front of the landing gear only. For the skids, the upward load of 1.5G was neglected since the structure can also withstand this when designed for a downwards load of 4G.

To analyze the loads in the poles, the forces were assumed to be divided evenly over the four poles connecting the helicopter to the skids, except for the load case with the force under a 45° angle, which is assumed to be divided over the two front poles. The forces in the poles, skids and in the frond ends were derived for each load case and the parts were sized accordingly. To demonstrate how the loads were derived and how the parts were sized, the load case for a load coming from the front under a 45° angle will be taken as an example.

First, the load is transformed into a force per pole. This is done using equation 10.3, where the total load has been divided by two.

$$F = \frac{G \cdot MTOW \cdot g}{2} = \frac{1.33 \cdot 1068 \cdot 9.81}{2} = 6967N \tag{10.3}$$

Note that the MTOW as derived in the Mid Term Report [8] is used. Next, a unit vector is derived for the pole. In order to take away any confusion, an axis system is set up with the x-axis pointing in flight direction, the y-axis towards the left of the helicopter and the z-axis up. The unit vector is given in equation 10.4.

$$\hat{u}_{pole} = -\frac{h}{\tan(a)l}i - \frac{\tan(b)h}{l}j + \frac{h}{l}k \tag{10.4}$$

In equation 10.4, a is the angle between the horizontal and the pole when looking at the helicopter from the side and i, j and k are the unit vectors on the x, y and z axis, respectively. Next, the force is written as a vector in this axis system. The force in vector format is given in equation 10.5.

$$\bar{F} = -F\cos(45°)i + F\sin(45°)k \tag{10.5}$$

In equation 10.5, F is the magnitude of the force. With the unit vector in the direction of the pole and the force also in vector format, the force can now be split in two parts; one parallel to the pole and one orthogonal to it. This is simply done by taking the dot product of the force vector with the pole unit vector to obtain the vector of the force parallel to the pole, which can be seen in equation 10.6. Subtracting that vector from the original force vector, results in the vector of the force orthogonal to the pole, as can be seen in equation 10.7. Taking the magnitude of these vectors, the magnitude of both forces can be derived. For both calculations, 80° was taken for the angle a to verify the model. Later, an optimum will be found, to minimize weight.

Table 10.3: Material properties for aluminum and steel.

Aluminum 6061-T6	**Value**	**Unit**	**Steel**	**Value**	**Unit**
E	6.89	Gpa	E	220	Gpa
yield	276	Mpa	yield	207	Mpa
Density	2700	kg/m^3	Density	7850	kg/m^3

$$F_{\parallel} = \bar{F}\hat{u}_{pole} = (-F\cos(45°))\left(-\frac{h}{\tan(a)l}\right) + (F\sin(45°))\left(\frac{h}{l}\right) = 4066.4N \tag{10.6}$$

$$F_{\perp} = |\bar{F} - (F_{\parallel} \cdot \hat{u}_{pole})| = 5657N \tag{10.7}$$

Now the forces parallel and orthogonal to the pole are known, the pole can be sized. Here, bending, buckling and compression will be taken into consideration. Since tension is not a critical load, as the only tension forces the skid poles will experience are due to the weight of the skids, which are assumed to be small compared to the other stress criteria, it will not be taken into account. Torsion is also neglected, since there are no torsional bending moments acting on the poles.

To size for buckling, equation 10.8 was used to determine the minimum buckling load.

$$F_{buck} = \frac{\pi^2 EI}{(Kl)^2} \tag{10.8}$$

In this equation, E is the modulus of elasticity of the material, and I is the moment of inertia of the beam. With the purpose of verifying the calculations with Inventor at a later phase in mind, a steel, solid, circular beam is assumed. The E modulus for steel is 200 GPa, as can be seen in table 10.3 and the moment of inertia of a circular solid beam is equal to $\frac{\pi}{4}r^4$. l is the length of the beam, and K is a measure for how the beam which is considered is fixed. The pole is assumed to be fixed at both ends (so both ends can withstand a bending moment). For that case, K is equal to 0.5. With all this information, putting $F_{\parallel}$ as the buckling force, the minimum moment of inertia can be derived, which results in a minimum radius the pole must have in order to resist buckling. This radius is derived in equation 10.9.

$$\sqrt[4]{\frac{4F_{\parallel}(Kl)^2}{\pi^3 E}} = r_{min_{buck}} = 0.0042m \tag{10.9}$$

$$\sigma = \frac{My}{I} \tag{10.10}$$

To check for bending, equation 10.10 is used. Here, σ is the stress in the point of interest, M is the bending moment on the beam, y the distance from the neutral axis to the point which is under consideration and I the moment of inertia. The maximum load case is of interest and therefore the maximum moment and the maximum distance y are needed. The maximum moment in the beam is equal to the orthogonal force $F_{\perp}$ times the length of the pole, l. However, a certain component has yet to be added; this is the component due to the fact that the force on the skids does not act directly on the skids, but is modelled to act on the front end of the skid system. The moment this adds to the pole is equal to the orthogonal distance from the point where the pole touches the ground skid multiplied by the force. This distance is given by $r\sin(45°)$. With a radius of 10 cm as specified, this moment is equal to 492 Nm. The maximum distance from the neutral axis to the point of interest, y, is equal to the radius of the beam. Assuming a solid circular beam, one can now come up with an expression for the minimum radius to withstand bending, inserting the yield stress and the moments. Thus, equation 10.10 can be rewritten to equation 10.11.

$$\sigma_{yield} = \frac{(0.1\sin(45°)F + F_{\perp}l)\, r_{min_{bend}}}{\frac{\pi}{4}r^4_{min_{bend}}} : r_{min_{bend}} = \sqrt[3]{\frac{(492+3960)}{\frac{\pi}{4}\sigma_{yield}}} = 0.0302m \tag{10.11}$$

Assuming the maximum compression strength of a member is approximately equal to the yield stress, a minimum area for the beam can be derived resulting in, when assuming a solid circular beam, a minimum radius, as stated in equation 10.12.

$$A_{min_{comp}} = \frac{F_{\parallel}}{\sigma_{yield}} : r_{min_{comp}} = \sqrt{\frac{F_{\parallel}}{\sigma_{yield}\pi}} = \sqrt{\frac{4066}{207\cdot 10^6\pi}} = 0.0025m \tag{10.12}$$

When comparing $r_{min_{buck}}$, $r_{min_{bend}}$ and $r_{min_{comp}}$, one can observe that the largest minimum radius is $r_{min_{bend}}$, which equals 3.02 cm. Thus, this is the radius a solid circular beam must have to be able to withstand this load case. If other load cases would result in a bigger minimum radius, the bigger radius would of course be used.

Next, the loads in the front end will be considered. Since this is a very small part, buckling is not of interest and only bending will be considered. The maximum moment was derived earlier and determined to be 492 Nm. Using the same approach as in equation 10.11. This results in a minimum radius of 1.44 cm. Since this is the only load case for the front end (the other loads are assumed to act directly at the pole-skid connections) this is the load case for which the front end will be designed.

As a last step, the ground skids need to be designed. However, since the loads are modelled as point loads at the end of the poles, and since the 45° degree force must be retained by only the front poles, the skids are not carrying any loads from this perspective. Thus, to model the skids, an assumption has to be made. It is assumed that the skids carry the x-axis component of the force acting on 1 pole. This assumption follows from the assumption that the forces are equally distributed over the 4 poles since the skid then needs to transfer half of the load the front pole gets to the back pole. For the 45° degree force load case, the skid force is zero since the front poles alone have to carry this load. The skid sizing will thus be shown for the only load case where the skid carries a load; the frontal load case of 4 G. The parallel force is found by taking the dot product of the force vector $(-Fi)$ and the unit vector in direction of the pole. This force is derived in equation 10.13.

$$F_{skid} = \bar{F} \cdot i = \frac{4 \cdot MTOW \cdot g}{4} = 10477N \tag{10.13}$$

The skids will only be sized for buckling since they are long and are assumed not to carry any bending loads. Entering the skid force in equation 10.8 provides again a minimum moment of inertia, which results in a minimum radius, as can be seen in equation 10.14.

$$I = \frac{\pi}{4} r_{min}^4 = \frac{F_{skid}(Kl)^2}{\pi^2 E} : r_{min} = \sqrt[4]{\frac{4 \cdot 10477(0.5 \cdot 2)^2}{\pi^3 220 \cdot 10^9}} = 0.009m \tag{10.14}$$

The length of the ground skids, l in the equation, is assumed to be 2 m, derived from the helicopter geometry. All parts are now addressed. The final radius of the pole will be the minimum radius for the load case which results in the highest minimum radius needed to withstand that case. From the model, it became clear that the forward force was the most critical for the poles, resulting in a pole radius of 0.036 m. The front end was sized for the 45° degree load case, since this is the only case for which the front end bears a load. This resulted in a radius of 1.44 cm for the front end. The skids are sized for the forward load, since this is the only case for which the skids bear a load. This resulted in a skid radius of 0.9 cm.

Please note that the skid components were modelled as steel solid circular beams for the purpose of validating the model against Inventor only. The actual skids might not be made of steel and might not be solid circular beams. The final design is an output of our CAD program, and can be found in chapter 12.

10.2.3. Inventor validation

The sized skid was put in inventor and the stresses were calculated for the loads cases. The stresses calculated in Inventor, along with the stresses calculated by the model and the differences between the two can be found in table 10.4.

In table 10.4, one can observe the difference in percentage between the model calculated stresses and the stresses calculated using Inventor. Two aspects of these differences are interesting; at some points the model estimates zero load but inventor does calculate a small load and bending loads have a higher discrepancy than axial stresses. Two reasons for the discrepancies can be addressed. The first is that Inventor takes gravity into account, which results in small stresses in members where the model assumes no load. This is also why the bending loads differ more; the bending moment increases by the length times the force so the moment differs more than just the extra force due to gravity. The second reason for small discrepancies is that Inventor does not let the user specify beam dimensions exactly, one can only choose out of a list of preset thicknesses. While this closely resembles the skid, it is not exactly the same. All in all, the model showed sufficient resemblance and differences in the range of 3-10 percent are acceptable, seeing as Inventor takes gravity into account. The results Inventor provides, are thus considered to be accurate. Thus, Inventor calculations can be used for stress calculations during the sizing of the structure.

Table 10.4: Stresses calculated by the model and Inventor compared.

Load Case	**Load**	**Inventor** [Mpa]	**Model** [Mpa]	**Difference** [%]
45 degree force	axial pole	0.899	0.875	2.7
	bending pole	120.85	133.118	10.2
	axial skid	0.899	0	-
Downward	axial pole	1.922	1.861	3.2
	bending pole	151.9	146.371	3.6
	axial skid	0.01	0	-
Sideward	axial pole	0.958	0.93	2.9
	bending pole	78.816	73.186	7.1
	axial skid	0.028	0	-
Frontal	axial pole	0.053	0	-
	bending pole	228.728	207	9.5
	axial skid	41.045	42.548	3.7

Table 10.5: First iteration skid sizing.

	Length [cm]	**Outer radius** [cm]	**Inner radius** [cm]
Pole	70	3.2	-
Ground skids	200	1.3	1.2
Front ends	16	1.5	1

10.2.4. First iteration skid sizing

Now Inventor and the model are both validated, the model is used once more to come up with a first iteration on the skid size. First the material was selected. It was found that by making the poles out of aluminum and the skids and front end of steel, the skids were light yet resistant to impact. These materials cannot be welded together and will be joined using bolts. Since aluminum has a lower Young's modulus than steel, the poles can absorb more energy on impact, thus reducing impact shocks for the pilot. It was decided to keep the members circular in order for them to be able to withstand loads in every direction with the same strength. However, it was decided to make some members hollow, circular beams in order to decrease their weight. Since the poles are already very big, only the steel skids and front ends were made hollow. This was done by first taking the biggest possible outer radius for the ground skid such that the moment of inertia was kept constant but it still had enough area to withstand pure compression. This outer radius was found to be 1.3 cm, corresponding to an inner radius of 1.2 cm. The front end was then sized to be about as big as the skid in the same way. This resulted in an outer radius of 1.5 cm and an inner radius of 1 cm. These final skid parameters can be found in table 10.5.

10.3. Body structure

The body structure design can be divided in the following subsections: legislation, body types, materials and design. In the next subsections the steps taken to get a body structure are explained.

The body structure should comply to the legislation and mission need. This section explains the design of the structure. After the legislation is analyzed, different body types are compared, a material is selected, and the final structural design will be presented.

10.3.1. Legislation

The requirements in table 10.2 also apply to the design of the main structure. As can be seen in the table, EASA has defined a maximum load factor of 4g on load bearing structures. This is a legislative requirement which can be found in CS-27 [68]. There are two other load cases found in this document. One load case can already be found in section 10.2: this is the load of 1.33 MTOW under an angle of 45°. Another load case to consider occurs during flight. This is a gust load of three and a half times the natural acceleration.

Table 10.6: Summary of different body types.

	Advantages	**Disadvantages**
Tubular	High strength to weight ratio Can usually be repaired at field level Strong in every direction	High cost of manufacturing Labour intensive due to manual labour Takes up internal volume
Monocoque	Easy to manufacture Space efficient	lowest strength to weight ratio
Semi-Monocoque	Lighter than monocoque	Relatively low strength to weight ratio
Bonded	Reduced construction cost Little manual labour required Composites	High safety needed factors due to fatigue

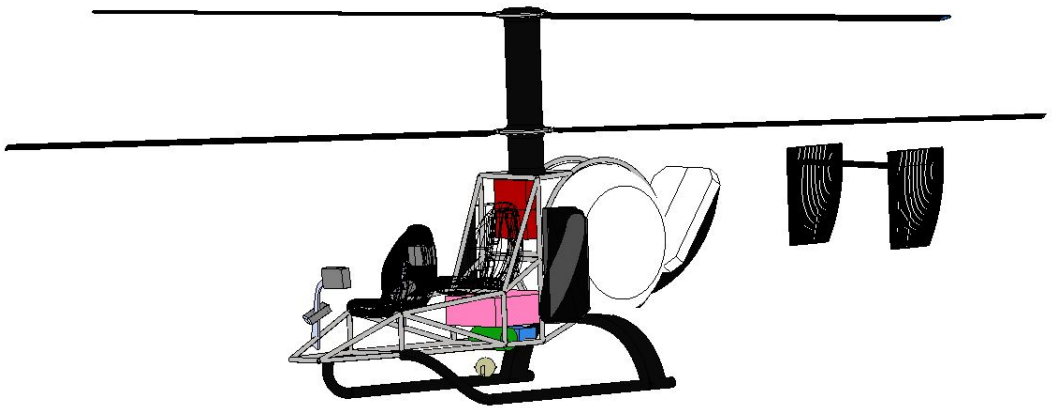

Figure 10.2: Packaging of the subsystems.

10.3.2. Body types

In current helicopter design, four body types are often used; tubular, monocoque, semi-monocoque and bonded. These body types are considered for the fuselage design. The different body types are briefly explained and table 10.6 is made to compare the advantages and disadvantages [69].

A tubular structure is a chassis made of welded or bolted tubes. A monocoque is a structure with a skin that will carry loads, with stringers and longerons added for structural rigidity. A semi-monocoque is a crossover between monocoque and tubular. A bonded structure is a load bearing structure made of composites.

In table 10.6 the trade off between body structures can be seen. It was decided to work with the tubular body structure due to ease of maintenance and time constraints.

10.3.3. Materials

The following materials were considered for the tubular structure: steel, aluminum, tungsten and titanium. Due to heavy vibrations, the fatigue stress was considered the critical parameter. Therefore, the main material for the tubular structure is chosen to be steel, which has significantly better fatigue properties than the other metals considered[70]. Other advantages of steel are its low price and its ease of production.

10.3.4. Design

In order to design the truss structure, a packaging is made first. The packaging used can be seen figure 10.2. It is explained in detail in chapter 12. As seen from the figure, the elements of mass are placed close to the centre of gravity. This is done to keep the centre of gravity as close as possible to the centre of the hub, and to limit the bending moments in the trusses.

The structure is designed with respect to the approximate loads. The point loads were assumed to act on the points in the structure where the beams collide. Thus the points where the masses are connected, at that point the beams should collide. Therefore a number of colliding points were specified and from there a tubular

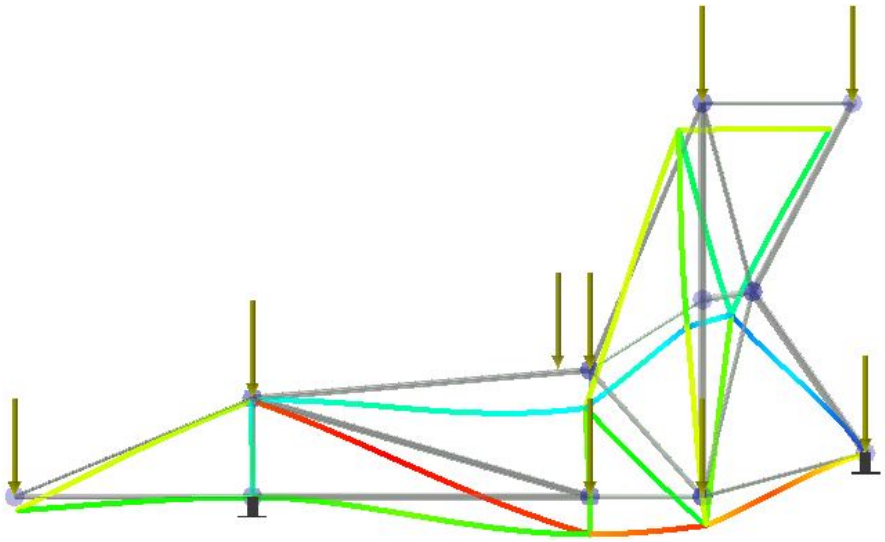

Figure 10.3: An example of a load case.

structure is designed. The beams connecting the point loads were strategically chosen to provide enough rigidity for carrying the loads.

From this design each of the six load cases described in the legislation were modeled in Autodesk Inventor. The four load cases described in table 10.2 are tested with the fixed constrains on the landing gear. These constraints are on the landing gear because CS-27 describes these are the loads in a emergency landing. The load case of 1.33 maximum take off weight in a direction of 45 degrees upward and aft is also taken into account. The final load case is a 3.5g acceleration during flight. An example of a load case is shown in figure 10.3. This example is the load case of four times the natural acceleration in upward direction.

The loads per beam can be read from Autodesk Inventor. The required diameter for a beam can be calculated by the buckling stress equation 10.9, which is already stated in section 10.2.2. The required area was calculated using equation 10.12. Putting this all together gives a configuration which can be seen in table 10.7 and figure 10.4.

The final weight of the truss structure is 128.1 kg. Therefore the weight budget is not met. Even though the budget is not met, together with the landing gear the total weight is just over budget. The total budget of these components was 154 kg. The final preliminary design weight is 164 kg.

10.4. Interior Design

Now the body of the helicopter is designed, it is still empty and some critical systems need to be put into it. Systems which will be considered and discussed are:

- Lighting
- Interior
- Avionics
- Mission Payload

These subsystems will be eleborated upon below.

Table 10.7: Final parameters of the truss structure.

	LC1 (MPa)	LC1 (N)	LC2 (MPa)	LC2 (N)	LC3 (MPa)	LC3 (N)	Length (mm)	r_LC1 (mm)	A_LC1 (mm2)	r_LC2 (mm)	A_LC2 (mm2)	r_LC3 (mm)	A_LC3 (mm2)
1	20.6	2472	12.7	1524	94.6	11352	917.8	x	11.94	x	7.36	6.06	54.84
2	-17.3	-2076	-13.5	-1620	-203	-24360	854.9	2.41	-10.03	2.13	-7.83	8.27	117.68
3	-47.3	-5676	-10	-1200	-442	-53040	354	1.65	-27.42	0.76	-5.80	5.05	256.23
4	-50	-6000	55.5	6660	-200	-24000	1204	5.78	-28.99	x	32.17	11.56	115.94
5	59.5	7140	-43.6	-5232	232	27840	1250	x	34.49	5.60	-25.28	12.92	134.49
6	-17	-2040	-21.7	-2604	262	31440	1201	3.36	-9.86	3.80	-12.58	13.19	151.88
7	-8.1	-972	26.2	3144	-122	-14640	450	0.87	-4.70	x	15.19	3.37	70.72
8	18.8	2256	73.7	8844	-164.7	-19764	1031	x	10.90	x	42.72	8.98	95.48
9	-57.5	-6900	-21.7	-2604	-285	-34200	473	2.43	-33.33	1.50	-12.58	5.42	165.22
10	-21.8	-2616	41.8	5016	-238.1	-28572	603	1.91	-12.64	x	24.23	6.31	138.03
11	61.5	7380	-64.2	-7704	780	93600	401	x	35.65	2.18	-37.22	7.60	452.17
12	16.5	1980	0	0	-257.9	-30948	556	x	9.57	0	0.00	6.06	149.51
13	-36.9	-4428	23.9	2868	339.8	40776	713	2.94	-21.39	x	13.86	8.92	196.99
14	-61.8	-7416	-33.9	-4068	-543.3	-65196	242	1.29	-35.83	0.96	-19.65	3.83	314.96
15	-2.9	-348	-52.3	-6276	-260	-31200	768	0.89	-1.68	3.77	-30.32	8.40	150.72
16	70.3	8436	-17.4	-2088	337	40440	612	x	40.75	1.73	-10.09	7.62	195.36
17	-37.1	-4452	-55.2	-6624	-672	-80640	759	3.14	-21.51	3.83	-32.00	13.35	389.57
18	-78.2	-9384	31.1	3732	-883.9	-106068	700	4.20	-45.33	x	18.03	14.12	512.41
19	18.4	2208	36.4	4368	-211.5	-25380	1400	x	10.67	x	21.10	13.82	122.61

Lighting

For the lighting of the plane, a distinction can be made between outside signal lighting and inside cabin lighting. The CS27 requirements stipulate the need for a green/red light on both sides on the outside of the aircraft. A tail light is also required. Lights from 'Whelen' were chosen due to their affordable price. The Whelen microburst II with tail light kit was chosen to mount on the helicopter for its light weight and low cost. This package consists of two microburst II lights, one green and one red light, depending on which side of the helicopter they are mounted on, and a white tail light, the microburst I. The specifications of these lights can be found in table 10.8. The interior lighting is not treated in this report, as it is assumed to be relatively cheap and not use much power. Points of interest for helicopter interior lighting would be, for example, vibration resistance.

Interior Systems

For the interior, three main components are considered. Firstly, the helicopter needs two seats. The company 'Fischer+Entwicklungen' has kevlar helicopter seats available of 10 kg[71]. A price is not listed, but $10,000 is budgeted per seat.

Next, a fire extinguisher is needed, as this is a necessary precaution every helicopter must have. A company called H3R Aviation [72] sells Halon fire extinguishers. Halon is a extinguishing agent which is used a lot in aviation. Since Halon damages the ozone layer, its production is prohibited. However, for the aviation industry, Halon is recycled and approved for use. The benefit of using halon is that it is a non toxic gas. As opposed to liquid or powdered extinguishing agents, it does not leave any trace after use and thus requires no clean up and does not damage any equipment. The H3R model A344T Halon 1211 Fire Extinguisher was chosen, as the H3R company recommends this extinguisher for small rotorcraft for 4 passengers or less - including the pilot. The specifications of this extinguisher can be found in table 10.8.

Last, the control sticks must be put in the cabin. Since this helicopter will fly using a fly-by-wire system, and since such a system has not frequently been used in rotorcraft, this component is difficult to size. It was assumed that every pilot needs two high-end joysticks (collective and cyclic). It is a requirement that, for a two person helicopter, both seats must be fully equipped to control the aircraft. Therefore a total of 4 high-end joysticks must be incorporated. A computer must also be taken on board to process the inputs to outputs to the system. This computer will be assumed to weigh 20% of the four joysticks. This number is a very rough estimate, as no literature has been found on this topic. It is thus more a goal than an actual sizing. For the sticks themselves, Olaf Stroosma, who works with the Control and Simulation department at the faculty of Aerospace Engineering as lab manager of the 'Simona' aircraft simulator, was contacted. He stated that, while the control sticks were relatively cheap (±$250 per stick, including attachments [73]), the cost of control systems needed would be of another order of magnitude. Based on these first estimation prices, $8,000 is budgeted for the

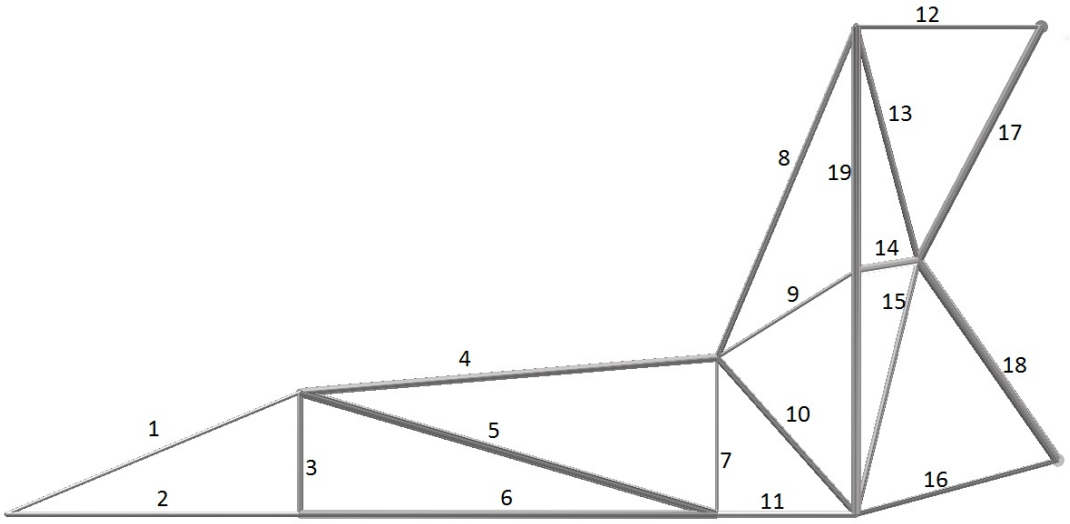

Figure 10.4: Final configuration of truss structure.

entire control system. The system is estimated to weigh 4 kg and use 20 W of power. This again is a rough estimation because of lack of literature, based on simple size of the sticks et cetera.

Avionics

The helicopter will need to have the required instruments on board. It was chosen to use the 'Glass Cockpit' concept, meaning that all-digital instruments were chosen. Since the helicopter has two seats from which the helicopter needs to be controllable, two full sets of flight instruments need to be available. The necessary equipment per pilot for a helicopter consists of:

- Standard Sixpack instruments (altimeter, airspeed indicator, turn and bank indicator, vertical speed indicator, attitude indicator, heading indicator)
- A gps system
- A communications system
- A pitot static system
- A flight data computer to digitize the data from the pitot static system

Big manufacturers like Robinson helicopters are frequently seen to sport Garmin flight decks aboard their helicopters. Since Garmin has a clear catalogue of available products and since their products can be used for multiple purposes, it was chosen to implement Garmin avionics in the H2Copter. As a replacement for the standard six pack avionics, the Garmin G500H was chosen. This contrapment consists of two electric Multi Functional Displays (MFD's), one showing the standard sixpack instruments, and the other MFD showing what it is the pilot wants it to show. It is exactly this kind of flexibility what makes the G500H suitable for this helicopter, the avionics can be adapted for the kind of mission that has to be flown. The possibility even exists to equip the helicopter with more functions such as weather and traffic mapping, plugging these functions into the MFD. In section 10.4, another use for the MFD will be presented. The specifications of the G500H can be found in table 10.8. Next, a GPS system is needed. Garmin again has a suitable system available, combining a communications system with a gps receiver. This is the Garmin GTN635. The GTN635 was chosen for its relative simplicity, nothing more than a plain gps and communications system are needed. The specifications of the GTN635 can be found in table 10.8. Note that the two Garmin systems can be fully integrated; the GTN635 data can be displayed on the G500H and vice-versa. This further increases ease of use for the pilot.

Next, a pitot static system is needed. For pitot tubes, the Aerogizmos Pitot Tube was chosen for its compact, aerodynamic design and its relative low cost. No specifications of this tube can be found, therefore an estimated guess is made with respect to its weight; 0.4 kg per tube. Note that two pitot tubes are necessary; this is for redundancy purposes.

Table 10.8: Specifications of interior systems [71, 72, 74–77].

Component	**Quantity**	**Power** [W] (per unit)	**Weight** [kg] (per unit)	**Cost** [USD] (per unit)
Whelen Microburst I	1	2.1	0.07	166
Whelen Microburst II	2	0.8	0.09	166
Fischer Seats	2	-	10	(10,000)
H3R Halon Fire Extinguisher	1	-	1.02	100
Control Systems	1	(20)	(4)	(8,000)
Garmin G500H	2	44	2.9	25,000
Garmin GTN635	2	10	2.8	10,400
Aerogizmos Pitot Tube	2	-	(0.4)	160
Honeywell PG1152BC	1	3	0.65	(1,000)
Total without FLIR		134.7	38.12	100,718
UAV Vision CM202	1	55	3	(20,000)
Total with FLIR		189.7	41.12	120,718

Of course, the pressures obtained by the pitot tubes are analog, they need to be converted to digital data in order to be used by the glass cockpit. A flight data computer is needed for this. However, as aerospace engineering companies are quite secretive with regard to the flight data computers they produce, it was not possible to obtain a a flight data computer for which all the specifications were know. Honeywell has a flight data computer, the Honeywell PG1152BC Air Data Module (ADM), which seems capable to cope with the requirements for the helicopter. The price of the ADM was again estimated roughly, since Honeywell did not list a price, the estimate being $1.000 USD, based on the current price of a good quality laptop. Honeywell was contacted with regard to the price. The other specifications were found and can be seen in table 10.8. Note that one ADM is used, if this ADM however has only one input, two must be used.

Payload

The payload that is taken on board for the mission is dependant on the mission itself. Since this helicopter is designed as surveillance helicopter from origin, surveillance equipment is looked at in this report, consisting of a Forward Looking Infra Red (FLIR) surveillance camera. Some cameras were found but most of them were very heavy and big. This was because these cameras are mostly designed for big aircraft which fly high. Since this helicopter flies at a relatively low altitude, a smaller camera can be used, and the Unmanned Aerial Vehicle (UAV) market for FLIR cameras was analyzed. A small FLIR camera weighting 3 kg is found: UAV Vision's CM202 [74]. It has multiple sensors; Electro-Optical (EO), Infra Red sensors, a Laser Range Finder and an Illuminator. It is capable of object tracking, real-time video stabilisation motion detection and geo-lock. The images of this camera can be displayed on the MFD's of the G500H. This way, one person can fly the plane and one can focus on surveillance, using the G500H as a surveillance screen. The CM202 price is not found, the company would not specify the cost of this gimbal. $20,000 USD is put aside for the camera, as a rough goal. Please note that installing the CM202 is optional; it is not a necessity to put on the helicopter. Therefore two totals will be given; one with and one without the FLIR camera. The specifications can again be found in table 10.8.

11

STABILIZERS AND CONTROLLER

Stability is known to be a crucial topic concerning helicopter design. Without help of a control system, helicopters can be unstable. A stability analysis is performed and a controller is designed. In section 11.1 the approach will be discussed, as well as the assumptions and the initial data. Then, an explanation will be given about the pilot controls in section 11.2. After this, the equations of motion will be derived in section 11.3 for symmetric and asymmetric flight. The drag coefficient will be explained in section 11.4. In section 11.5 an explanation will be given about the steps taken to determine the trim conditions. The longitudinal and lateral stability analysis will be explained in sections 11.6 and 11.7. The responses and controller gain implementation process will be discussed in section 11.8, which uses the requirements set by EASA. Finally the stabilizers design process will be shown in section 11.9. The validation and verification process, which also includes a sensitivity analysis is provided in section 11.10. The purpose is to have a stable design with horizontal and vertical stabilizers.

11.1. OVERALL APPROACH AND ASSUMPTIONS

The strategy to perform a stability analysis and to design the stabilizers is shown in figure 11.1. The stabilizers are important to provide trim conditions and stability. First one has to analyze several tail concepts and choose the most beneficial concept for the design. After this the equations of motion will be defined. This is first done for a conventional helicopter without tails, after which it will be extended to a coaxial configuration with tails After this process, the drag coefficients and the thrust distribution of the rotors will be determined. The stabilizers and tail boom will then be designed. This is an iterative process, because it is dependent on the trim conditions and the stability of the helicopter. Furthermore, a structural analysis will be performed and the stabilizers and tail boom should satisfy the legislation and flying qualities. Some dimensions used during the class II weight estimation will be chosen first, after which it will be updated to achieve the optimum design. The lift coefficient of the stabilizers will be determined with the lifting line theory. After linearizing the equations of motion, the eigenmotions will be analyzed and controller gains will be implemented if necessary. This is also an iterative process, since it should satisfy the regulations and flying qualities. The blocks in green show the main aspects of this chapter, which also requires some important decisions. The design of the stabilizers is mainly influences by the trim conditions and the stability analysis. The decision has been made to first show the stability analysis in this chapter, before discussing the stabilizer design process. Before this process starts, an explanation will be given about the pilot controls.

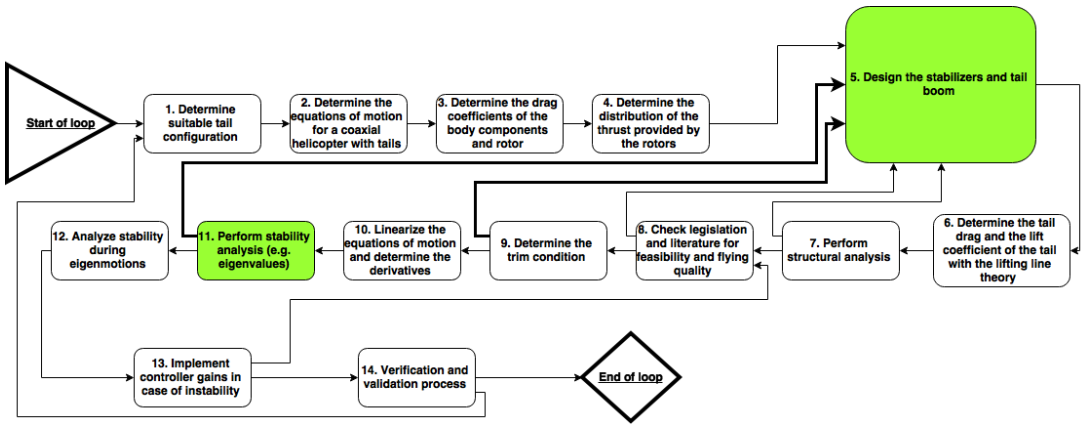

Figure 11.1: Graphical representation of the stability analysis and tail design.

Table 11.1: Initial data for the stability analysis.

Parameter	Value	Unit
Gravity constant	9.81	[m/s^2]
Lift slope	5.86	[rad^{-1}]
Blade solidity	0.0323	[-]
Lock number	6.7	[-]
Mass	1067	[kg]
Density	1	[kg/m^3]
Rotor radius	4.5	[m]
Mass moment of inertia (yy)	1738	[kg m^2]
Mass moment of inertia (xx)	870	[kg m^2]
Mass moment of inertia (zz)	2056	[kg m^2]
l_{R1}	1.85	[m]
l_{R2}	0.85	[m]

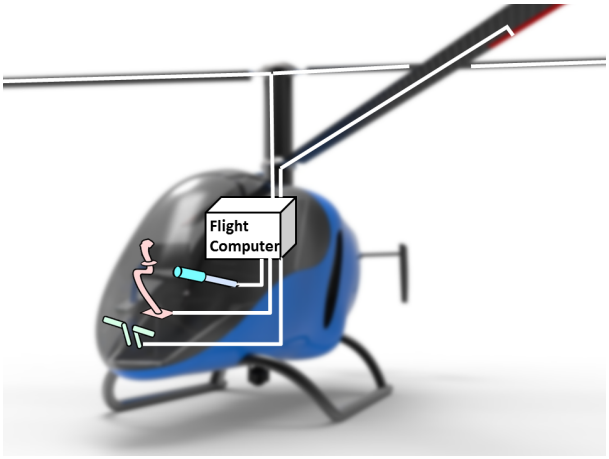

Figure 11.2: Pilot controls for the H2Copter.

The assumptions made during this process are listed below:

- The tail boom is assumed to be thin walled;
- Coupling effects of the symmetric and asymmetric equations of motion are neglected;
- Initial oscillation is neglected and constant RPM is assumed;
- Neglect center of gravity shift during flight;
- During trim, $a_{1R1} = \theta_{cR1}$, $a_{1R2} = \theta_{cR2}$, $b_{1R1} = \theta_{cR1}$ and $b_{1R2} = \theta_{cR2}$ and thus the tip path plane coincides with the shaft plane ;
- The vertical tail force is neglected in the longitudinal equations of motion, as is the horizontal tail neglected in the lateral equations of motion;
- The drag component of the vertical tail has been neglected;
- The S-force is neglected in the calculations;
- The matrix of inertia will be constant if the vehicle does not deform and aero-elastic effects are assumed to be small and can be ignored;
- An rotorcraft mass symmetry plane in the $\boldsymbol{X_b}$ and $\boldsymbol{Z_b}$ axis;
- The influence of the earth's curvature is negligible if the duration of the motion is short. Then, the normal earth fixed reference frame and the vehicle carried normal earth reference frame will coincide;
- Aircraft mass is constant over a small time-interval;
- The gravitational acceleration g is assumed to be 9.81 m/s^2;

The initial data used during this process is shown in table 11.1.

11.2. H2Copter pilot control

The H2Copter will be equipped with standard helicopter controls. This will assure comparable flight methods as other models making it easy for the crew to control. These controls include a stick, a collective and pedals, explained below.

- stick: push-pull input, forward and backward flying, pitch control
- stick: left-right input, sideways flight left and right, roll control
- collective:controlling rotor thrust
- pedals: directional control, yaw control

The pilot cockpit controllers itself are similar to other conventional helicopters. However, processing these inputs and linking them to the exact H2Copter maneuvers is different. This is because of the servo flaps on

the blades, which means there is no mechanical link to the pilot controls and a fly-by-wire system is required. Pilot's inputs go to the on board flight computer calculating the exact servo flap pitch at every moment in order to achieve the desired maneuvers of the pilot, figure 11.2. So for example if the collective is pulled up, the flight computer will calculate the different collective pitch angles of both rotors (since both rotors deliver a different thrust). For conventional helicopters, yawing is done by changing the tail rotor thrust. For the coaxial H2Copter, this is done by changing the thrust distribution over both rotors. If one rotor is loaded more than the other one, a moment is induced around the top axis and the H2Copter will yaw. This increase in rotor loading is achieved by setting a higher servo flap deflection on one of the rotors.

11.3. Derivations of the equations of motion

In this section, the reference frame with the center of gravity is defined first. After this, the equations of motion will be derived using free body diagrams. This step can be seen in figure 11.1 as block 2.

11.3.1. Reference frames

In order to stay consistent within the calculations, a reference frame will be defined. A body reference frame, right-handed orthogonal axis-system with the origin fixed at the center of gravity of the aircraft is used. In a horizontal flight, the x_b-axis points forward and is in the symmetry plane. The positive z_b-axis is directed downward and the positive y_b-axis points to the right of the rotorcraft. The latter axis is also perpendicular to the symmetry plane. The most commonly used body-fixed reference frame definition is the stability reference frame. In this frame the x_b is in the direction of the wind, which can be projected onto the plane of symmetry. This reference frame is shown in figure 11.3. In reality, adding the aerodynamic angle of attack θ_f and the aerodynamic side slip angle β to the body fixed reference frame seems more suitable. This results in the aerodynamic reference frame. In this reference frame, the origin is still the same. This is shown in figures 11.4 and 11.5. One may also notice the angles a_1, which is the longitudinal flapping angle, b_1, which is the lateral flapping angle, θ_c, which is the cyclic pitch angle, a_c, which is the control plane angle and a_d, which is the disc plane angle. The packaging will be discussed in chapter 12. The center of gravity will be beneath the rotors during the entire flight envelope. This will be achieved by placing the hub above the center of gravity location during early design phase. The decision has been made to assume no center of gravity shift during the calculations of this chapter.

11.3.2. Longitudinal equations of motion

In this section, the equations of motion will be explained in several steps. It is highly recommended to follow these equations with figure 11.4. The equations of motion are shown in equation 11.1 [78] for a simplified model, where the rotor drag is neglected, as well as the tail.

$$\begin{aligned} X &= -W\sin(\theta_f) - D_{body}\cos(\theta_f) + T_1\sin(\theta_{cR1} - a_{1R1}) \\ Z &= W\cos(\theta_f) - D_{body}\sin(\theta_f) - T_1\cos(\theta_{cr1} - a_{1R1}) \\ M &= -T_1 l_{R1}\sin(\theta_{cR1} - a_{1R1}) \end{aligned} \tag{11.1}$$

Equations 11.2-11.4 are used in the design process and stability analysis. In these equations, the H-force is tken into account, as well as the fact that the design is coaxial. These include the horizontal stabilizer and the bending moment caused by the shaft and the hubs. In the X and Z equations the drag caused by the shaft and the hubs are included in the body drag, which is assumed to be a point force in the center of gravity. However, in order to achieve more realistic results, they are used as separate drag forces in the moment equation. Note that the arm of the shaft force is partly inside the fuselage. This leads to the distance term next to the shaft drag term in the pitch moment equation, 11.4.

$$\begin{aligned} X = -W\sin(\theta_f) - (D_{body} + D_{emp})\cos(\theta_f) + T_1\sin(\theta_{cR1} - a_{1R1}) + T_2\sin(\theta_{cR2} - a_{1R2}) \\ - H_{rotor1}\cos(\theta_{cR1} - a_{1R1}) - H_{rotor2}\cos(\theta_{cR2} - a_{1R2}) \end{aligned} \tag{11.2}$$

$$\begin{aligned} Z = W\cos(\theta_f) - (D_{body} + D_{emp})\sin(\theta_f) - T_1\cos(\theta_{cr1} - a_{1R1}) - T_2\cos(\theta_{cR2} - a_{1R2}) \\ - H_{rotor1}\sin(\theta_{cR1} - a_{1R1}) - H_{rotor2}\sin(\theta_{cR2} - a_{1R2}) - L_h \end{aligned} \tag{11.3}$$

$$\begin{aligned} M = -T_1 l_{R1}\sin(\theta_{cR1} - a_{1R1}) - T_2 l_{R2}\sin(\theta_{cR2} - a_{1R2}) - L_H l_h \\ + H_{rotor1} l_{R1}\cos(\theta_{cR1} - a_{1R1}) + H_{rotor2} l_{R2}\cos(\theta_{cR2} - a_{1R2}) \\ + D_{hub}(l_{R1} + l_{R2}) + D_{shaft}(0.5(l_{R1} - 0.75) + 0.75) \end{aligned} \tag{11.4}$$

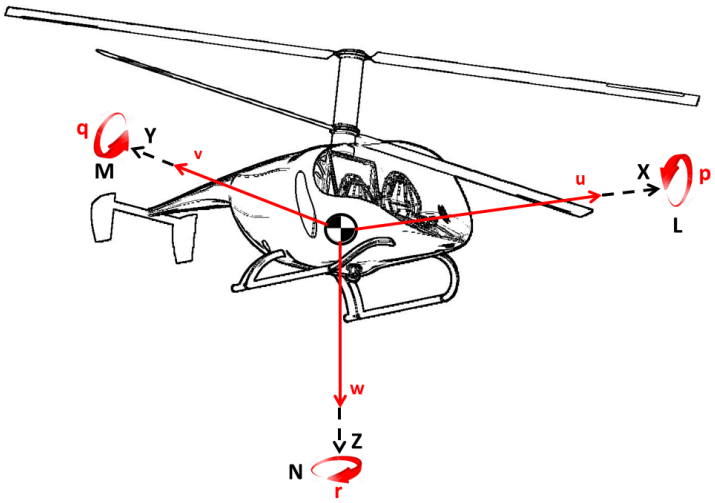

Figure 11.3: Reference frame

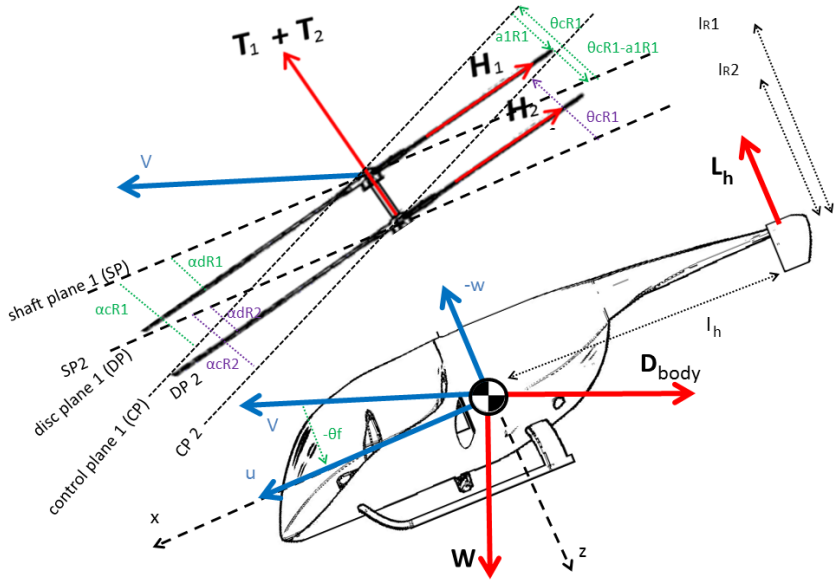

Figure 11.4: Longitudinal free body diagram.

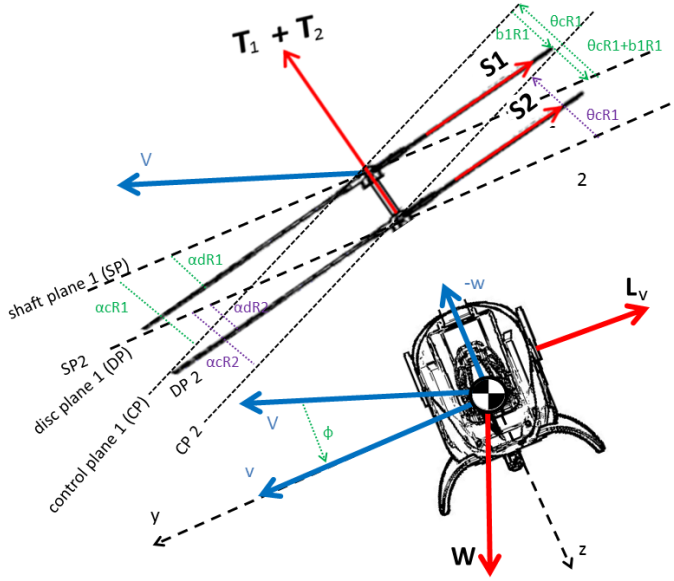

Figure 11.5: Lateral free body diagram.

Table 11.2: Frontal flat plate area determination.

Input		Output	
Fuselage			
Fuselage frontal area	$1.7m^2$		
Fineness ratio	3.17	f_f	$\mathbf{0.0765}m^2$
C_{D_f}	0.045		
Hub and shaft			
Hub frontal area	$0.1m^2$		
Shaft frontal area	$0.5m^2$		
Diameter shaft	0.3m	f_{ms}	$\mathbf{0.15}m^2$
$C_{D_{mh,rpm0}}$	0.47	f_{mh}	$\mathbf{0.0494}m^2$
Drag ratio	1.05	f_{mh}	$\mathbf{0.0494}m^2$
$C_{D_{ms}}$	0.3		
Interference factor	1		
Landing gear			
Landing gear frontal area	$0.09m^2$	f_{land}	$\mathbf{0.072}m^2$
$C_{D_{land}}$	0.8		
Rotor / fuselage interference			
Delta C_D	0.018	f_{int}	$\mathbf{0.0306}m^2$
Miscellaneous			
Camera, door handles, pitot static tubes etc.	-	f_{misc}	$\mathbf{0.08}m^2$

The drag coefficients in these equations will be discussed in section 11.4.

11.3.3. Lateral equations of motions

The lateral equations of motion during forward flight are shown in equations 11.5-11.7. This includes the effect of the rotors thrust and the vertical tail. A free body diagram is shown in figure 11.5.

$$Y = W\sin(\phi) + T_1\sin(\theta_{cR1} + b_{1R1}) + T_2\sin(\theta_{cR2} + b_{1R2}) \tag{11.5}$$

$$L = T_1 l_{R1}\sin(\theta_{cR1} + b_{1R1}) + T_2 l_{R2}\sin(\theta_{cR2} + b_{1R2}) + L_v l_v \tag{11.6}$$

$$N = L_v l_v \tag{11.7}$$

As one may notice in these equations, the S force is assumed to be small and is neglected in these equations.

11.4. Drag coefficients

The drag coefficients of several components will mainly be estimated by the methods described in Prouty [9]. The drag coefficients determination is shown in figure 11.1 as block 3. The method in Prouty is based on references and statistics. One should for example determine the fineness ratio of the fuselage, which is the length divided over the width. With this value, the drag coefficient of the fuselage can be determined with the reference graphs in Prouty. This is done for the fuselage, the hub, the shaft and the landing gear. Each of them needs different parameters as input. Furthermore the rotor and fuselage interference has been estimated as well as the miscellaneous drags, including the camera, door handles and pitot static tubes. The results are shown in table 11.2. Note that the drag coefficient at the output column is already including the frontal area. The H force (drag) coefficients of the rotor were determined with the method described in chapter 7.

The drag coefficients can be used to determine the drag forces. This is done by taking the product of the drag coefficients including the area and the dynamic pressure. With the methods described in Prouty [9], one

Table 11.3: Tail drag coefficients.

Profile drag coefficient	0.01
Junction drag coefficient	0.072
Induced drag coefficient	0.008

$$c_{d_{ind_{tail}}} = \frac{c_{l_{tail}}^2 (1+\delta_h)}{\pi AR} \tag{11.8}$$

can also determine the drag coefficient of the tail. This consists of the following components: profile drag coefficient, induced drag coefficient and junction drag coefficient.

The profile and junction drag can be estimated with the tail dimension and profile. The induced tail drag coefficient can be determined with equation 11.8. In this equation δ_h is the span efficiency, which is estimated at 0.1. As one may notice, the determination of the tail drag coefficient is an iterative process with the design of the tails. It is dependent on the aspect ratio, surface area and lift coefficient. These parameters will be discussed later. The results of the final iteration are shown in table 11.3.

11.5. TRIM CONDITION

To assure comfortable and safe flying conditions, the trim state is determined. The trim state is also important for the linearization process. This chapter will elaborate on the trim during forward, stationary, horizontal flight and therefore includes the blocks 4 and 9 of figure 11.1. The blocks in between will be discussed in section 11.9, where the stabilizers design process will be explained. The whole process contains a lot of equations, steps and loops. Therefore, a flowchart has been made to make this entire process from determining the trim conditions to calculating the eigenvalues more clear. This is shown in figure 11.6. In this figure, the calculations concerning the trim conditions are listed, as well as the next steps including the linearization process. This flowchart is therefore divided into two main groups. For each group the section number, in which the steps are explained, is displayed.

Trim is defined as all accelerations being zero, which is also defined by equation 11.9. For each flight speed a collective and cyclic rotor pitch, horizontal and vertical speed and a pitch angle are found. The horizontal and vertical speeds can be determined with equations 11.10 and 11.11.

$$\dot{u} = \dot{w} = \dot{q} = \dot{\theta_f} = 0 \tag{11.9}$$

$$u = V\cos(\theta_f) \tag{11.10}$$

$$w = V\sin(\theta_f) \tag{11.11}$$

The equations of equilibrium for trim are obtained by setting equations 11.2-11.4 equal to zero.

During trimmed flight the tip shaft plane is assumed to coincides with the shaft plane for both rotors, $a_{1R1} = \theta_{cR1}$ and $a_{1R2} = \theta_{cR2}$. This will ease solving the mathematical equations. The thrust is needed for further computations, this can be found using the equilibrium equations in the Z-direction, as shown in equation 11.12. Total thrust is provided by both rotors working together.

$$T_{tot} = T_1 + T2 = W cos(\theta_f) - (D_{body} + D_{emp})\sin(\theta_f) \tag{11.12}$$

The total thrust required to comply with the equilibrium equations is found. From the aerodynamic calculations shown in chapter 7, the thrust distribution on both rotors is calculated in function of flight speed. The rotors are loaded unevenly, at a certain flight speed, 43 m/s, the distribution becomes 50%-50%. At several speeds, the distribution n was computed. Afterwards, this is formed into continuous relationships with flight speeds using a polynomial fit over these discrete points, shown in equation 11.5.

$$n(V) = \begin{cases} 1.5e^{-0.02V} & \text{if } 20m/s \geq V \\ 2\cdot 10^{-5} - 5V^2 - 0.0014V + 1.0293 & \text{if } 20m/s < V < 43m/s \\ 1 & \text{if } V \geq 43m/s \end{cases}$$

The total thrust is divided over both rotors, shown in equations 11.13 and 11.14.

$$T_{R1} = \frac{1}{1+n} T_{tot} \tag{11.13}$$

$$T_{R2} = \frac{1}{1+\frac{1}{n}} T_{tot} \tag{11.14}$$

The thrust coefficients for both rotors are found, as shown in equations 11.15 and 11.16.

$$CT_{R1} = \frac{T_{R1}}{\rho(\Omega R_{R1})^2 \pi R_{R1}^2} \tag{11.15}$$

$$CT_{R2} = \frac{T_{R2}}{\rho(\Omega R_{R2})^2 \pi R_{R2}^2} \tag{11.16}$$

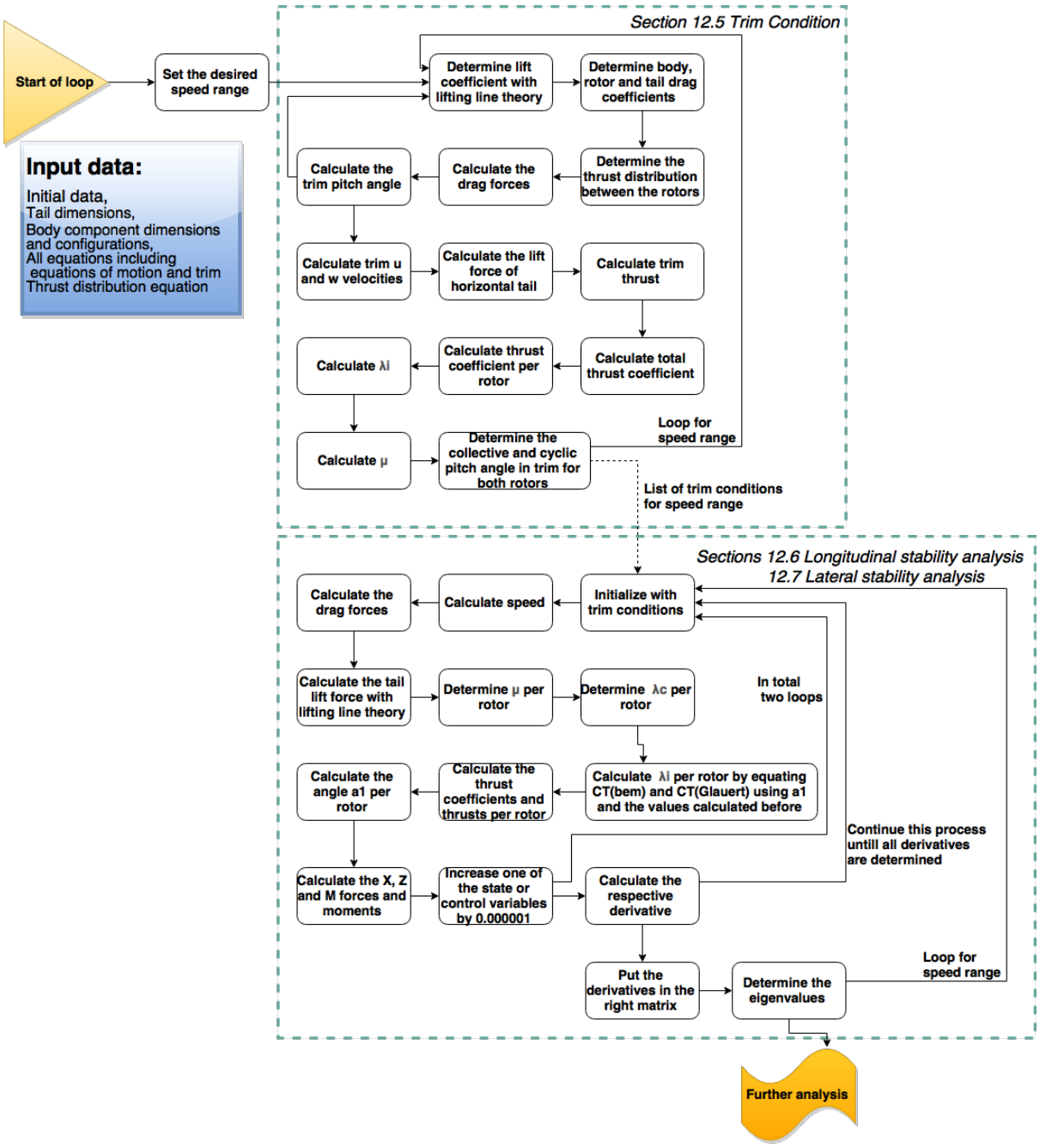

Figure 11.6: Graphical representation of the steps taken.

From this point on, computations are similar for both rotors and thus performed twice. Relationship between α_c and θ_c is given by 11.17. Combined with the assumption of $a_1 = \theta_c$ and the trim equation, the following angles are defined, equations 11.18-11.19.

$$\alpha_c = \theta_c - \arctan\left(\frac{w}{u}\right) \quad (11.17) \qquad \alpha_c = \theta_c - \theta_f = a_1 - \theta_f \quad (11.18) \qquad \alpha_d = \alpha_c - a_1 = -\theta_f = \frac{D_{tot}}{W} \quad (11.19)$$

Glauert's theory, equation 11.20 [4], states the thrust coefficient with the implementation of equation 11.19. The thrust coefficients were already found for both rotors with equations 11.15 and 11.16 using the thrust out of the equations motion. Glauert's theory is used to find the non-dimensional induced velocity λ_i.

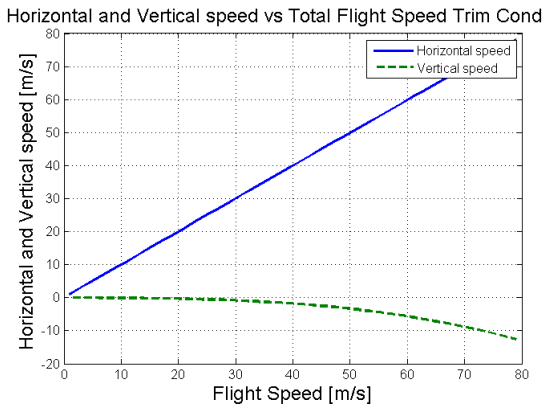

Figure 11.7: Horizontal and vertical flight speed for each trim condition.

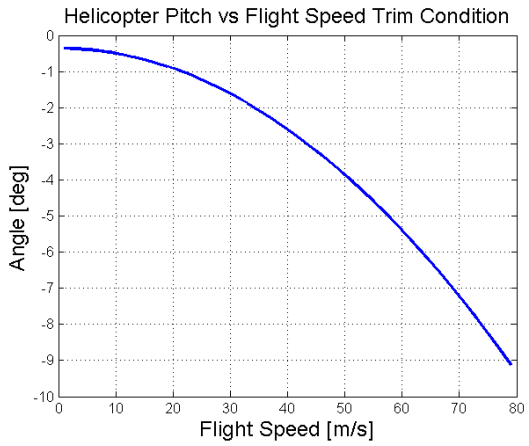

Figure 11.8: Pitch for each trim condition

$$Ct_{Glau} = 2\lambda_i \sqrt{\left(\frac{V}{\Omega R}\cos\left(\frac{D_{tot}}{W}\right)\right)^2 + \left(\frac{V}{\Omega R}\sin\left(\frac{D_{tot}}{W}\right) + \lambda_i\right)^2} \tag{11.20}$$

Compliance is also required for the blade element theory and the flapping equation for the thrust coefficient and non-dimensional induced velocity computed earlier. Assuming small angles and using equations 11.21 and 11.22 the longitudinal and cyclic pitch can be determined. The problem comes down to a system of linear equations with 2 equations and 2 unknowns per rotor. Cyclic pitch, knowing that $a_1 = \theta_c$, is found from the flapping equations 11.23 [78] and the collective pitch θ_0 in the blade element theory equation for CT, as shown in equation 11.24.

$$\mu = \frac{V}{\Omega R} \tag{11.21}$$

$$\lambda_c = \mu a_1 + \mu \frac{D_{tot}}{W} \tag{11.22}$$

$$a_1 = \frac{\frac{8}{3}\mu\theta_0 - 2\mu(\lambda_c + \lambda_i) - \frac{16q}{\gamma\Omega}}{1 - \frac{1}{2}\mu^2} \tag{11.23}$$

$$Ct_{BEM} = C_{L_\alpha}\frac{\sigma}{4}\left[\frac{2}{3}\theta_0\left(1 + \frac{3}{2}\mu^2 - (\lambda_c + \lambda_i)\right)\right] \tag{11.24}$$

So in the end, the system for 2 rotors solving for the required cyclic and collective pitch for each rotor consist of twice equation 11.23 and twice 11.24. This gives 4 equations with 4 unknowns: $\theta_{cR1}, \theta_{0R1}, \theta_{cR2}, \theta_{0R2}$, in matrix as shown in equation 11.25.

$$\begin{bmatrix} 1+\frac{3}{2}\mu^2 & -\frac{8}{3}\mu & 0 & 0 \\ -\mu & \frac{2}{3}+\mu 2 & 0 & 0 \\ 0 & 0 & 1+\frac{3}{2}\mu^2 & -\frac{8}{3}\mu \\ 0 & 0 & -\mu & \frac{2}{3}+\mu 2 \end{bmatrix} \cdot \begin{bmatrix} \theta_{cR1} \\ \theta_{0R1} \\ \theta_{cR2} \\ \theta_{0R2} \end{bmatrix} = \begin{bmatrix} -2\mu^2\frac{D_{tot}}{W} - 2\mu\lambda_{iR1} \\ \frac{4}{\sigma}\frac{Ct_{BEMR1}}{C_{L_\alpha}} + \mu\frac{D_{tot}}{W} + \lambda_{iR1} \\ -2\mu^2\frac{D_{tot}}{W} - 2\mu\lambda_{iR2} \\ \frac{4}{\sigma}\frac{Ct_{BEMR2}}{C_{L_\alpha}} + \mu\frac{D_{tot}}{W} + \lambda_{iR2} \end{bmatrix} \tag{11.25}$$

So for each speed, the required cyclic and collective pitch is found for both rotors, figure 11.9. One can notice a significant collective pitch angle difference between upper rotor R1 and lower rotor R2 since they both deliver a different amount of thrust. The upper rotor is delivering twice the thrust during hover. The difference in pitch angle becomes smaller and smaller when flight speed increases. The balance of thrust between the two rotors will approximate 1 at speeds over 20 m/s. Helicopter pitch angle and the horizontal and vertical speeds for trim conditions for each total flight speeds, as shown in figures 11.8 and 11.7.

The lateral equations of trim are obtained by setting equations 11.5-11.7 equal to zero.

The assumption has been made that $b_{1R1} = \theta_{cR1}$ and $b_{1R2} = \theta_{cR2}$. To achieve trim equilibrium the roll angle ϕ should be zero to have zero Y force. Furthermore, the sideslip angle should be zero to have zero L and N moment. This is because of the fact that the lift contribution of the vertical tail should be zero, which can only be achieved if the lift coefficient is zero. The vertical tail coefficient is zero, if the sideslip angle is zero. This means that at trim conditions, v, p, r and the roll angle are zero.

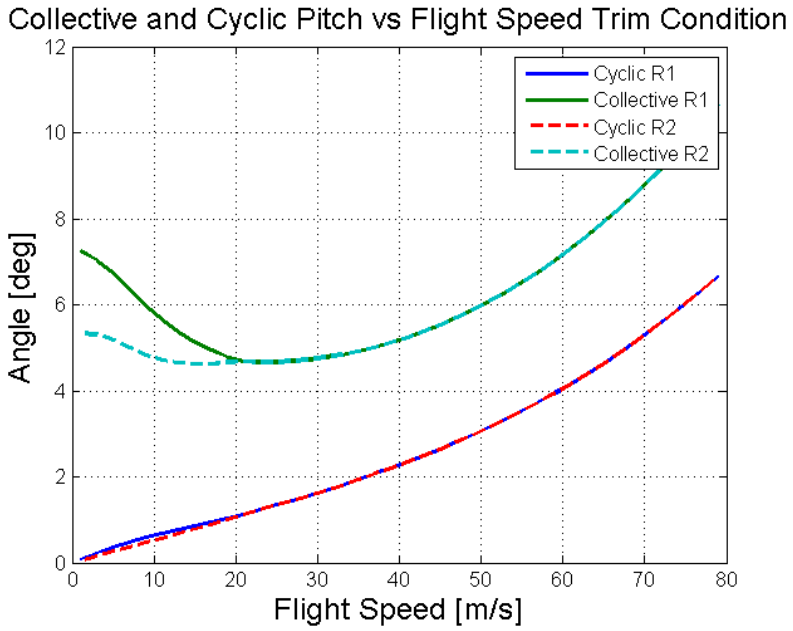

Figure 11.9: Required collective and cyclic pitch for trim conditions.

Table 11.4: Trim conditions at cruising speed.

Trim condition at V=39m/s	
u_0	38.96 m/s
w_0	-1.69 m/s
θ_{f_0}	-0.0435 rad
q_0	0 rad/s^2
θ_{0R1_0}	0.0895 rad
θ_{cR1_0}	0.0384 rad
θ_{0R2_0}	0.0891 rad
θ_{cR2_0}	0.0383 rad

11.6. LONGITUDINAL STABILITY ANALYSIS

In this and the following section, blocks 10, 11 and 12 will be discussed. In order to have a stability analysis, one should linearize the equations of motion at a certain equilibrium condition. The non-linear equations of motion for the symmetric flight are shown in equations 11.26-11.28. The decision has been made to analyze a decoupled system, which means that the symmetric and asymmetric stability will be analyzed separately. A decoupled system means in this case that the state variables v, p, r and the roll angle are zero. The asymmetric stability is discussed in the next section.

$$X - mg\sin(\theta_f) = m(\dot{u} + wq) \tag{11.26}$$

$$Z + mg\cos(\theta_f) = m(\dot{w} - uq) \tag{11.27}$$

$$M = I_y\dot{q} \tag{11.28}$$

X,Z and M are explained in equations 11.2-11.4. The defined forces and moments in these equations are slightly different than the X, Z and M to be used during the linearization, because the weight terms are treated separately.

The control variables are θ_0 and θ_c and the state variables are u, w, θ_f and q. The starting point of linearization is a stationary equilibrium situation for which the following applies:

- u=u_0
- w=w_0
- $\theta_f = \theta_{f_0}$
- q=0
- $\theta_{0R1} = \theta_{0R1_0}$
- $\theta_{cR1} = \theta_{cR1_0}$
- $\theta_{0R2} = \theta_{0R2_0}$
- $\theta_{cR2} = \theta_{cR2_0}$
- X=X_0=m g sin(θ_{f_0})
- Z=Z_0=-m g cos(θ_{f_0})
- M=M_0= 0

This leads to the linearized equations of motion shown in equation 11.29. The forces and moments will go through small changes in u, w, θ_f and q which result in perturbations.

$$\begin{bmatrix} \Delta\dot{u} \\ \Delta\dot{w} \\ \Delta\dot{\theta}_f \\ \Delta\dot{q} \end{bmatrix} = \begin{bmatrix} \frac{X_u}{m} & \frac{X_w}{m} & \frac{X_{\theta f}}{m} - g\cdot\cos(\theta_{f0}) & \frac{X_q}{m} - w_0 \\ \frac{Z_u}{m} & \frac{Z_w}{m} & \frac{Z_{\theta f}}{m} - g\cdot\sin(\theta_{f0}) & \frac{Z_q}{m} + u0 \\ 0 & 0 & 0 & 1 \\ \frac{\mathrm{M_u}}{I_y} & \frac{M_w}{I_y} & \frac{M_{\theta f}}{I_y} & \frac{M_q}{I_y} \end{bmatrix} \cdot \begin{bmatrix} \Delta u \\ \Delta w \\ \Delta\theta_f \\ \Delta q \end{bmatrix} + \Delta\theta_{oR1} \cdot \begin{bmatrix} \frac{X_{\theta_{oR1}}}{m} \\ \frac{Z_{\theta_{oR1}}}{m} \\ 0 \\ \frac{M_{\theta_{oR1}}}{Iy} \end{bmatrix} + \Delta\theta_{oR2} \cdot \begin{bmatrix} \frac{X_{\theta_{oR2}}}{m} \\ \frac{Z_{\theta_{oR2}}}{m} \\ 0 \\ \frac{M_{\theta_{oR2}}}{I_y} \end{bmatrix} + \Delta\theta_{cR1} \cdot \begin{bmatrix} \frac{X_{\theta_{cR1}}}{m} \\ \frac{Z_{\theta_{cR1}}}{m} \\ 0 \\ \frac{M_{\theta_{cR1}}}{I_y} \end{bmatrix} + \Delta\theta_{cR2} \cdot \begin{bmatrix} \frac{X_{\theta_{cR2}}}{m} \\ \frac{Z_{\theta_{cR2}}}{m} \\ 0 \\ \frac{M_{\theta_{cR2}}}{I_y} \end{bmatrix} \tag{11.29}$$

To determine the derivatives, one should know the relationship of the state variables with the forces and moments. During this phase, only the longitudinal derivatives will be determined, which means that the state variables of the lateral equations of motion will be set to zero. These are the v, p, ϕ and r. With equations 11.34 one can determine λ_i, which is needed to determine the thrust coefficients with equations 11.24 and 11.20. Equation 11.34 is actually the same as equating the thrust coefficient calculated with the blade element theory and the coefficient calculated with the Glauert theory. Equations 11.23, 11.30, 11.31, 11.32 and 11.33 are needed for the calculations. Note that these calculation should be done twice, for each rotor separately. In these equations, it can be noticed that the thrust is dependent on u, w, θ_f and q. The drags are determined with table 11.2 and the drag of the rotor was determined with the method described in chapter 7. The drags are dependent on u, w and θ_f. It should noted that the lift coefficient of the stabilizer is a function of the pitch angle. Figure 11.6 will make this process more clear.

$$V = \sqrt{u^2 + w^2} \tag{11.30}$$

$$a_c = \theta_c - arctan\left(\frac{w}{u}\right) \tag{11.31}$$

$$\mu = \frac{V}{\omega R} cos(a_c) \tag{11.32}$$

$$\lambda_c = \frac{V}{\omega R} sin(a_c) \tag{11.33}$$

$$C_{L_\alpha}\frac{\sigma}{4}\left[\frac{2}{3}\theta_0\left(1 + \frac{3}{2}\mu^2 - (\lambda_c + \lambda_i)\right)\right] = 2\lambda_i\sqrt{\left(\frac{V}{\Omega R}\cos(a_c - a_1)\right)^2 + \left(\frac{V}{\Omega R}\sin(a_c - a_1) + \lambda_i\right)^2} \tag{11.34}$$

In order to determine the derivatives, the algorithm to determine the forces and moments is used in a loop. If one for example wants to determine the derivative X_u, the effect of the perturbation of the state variable u on the force X will be determined. This means that during the first loop, the control and state variables will be kept at trim conditions. During the second loop the state variable u will be increased with a very small value (order: 10^{-6}), while the other state and control variables are kept at trim conditions. With this approach, the difference in the force X can be determined which is only caused by a difference in state variable u. This results in the state space system shown in equation 11.35. This system is determined during a flight speed of 39 m/s. At different speeds, the trim condition is different, as well as the derivatives. A plot has been made for the coefficients along different flight speeds. This is shown in figure 11.10.

$$\begin{bmatrix} \Delta\dot{u} \\ \Delta\dot{w} \\ \Delta\dot{\theta}_f \\ \Delta\dot{q} \end{bmatrix} = \begin{bmatrix} -0.02844 & -0.0161 & -9.816 & 2.223 \\ -0.02676 & -1.021 & 0.05745 & 38.96 \\ 0 & 0 & 0 & 1 \\ 0.005289 & 0.01415 & 0 & -0.4379 \end{bmatrix} \cdot \begin{bmatrix} \Delta u \\ \Delta w \\ \Delta\theta_f \\ \Delta q \end{bmatrix} + \Delta\theta_{oR1} \cdot \begin{bmatrix} -2.396 \\ -73.18 \\ 0 \\ 2.721 \end{bmatrix} + \Delta\theta_{oR2} \cdot \begin{bmatrix} 5.26 \\ 19.89 \\ 0 \\ -5.974 \end{bmatrix} + \Delta\theta_{cR1} \cdot \begin{bmatrix} -2.383 \\ -73.18 \\ 0 \\ 1.244 \end{bmatrix} + \Delta\theta_{cR2} \cdot \begin{bmatrix} 5.233 \\ 19.89 \\ 0 \\ -2.731 \end{bmatrix} \tag{11.35}$$

Table 11.5: Eigenvalues, period and half/double amplitude time at cruise speed.

Short period		
Eigenvalues (λ)	Period (P) [s]	Half amplitude time ($T_{\frac{1}{2}}$) [s]
-1.5396	0	0.45
-0.2959	0	2.34
Phugoid		
Eigenvalues	Period [s]	Double amplitude time (T_2) [s]
0.1740 + 0.2792i	22.5	3.98
0.1740 - 0.2792i	22.5	3.98

The eigenvalues can be calculated using equation 11.35. With this eigenvalue, some characteristics of the eigenmotions can be determined. The eigenmotions of the symmetric flight are the short period and the phugoid. The eigenvalues are shown in table 11.5. In this table, the period and the half/double amplitude time are also shown, which are calculated with equations 11.36 and 11.37.

$$P = \frac{2\pi}{Im(\lambda)} \tag{11.36}$$

$$T_2 = -T_{\frac{1}{2}} = \frac{ln(2)}{Re(\lambda)} \tag{11.37}$$

The conclusion can be made that the H2Copter is stable and non-oscillatory for the short period, because this eigenmotion only contains negative real values. The phugoid unstable and oscillatory. This means that a controller needs to be implemented in the design as will be discussed in section 11.8.

11.7. Lateral stability analysis

The non-linear equations of motion for the asymmetric flight are shown in equations 11.38-11.40. The decision has been made to analyze a decoupled system as has been explained before, which means that the symmetric and asymmetric stability will be analyzed separately. A decoupled system means in this case that the state variables u, w, q and the pitch angle are zero. However, after some trial and error it was concluded that this did not work. First of all, setting the velocies u and w to zero means that the flight speed is equal to the side velocity (v), which means that the helicopter is flying along the y-axis. Furthermore, the sideslip angle would be zero for the entire flight for the same reason. Therefore, the decision has been made to partly couple the system by using the u, w, q and the pitch angles as the values resulted from the trim conditions. Therefore, these state variables are not neglected in equation 11.38. However, an input will not be given to those variables. It will only be given to the control variables θ_0 and θ_c and the state variables v, p, ϕ and r.

$$Y + mg\cos(\theta_f)\sin(\phi) = m(\dot{v} + ru - pw) \tag{11.38}$$

$$L = I_x\dot{p} \tag{11.39}$$

$$N = I_z\dot{r} \tag{11.40}$$

Y, L and N are explained in equations 11.5-11.7 with the difference that the weight terms are excluded. The starting point of linearization is a stationary equilibrium situation for which the following applies:

- u=u_0
- w=w_0
- $\theta_f = \theta_{f_0}$
- q=0
- $\theta_{0R1} = \theta_{0R1_0}$
- $\theta_{cR1} = \theta_{cR1_0}$
- $\theta_{0R2} = \theta_{0R2_0}$
- $\theta_{cR2} = \theta_{cR2_0}$
- Y=Y_0=m g cos(θ_{f_0}) sin(ϕ_0)
- L=L_0=0
- N=N_0= 0
- β=0

This leads to the linearized equations of motion shown in equation 11.41.

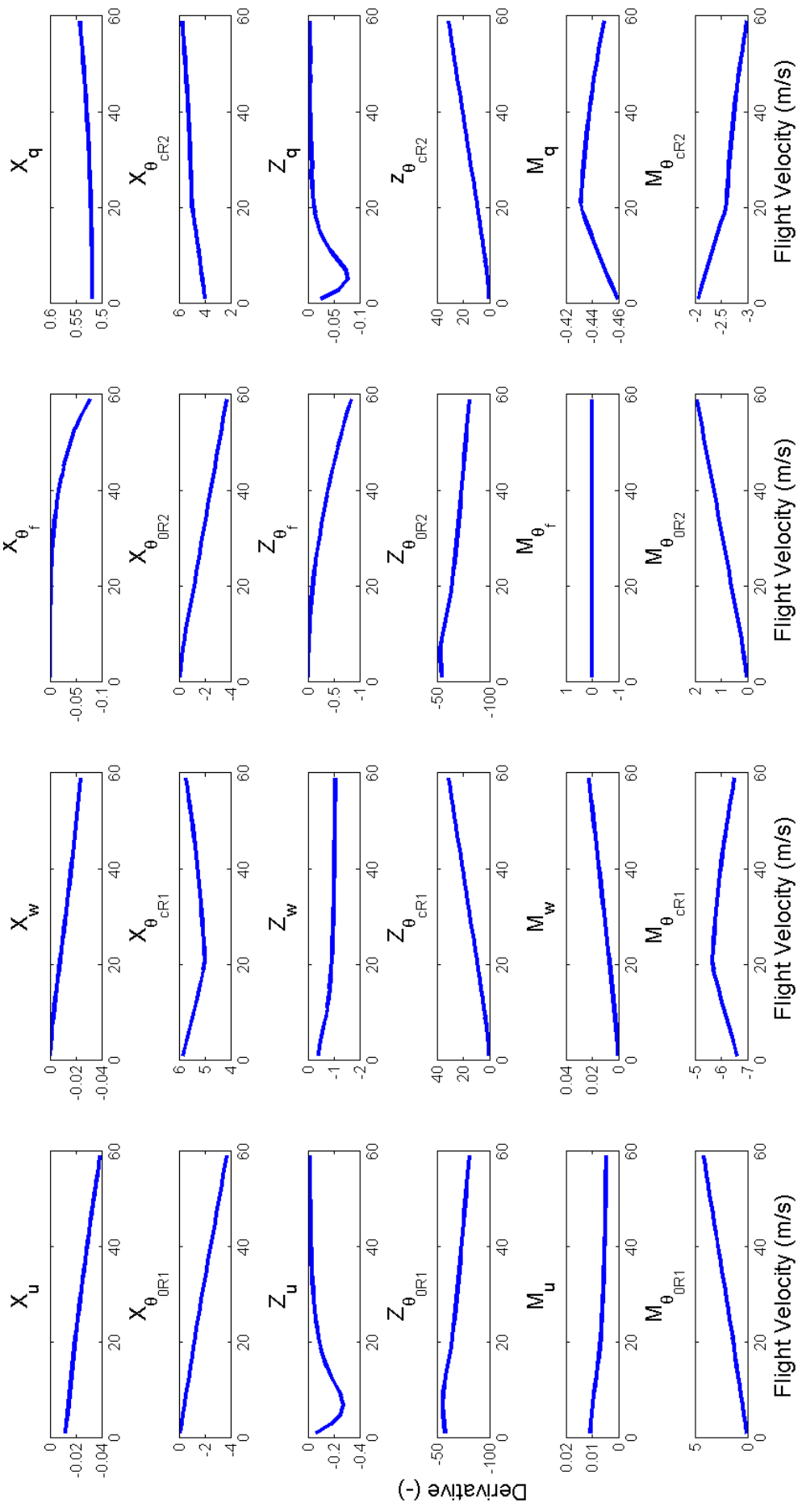

Figure 11.10: Derivatives for several flight speeds normalized by mass or moments of inertia.

$$\begin{bmatrix} \Delta v \\ \Delta p \\ \Delta \Phi \\ \Delta r \end{bmatrix} = \begin{bmatrix} \frac{Y_v}{m} & \frac{Y_p}{m} + w_0 & \frac{Y_\Phi}{m} + g \cdot \cos(\theta_{f0}) \cdot \cos(\Phi_0) & \frac{Y_r}{m} - u_0 \\ \frac{L_v}{I_x} & \frac{L_p}{I_x} & \frac{L_\Phi}{I_x} & \frac{L_r}{I_x} \\ 0 & 1 & 0 & 0 \\ \frac{N_v}{I_z} & \frac{N_p}{I_z} & \frac{N_\Phi}{I_z} & \frac{N_r}{I_z} \end{bmatrix} \cdot \begin{bmatrix} \Delta v \\ \Delta p \\ \Delta \Phi \\ \Delta r \end{bmatrix}$$
$$+\Delta\theta_{oR1} \cdot \begin{bmatrix} \frac{Y_{\theta_{oR1}}}{m} \\ \frac{L_{\theta_{oR1}}}{I_x} \\ 0 \\ \frac{N_{\theta_{oR1}}}{I_z} \end{bmatrix} + \Delta\theta_{oR2} \cdot \begin{bmatrix} \frac{Y_{\theta_{oR2}}}{m} \\ \frac{L_{\theta_{oR2}}}{I_x} \\ 0 \\ \frac{N_{\theta_{oR2}}}{I_z} \end{bmatrix} + \Delta\theta_{cR1} \cdot \begin{bmatrix} \frac{Y_{\theta_{cR1}}}{m} \\ \frac{L_{\theta_{cR1}}}{I_x} \\ 0 \\ \frac{N_{\theta_{cR1}}}{I_z} \end{bmatrix} + \Delta\theta_{cR2} \cdot \begin{bmatrix} \frac{Y_{\theta_{cR2}}}{m} \\ \frac{L_{\theta_{cR2}}}{I_x} \\ 0 \\ \frac{N_{\theta_{cR2}}}{I_z} \end{bmatrix} \tag{11.41}$$

With equations 11.42 one can determine λ_i, which is needed to determine the thrust coefficients with equations 11.24 and 11.20. Equation 11.42 is actually the same as equating the thrust coefficient calculated with the blade element theory and the coefficient calculated with the Glauert theory. Equations 11.45 [78], 11.46 [78], 11.43, 11.44, 11.32 and 11.33 are needed for the calculations. Note that these calculation should be done twice, for each rotor separately. In these equations, it can be noticed that the thrust is dependent on v, p, ϕ and q. It should be noted that the lift coefficient of the stabilizer is a function of the side slip angle, which is determined with equation 11.47

$$C_{L_\alpha} \frac{\sigma}{4} \left[\frac{2}{3}\theta_0 \left(1 + \frac{3}{2}\mu^2 - (\lambda_c + \lambda_i) \right) \right] = 2\lambda_i \sqrt{\left(\frac{V}{\Omega R} \cos(a_c + b_1) \right)^2 + \left(\frac{V}{\Omega R} \sin(a_c + b_1) + \lambda_i \right)^2} \tag{11.42}$$

$$V = \sqrt{u_0^2 + w_0^2 + v^2} \tag{11.43}$$

$$a_c = \theta_c - \phi \tag{11.44}$$

$$a_0 = \frac{\gamma}{2} \left(\frac{1+\mu^2}{4}\theta_0 + \frac{\lambda_c + \lambda_i}{3} + \frac{\mu p}{6\omega} \right) \tag{11.45}$$

$$b_1 = \frac{1}{1 + 0.5\mu^2} \left(\frac{4\mu a_0}{3} - \frac{16p}{\gamma\omega} \right) \tag{11.46}$$

$$\beta = \arctan \frac{v}{u_0} \tag{11.47}$$

With these equations, the derivatives can be calculated with the same method discussed before. This results in the state space system shown in equation 11.48. This system is determined during a flight speed of 39 m/s. At different speeds, the trim condition is different, as well as the derivatives. A plot has been made for the coefficients along different flight speeds. This is shown in figure 11.11. In some of the graphs in this figure, one can notice a clear change in slope at 20 m/s. This is probably due to the fact that there is a clear change in the thrust distribution between the rotors at that point.

$$\begin{bmatrix} \Delta \dot{v} \\ \Delta \dot{p} \\ \Delta \dot{\Phi} \\ \Delta \dot{r} \end{bmatrix} = \begin{bmatrix} 6.262e-10 & -2.119 & 12.06 & -38.96 \\ 0.1842 & -0.001127 & 0.005966 & 0 \\ 0 & 1 & 0 & 0 \\ 0.07796 & 0 & 0 & 0 \end{bmatrix} \cdot \begin{bmatrix} \Delta v \\ \Delta p \\ \Delta \Phi \\ \Delta r \end{bmatrix} + \Delta\theta_{oR1} \cdot \begin{bmatrix} 4.322 \\ 5.301 \\ 0 \\ 0 \end{bmatrix}$$
$$+\Delta\theta_{oR2} \cdot \begin{bmatrix} 4.647 \\ 5.7 \\ 0 \\ 0 \end{bmatrix} + \Delta\theta_{cR1} \cdot \begin{bmatrix} 4.303 \\ -5.277 \\ 0 \\ 0 \end{bmatrix} + \Delta\theta_{cR2} \cdot \begin{bmatrix} 4.628 \\ -5.676 \\ 0 \\ 0 \end{bmatrix} \tag{11.48}$$

The eigenvalues can be calculated using equation 11.48. The eigenmotion of the asymmetric flight are the roll subsidence, spiral mode and dutch roll. This is shown in table 11.6. In this table, the period and the half/double amplitude time are also shown, which are calculated with equations 11.36 and 11.37.

The conclusion can be made that all three eigenmotion are stable. They all contain a negative real part. Furthermore, the dutch roll is the only oscillatory eigenmotion, because of the imaginary part in the eigenvalues.

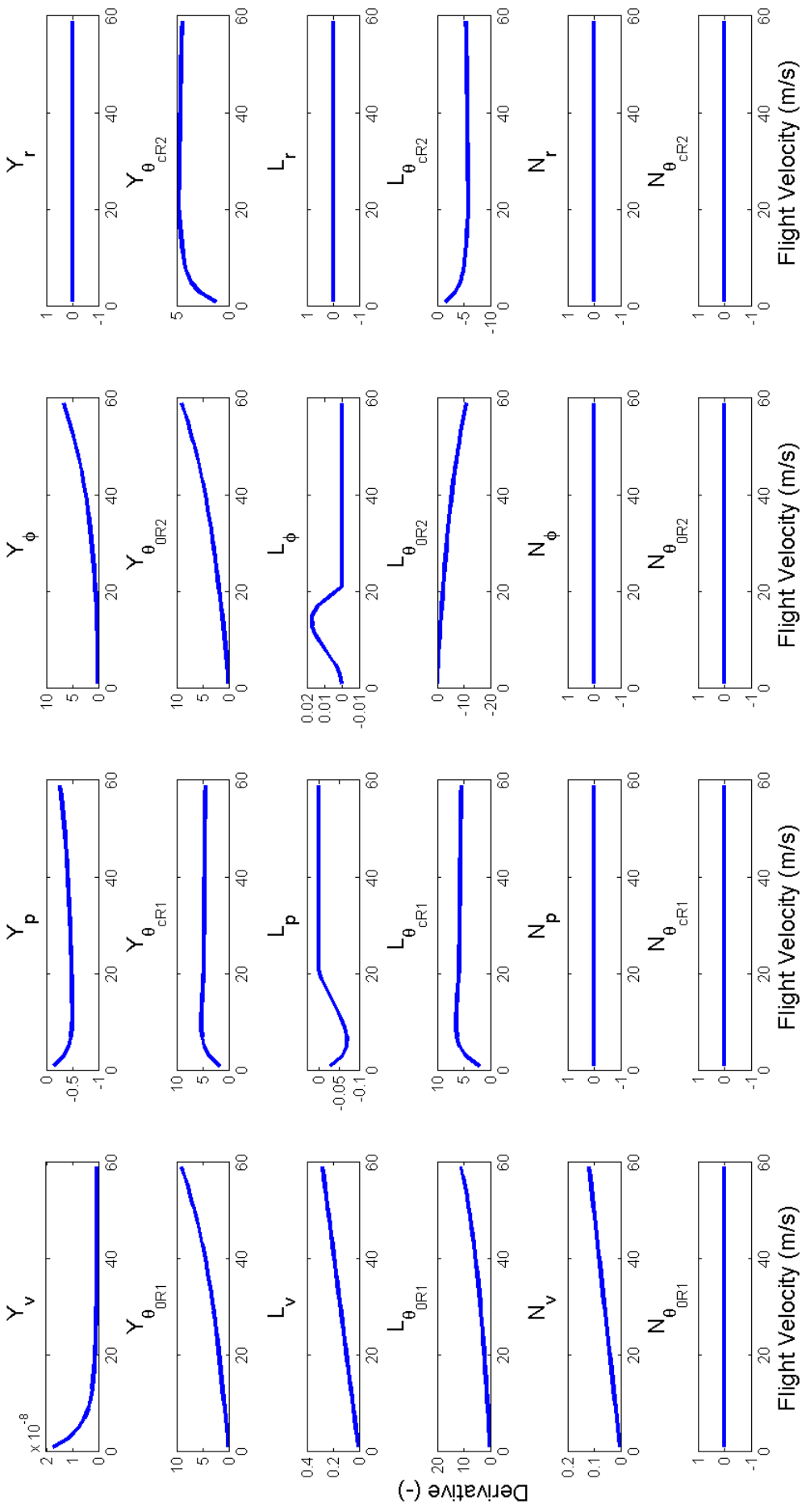

Figure 11.11: Derivatives for several flight speeds normalized by mass or moments of inertia.

Table 11.6: Eigenvalues, period and half/double amplitude time at cruise speed.

Subsidence roll		
Eigenvalues (λ)	Period (P) [s]	Half amplitude time ($T_{\frac{1}{2}}$) [s]
-0.2664	0	2.60
Spiral mode		
Eigenvalues (λ)	Period (P) [s]	Half amplitude time ($T_{\frac{1}{2}}$) [s]
-0.0081	0	85.57
Dutch roll		
Eigenvalues	Period [s]	half amplitude time ($T_{\frac{1}{2}}$) [s]
-0.1297 + 0.2996i	20.97	5.34
-0.1297 - 0.2996i	20.97	5.34

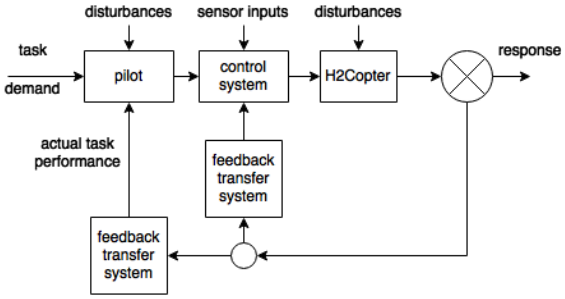

Figure 11.12: Pilot and control system vehicle interference representation [79]

11.8. EIGENMOTIONS AND CONTROLLER GAINS

In this section, only the longitudinal stability will be discussed. The results of the lateral stability seemed unreliable, which is explained in section 11.10. As discussed before, the symmetric eigenvalues of the H2Copter describe an unstable behaviour, which is common for helicopters. To reduce the workload of the pilot and improve the flying quality, a control system is implemented. This is block 13 in the process shown in figure 11.1. Several levels of control systems exist, this report only includes a Stability and Control Augmentation System SCAS. The highest level would be a fully operational autopilot. The flying control tasks and relations between the pilot, control system and the vehicle are represented by a closed-loop feedback system, figure 11.12. The pilot works as a key sensor and motivator of the system. Help is provided by the control system getting information from several sensors: rate gyroscopes and attitude gyroscopes measuring pitch, roll and yaw rates. The control system is also placed in a closed-loop.

SCAS is implemented in the flight computer which is linked to the movements of the servo flaps on the rotor, also shown in figure 11.2 The SCAS is used to damp disturbances caused by for example turbulence. This assures comfortable flying qualities for the pilot who can now concentrate more on the mission and should not perform continuous corrections to maintain stable flight.

Figure 11.13 shows the implemented correcting augmentation system using the pitch rate and pitch angel times a gain in a feedback loop.

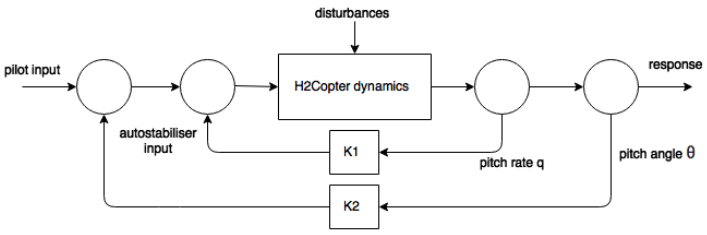

Figure 11.13: Feedback augmenting damping system, PD-controller.

The SCAS for longitudinal stabiliy in this design will use feedback of 2 different state variables, the pitch angle and pitch rate. This corresponds with a PD-controller (Proportional, Derivative mode). The Proportional mode (P) will be a reaction to the change of the process variable pitch angle, helping the process to converge faster to a desired set point (this is the first part of equation 11.49 with gain factor K_1). The Derivative mode (D) is proportional to the rate of change q, transforming spikes in the H2Copters behaviour to a kick with a moderate decay. This means 2 different gain factors need to be chosen, K_1 and K_2. These can be implemented analytically in the matrix as done in 11.50 by using equation 11.49. The stability of the H2Copter is evaluated through investigating the longitudinal eigenmotions phugoid and short period. a small rap up: the equations of motions were derived, linearised and stability coefficients were found. An evaluation of the eigenvalues were found using this linearized model. Now one arrives at block 13 were the gains needs to be found in order to stabilize the H2Copter. For choosing suitable gains, a non-linearised model was used since this approaches more reality. Choosing gains in a linearised system give poor results and are less applicable to real flight conditions. Gains are tuned so until compliance with EASA CS-27 regulations explained later.

$$\theta_c = K_1(\theta_f - \theta_{f_{ref}}) + K_2(q) \tag{11.49}$$

$$\begin{bmatrix} \frac{X_u}{m} & \frac{X_w}{m} & \frac{X_{\theta_f}}{m} - g\cos(\theta_{f0}) & \frac{X_q}{m} - w_0 \\ \frac{Z_u}{m} & \frac{Z_w}{m} & \frac{Z_{\theta_f}}{m} - g\sin(\theta_{f0}) & \frac{Z_q}{m} + u_0 \\ 0 & 0 & 0 & 1 \\ \frac{M_u}{I_y} & \frac{M_w}{I_y} & \frac{M_{\theta_f}}{I_y} & \frac{M_q}{I_y} \end{bmatrix} \Rightarrow$$
$$\begin{bmatrix} \frac{X_u}{m} & \frac{X_w}{m} & \frac{X_{\theta_f}}{m} - g\cos(\theta_{f0}) - \frac{K_1 X_{\theta_{cR1}}}{m} - \frac{K_1 X_{\theta_{cR1}}}{m} & \frac{X_q}{m} - w_0 - \frac{K_2 X_{\theta_{cR1}}}{m} - \frac{K_2 X_{\theta_{cR2}}}{m} \\ \frac{Z_u}{m} & \frac{Z_w}{m} & \frac{Z_{\theta_f}}{m} - g\sin(\theta_{f0}) - \frac{K_1 Z_{\theta_{cR1}}}{m} - \frac{K_1 Z_{\theta_{cR2}}}{m} & \frac{Z_q}{m} + u_0 - \frac{K_2 Z_{\theta_{cR1}}}{m} - \frac{K_2 Z_{\theta_{cR2}}}{m} \\ 0 & 0 & 0 & 1 \\ \frac{M_u}{I_y} & \frac{M_w}{I_y} & \frac{M_{\theta_f}}{I_y} - \frac{K_1 M_{\theta_{cR1}}}{I_y} - \frac{K_1 M_{\theta_{cR2}}}{I_y} & \frac{M_q}{I_y} - \frac{K_2 M_{\theta_{cR1}}}{I_y} - \frac{K_2 M_{\theta_{cR2}}}{I_y} \end{bmatrix} \tag{11.50}$$

PHUGOID

The phugoid motion is obtained after a relatively long pitch input after 3 seconds of stable flight, 1 degree pitch during 3 seconds in this case. Afterwards, the pilot releases the controls and the aircraft shall go into its eigenmotion. This is a way to simulate this behaviour, the pitch motion can also be caused by turbulence. The desired behaviour would be the aircraft returning to it's original state before the perturbation. One should also consider how this is done by investigating the oscillations and the time it takes to stabilize again.

The PD-controller is shown in in equation 11.49. Now K_1 and K_2 are varied and the effect on the phugoid behaviour is studied. Figure 11.14 shows the impact of K_2 using q as feedback again into the system. The effect of three different K_2's are plotted: 0.05, 0.15 and 0.25. Increasing gain shows a decrease in oscillations and amplitude. The gains are raised until compliance with the CS-27 EASA regulations, explained in 11.8, $K_2 = 0.25$ is chosen.

Next, the effect of varying K_1 is studied and shown for the following values: 0.15, 0.2 and 0.27, figure 11.15. Similar effects are noticeable by increasing this gain. A gain of $K_1 = 0.27$ is found to be sufficient for stability.

The PD-control equation including the chosen gains will look like this, equations 11.51.

$$\theta_c = 0.27(\theta_f - \theta_{f_{ref}}) + 0.25(q) \tag{11.51}$$

SHORT PERIOD

The same procedure was carried out for the short period eigenmotion, 1 degree input during 0.1 seconds. The gains found out of the phugoid analysis seem to be also valid for the short period stability. This eigenmotion was already stable before implementing a PD-controller.

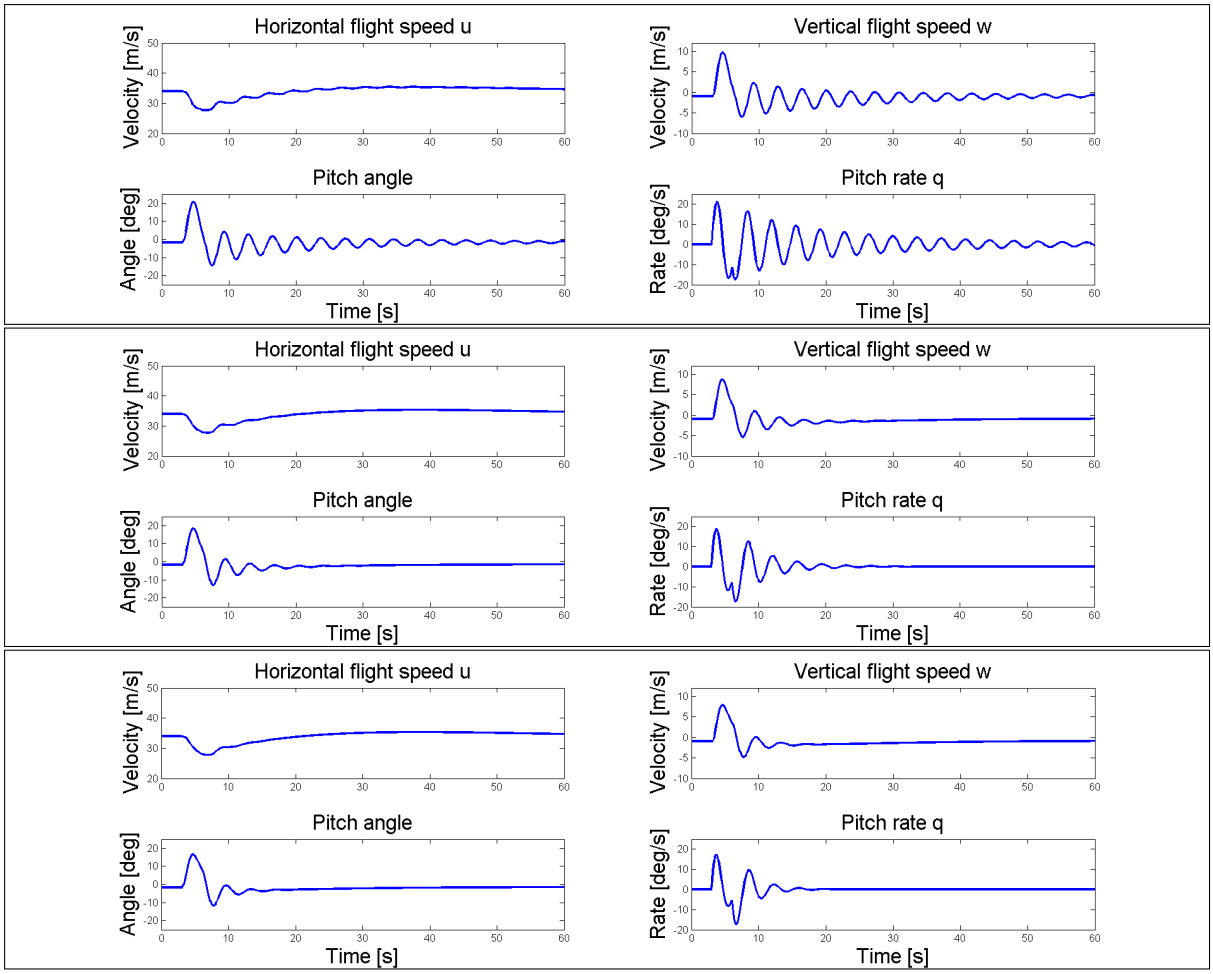

Figure 11.14: Phugoid: 1 deg pitch input during 3 sec, $K_1 = 0.27, K_2 = 0.05$ (upper) 0.15 (middle) 0.25 (lower)

Table 11.7: EASA CS-27 helicopter (minimum 2 crew), dynamic stability requirements [67].

EASA CS-27 helicopter (minimum 2 crew), dynamic stability requirements
Oscillation with period less than 5 sec must damp to 1/2 amplitude in less than 2 cycles
Oscillation with period less between 5 sec and 10 sec must be damped
Oscillation with period more than 10 sec may not achieve double amplitude in less than 2 cycles

Discussion of gains

These gains are found to be high compared to other helicopters stated by Padflied in chapter 2 [79]. The result might be a quick saturating of the augmentation during manoeuvres or moderate turbulence. Also during the design, one should consider how the augmentation system is interfering with the pilot controls. Two options: the input of the system can be mixed with the pilot's input or the pilot will always override the augmentation system. Because in this case, gains are high, it might be an option to override the systems controls with the pilot input. Otherwise the gains will only try to fight the intended manoeuvres of the pilot.

Described in the CS-27 EASA helicopter regulations are requirements on the dynamic stability, which are shown in table 11.7.

This is checked for both longitudinal eigenmotions as described below for an example of the pitch rate during a short period, figure 11.16. The period is less than 5 seconds and the amplitude is decreasing with 1.6 degrees in one cycle. Taking into account a little average shift of 0.2 degrees, decreasing the first peak of -0.5 degrees with 1.6 degrees is more than a 1/2 amplitude decrease in one cycle.

The following motion is plotted to give an idea about the helicopter's behaviours during an operation manoeuvre. Here, the helicopter is hovering above the ground, zero airspeed (assumed no wind). The pilot starts

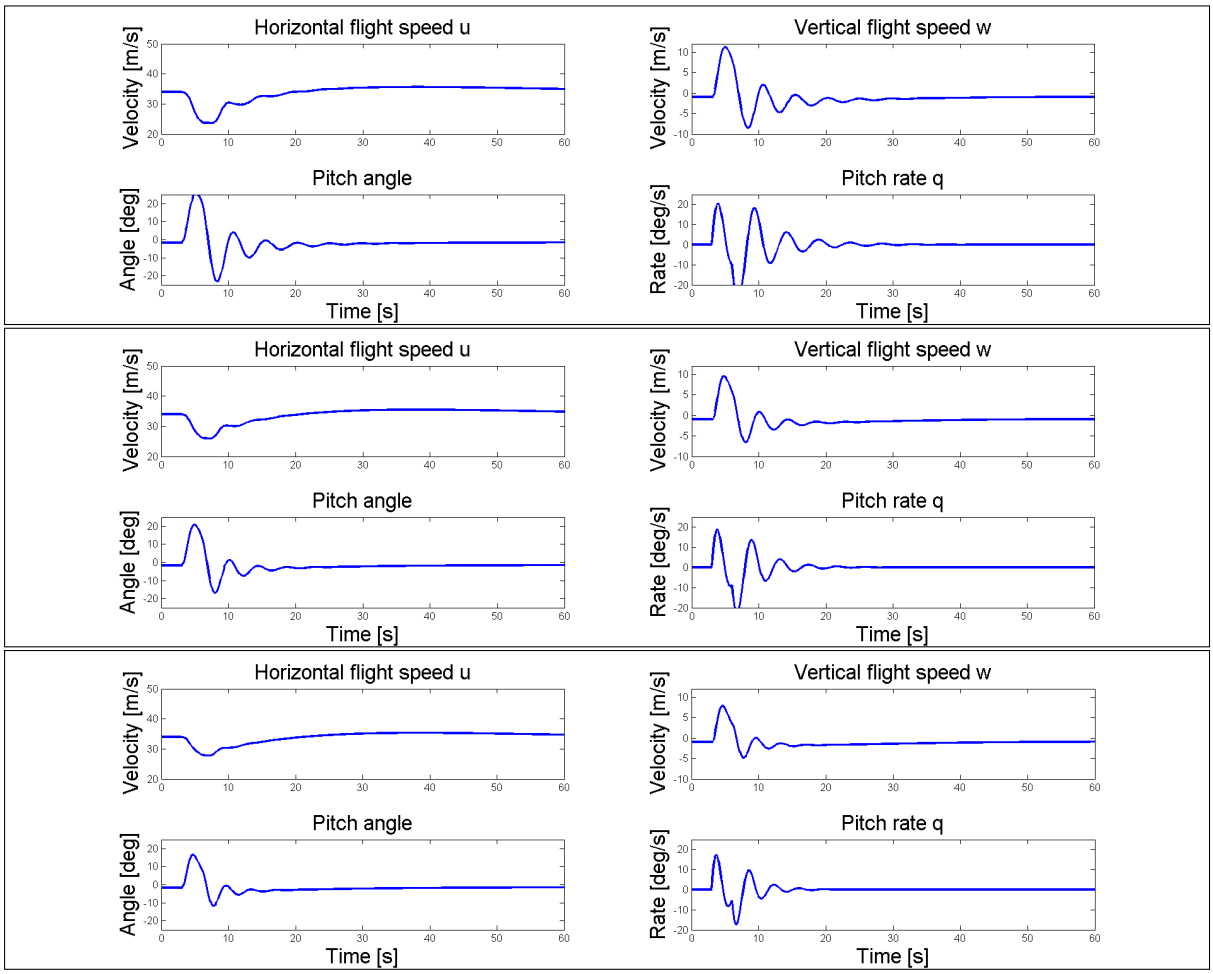

Figure 11.15: Phugoid:1 deg pitch input during 3 sec, K_1= 0.15 (upper) 0.2 (middle) 0.27 (lower), K_2= 0.25.

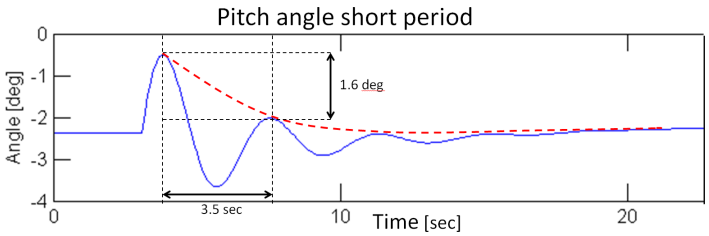

Figure 11.16: Pitch behaviour after a short period, 1 degree pitch input during 0.1 sec after 3 seconds of stable flight, K1=0.27 and K2=0.25

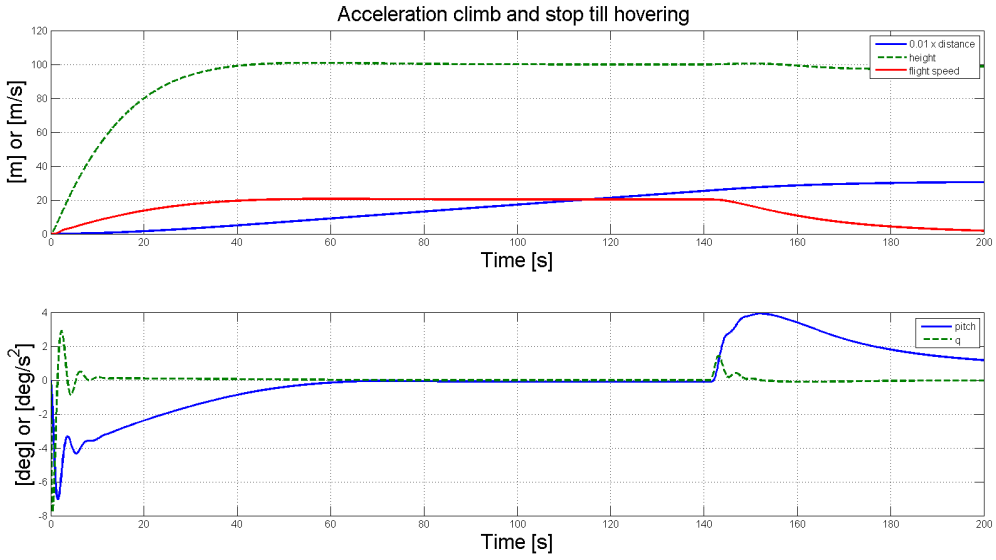

Figure 11.17: Accelerating and climbing till 100m, after 90 sec return to hover situation.

accelerating and climbing till 100m, 20m/s. After 90 seconds, the pilot wants the helicopter to stop and return to a hover situation at 100m. These plots describe the motion and the pitch angle and pitch rate changes of the helicopter during this manoeuvre, figure 11.17.

11.9. EMPANNAGE

In this section, the design process of the horizontal and vertical stabilizers will be shown. This is a challenging phase during the design process. In section 11.9.1 the horizontal tail design process will be discussed and in section 11.9.2 the vertical tail design process will be shown. Blocks 1, 5, 6 and 7 of figure 11.1 will be described in these sections.

11.9.1. HORIZONTAL TAIL SIZING

The horizontal tail carries two primary functions, trimming the rotorcraft and providing stability. Sometimes there might be a third functions, which is to control the rotorcraft. However for the H2Copter, elevators are not implemented and control functions will be carried out by the rotors. This means that the tail will be fixed. The tail is primary sized for the trim conditions during cruise. The equations for the trim condition are already shown in section 11.5. The forces in the x-direction and z-direction are already zero in the determined trim condition, which is done by changing the collective and cyclic pitch angle. However the pitching moment equation is not. This equation is shown in 11.52, while still assuming that θ_c=a_1.

$$\sum M_y = 0 = D_{rR1} \cdot l_{R1} + D_{rR2} \cdot l_{R2} - L_h \cdot l_h \tag{11.52}$$

To achieve this condition, three main design parameters can be changed, these are the tail arm, the surface area and the incident angle of the tail. Other design parameters which are considered are the airfoil choice and the aspect ratio.

HORIZONTAL TAIL CONFIGURATION

Prouty states 3 main types of horizontal stabilizers summarized in table 11.8 , [9]. The H2Copter is a heavy but compact helicopter. The hydrogen propulsion system and tank are the main contributors to total mass, which led to long rotor blades. The backward mounted tail and the T-tail both need a tail boom long enough to install the horizontal stabilizer behind the rotor. For the H2Copter design, this would mean a long tail boom since the helicopter itself is compact but has a large rotor radius. It would not be structurally efficient to make a tail boom even longer than the rotor radius. Secondly, to avoid a drastic change in pitching moments caused by the rotor wake impacting on the horizontal tail while accelerating, a forward mounted tail is chosen. One rather wants a continuous rotor wake impact on the tail slightly reducing the hover capabilities.

Table 11.8: Horizontal tail configuration trade off [9].

Horizontal Tail configuration		
Forwards mounted horizontal tail	**Low backwards mounted**	**T-tail configuration**
• Always in wake of rotor, no sudden moments created by changes in the rotor wake • Small penalty during hover	• Different flight speeds, tail in and out of rotor wake inducing undesired pitching moments • Efficiency loss due to separated flow from fuselage • Long boom critical for ground clearance • Popular design for small/medium helicopters	• Outside rotor wake • Smaller wing area required • Longer and stronger boom, heavy
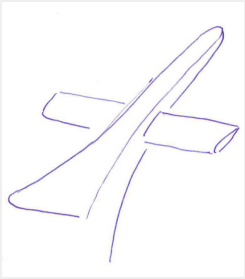	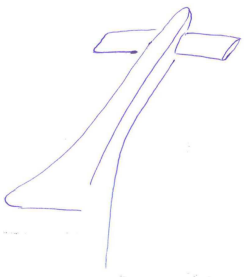	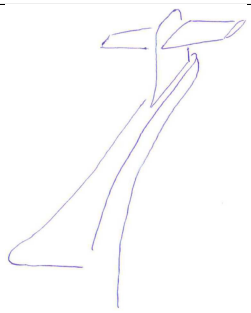

Airfoil selection

The slope of the tailplane airfoil lift curve should be as large as possible with a wide range of usable angle of attacks. It is possible that the center of gravity changes during the flight, which means that the tail should be able to provide both positive and negative lift. This means that a symmetrical airfoil should be used. A common airfoil used in the industry is the NACA0012, because of its simplicity. This is also the airfoil used for the H2Copter tail.

Lift coefficient

With equation 11.53 the lift of the horizontal stabilizer can be determined. During trim lift times the tail length shall provide a bending moment of 338Nm during cruise to counter the pitching moment. This value is divided by the dynamic pressure, which resulted in the value 0.45 m^3, which should be the product of the lift coefficient times the tail arm times the surface area.

$$L_h = \frac{1}{2}\rho V^2 c l_h S_h \tag{11.53}$$

The lift coefficient is found from the 'lifting line theory'. One half of the tail will be divided into several segments. The higher the number of segments, the more accurate the result. Each segment has a unique chord and may have an unique span. The angles corresponding to each section will be calculated. The angles are functions of lift distribution along half of the span. The angles are defined as the angle between the horizontal axis and the intersection between lift distribution curve and the segment line. At first the assumption will be made that the lift distribution is elliptical, which will be corrected during a later phase. The angle is zero for the last segment. A visualization of this theory is shown in figures 11.18 and 11.19.

$$\mu(a_0 - a) = \sum_{n=1}^{N} A_n sin(n\theta)\left(1 + \frac{\mu n}{sin(\theta)}\right) \tag{11.54}$$

In this equation, a is the angle of attack of the segment and a_0 the zero lift angle of attack, which is only the downwash angle of 1.9 degrees, determined in chapter 7. A_n are the coefficients which are to be determined. μ is defined in equation 11.55, where $\bar{C}_i$ is the mean geometric chord of the segment, which is equal for each segment if the taper ratio is 1 and C_{l_α} is the lift slope, which is 6.3 per rad.

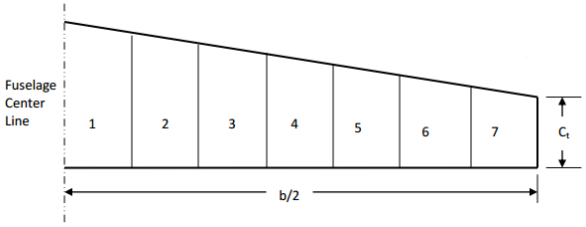

Figure 11.18: Dividing a tail into several sections [80].

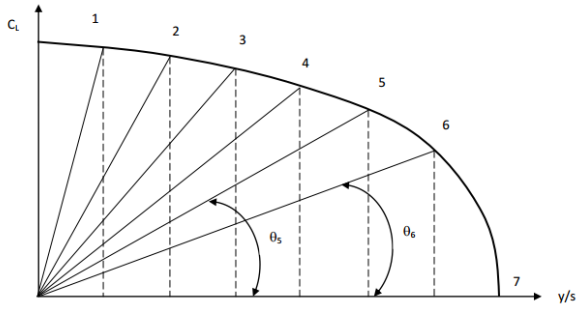

Figure 11.19: Angles corresponding to each segment in lifting-line theory [80].

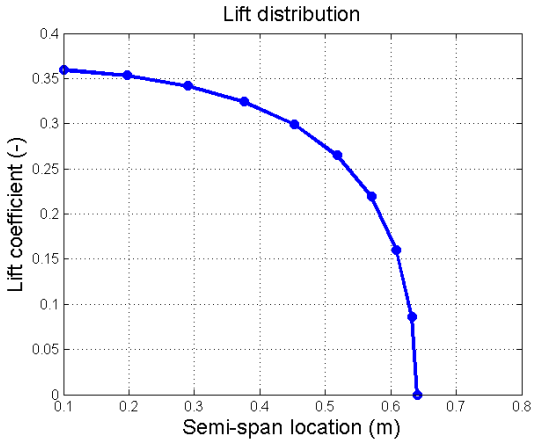

Figure 11.20: Lift distribution of the horizontal tail.

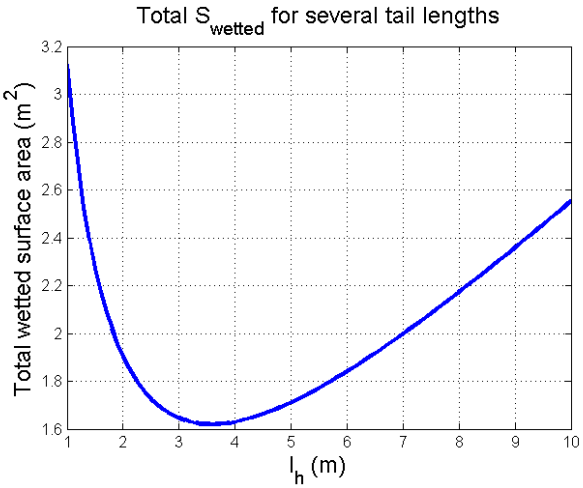

Figure 11.21: Selecting optimum tail arm.

$$\mu = \frac{\bar{C}_i C_{l_\alpha}}{4b} \tag{11.55}$$

The lift coefficient per segment can be determined with equation 11.56 and the final lift coefficient can be determined with equation 11.57.

$$C_{l_i} = \frac{4b}{\bar{C}_i} \sum A_n sin(n\theta) \tag{11.56}$$

$$C_{l_h} = \pi AR A_1 \tag{11.57}$$

This whole process will be iterative with the next steps, because the surface area and aspect ratio might change. It was desired that the final span of the horizontal tail will be wider than the fuselage, which is aerodynamically beneficial. Although this benefit was not accounted for during the calculations. The final lift distribution of the horizontal tail is shown in figure 11.20. The resulting lift coefficient is 0.309, using an aspect ratio of 4. This means that the required product of the tail length and the surface area is 1.46 m^3.

Optimum tail arm and surface area

The tail arm is defined as the location of the horizontal tail center of pressure to the H2Copter center of gravity. To maintain the longitudinal trim, one can for example use a large surface area and a short tail arm, or a small surface area and a longer tail arm. Both are capable to satisfy the trim requirement. In order to design the optimum configuration, the drag should be minimized. This can be achieved by minimizing summation of the wetted area of the tail boom and the tail. The equations to determine the wetted surface area of the tail boom and horizontal stabilizer are shown in 11.58 and 11.60 respectively with equation 11.59 showing the required volume. The tail will have a conical shape, which is common in the rotorcraft industry to have better aerodynamic properties, for example lowering the skin drag.

$$S_{wetted_{tb}} = \frac{1}{2} \pi D_{tb_{max}} l_h \tag{11.58}$$

$$V_{needed} = l_h S_h = 1.46 m^3 \tag{11.59}$$

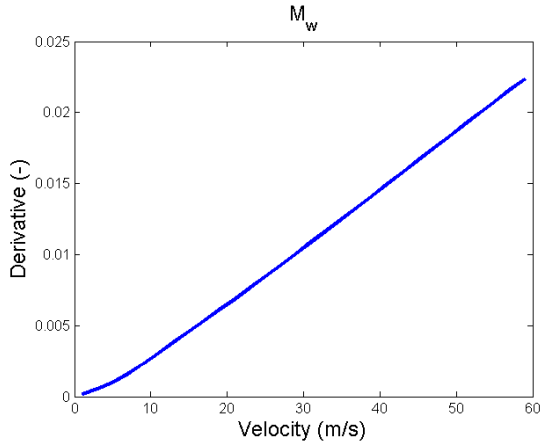

Figure 11.22: M_w derivative.

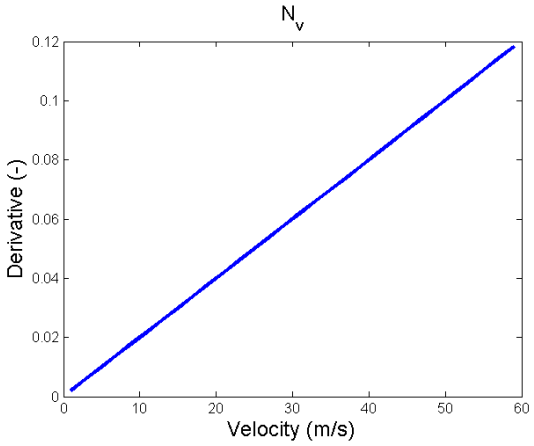

Figure 11.23: N_v derivative.

$$S_{wetted_h} = 2S_h = 2\frac{V_{needed}}{l_h} \tag{11.60}$$

In equation 11.58, one should first define the maximum diameter of the tail boom. This can be determined by applying the a analysis. This means that the stress along the tail boom is lower than the failure stress of the material used. The failure stress is determined to be 110 MPa (composite structure). A safety factor of 1.5 will be used. The stress calculation at the start of the tail boom can be done with equation 11.61. The moment required by the tail is 338 Nm. From EASA CS-27 regulation, this structure shall able to carry 3.5 times that load, due to gusts. This means that the tail boom will be designed for a bending moment of 1183 Nm.

$$\sigma = \frac{M_{tail}y}{I_{tb}} = \frac{M_{tail}R_{tb}}{\pi t R_{tb}^3} == \frac{M_{tail}}{\pi t R_{tb}^2} \tag{11.61}$$

This results in $R_{tb_{max}}$ being 0.072 m. With equation 11.62 and figure 11.21 one can determine the optimum tail arm by selecting the minimum total wetted surface area. The optimum tail arm can also be determined by differentiating equation 11.62, which leads to equation 11.63.

$$S_{wetted} = \frac{1}{2}\pi D_{tb_{max}} l_h + 2\frac{V_{needed}}{l_h} \tag{11.62}$$

$$l_{h_{optimum}} = \sqrt{\frac{4V_{needed}}{\pi D_{tb_{max}}}} \tag{11.63}$$

This resulted in a tail length of 3.65 m. This means that the surface area is 0.41 m^2 with a tail span of 1.28 m and a constant tail chord of 0.32 m, summarized in table 11.9. Might the surface area or tail arm be unrealistically large, an incident angle can be used to increase the tail lift coefficient. However this was not necessary.

M_w DERIVATIVE

During an unintended increase in speed, the rotor should flap back and produce a nose-up pitching moment. This stabilizing effect can only be achieved if the M_w derivative is positive. Therefore, a check should be made whether this derivative is positive during the entire flight envelope. This is indeed the case as can be seen in figure 11.22.

HORIZONTAL STABILIZER STRUCTURAL DESIGN

Now the dimensions are determined, the structure and material of the horizontal tail should still be defined. This will be comparable with that of the rotor. The main difference is the airfoil choice and the loads. To increase the life span, which is one of the project objectives, composite material will be used instead of metal assuring a longer life time due to better resistance to corrosion. The core material of the tail is Compaxx 700-X foam and for the skin and webs carbon fibre reinforced plastic. A load of 338 N times a safety factor of 3.5g

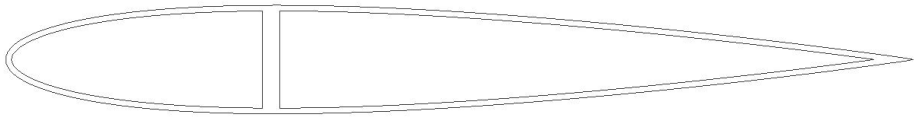

Figure 11.24: 3D representation of the horizontal stabilizer.

caused by the lift of the tail will be accounted for during the design process as well as a safety factor of 2 for the structure failure. Furthermore, one should also account for the load caused by the weight of the vertical tails at the tips, which will be explained later. Using Autodesk Inventor, this resulted in a skin thickness of 2mm and a web thickness of 5.0 mm. The final weight is 4.9kg. The design is shown in figure 11.24. The results are summarized in table 11.9.

11.9.2. VERTICAL TAIL SIZING

Here the vertical tail is sized for directional stability. The lateral trim conditions are already achieved during forward flight, since the yawing moment, rolling moment and side forces are zero. However, perturbations might still occur. This means that the derivative which notes the effect of a perturbation of the sideslip angle on the yawing moment is very important, since this phenomenon should be stable. This means that the H2Copter should always tend to yaw in the direction of the sideslip angle, recovering from a slipping flight. During forward flight, the vertical tail should provide zero lift, which means that the incidence angle is zero. For the same reason, the airfoil should be symmetric. NACA0012 will be used also for the vertical stabilizer. Furthermore, the location of the vertical stabilizer will be the same if the vertical stabilizer is not too high, which means that it should not interfere with the rotors.

The stability derivative to be designed for is N_v. This derivative should be positive for all flight speeds and have a minimum value. Many of lateral derivatives found were not valid when compared with references, however, N_v was valid as will be discussed in the next section. The derivative is dependent on the tail lift force and the tail length. The tail lift force is dependent on the lift coefficient, which is calculated with the lifting line theory. This theory uses the sideslip angle and therefore the side velocity v as input. From the book 'Helicopter flight dynamics' by Gareth D. Padfield [79] it can be noticed that the average derivative for 39m/s should be 0.0732. This can be achieved by changing the aspect ratio and the surface area. This is an iterative process, which resulted in a surface area of 0.75m^2 with an aspect ratio of 2. The decision was already made to split the total vertical tail in two parts, at each tip of the horizontal stabilizer one. The total span is 1.22m, which means 0.61m per tail. This value is below the height of the bottom rotor. The chord of the vertical stabilizer is 0.61m.The N_v graph is shown in figure 11.23

The structure of the vertical tail should still be defined. This is done by using the same structure as the horizontal tail, but with different dimensions. Furthermore, the load is different. A load of 450 N times a safety factor of 3.5g caused by the lift of the tail will be accounted for during the design process as well as a safety factor of 2 to prevent structure failure. This includes a sideslip angle of 15 degrees, which it should be designed for. Using Autodesk Inventor, this resulted in a skin thickness of 2mm and a web thickness of 6.0 mm. The final weight is 9kg. The results are summarized in table 11.9.

11.10. VERIFICATION AND VALIDATION

The derivatives actually provide the sensitivity of the model. It shows how much the forces and moment are affected by certain state and control variables. As described in section 11.8, the gains are very sensitive. A small change in value could have a huge impact on the responses.

The derivatives are important results before performing the stability analysis. Therefore it is necessary to validate these results. This is done by comparing the figure 11.10 with the graphs shown in the book 'Helicopter flight dynamics' by Gareth D. Padfield [79]. It can be concluded that many graphs coincide with the graphs shown considering the increase or decrease along the range of flight speeds and the range of possible values for the derivatives. The only exception are the derivatives Z_{θ_c} for both rotor one and rotor 2. For high flight speeds, the cyclic pitch angles have a larger influence on the Z force than expected. The reason should still be investigated.

Table 11.9: Stabilizers parameters.

Horizontal stabilizer	
Surface area	0.41 m^2
Tail length	3.65 m
Aspect ratio	4
Weight	4.9 kg

Vertical stabilizer	
surface area	0.75 m^2
Tail length	3.65 m
Aspect ratio	2
Weight	9.0 kg

Table 11.10: Analytical eigenvalues, period and half/double amplitude time for cruise speed.

Short period		
Eigenvalues (λ)	Period (P) [s]	Double / Half amplitude time ($T_{\frac{1}{2}}$) [s]
-1.8274	0	0.38
0.0929	0	7.46

Phugoid		
Eigenvalues	Period [s]	Double amplitude time (T_2) [s]
0.0633 + 0.2890i	21.74	10.95
0.0633 - 0.2890i	21.74	10.95

This validation process has also been performed on the derivatives of the asymmetric motion. As can be noted many of the derivatives of the H2Copter remain almost zero and also do not coincide with the increase or decrease along the range of flight speeds and the range of possible values for the derivatives of the validation data. One of the reasons is that there is no tail rotor in the H2Copter, which might have huge influences on the yaw rate derivatives, as well as the N moment derivatives. However, the other differences remain unexplained, which means that it can be concluded that the results are too unreliable for a proper further stability analysis.

Many of the calculations can be done by hand to verify. However, calculating the eigenvalues from a 4 by 4 matrix might be difficult. Therefore assumption will be made in order to simplify the model and make an approximation of the eigenvalues. The eigenvalues of the linearized model shown in table 11.5 will be verified with an analytical method.

For the phugoid the following assumptions are made that lead to equation 11.64:

- Assume that the contribution of the perturbation of velocity w to this mode is negligible
- Combining u and pitch q equations, neglecting X_q

$$\lambda\left(\lambda - \frac{X_u}{m}\right)\left(\lambda - \frac{M_q}{Iy}\right)\frac{Iy}{M_u} + g = 0 \tag{11.64}$$

For the short period the assumptions below lead to equation 11.65:

- Assume that the contribution of the perturbation of velocity u to this mode is negligible
- Combining w and q equations, neglecting Z_q

$$\lambda^2 - \left(Z_w + M_q\right)\lambda + Z_w M_q - M_w u_0 = 0 \tag{11.65}$$

The same parameters are calculated as in table 11.5 for comparison. This is shown in table 11.10

The largest difference can be noted in one of the poles of the short period. This pole is turned from negative to positive, noting an unstable motion. Furthermore the half or double amplitude time determined by the analytical method is not accurate enough. The determined period is accurate anough with just an error of 3.5%. This means that the assumptions about the velocities u and w were not accurate. However, without these assumtion, hand calculation would become too complicated. It can be verified that the period is correct and that the short period is non-oscillatory and the phugoid is oscillatory. Furthermore, the real term of the eigenvalues of the phugoid is lower than those of the short period in absolute values.

For the roll subsidence the assumption is made to only use the contribution of the roll motion, which leads to equation 11.66:

$$\lambda - L_p = 0 \tag{11.66}$$

For the spiral mode the assumption is made to only use the contribution of the yaw motion, which leads to equation 11.67. For the dutch roll the roll motion is neglected, this resulted in equation 11.68.

$$\lambda - N_r = 0 \tag{11.67}$$

$$\lambda^2 - (Y_v + N_r)\lambda + Y_v N_r - N_v u_0 = 0 \tag{11.68}$$

Table 11.11: Analytical eigenvalues, period and half/double amplitude time for cruise speed.

Subsidence roll		
Eigenvalues (λ)	Period (P) [s]	Half amplitude time ($T_{\frac{1}{2}}$) [s]
-0.0011	0	630.134
Spiral mode		
Eigenvalues (λ)	Period (P) [s]	Half amplitude time ($T_{\frac{1}{2}}$) [s]
0	0	0
Dutch roll		
Eigenvalues	Period [s]	half amplitude time ($T_{\frac{1}{2}}$) [s]
0.1961i	32.04	0
- 0.1961i	32.04	0

The same parameters are calculated as in table 11.6 for comparison. This is shown in table 11.11

As one may notice, the results of the numerical and analytical are very different. One reason is that the analytical model is too simplified, which is necessary to do hand calculations. However, the main reason is that many of the derivatives concerning the N moment and yaw motion are zero. This led to unreliable analytical solutions. The only conclusions that can be made is that the dutch roll is oscillatory and that the subsidence roll is probably stable. The gains are also validated with the possible range of gains as discribed in 'Helicopter flight dynamics' by Gareth D. Padfield [79], which is also discussed in section 11.8.

Furthermore, the results of the lifting line theory are validated with the method described in Prouty. Here it uses reference graphs to determine the lift slope. The product of this value and the angle of attack and downwash angle provides the lift coefficient. For cruise speed the method in Prouty resulted in a lift coefficient of 0.26, while the lift coefficient calculated is 0.3.

The conclusion can be made that the design is longitudinal stable after the implementation of a controller gain. More research should be done on the derivatives that did not fully coincide with literature. However, the values of the derivatives found in literature are for a conventional helicopter. This might lead to the different values. This might also be the case for the lateral derivatives. Furthermore, the derivatives required for the tail design did coincide with literature. The resulting dimensions for the stabilizers are in the range of the dimensions used in the industry. The conclusion can be made that the designed stabilizers are reliable.

12

FINAL DESIGN

To conclude the design part of this report, the following chapter will provide an overview of the complete H2Copter. In four sections, the combined subsystems will be presented. First, a three view drawing of the H2Copter is presented in 12.1. Next, a table of the class II weight estimation budget versus the actual weight budget will be shown in section 12.2. The third section, 12.3, will provide an electric block diagram of the electrical subsystems. Finally, a communication and data diagram will show the flow of data between the subsystems in section 12.4.

12.1. THREE VIEW DRAWING

The schematic front, side and top views of the final design are presented in figures 12.1 - 12.3.

12.2. COMPARISON TO CLASS II WEIGHT ESTIMATION

Table 12.1 shows the estimated weight budget next to the realized weight budget. As can be concluded, the realized MTOW is on budget. The difference is less than 1%, which indicates that the preliminary design has been performed correctly. It should be noted that some weight predictions are still rough and may be subject to alteration, due to changes in material composition in, e.g. the skin. Furthermore, there is no contingency for the added weight of fasteners, bolts and other small parts. However, the major components have been sized accurately, and the changes in MTOW are likely to be limited.

12.3. DC/DC CONVERTERS

The motor and its controller are selected such that they can be connected directly to the controller. The avionics and cooling pumps, however, only work at 24 V. The cooling fans require a 12 V supply. DC/DC converters are still required to provide the power for those components. Since they do not require a lot of power, the converters can be light.

There are three types of converters required to supply these powers. The SynQor MCOTS-B-600-31-HT converter [42] brings the fuel cell voltage down to an acceptable level. It simply scales the voltage with a factor of approximately 0.055, which is defined as low voltage (LV). Next, the SynQor MCOTS-C-28-24-HZ [42] converts the voltage to 24 V, or the SynQor MCOTS-C-28-12-HZ [42] provides a 12 V supply. No converter was found that could bring the fuel cell voltage to 12 or 24 V directly, so a two-step approach is required. Table 12.2 provides some data on the selected converters. It can be seen that they are lightweight components, but they do not provide enough power for all subsystems. Figure 12.4 shows how the converters have been connected. This figure only shows the power electronics; the communication and data handling lines are shown in figure 12.5.

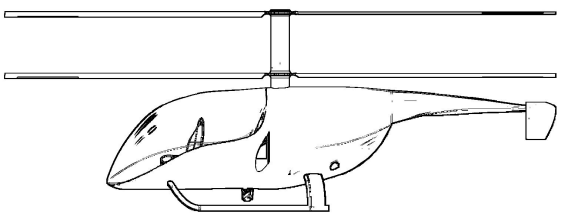

Figure 12.1: Schematic side-view

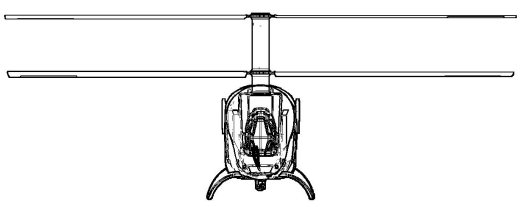

Figure 12.2: Schematic front-view

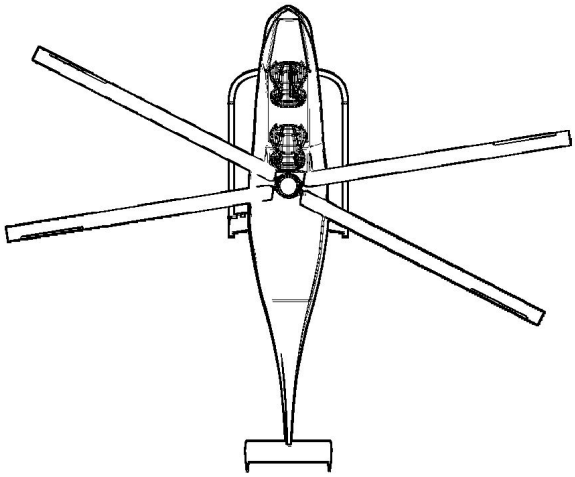

Figure 12.3: Schematic top-view

Table 12.1: Class II weight estimation budget versus realized weight budget with the computation method used.

Subsystem	**Class II** [kg]	**Realized** [kg]	**Means of computation**
Rotor blades	73	56.8	Autodesk Inventor
Hub and hinge	51	36	Autodesk Inventor
Stabilizers	8.6	13.9	Autodesk Inventor
Fuselage	90	128.1	Autodesk Inventor
Skids	64	36	Autodesk Inventor
Power plant	228	303	Statistics [36]
Fuel	16.1	17.4	Analytically [36]
Electric motors	54	87.7	Datasheet [29]
Fuel tank	259	164.4	Analytically [47]
System controls	9.7	0.7	Datasheet [42]
Avionics, instruments and cockpit control	24.5	17.1	Datasheet [73, 75–77]
Furnishing and Equipment	8.3	21.02	Datasheet [71, 72]
Payload	180	183	Requirements and datasheet [74]
Maximum take-off weight	1064	1065	

12.4. Communication and Data Handling

In this section the communication of the final design is addressed. In figure 12.5 the communication can be seen in a schematic manner.

In this figure two specific connections can be seen. The filled lines are data and the dashed lines are physical connections. With respect to the mid-term report the data recorder is added since this is a requirement in the CS 27 [67].

12.5. Packaging and Body

This section concentrates on the issue and effect of the packaging, placement of components, and the body, the cover surrounding most vital components of the helicopter.

12.5.1. Component Packaging

The process of packaging components to form the helicopter affects many fields. To push maneuverability to a good level a small mass moment of inertia is wanted, meaning to locate components as close to the center of gravity as possible. Since control forces get induced by the rotors, the center of gravity is preferred to lie close to the rotor centers. With that in mind the goal becomes to move the components with large inertia and mass close to the axis of the rotor blades. The pilot, hydrogen tank and the fuel cell position is of great influence

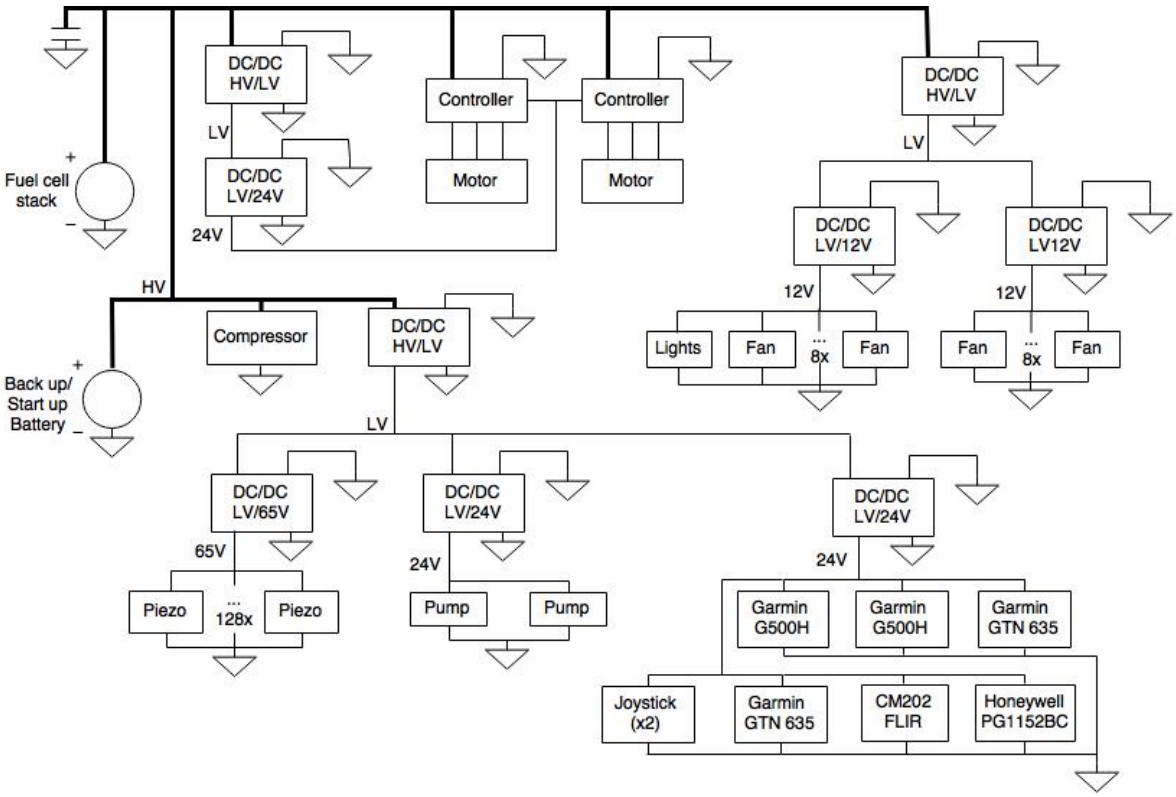

Figure 12.4: Electric block diagram

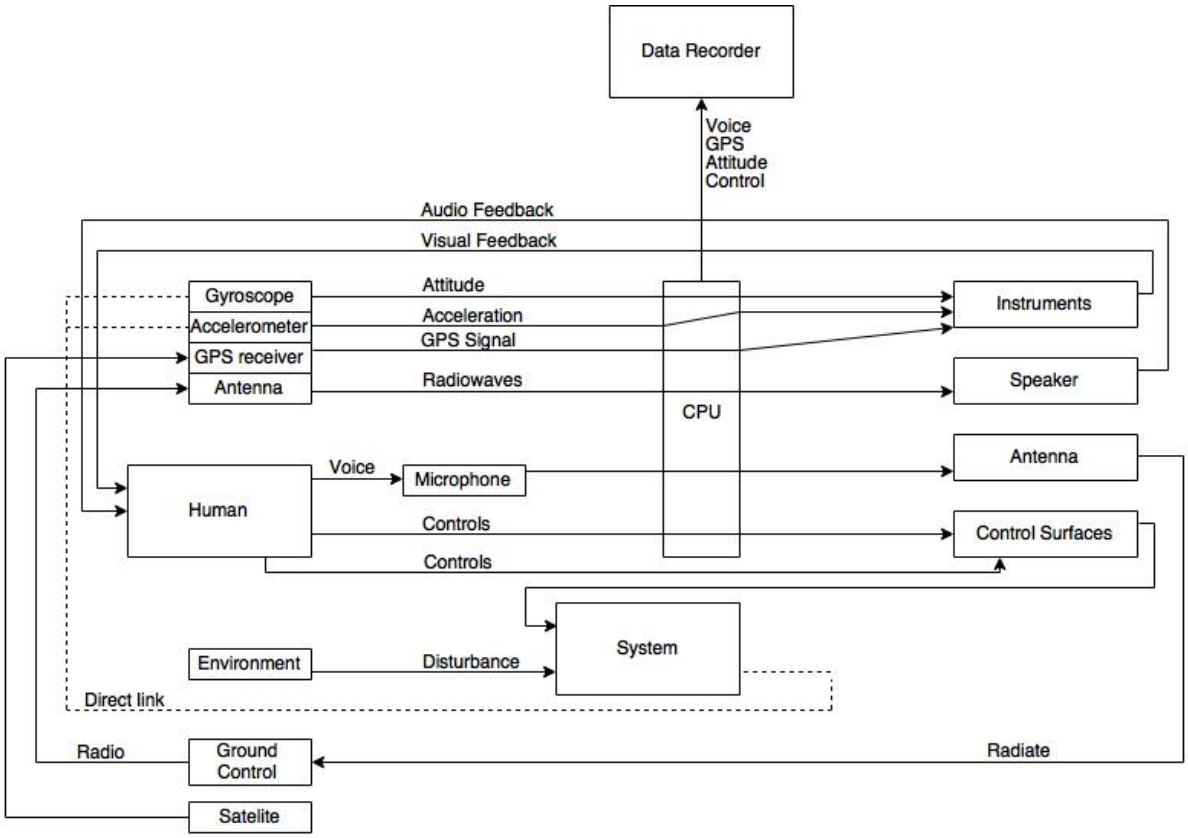

Figure 12.5: Communication and data Diagram

Table 12.2: Characteristics of the DC/DC converters that are used.

Converter	HV/LV	LV/24V	LV/12V
Type	MCOTS-B-600-31-HT	MCOTS-C-28-24-HZ	MCOTS-C-28-12-HZ
Input voltage [V]	440 - 700	16 - 40	16 - 40
Output voltage [V]	24.5 - 40.4	24	12
Maximum output current [V]	32.5	21	42
Maximum power [W]	1000	504	504
Efficiency [%]	94.9	94	94
Weight [kg]	0.137	0.139	0.146

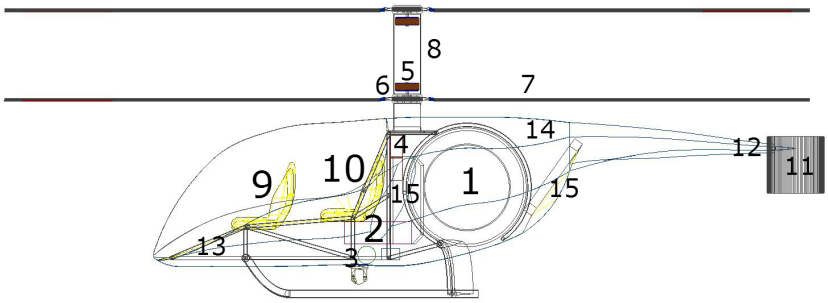

Figure 12.6: Schematic side-view, showing the component packaging of the rotorcraft

on the overall position. Given by the requirements the copilot is required to have a sufficient view towards the ground to perform best possible surveillance. Derived from that a tandem seat position is chosen where the copilot is seated ahead of the pilot. The hydrogen tank mounted close aft the cockpit area as well as the fuel cell mounted underneath the pilot position underlines the philosophy to generate a performance orientated packaging. To keep all components right in place, a structural support in form of a chassis follows.

Another affected field is the aerodynamics. Decreasing the frontal area of the rotorcraft increases its high speed efficiency due to decreased drag. Ruling is the hydrogen tank and the cooling unit. Whereas the tank purely consumes space, the cooling unit requires space and functional placing. Since the radiators only work when airflow is guaranteed, pressure fields around the rotorcraft have to be used to increase its performance. The main air inlet is thus place right and left aft the cockpit. The outlet on the rear enables a natural flow due to the pressure gradient from the side towards the lower pressure behind the rotorcraft. Nevertheless, fans mounted on the radiators guarantee a sufficient amount of airflow even in hovering phase where the pressure gradient around the body can be assumed to be zero.

12.5.2. Body

As described in chapter 10, the load carrying structure of the rotorcraft is designed to be a steel frame. Nevertheless components and pilots need to be covered for aerodynamic and protection reasons. The material of choice is glass fiber reinforced plastic, due to its lower cost and environmental impact in comparison to carbon fiber reinforced plastics. Even though the structure is defined as non load carrying, it has to be designed to withstand the aerodynamic forces during flight. The Plexiglas canopy is up to certification standards and covers the vision field of the pilots. A combined weight of 70 kg can be achieved.

Nr.	Component	Nr.	Component	Nr.	Component
1	Hydrogen tank	6	Gearbox	11	Vertical tail
2	Fuel cell	7	Rotor blades	12	Horizontal tail
3	Super charger	8	Hub	13	Chassis
4	Motor controllers	9	Co-pilot	14	Body
5	Motors	10	Pilot	15	Radiators

Table 12.3: Component list

Part III

Design analysis

13

FLIGHT LIMITS

In this chapter, some performance characteristics of the H2Copter are shown and discussed. First, dependance of performance on altitude will be evaluated in section 13.1. A flight envelope will be derived in section 13.2.

13.1. ALTITUDE PERFORMANCE

Reciprocating and turbine engines are known to lose performance with increasing altitudes. For the fuel cell stack on its own this is not the case, since its working environment is controlled, being at a temperature of 80° C and a pressure of 2 atmosphere. However, to control the pressure a compressor is necessary. When the altitude increases and the ambient pressure decreases, the compressor will require more power from the fuel cell stack. This power cannot be used to power the electric engines anymore, thus the maximum available net power available to power the engines will decrease with increasing altitude. Another limiting factor is the compressor motor, which has a power of 23.2 kW. Therefore, the required air flow might not be achievable due to the high pressure difference that has to be overcome, resulting in a lower airflow and a thus a lower power the fuel cell can deliver. This happens at an altitude of about 2500 m. The performance of the stack with reference to the altitude is shown in figure 13.1.

In figure 13.1 two different lines are drawn, the power required to hover and to climb at a rate of 900 fpm at different altitudes. It can be seen that the power to hover remains nearly constant with changing altitude, a surprising result. The power to hover will always remain beneath the available power, meaning that the power is not a limiting factor. However, at a altitude higher than 3750 m the collective of the lower rotor will be so high that the blade will stall at certain elements of the blade, causing a high loss in in lift unable to compensate for by the other rotor. Another limitation is the maximum altitude at which the helicopter can fly without being pressurized, but this is not taken into account in this analysis.

Another conclusion that can be drawn is that the powerplant will not be able to deliver the required power to the rotor to climb at a rate of 900 fpm. At sea level altitude it can provide 144.8 kW, which makes the helicopter climb at 4.27 m/s, or 840 fpm. At cruise altitude, 140.6 kW is available, which makes the climb rate a bit lower, 4.00 m/s or 787 fpm. Both values are calculated with a forward speed of 24.42 m/s, optimal for climb (as explained in chapter 7).

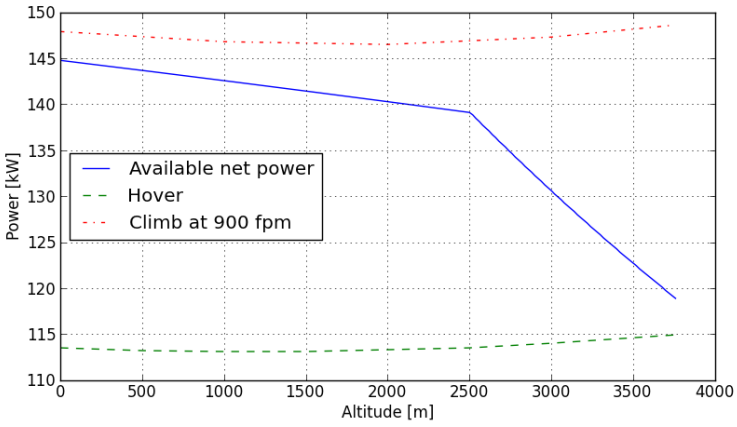

Figure 13.1: The power available and power required at different altitudes.

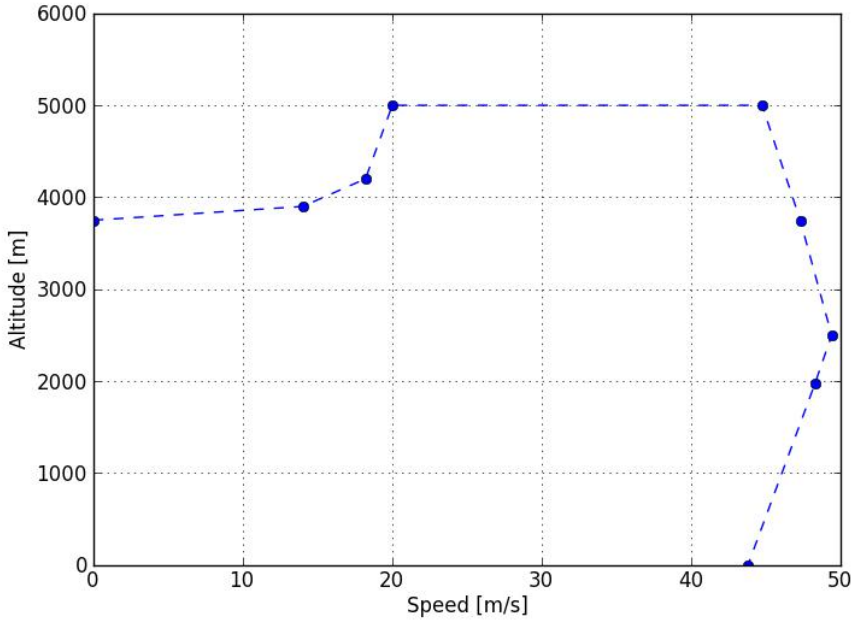

Figure 13.2: H-v diagram of the H2Copter

13.2. FLIGHT ENVELOPE

With the rotor computation programs described in chapter 7 the maximum speed is 48.3 m/s at cruise height, with a power available of 140.6 kW. At sea level it is 43.8 m/s with a power of 144.7 kW. The maximum and minimum speed at different levels are also calculated, which gives a flight envelope for the helicopter, shown in figure 13.2. The ceiling is set to 5000 m. Theoretically the H2Copter could go higher, but it also needs to be certified for these altitudes, which already go way past the requirements. Operational limits can be chosen from this envelope, which only gives an indication what the helicopter is capable of.

With a hover power of 113.5 kW at sea level, it can be calculated with the programs in chapter 8 that for this state a hydrogen flow of 2.05 g/s is required. If the pilot wants to hover for one minute, he will pay for that with either 66 seconds of surveillance time, or a decrease in range of 1.3 km. Especially the first one is a result to keep in mind, since hovering is not as bad for the performance as it was expected to be.

14

OPERATIONS AND LOGISTICS

This chapter deals with the systems and the infrastructure necessary to support the helicopter mission which have not been included in the design thus far. A wide range of topics will be covered in the following sections. Both on an operational as well as a tactical level, the systems, personnel and organization of helicopter surveillance will be discussed. On an operational level, the direct operating procedures of the H2Copter are analyzed. On a tactical level the organizational and logistical planning will be examined. Surveillance missions, similar to those currently flown by civil services such as police and firefighters, will be at the center of the following discussion. The operations and logistics will be reviewed from their position and compared to current practice. The Dutch helicopter police force, also known as air support & aviation police, will be taken as a benchmark.

In section 14.1, the operation bases, including take-off and landing are discussed. Maintenance of the helicopter will be treated in section 14.2, and pilot training in section 14.3.

14.1. OPERATING BASES

The H2Copter has been designed to be as capable as current helicopters and to land in the tight spots often required by operations. To prove that the H2Copter has the same flexibility when it comes to choosing take-off and landing area locations, the usability of the current designated areas needs to be assessed. The dimensions and weight of the H2Copter need to be compared to the limits imposed on the dimensions and weight of the currently used helicopters.

The lightest helicopter the air support & aviation police operates, is the Eurocopter EC-135. It has an MTOW of 2910 kg, an empty weight of 1455 kg, and a rotor diameter of 10.20 m [81]. The weight and the dimensions of the H2Copter fall within these constraints, which means that current take-off and landing locations are suitable for the new design. A quick check among the Dutch helipads and rooftop landing areas at e.g. hospitals, show that the H2Copter can even make use of these weight sensitive locations [82]. Thus, on an operational level, it seems the take-off and landing areas do not need to be altered to comply with the H2Copter. On a tactical level however, changes will have to be made, as will be discussed in the following paragraphs.

The EC-135 has a maximum range of 550 km, significantly more than the H2Copter, which has a range of 317 km. This might indicate that more bases are required to cover all areas of operation. However, when taking off from Schiphol airport, one of the main bases of the air support & aviation police, the maximum radius of the EC-135 far exceeds the borders of the Netherlands, and so does the range of the H2Copter. The operational radius of the H2Copter however, which has been dictated by the mission profile and has been set at 100 km, does not cover all of the Netherlands. Here, an important problem comes to light. Currently, there are no hydrogen refueling stations at airports or helipads in the Netherlands [82]. Every operating base should therefore be newly equipped with a refueling station that is compatible with the H2Copter. This greatly limits potential operating areas, as the H2Copter will not be able to refuel at every airfield.

New infrastructure will need to be designed and constructed that reaches from the raw material production to end use. Multiple supply chain options exist that have specific benefits and drawbacks. When it comes to supplying hydrogen at operating bases, there are two options. It can either be created on site, or it has to be transported from centralized production facilities. Hydrogen can be produced from electrolysis or from the reforming of hydrocarbon (HC) fuels. The former is the process of using electricity to separate water molecules into oxygen and hydrogen. The latter can be performed using several procedures. The preferred choice is the option that yields the lowest cost, assuming that the hydrogen availability of both options is equal. As the majority of fuel cell powered vehicles are automotive, a comparison with the capital and operational costs of automotive refueling stations is made. In 2013, the National Renewable Energy Laboratory performed a comprehensive study into hydrogen fuel stations in the Los Angeles area [83]. From this study, it can be concluded that current state reforming stations are significantly more expensive than transportation from a centralized production facility. At the relatively high demand of 100 kg of hydrogen per day, the capital cost (one time

investment cost) of installing a reforming station is estimated to be anything between 2.59 million to 3.18 million dollars. The delivery of compressed hydrogen to the operating base by truck is a cheaper solution, at around 2.22 million dollars. The cheapest solution is expected to be a mobile refueling station, costing roughly 1.0 million dollars. In the latter concept, the entire refueling infrastructure is mounted on a mobile platform. This platform has to refuel its reservoirs at centralized production sites, whenever the on board reserves are depleted. The total capital cost for a refueling installation with a capacity tailored to the Dutch air support & aviation police is not known. Due to the low demand from such operations, compared to the larger clientele of an automotive refueling station, it is difficult to predict what the effect of scale might be on the cost. If a 100 kg/day refueling station would supply fuel to the air support & aviation police only, more than five maximum range flights should be performed daily in order to use its full potential.

It should be noted that this section does not intend to give a full evaluation of possible hydrogen refueling options. Its aim is to indicate the financial challenges of establishing enough hydrogen refueling stations to keep performing standard operations. Operators of the H2Copter should consider sharing facilities with other hydrogen consumers. These could be automotive hydrogen vehicles, but also other operators such as larger airfields are of interest. Hydrogen is becoming an increasingly popular fuel for short range utility vehicles like forklift trucks [84], as well as for auxiliary power units (APU's) in commercial aircraft [85]. If the popularity of hydrogen as a replacement for fossil fuels keeps increasing, an early investment in refueling stations might be a profitable strategic decision, as stipulated in chapter 6.

One of the scenarios that may reduce costs of operating and maintaining refueling stations on several bases, is to keep a mixed fleet of helicopters. The most active bases would be equipped with the H2Copter, while some other remote locations would operate conventional helicopters with a longer range than the H2Copter. These conventional helicopters would then cover the areas that demand less aerial surveillance. This approach is not limited to application within the Dutch air support & aviation police, but may be used in many other countries that need a combination of short- and long-range surveillance helicopters.

The refueling process in itself is not very different from tanking current aviation grade fuels. Although, due to pressurization issues, the refueling time may increase. However, it is shown to be within reasonable bounds. The department of energy of the United States had set a target for 2006, of a refueling rate of 1 kg/min [86]. Analysis of refueling rates of the same year shows that these refueling rates are in fact achievable.

14.2. Maintenance

The H2Copter introduces some new technologies that change the maintenance procedures currently in place, while other maintenance routines can conveniently be kept. All systems that the H2Copter has in common with currently flown helicopters, can easily be maintained by the personnel and the facilities that are located at several airfields. These systems include the rotors, structure and some internal components like turbopumps or cooling systems. The major differences with conventional helicopters are the fuel cell propulsion system and the electric motors. Maintenance personnel will have to be trained to work with these systems, and their supporting facilities will have to be adapted. Unlike reciprocating and turbine engines, the fuel cell stack has no moving parts, which usually indicates less need for servicing and maintenance. It does have limited lifetime however, after which it will need to be replaced in its entirety. That means that there will have to be facilities to performs this replacement, which is relatively straightforward. Analysis of previously operated fuel cells has shown that the majority of maintenance needs to be performed on the supportive systems and power electronics [87]. As stated before, the knowledge and facilities to maintain the supportive systems e.g. compressors, valves pumps and radiators, are already available. According to the manufacturer, the electric motor does not need any maintenance during its service life. Taking everything into account, it can be concluded that maintenance of the H2Copter will not require major alterations to the currently existing facilities or personnel training.

14.3. Pilot training

The H2Copter has been designed with the current pilot training courses in mind. The pilot will have the same controls to his disposal as any other helicopter i.e. a collective and a cyclic. The envisioned customers are all experienced helicopter operators, with access to pilots and training facilities. Due to the dual control cockpit configuration, conversion training can be given by experienced H2Copter pilots to new pilots during training flights. That way, the new pilot can achieve his type rating for the H2Copter, necessary to legally fly this helicopter type. Initially, training locations will need to be set up that are operated by the manufacturer. At these

facilities, first-time users can be taught to handle the H2Copter. When a sufficient amount of instructors have been trained at these facilities, they can take over the training of new pilots at other locations. This approach has already been adopted at some helicopter manufacturers.

On an operational level, the pilots will have to work with novel technologies. Most notably, the powerplant with the servo flaps will have different responses to control inputs than the more conventional turbine or combustion engines with swashplate controlled rotors. However, there is no indication that servo flap controlled helicopters are inherently more difficult to fly. The response time of fuel cells to changes in required power might be different from what some pilots are used to. It varies with the fuel composition and internal environmental conditions of the stack [37].

15

SUSTAINABLE DEVELOPMENT

In the baseline report [10], six goals of sustainable development were described. These are repeated below.

1. Reduce the direct emission of polluting gases;
2. Reduce the direct emission of free particles;
3. Reduce the use of chemicals;
4. Reduce the amount of waste material;
5. Reduce the noise;
6. Reduce the environmental load of the supporting systems.

Because the fuel cell only produces water, the first two goals are met directly. This does not mean that there will be no emission related to the H2Copter: there are still emissions related to production and disposal. Also, the hydrogen needs to be produced and stored. A life cycle assessment was performed in section 15.1, to quantify the environmental load of the helicopter. The results of emmissions are stated in section 15.2. The life cycle assessment takes into account all six goals, except for the noise. This will be treated separately in section 15.3.

15.1. LIFE CYCLE ASSESSMENT METHOD

The approach is based on the approach that Johanning and Scholz have adopted [88]. This approach is used to perform a life cycle assessment on a conventional airplane. The method is adapted to be suitable for a hydrogen-powered helicopter. The life cycle assessment treats the design, production, operation and disposal of the helicopter. It calculates the emission of many substances on a passenger-kilometer basis, sorts them in different categories, and weights them. In this way, a single score can be obtained for the sustainability of the concept.

15.1.1. EVALUATION OF THE SCORE

In order to compare different emissions, the ReCiPe method [89] was adopted. This is a very broad method to evaluate sustainability. It uses a weighted sum of many types of emissions in order to determine a single score for the sustainability of a product. In this case, fifteen substances are considered. The emission per passenger-kilometer of substance i is indicated with x_i. Twelve midpoint categories are considered, as given in table 15.2. Midpoint scores in category j are indicated by MP_j. The method prescribes the characterization (weighting) factors $CF_{MP,ji}$ and units for all substances affecting a category. Units for the categories are also presented. The midpoint score can be calculated according to equation 15.1. The midpoint score is measured in equivalent units, that take into account the different effects of substances. As an example, it can be seen from table 15.2 that 1 g of CF_4 is equivalent to 7390 g of CO_2 eq. The midpoint categories can be combined into broader endpoint categories with the characterization factors $CF_{EP,kj}$ as given in table 15.1 according to equation 15.2. The endpoint categories are combined into a single score according to equation 15.3.

$$MP_j = \sum_{i=1}^{1} 5CF_{MP,ji}x_i \qquad (15.1) \qquad EP_k = \sum_{j=1}^{1} 2CF_{EP,kj}MP_j \qquad (15.2) \qquad SS = \sum_{k=1}^{3} \frac{EP_k W_k}{NF_k} \qquad (15.3)$$

There are three endpoint categories. Endpoint category k is indicated by EP_k. Damage to human health is measured in DALY (disability-adjusted life years), a measure in life year reduction due to disease. Damage to ecosystem diversity is measured in species lost. Damage to resource availability is measured in dollars. The midpoint scores have different orders of magnitude and importance. Because of this, the results have to be normalized by dividing through a normalization factor NF_k, and weighted with W_k. Normalization factors and weights are also given in table 15.1. The endpoint scores can then be combined into a single score SS.

Table 15.1: Endpoint categories and characterization factors [88]

Endpoint CF	Human health	Ecosystem diversity	Resource availability
Climate change	1.40E-09	7.93E-12	
Terrestrial acidification		5.80E-12	
Marine eutrophication			
Human toxicity	7.00E-10		
Photochemical oxidant formation	3.90E-11		
Particulate matter formation	2.60E-07		
Terrestrial ecotoxicity		1.51E-10	
Freshwater ecotoxicity		8.61E-13	
Marine ecotoxicity		1.76E-13	
Water depletion			
Metal depletion			7.15E-05
Fossil depletion			1.65E-04
Normalization factor	1.36E-02	9.17E-04	245
Weight	400	400	200

This is a powerful method, because all the characterization factors have been obtained scientifically [89]. The single score can be computed separately for different phases of the life cycle of the helicopter. This makes it possible to compare them objectively.

15.1.2. Evaluation of life cycle phases

From [88], it is found that different components of the life cycle cause different emissions. For all activities, one value is found indicating the extend to which the activity takes place. This is for example the energy in kWh that is required for engineering. This is converted to emissions by means of emission factors, given in table 15.3. Some activities have multiple values. Also, some emission factors can be used for multiple phases. An explanation of all the activities and their indicators is provided below.

Engineering

The design of the helicopter requires computers, which may use significant power. Johanning [88] states that an average office computer uses $E_d = 0.31$ kWh per day. With n_d the total number of engineering days, the energy required for the design of the aircraft follows from $E = E_d n_d$. n_d was estimated by dividing the total development cost by a cost of 240 USD per engineer per day, assuming 75% of the cost is spent on engineering. This is measured in kWh. The emission factors were obtained by looking at the current electricity mix on the power net.

Wind tunnel tests

When developing an aircraft, about 1000 wind tunnel testing days are required nowadays [88]. Using information on NASA test facilities, an average wind tunnel produces 18600 metric tons of CO_2 per year, equivalent to 50958 kg per day. The tunnel testing is measured by the amount of test days.

Test flights

For the certification of the helicopter, test flights are required. Johanning stated that 3100 hours of flight are required on average to test and certify an aircraft [88]. Furthermore, five test aircraft are required just for testing. The emission of flight testing is caused by the emission of flying for 3100 h, and the emission to produce and dispose five test aircraft. Test flights are not indicated in the table. Instead, the emission is obtained by scaling the lifetime emission of the useful fleet to 3100 flight hours and the production and disposal of five aircraft.

Table 15.2: Evaluated categories and substances [88].

Midpoint CF	Unit	Crude oil	CO_2	NO_x	SO_2	PM_{10}	Hg	CF_4	N_2O	CO	HC	Pb	O_2	H_2O	Fe	Al
Climate change	g CO_2		1					7390	298							
Terrestrial acidification	g SO_2			0.56	1											
Marine eutrophication	g N			0.039												
Human toxicity	g 1,4-DB						518184				0.115	15779				
Photochemical oxidant formation	g NMVOC			1	0.081					0.046	0.476					
Particulate matter formation	g PM_{10}			0.22	0.2	1										
Terrestrial ecotoxicity	g 1,4-DB						102				0.000039	0.07				
Freshwater ecotoxicity	g 1,4-DB						3.29				0.000034	0.0048				
Marine ecotoxicity	g 1,4-DB						593				0.00077	1.55				
Water depletion	m^3													0.001		
Metal depletion	g Fe											1.8			1	0.1
Fossil depletion	g oil	1														

Table 15.3: Emission factors used in the life cycle assessment [88]. Output is in kg emission.

Emission factors	Unit	Crude oil	CO_2	NO_x	SO_2	PM_{10}	Hg	CF_4	N_2O	CO	HC	Pb	O_2	H_2O	Fe	Al
Electric energy	kg/kWh	0.72	0.56		3.30E-03	1.42E-04										
Aluminium production	kg/t	7089	2539		8.7	1.62		0.019								1100
Composite production	kg/t	98500	83200		450	19										
Steel production	kg/t	27.5	1454		2.6	1.18	8.20E-05		0.08			1.90E-03			1100	
Production facilities	kg/seat		2640	1.97										23540		
Fuel cell production	kg/kW		43		0.25											
Hydrogen burning	kg/kg													9		
Hydrogen production	kg/MJ		0.00685		0.00002	0.000015										
Hydrogen compression	kg/MJ		0.01514701													
Hydrogen distribution	kg/MJ		0.00313													
Airport emission	kg/emp pkm		22100	14.7	122	49										

Material production (aluminium, composites and steel)

The production and processing of materials requires not only the materials itself, but also a lot of energy to process the raw materials into parts. Average values for the production and processing of aluminium, composites and steel were found [88]. The characterization factors for the material use are from [90]. These are based on the mass of the material that is actually extracted from the environment: this is equal to the total mass of the material in the aircraft, minus the mass that can be obtained by reusing the material when the aircraft's life has ended. Emissions were only found for aluminium, steel and carbon fiber reinforced plastics (CFRP). The production of CFRP causes the largest emission by far, while the production of steel is the least harmful for the environment. For simplicity, all composite materials and plastics are considered CFRP in this analysis. Similarly, all metals (except for steel) are considered aluminium. Unknown materials are also included in the aluminum category. The material production can be measured in tons of material.

Use of production facilities

The facilities that are not directly related to material production also use power. Johanning [88] provides the emission of the production facilities per seat of the aircraft produced. The emissions of the production facilities are thus quantified by the number of seats of the aircraft. Although these emissions are based on much larger aircraft, they are used as a first approximation for the emissions of the H2Copter.

Fuel cell production

It is important to consider the production of a fuel cell separately, since the fuel cell is specific to the concept. The adopted approach is similar to the approach for the material production. Pehnt [91] has found values for the emission caused by producing a fuel cell. These values are given per kW of fuel cell produced. They include the reuse of the platinum catalyst. This means that the disposal of the fuel cell is included, and cannot be considered separately.

Hydrogen burning

During the flight, hydrogen is burned. The only emission in this process is pure water in its liquid phase. Since this water is lost, it is accounted for in the lifecycle analysis. Hydrogen burning is very easily quantified by means of the mass of hydrogen that is burned, given in kg. The ReCiPe method does not have separate emission factors for water vapor. In accordance with [88], it is assumed that the average mission that will be flown consists of 80% of the maximum capability. This means that the average mission consists of 160 km of cruise flight and 24 minutes of surveillance.

Hydrogen production

Hydrogen is currently mostly produced as a side product in oil refineries. These refineries have very large emissions. Another method of producing hydrogen is by electrolysis. Since the power net is currently powered by fossil fuels, this would not be better for the environment than a conventional helicopter. Granovskii [92] has investigated the best method to produce hydrogen. It turns out that it is currently possible to produce 1 MJ of hydrogen with an equivalent emission of 6.85 g CO_2 by means of electrolysis with wind energy. The 1 MJ of hydrogen can be converted to a regular mass via the lower heating value of 119.96 MJ/kg. Koroneos [93] has found values for other equivalent emissions of hydrogen production. His analysis is less detailed, but in compliance with Granovskii's results. All these emissions are already given in equivalent units. The amount of hydrogen is measured in MJ, in compliance with the literature.

Hydrogen compression

The compression of hydrogen to 350 bar requires significant energy. Granovskii [92] has evaluated the energy required to compress 1 mol of hydrogen isothermally by means of equation 15.4.

$$\Delta E = \frac{RT_0}{\eta_{total}} \ln \frac{p_{max}}{p_{min}} \tag{15.4}$$

The emission of compressing hydrogen to 200 atm is provided as well [92]. Using equation 15.4, the assumption was made that this emission can be scaled with the natural logarithm of the pressure to be applicable to other pressures. The amount of hydrogen was again given in MJ.

Table 15.4: Disposal methods for different materials.

Material	Aluminium	Composites	Steel
Reuse [%]	2	5	56
Landfill [%]	24	48	21

HYDROGEN DISTRIBUTION

With the assumption that the hydrogen has to be transported over 300 km by a truck, Granovskii [92] found that 3.13 g of CO_2 is required for the transport of 1 MJ of hydrogen. The amount of hydrogen to be transported is again given in MJ.

AIRPORT OPERATION

Johanning [88] has made an estimation for the emission of the airport. His estimation includes passenger and luggage handling, as well as aircraft maintenance. This estimation is again based on airplanes; it is used as an approximation for helicopters. The data is based on the emission of Hamburg airport, and is scaled to obtain values per passenger-kilometer according to equation 15.5.

$$x_{pkm,i} = \frac{EF_i n_e mp}{N_{PAX,AP} d_f} p_{PAX,AP} \tag{15.5}$$

$n_e mp = 1619$ indicates the amount of employees of Hamburg airport; $n_{PAX,AP} = 13,000,000$ is the yearly amount of passengers of the airport. d_f is the distance per flight, and $p_{PAX,AP} = 0.95$ is the percentage of passenger mass compared to the total payload.

MATERIAL DISPOSAL (ALUMINIUM, COMPOSITES AND STEEL

In compliance with [88], it is decided that reusing the material can be implemented by reducing the amount of material required. This is included in the production calculations. Recycling and incineration are considered neutral, so these processes do not affect the sustainability score. Dumping the material on a landfill is considered as a direct emission into the environment; this emission is considered equal to the emission required to produce the material. Again, the values are given in tons of material used. Table 15.4 indicated values for the reuse and landfill percentages of the three materials aluminium, composites and steel.

15.1.3. SCALING TO PASSENGER-KILOMETER VALUES

For different means of transport, the best way to compare the emissions is by looking at the values per passenger-kilometer (pkm). This also makes it possible to look at the production and operational emission on the same scale. The conversion can be performed by dividing the obtained emissions by the correct pkm value [88]. With R the maximum range, p_d the fraction of the range that is actually flown, $n_{f,a}$ the number of flights per year, $n_{a,o}$ the lifetime of the helicopter in years and $n_{a/c,b}$ the number of aircraft built, equations 15.6 to 15.9 provide the distances and pkm values.

$$d_f = R p_d \qquad pkm_f = n_{PAX} d_f \tag{15.6}$$

$$d_a = n_{f,a} \qquad d_f = n_{PAX} d_a \tag{15.7}$$

$$d_l = n_{a,o} d_a \qquad pkm_f = n_{PAX} d_l \tag{15.8}$$

$$d_{l,b} = n_{a/c,b} d_l \qquad pkm_{l,b} = n_{PAX} d_{l,b} \tag{15.9}$$

Equations 15.6 to 15.9 indicate the total passenger-kilometer values per flight, year, operational life and for the whole fleet, respectively. Division by pkm_f is performed for the emissions of hydrogen burning, production, compression, and distribution. The material production, production facilities, fuel cell production and material disposal emissions are divided by pkm_l. The emissions due to engineering, wind tunnel tests and test flights are distributed over the entire fleet by dividing through $pkm_{l,b}$. The airport operation was considered in a different way; it is already given per passenger-kilometer.

Table 15.5: Results of the life cycle assessment.

	Value	**Unit** (per pkm)
Midpoint category		
Climate change	1.38E+02	g CO_2
Terrestrial acidification	1.84E-01	g SO_2
Marine eutrophication	5.46E-05	g N
Human toxicity	1.95E-03	g 1,4-DB
Photochemical oxidant formation	1.62E-02	g NMVOC
Particulate matter formation	1.04E-01	g PM_{10}
Terrestrial ecotoxicity	2.28E-07	g 1,4-DB
Freshwater ecotoxicity	7.49E-09	g 1,4-DB
Marine ecotoxicity	1.38E-06	g 1,4-DB
Water depletion	3.38E-01	m^3
Metal depletion	4.54E-02	g Fe
Fossil depletion	1.36E+01	g oil
Endpoint category		
Human health	2.21E-07	DALY
Ecosystem diversity	1.10E-09	species
Resource availability	2.25E-03	$
Single score	**8.79E-03**	points

15.2. Damage to Environment

The midpoint, endpoint and final scores are given in table 15.5. The single score is equal to 0.00879 points/pkm. In order to determine the improvement over a conventional helicopter, a conventional helicopter (non-coaxial and powered by kerosene) was sized specifically for this mission, following the approach used in the mid-term report [8]. It was determined that this helicopter would have an operational empty weight of 326 kg, a fuel weight of 33.2 kg (excluding reserve fuel) and a gross weight of 551 kg. Assuming the components would be made of the same materials as in the H2Copter, the ReCiPe method was followed again. This resulted in a single score of 0.0252 points/pkm. It is concluded that the use of hydrogen as a fuel source outweighs the reduction in mass. Over its entire life cycle, the H2Copter is found to have 65% lower emission than a comparable conventional helicopter.

Johanning [88] followed a similar process for the Airbus A320-200, and arrived at a single score of 0.0101 points/pkm. Thus, the H2Copter is found to be about 13% more sustainable than a conventional airplane. Considering that aircraft are known to be more efficient than helicopters, this result indicates that the design is relatively sustainable. Moreover, the A320 is designed for 60000 flight cycles and a range of 2797 km [88]. For such high values, the influence of production and disposal decreases.

Figures 15.1 to 15.3 provide additional insight in the contributors to the single score. From figure 15.1, it can be seen that damage to human health is the biggest contributor. Resource availability is also affected considerably, while ecosystem diversity is not affected much. Figure 15.2 shows that most midpoint categories have negligible effect. The majority of the single score is caused by climate change and fossil depletion. Particulate matter formation also has significant impact. The midpoint categories can be linked to the goals of sustainability. Climate change is linked to the exhaust of gases, while particulate matter formation is due to the emission of solid particles. The use of chemicals is reflected in the ecotoxicity categories: the effect of this is negligible (within the scope of the current analysis).

Figure 15.3 shows the contributions to the single score of all activities in the life cycle. The largest contributor is the compression of hydrogen. While high pressures are inevitable, it might be better to use a slightly lower pressure in order to increase sustainability, at the expense of a larger and heavier helicopter. Hydrogen production is a significant contributor. The use of composite materials also seems to have a very large contribution. This is due to the large carbon dioxide emission during production, and their limited recyclability. It is recommended to limit the use of composites, since aluminium and especially steel cause much lower emission. The fuel cell only has a small contribution. Due to the relatively small product series, the tunnel testing has a notable impact.

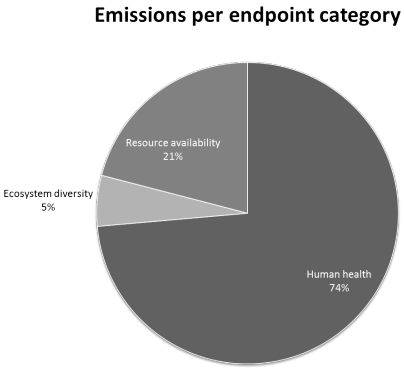

Figure 15.1: Intersection of wake from upper rotor with lower rotor.

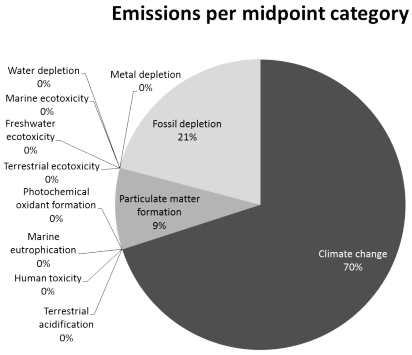

Figure 15.2: Wake area approximation on lower rotor.

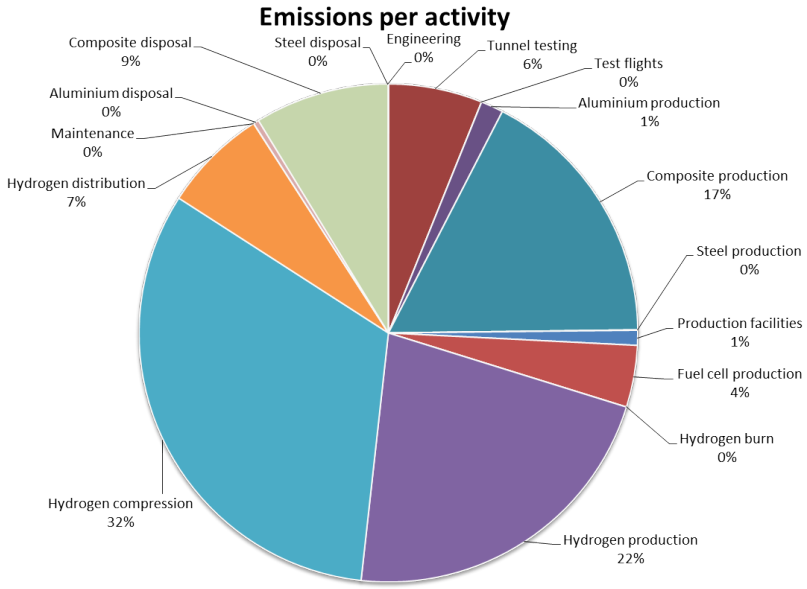

Figure 15.3: Contributions to the single score of the life cyle activities

15.3. NOISE

The life cycle assessment did not treat the fifth goal of sustainability: the reduction of the acoustic emission. This is because the noise is not accommodated in the ReCiPe method. This section will treat the noise of the H2copter separately.

In the mid-term report [8], a noise estimation for conventional helicopters was established based on statistics. The method is altered to be applicable to coaxial helicopters. Several noise sources are distinguished in order to make an estimation:

- Main rotor
  - Periodic
    - Loading noise
    - Thickness noise
    - Blade-vortex interaction (BVI)
  - Broadband
    - Self-noise

- Blade-wake interaction (BWI)

- Tail noise
- Engine noise

Loading noise is due to the creation of lift of the rotor. Azimuthally dependent loading causes aero-elastic vibrations in the rotor, which is the source of a periodic type of noise. The thickness noise is caused by an airfoil moving the air around it. As the name suggest, a larger thickness increases this type of noise. Thickness noise is highly directional: it is focused in the rotor plane. The measurement points for certification [94] are not in this plane, so thickness noise will be neglected.

The blade-vortex interaction is the most difficult type of noise to predict. When the tip vortices of a blade is crossed by the next blade, and impulsive load is exerted on this blade. This causes a periodic and very directional type of noise. The noise is generally directed downwards in two distinct beams, with one beam directed to the front and one beam directed to the rear side of the helicopter. BVI noise is generally considered the most annoying type of noise, because of its frequency.

The broadband noise is not focused at one particular frequency with harmonics. They are caused by turbulence, which leads to a more even spectrum. Especially the higher frequencies are dominated by broadband noise. The self-noise is due to the interaction of the blade with the boundary layer turbulence [95]. Blade-wake interaction noise is caused by turbulence in the wake. The wake may interact with the rotor itself. This type of noise is easier to predict than BVI, because the overall shape of the wake is predictable.

The noise from the tail essentially has the same sources as the noise from the main rotor, but its constituents have different magnitudes. For the tail rotor, the greatest amount of noise is caused by the interaction of the tail rotor with the turbulent wake. Further away from the main rotor, the wake becomes more turbulent. The interaction between the tail rotor and this turbulent wake is in some cases the largest source of noise. The coaxial helicopter is not influenced by this type of noise. It is assumed that the interaction between the tail plane and the wake can be neglected.

The engine of a helicopter can be very noisy, but its effect on the certification noise is small. For turboshafts, the noise is highly directional, and usually directed to the front and back. This is not picked up by the measurement microphones that are 150 m below the helicopter [94]. In the regression analysis, no statistically relevant effect of the power installed is found. Even installing more powerful engines on the same type of helicopter is not statistically linked to a higher noise level. Therefore, it is decided to neglect engine noise for this analysis.

15.3.1. Effect of tail rotor on noise

In order to quantify the effect of removing the tail rotor, the noise of the tail rotor on a conventional design is considered. In the mid-term report, noise estimations in the form of equation 15.10 were derived, with $N[dB]$ the noise level in dB, W the gross weight and D the main rotor diameter. The coefficients a, b and c are derived by means of regression analysis. No distinction was made between conventional tail rotors and ducted fans, even though it is known that ducted fans have decreased noise. In order to estimate the noise generated by the tail, the same analysis is performed separately for conventional tail rotors and ducted fans. The results are given in table 15.6.

$$N[dB] = a + b\log W + c\log D \tag{15.10}$$

Table 15.6: Noise estimations coefficients for helicopters with tail rotors and ducted fans.

Tail type	Measurement	a	b	c	r^2
Rotor	Ch. 8 Overflight	53.79	7.09	9.87	0.52
	Ch. 8 Take-off	59.36	2.33	20.99	0.59
	Ch. 8 Approach	61.62	8.46	1.49	0.61
	Ch. 11 Overflight	50.45	-2.40	40.99	0.51
Ducted fan	Ch. 8 Overflight	17.48	32.97	-44.85	0.50
	Ch. 8 Take-off	32.66	31.66	-52.39	0.61
	Ch. 8 Approach	38.12	22.32	-21.43	0.71
	Ch. 11 Overflight	-117.71	36.89	71.39	0.26

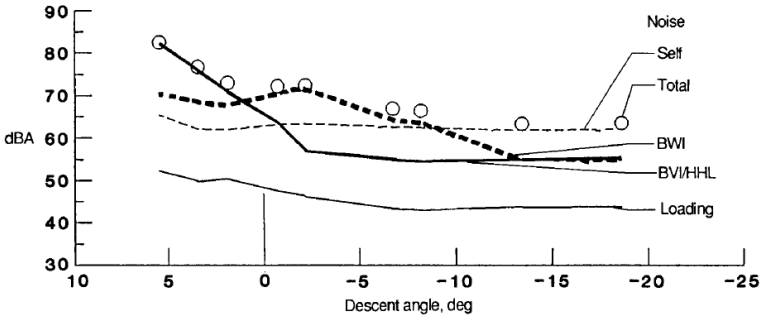

(b) Advance ratio = 0.172.

Figure 15.4: Noise breakdown of a conventional helicopter [95].

Making a distinction between tail rotors and ducted fans increases the quality of the regression. The chapter 11 noise for conventional tail rotors now has an acceptable value of r^2, although the negative b coefficient is an indication that the model is overfitting. Chapter 11 noise for ducted fans can not be estimated with acceptable accuracy. It is interesting to see that the numerical coefficient b for the effect of D changes sign for different types of tail rotor. An explanation is that a larger main rotor is statistically linked to a larger tail rotor [96]. This causes strongly increased noise for the conventional tail rotor, but not for the ducted fan, which apparently profits from a larger main rotor.

Tail designs with a ducted fan are often optimized to reduce noise. The blades are unevenly spaced to avoid harmonic loads. Because the duct of the ducted fan shields the radial direction, the noise from a ducted fan is more directional than the noise of a conventional rotor. The noise is directed outwards, and not picked up by the microphones below the helicopter. It is therefore acceptable to assume that the contribution of a ducted fan to the total helicopter noise is negligible with respect to the noise generated by the main rotor. With this assumption, the estimation method for the ducted fan-equipped helicopter can be used as a baseline for the coaxial configuration.

15.3.2. Correction for coaxial configuration

The configuration with two rotors has different acoustic characteristics than a conventional helicopter because of interference between the two rotors. Due to the non-linearity of the prediction equation, modelling the helicopter as two isolated rotors yields a severe underestimation of the loads.

Brooks [95] has quantified the noise levels of the remaining sources separately as a function of the descent angle (downwards positive). This result is visible in figure 15.4. It can be seen that during descent, BVI becomes the dominant noise source. For steady flight and moderate climb, BWI causes most of the noise, while self-noise is dominant during steep climbs. These results are in given in dBA, while the chapter 8 noise is measured in EPNdB. Computing the noise levels in EPNdB requires arrays of noise levels measured from different position, so a conversion is not possible. It is assumed that the figure is also valid for chapter 8 noise.

The noise measurements for overflight are performed at a constant altitude of 150 m. The approach path is defined to have a 6° descent angle, and is followed at the forward speed for maximum climb rate [94]. For the take-off procedure, maximum certified climb rate must be achieved during the noise measurements. These three measurement sets are characterized by different skew angles. Table 15.7 provides the noise breakdown during the three flight phases of interest. The noise fractions are used to determine the contributions to the baseline noise prediction. These contributions are altered separately to include the effect of the coaxial configuration.

Because loading noise is not directly related to the wake, the assumption is made that this type of noise is unaltered by the coaxial configuration. In this case, the rotor is considered equivalent to a single rotor with two blades.

Kim [97] has shown that the wake of a coaxial rotor has increased vorticity. His wake geometry is shown in figure 7.25. Since the size of the vortices increases approximately by a factor 2, it is assumed that BVI noise increases by a factor 2.

Self-noise is caused by the blade itself, a coaxial rotor with two blades should have the same effect as a single rotor with four blades. For BWI, it is expected that there is a difference. Using equation 7.10, the wake overlap

Table 15.7: The three flight phases and noise breakdowns for a conventional helicopter.

Condition	Overflight	Take-off	Approach
Descent angle [deg]	0	-11	6
Skew angle [deg]	82.0	72.8	68.1
Overlap area [m2]	7.1	35.2	41.5
Noise fractions [-]			
Loading	0.0048	0.0086	0.0009
BVI	0.2402	0.1081	0.9225
Self	0.1516	0.5416	0.0184
BWI	0.6034	0.3417	0.0582

Table 15.8: Noise breakdown and noise limits of the H2Copter.

Condition	Overflight	Take-off	Approach
BVI	2	2	2
BWI	1.056	1.276	1.326
Noise [EPNdB]			
Loading	51.4	58.0	55.0
BVI	71.5	72.0	88.0
Self	66.4	76.0	68.0
BWI	72.7	75.1	74.2
H2Copter total (limit)	75.7 (82.3)	79.5 (84.3)	88.2 (87.3)

area is estimated. It is assumed that this area is the only region where the upper rotor causes BWI on the lower rotor. This area is added to the total area of both rotors to determine a scaling factor for the BWI noise. Because of the different overlap areas, this factor is different for the three flight phases. With these four corrections, the final noise prediction is made. The noise breakdown of the H2Copter is shown in table 15.8.

The removal of the tail has made it possible to meet the requirements on overflight and take-off noise with great confidence. During the BVI-dominated approach phase, the increase in BVI cancels the removal of the tail. Because of this, the analysis shows that the requirement on approach cannot be met. The limits in table 15.8 include the 3 dB margin on certification requirements that was adopted in the baseline report [10]. Certification requirements are all met by the H2Copter, so the failure to meet this requirement is not critical. A possible easy solution to reduce the noise is to reduce the main rotor angular velocity during approach. This will increase the power required, but the current design has some excess power.

16

RETURN ON INVESTMENT

The following chapter presents an overview of the expected costs and revenues throughout the development and manufacturing of the H2Copter. The goal of this chapter is to give an indication of the expected production volume, selling price and market share, necessary to reach a break even point within the production lifetime. Using life cycle assessment methods, and cash flow visualizations, an insight will be provided into the viability of the H2Copter on the helicopter market.

In section 16.1, the method will be explained and in section 16.2, the results will be given.

16.1. METHOD

The first step in the return on investment analysis, is to identify the key elements that drive the costs of the project. The project encompasses all aspects of the design, testing and production of the H2Copter. Little data is available on the exact cost of previous helicopter development. However still, some statistical research has been done into military helicopter projects. Using these findings, an estimate has been made of the total costs throughout the development and the production of the H2Copter. The costs were split into development and production costs.

First, the costs of individual parts of the H2Copter have been researched. These include the avionics, frame materials, and electric motors among others. Then, using [98], the manufacturing costs for the subassemblies were estimated. Using the combined cost of the parts and manufacturing, the complete unit production cost was derived. The total development cost has been estimated to be 120 times the unit production cost. This estimate is taken from [99]. Next, the revenues of selling the H2Copter were estimated. Using the market analysis performed in [8], an annual production rate was established. Combined with a projected production lifetime, i.e. years that the H2Copter will be produced, the profitability of the concept was established. In these calculations the time-value of money was taken into account. That is, the future value of money spent earlier. Equation (16.1) gives the relation between the future value F in \$, the current value (principal amount) P in \$, the interest rate i in %, and n, the number of years that have passed since the principal amount was deposited.

$$F = P \cdot \left(1 + \frac{i}{100}\right)^n \tag{16.1}$$

For each year between the start of the project and its termination, the net cash flow was established. For each year, the future value of that cash flow, negative or positive, was converted to the value at the end of the production lifetime. The total profit of the project was obtained by a summation of these future values.

16.2. RESULTS

In table 16.1, a cost breakdown is shown for the sub-assemblies of the H2Copter. Labor has already been included in the calculations. The listed sub-assemblies are different than those listed in the Class II weight estimation. This is due to the method used in [98]. Here, the parts of the helicopter are grouped together differently than in [9]. However, both lists consist of the same parts.

The costs of individual parts have been obtained through various methods. Some where estimated from similar helicopters e.g. the gearbox. Others were directly available of the shelve, with prices given by the supplier, e.g. the motor controllers.

The results that are presented in the rest of this section are based on the predicted production rates from the Mid Term Report [8]. It is expected that the demand for the H2Copter will be such that 50 helicopters will be delivered per year. The time span for production is estimated to be 30 years. Production will start in 2020 and will possibly terminate in 2050. The termination date has been chosen because of the unpredictability of improved propulsion technologies that might be developed. Until that year, it can be assumed that hydrogen

Table 16.1: Production costs per component

Cost contributor	**Cost** [$]
Airframe	124,246
Powerplant	60,641
Rotor	53,666
Gearbox	10,000
Avionics	100,718
Total	349,271.00

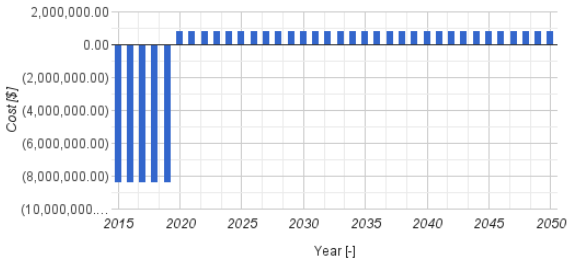

Figure 16.1: Overview of cash flows during project lifetime.

Table 16.2: Evolution of selling price

Selling Price (Mid Term Report) [$]	333,118
Selling Price (break even in 2050) [$]	381,490
Relative difference [%]	14.52

fuel cells will provide the best performance, compared to any other sustainable powerplant available on the market. However, with increasing interest from various industries, research into improved forms of energy storage might change the landscape. Therefore, whether the production of the H2Copter should be extended beyond 2050, depends on the competitiveness of hydrogen fuel cells in the future.

In the following step, a timeline of cash flows is constructed. The predicted development costs have been spread out over 5 years, prior to the start of production. Furthermore, an interest rate of 1% has been assumed, already corrected for inflation. This interest rate has been kept constant for all years and it is based on U.S. government long term bonds [100]. As the production cost of the H2Copter is already higher than the projected selling price of $333,118 [10], the profit margin must be kept low. If not, a high selling price might scare off potential customers. Using the cash flow timeline, the minimum profit margin was obtained to break even. That means that enough revenue is produced to overcome both the production costs as well as the development costs. It was found that a minimum profit margin of 8.45% must be incorporated in the selling price. In that scenario, the project will break even in 2050. All results have been summarized in figure 16.1 and table 16.2. A profit margin higher than 8.45% will result in a net profit at the end of the production period, if enough H2Copters are sold on an annual basis.

In conclusion, within the expected production period, the H2Copter can turn a profit. Although the selling price will be higher than anticipated in the MTR, the resulting profit margin is reasonable, and the difference with the MTR not too large. Of course there are some uncertainties in the predictions shown here. Especially the production rate may vary significantly. As stated before, the current value is based on the Robinson R22; a relatively light and simple type of helicopter. On the other hand, with the necessary updates to the H2Copter, the production might be expanded beyond 2050. In that scenario, the development costs will be spread out over a greater number of H2Copters, reducing the selling price.

17

RISK ANALYSIS

The risk of the design will be evaluated using a Failure Mode and Effects Analysis (FMEA). An FMEA is an analysis performed during the development or manufacturing of a product and will try to find the weaknesses of the design before it reaches the customer. The FMEA analysis can be divided into two levels: a System FMEA, which can be found in table 17.2, assessing the risk of the system itself and a Design FMEA, which can be found in table 17.3, assessing the risk of subsystems and components.

An FMEA is made as follows:

- Find the potential failure modes
- Identify the effects and the severity of failures on the system or end users
- Make a risk ranking
- Propose and perform corrective actions, priority goes to problems with a higher risk ranking

Table 17.1 will provide a risk ranking, critical risk can be distinguished from others. The criticallity of a risk is determined multiplying the severity (SEV), occurrence (OCC) and the detectability (DET) to come to the risk priority number (RPN). Peak risks are marked in the tables. Some general risk mitigation techniques are included.

Table 17.1: Scaling of severity, occurrence and detectability

Category (Product)	Criteria: Severity of Effect (Effect on Product)	Rank
Failure to Meet Safety or Regulatory Requirements	Potential failure mode affects safe operation or regulatory requirements, without warning	10
	Potential failure mode affects safe operation or regulatory requirements, with warning	9
Loss or Degradation of Primary Function	Loss of primary function	8
	Degradation of primary function	7
Loss or Degradation of Secondary Function	Loss of secondary function	6
	Degradation of secondary function	5
Annoyance	Item operable, but with annoyance noticed by >75% of customers	4
	Item operable, but with annoyance noticed by 50% of customers	3
	Item operable, but with annoyance noticed by <25% of customers	2
No Effect	No noticeable effect.	1

Opportunity for Detection	Likelihood of Detection	Rank
No detection opportunity	Absolute Uncertainty	10
Not likely to detect at any stage	Very Remote	9
Post Design Freeze and prior to launch	Remote	8
	Very Low	7
	Low	6
Prior to Design Freeze	Moderately	5
	Moderately High	4
	High	3
Virtual Analysis Correlated	Very High	2
Detection N/A; Failure Prevention	Amost Certain	1

Likelihood of Failure	Criteria: Occurrence of Cause	Rank
Very High	New technology/new design with no history.	10
	Failure inevitable with new design, new application, or change in operating conditions.	9
High	Failure likely with new design, new application, or change in operating conditions.	8
	Failure uncertain with new design, new application, or change in operating conditions.	7
Moderate	Frequent failures associated with similar designs or in design testing.	6
	Occasional failures associated with similar designs or in design testing.	5
	Isolated failures associated with similar design or in design testing.	4
Low	Only isolated failures associated with almost identical design or in design testing.	3
	No observed failures associated with almost identical design or in design testing.	2
Very Low	Failure is eliminated through preventative control.	1

Table 17.2: System FMEA table

Item	Function	Potential failure mode	Potential effect of failure	SEV	Potential cause of failure	OCC	Current design Controls (Prevention; Detection)	DET	RPN	Recommended actions
H2Copter	perform surveillance mission	obstructed view of crew	unable to do proper surveillance	8	issue not taken into account during design	1	tandem configuration large canopy	1	8	
		limited performance		9	power train-, energy storage-, control- failure	2	safe design, redundant systems	4	54	flight crew training to evaluate these situations
	guarantee flight safety	insufficient cockpit reinforcement	crew injured	9	unexpected load cases	4	cockpit design according to regulation load cases	4	144	perform tests
		unable to perform autorotation	uncontrolled flight crash after engine failure	10	control problems after engine failure, blocked rotor	2	fail safe and redundant controls (piezos)	3	60	detailed testing of control systems
	guarantee flying quality	becoming unstable during flight	loss of control, high workload on pilot	9	helicopter damage, unexpected flight conditions	3	stability and control augmentation system SCAS	4	108	detailed flight tests, simulate all possible flight conditions
		limited controllability		9		4	redundant controls (piezos)	4	144	check interaction with SCAS
	minimize emissions	violating limitations	impossible to certify, no permit to fly	8	noisy design, polluting development or manufacturing	3	sustainable design, no gas emissions, reduced noise	1	24	
	flying required flight profile	unable to perform vertical take-off	unable start mission	7	propulsion system-, energy system-, rotor- failure	2	Performance computations and simulations, monitoring of systems, maintenance,	2	28	test over long life time of design
		unable to climb	unable achieve sufficient altitude to perform mission	7		2		2	28	
		limited range	unable to reach or return form mission location	7		3		2	28	
		limited endurance	limited surveillance time	7		3		2	14	
	comply with EASA CS27	violating regulations	no permit to fly	9	inattention during design phase	1	compliance matrix check if requirements are met	1	27	

Table 17.3: Design FMEA table

Item	Function	Potential failure mode	Potential effect of failure	SEV	Potential cause of failure	OCC	Current design Controls (Prevention; Detection)	DET	RPN	Recommended actions
Rotor	provide lift	loosing lifting capabilities	potential crash situation	9	rotor impact	1	checking distance between 2 rotors and between rotor and fuselage	2	18	increase distance between parts if necessary
					rotor fatigue	3		6	162	regular inspections
	provide control	jammed or malfunction of controls	uncontrollable flight	9	impact, extreme flight conditions	2	Evaluate entire mission and possible extreme situations	2	36	
electro motor	provide power and transfer to rotor	overheating	motor failure, auto rotation mode required	9	cooling failure	2	reliable cooling system	4	54	additional tests
		Operation outside power limits		9	controller failure	2	reliable controller	3	36	
fuel cell	converting hydrogen into power	fuel leakage	reduced endurance because of fuel leaking, power loss	8	fatigue, system failure	3	reliable systems	3	72	redundant systems and regular inspections
		system cut	power loss	9	by electricity or compressor failure	2	safe electricity network	2	36	more redundancy in electricity circuit
fuel tank	hydrogen storage	carbon tank rupture	loosing fuel, might explode when in contact with high temperatures	8	fatigue of tank	2	safety factor on tank design	4	64	fatigue testing
cooling system	cooling of power train systems	overheating	power cut, motor failure, autorotation mode required	9	not enough air intake,	4	overheating is a critical point of the design, huge cooling systems are installed	3	108	maybe even more cooling is needed in certain extreme situations
motor conroller	provides input to motor	failure or malfunctioning of the system	motor damage which can lead to a power cut, uncontrolled fligth	9	error in the system, bad design	1		1	9	
		operating outside power limits		9	fuel cell delivering too much power	2	implementing of protective devices	2	36	
converters	provide correct power to motors	operating out of it's power limits	motor damage which can lead to a power cut	9	the input power is to low or too high	2		2	36	
structure	provide a solid frame for components and crew	overstress of structure	helicopter looses structural rigidity	9	impact, fatigue	1	strong frame with safety factor	1	9	
	provide crew visibilty	blocked view	decrease of surveillance capabilities	8	bad design	1	already taken into account from the beginning of the design	1	8	
	component protection	skin or frame damage	damage of components	8	impact or fatigue	1	smart packaging of compontens	1	8	careful handling and regular inspections
empannage	provide horizontal and directional stabiltiy	damage to tail	uncontrollable flight, helicopter out of balance	8	impact, fatigue, extreme turbulence or flight manoeuvres	2	strong construction with safety factor	4	64	crew training, regular inspections

18

RAMS CHARACTERISTICS

RAMS is an acronym for **R**eliability, **A**vailability, **M**aintainability and **S**afety. The characteristics for the H2Copter concerning these topics are explained in section 18.1 for the reliability, 18.3 the availability, the maintainability in section 18.2 and finally the safety in section 18.4.

18.1. RELIABILITY

The reliability of the design should be determined in order to define which subsystems should be designed with extra safety and which subsystems need extra maintenance. Sometimes, new techniques should be developed in order to increase the reliability. A study has been performed by NASA [101] to determine the relative failure rates of several subsystems in helicopter, which are shown in table 18.1. Together with the possible means of failure it is determined on how these problems are applicable on the H2Copter.

PROPULSION SUBSYSTEM

- **Fuel control problem:** Contamination from the actuating media or from the fuel itself, wear on moving elements, fatigue failure and maladjustment;
- **Fuel governor problem:** Rpm drop, torque and temperature variations;
- **Compressor failure:** Corrosion/erosion, blade/disk fatigue, diffuser cracking and leakage, compressor wear and cracking, variable stator and bleed failure;
- **Engine and accessory lubrication system failures:** Leakage of pumps, coolers and filters
- **Fuel pump spline:** Wear on fuel pump splines;
- **Turbine failure:** Nozzle band cracking. nozzle support structure wear/cracking, nozzle erosion/burning/sulfidation;

At first some failure probabilities can be removed from this list, simply because they are not present in the helicopter. For the hydrogen propulsion system no fuel govenor, fuel pump or turbine is needed. This gives a huge advantage compared to conventional helicopters since propulsion is one of the main causes of failure. With the use of hydrogen propulsion systems the fuel control problem is improved a small amount because of the absence of any moving parts. The compressor is still being used for compressing air for the fuel cell, which means no change for this part. The electric motors are highly reliable compared to turbine engines, so this will not have a big impact on the reliability of the propulsion system.

AIRFRAME SUBSYSTEM

- **Airframe skin and structure cracking:** High localized vibration and pulsating air loads due to rotor downwash on top surfaces, load concentrations at door/landing gear/tailboom/engine attachments and

Table 18.1: Relative failure rate of the subsystems [101]

Subsystem	**Relative failure rate** (%)
Propulsion	35.3
Drive	13.9
Rotor	12.2
Airframe	19.9
Landing gear	9.4
Fuel	5
Hydraulics	4.1

maintenance originated damage;

- **Small hardware (hinges, latches, rivets, screws) loss or failure:** Vibration induced failures, maintenance damage, manufacturing tolerance variations that cannot be applied without damage to fasteners;
- **Metal skin unbending:** Manufacturing/processing methods have been at fault, some hygroscopic bonding materials have been used, attachments are not sealed, mechanical failure;

The airframe as well as the small hardware failure probability does not change for the H2Copter, since it has a typical steel frame. The failure probability due to vibrations may be a bit lower, since no reciprocating or turbine engine is present to cause additional vibration. Obviously, the vibrations due to the rotary wing remain.

Drive subsystem

- **Transmission bearing spalling:** Unanticipated loads, inclusion of flaws, misalignment in assembly, contamination of the lubricant;
- **Tail rotor transmission mount cracking:** High vibrations;
- **Transmission housing:** Cracks in the attachment of the transmission;
- **Hanger bearing failure:** Does not provide enough axial and angular freedom for shaft deflection;
- **Gear scuffing and spalling:** surface distress phenomena;
- **Drive shaft spline:** Wear of a spherical spline used in each of-the two flexible couplings of the drive shafting from the engine to the main transmission;

Because of the concept of both electric motors in the rotor hub, most transmission lines are left out of the powertrain. A single stage gearbox is placed directly between the rotor and the electric motor. From the above list of possible failures, this is the only one that remained an issue.

Rotor subsystem

- **Blades failure:** Cracks and corrosion;
- **Hub and swashplate support failure:** Cracking, corrosion and bearing in components of the rotor hub and swashplate;
- **Rotor hub bearing failure:** pitch-change bearings and teetering-hinge bearings;
- **Tail rotor grip bearing failure:** Less retention against centrifugal force;
- **Main rotor mast:** Corrosion occurrence;
- **Rotor hub seal leaks:** Leaking of oscillating seals in the rotor hub causes less leaking of the oil for the main rotor hinge-bearing lubrication;

Since the H2Copter is a coaxial rotor, the failure probability for the blades is quite high. The lack of a swashplate rules out another probable cause of failure. Furthermore, the vehicle does not possess a tail rotor, removing another failure cause.

Fuel subsystem

- **Fuel pressure switch problems:** Susceptibility to fuel contamination, maintenance damage and deterioration from the vibratory environment;
- **Fuel pump failure:** Malfunction in fuel boost pump (transports fuel from fuel tank to engine) and engine mounted pump (maintains controlled pressure);
- **Fuel cell leakage:** Mechanical failure, delamination, stress concentration, age- and sunlight sensitive, cell material stiffening in cold;

The fuel subsystem is probably the most unreliable part of the complete helicopter. The fuel cell is sensitive for temperature changes, that can cause degradation in performance or even failure. Leakage will at first be bad for fuel consumption, but if it fills up the fuselage it can be harmful for the other systems.

Conclusion

In general it can be concluded that because of the lack of complex systems, such as hydraulics, swashplates, mechanical engines and drivetrains, the probability of failure is highly reduced. On the other hand, the implementation of a innovative power source as a hydrogen fuel cell, complicated problems may occur because it has never been implemented in a helicopter. However, this improved reliability because of the absent complex systems is highly in favor compared to the increased failure probability because of the fuel cell.

18.2. Maintainability

Since no extraordinary complex systems are added or even removed, as explained in 14.2 it is assumed that the inspection interval is similar or even less than comparable conventional helicopters. Comparable helicopters considered for this purpose are the Robinson R22 [102], which has comparable payload weight, and the Robinson R44 [103], which has a similar gross weight. For both helicopters inspection is required after 100 flying hours, 42 design missions, or 12 months, whichever comes first. A typical price for a R44 inspection is $1,440 at a rate of $90/hour [104], which means 16 hours of inspection when tooling and materials are included in this price. Compared to the R44 inspection, a couple of differences can be seen: in the H2Copter no reciprocating engine, drive train, tail rotor, hydraulic control systems or fuel injection system is present. However, a coaxial helicopter has a double rotor, which means double the inspection time for that part although for a normal helicopter most of the time is because of the swash plate, which is not used either. When going through the maintenance manuals [102, 103], it can be seen that a high amount of actions is required on the absent systems. Therefore it is assumed that the time to inspect can be approximately be done in half of the time, which is 8 hours. With less specific tooling required, it is estimated that the price will be $720 with a down time of 8 hours. Normally additional checks and thus costs are required every 300 and 500 hours, but this does not apply on the H2Copter this applies only to the powerplant and hydraulic systems.

Most probably unscheduled inspection will be required, after e.g. a rough landing. It is assumed that every 8 hours of flying requires 1 hour of unexpected maintenance, which can include repairs or additional inspections. Single digit times are typical for helicopters, and since less complexity is present a high number within the single digits is assumed.

After 2200 hours or 12 years the Robinsons need a complete overhaul. For this overhaul it will be completely disassembled, all parts overhauled or renewed and reassembled again. The total factory costs for this $204,000, including new parts and 240 hours of labour. Assuming that the same procedure is followed for the H2Copter, the costs will be significantly lower because of the missing complex systems. At first there will be a savings of $48,000, for the engine, and when looking at the list of necessary actions, approximately 20% of the time can be saved. This saves another $4,320 on the price. After 44 hours, the servo flap assembly needs to be renewed: half of the servo flaps, since the other half is redundant, will be replaced by new ones for a total price of $19,200. A proton exchange membrane fuel cell in vehicle applications has a typical lifetime of 2000 hours [105]. Therefore a completely new fuel cell has to be implemented with the overhaul. This will cost about $33,300. New blades will be used for $15,000 and a new pair of gear boxes will be approximately $10,000. Most remaining parts that will be renewed are for the hydraulics and other systems which are not present.Selecting the remaining necessary parts from the R44 overhaul list the price for exchange parts will be about $150,000. Combining this with the labour price, the total price for an overhaul is $175,000. The time to perform this overhaul every 2000 hours, the limiting time of a fuel cell, is 192 hours of labour. When working at maximum productivity five technicians can complete this in one week.

It can be concluded that every 2000 hours of flying, when the helicopter is used frequently, there will be a labour time of 602 hours. For one cycle of 2000 hours a total of $211,900 is required, which results in a maintenance rate of $105.95 per hour of flying.

18.3. Availability

Generally availability is defined probability will be ready for use when required. Three different classifications of availability can be distinguished for the H2Copter: Inherent, achieved and operational availability;

Inherent availability is the probability that the helicopter will operate satisfactory when required. This means that there will be looked at the unscheduled maintenance. As explained in section 18.2 every 8 hours flight time 1 hour of maintenance is required. This results in an inherent availability of 88.9%;

Achieved availability is the inherent availability, but with scheduled maintenance included. As stated before every 100 hours regular inspection is needed and every 2000 hours a complete overhaul is required. The in-

spection takes approximately 8 hours and the overhaul in the worst case, when one person is working, 192 hours. For every 2000 hours of flying, the helicopter will be unavailable for 312 working hours, or 15.6% of the time. Thus the H2Copter will be available for 84.4% of the time;

Operational availability not only includes the time to solve all the problems, but also the unpredictable delays, such as logistics and administrative. No good estimation can be made for these delay times since they depend on the location the helicopter will be used. However, since no special tooling is required for the H2Copter it can be maintained at any airport that has helicopters;

18.4. Safety

During the design phase safety has been taken into account as well. Safety can relate to many different factors: human beings, the system itself, other systems and the environment.

- **Loss of life or injury to human beings:**
  - The chassis is designed to withstand loads higher than those that are probable to ever occur.
  - The landing gear are designed to cope with loads that can occur during rough emergency landings.
  - The hydrogen tank is firstly designed with a safety factor of 1.5 and placed all the way to the back to make sure that the pilots will not be harmed when a tank bursts in flight. Moreover, the type of fuel tank that is being used is unlikely to rupture because of an impact [106].
  - Redundant Piezo servos are placed on the control flaps.
  - A back-up battery is present to deliver power for a small amount of time, but enough for the pilot to bring the rotorcraft into autorotation state.
- **Damage to the system being designed or developed.**
  - Safety factors are used for structural design to protect the systems within the helicopter.
  - Active cooling is implemented to protect the relevant systems from overheating.
  - Ventilation shafts are used to make leaked hydrogen escape out of the fuselage. This in order to prevent pressurizing of the hydrogen which can cause fire danger.
- **Damage to other systems.**
  - A navigation system for both pilots is implemented to prevent collisions with other aircraft.
  - Lights are mounted on the outside for visibility purposes during night time as discussed in section 10.4.
  - As explained in section 11.8, an SCAS is implemented to reduce the pilot's workload.
- **Damage to the environment.**
  - An electric powertrain is used in combination with hydrogen as fuel. This combination gives no direct emissions.
  - The absence of a tail rotor highly reduces the noise created by the H2Copter compared to conventional helicopters with similar gross weight (section 15.3)

19

COMPLIANCE MATRIX

Table 19.1 shows the degree of compliance of the H2Copter design with the prescribed requirements listed in chapter 4.

The following requirements were not met are to be determined (TBD):

- **NFR.5**: A climb rate of 900 feet per minute is not achievable, instead 840 feet per minute on sea level.
- **NFR.10.3**:A climb ratio of 1/6 is not always achievable, current ratio is 1/6.1 on sea level.
- **NFR.10.9**: To be determined in future development.
- **NFR.10.13**: not applicable.
- **MR.11**:To be determine in future development, study relations between pilot control and Piezo-actuated blade control.
- **MR.12**: The H2Copter is in compliance with the EASA CS-36 regulations but violates the 3 EPNdB margin set in the baseline report [10].
- **COD.1**: The H2Copter is slightly more expensive than expected. The prescribed selling price was $333,118, and is now set at $381,490.

Table 19.1: Compliance matrix

FUNCTIONAL REQUIREMENTS													
FR.1	✓	**FR.2**	✓	**FR.3**	✓	**FR.4**	✓	**FR.5**	✓				
NON-FUNCTIONAL REQUIREMENTS													
NFR.1	✓	**NFR.2**	✓	**NFR.3a**	✓	**NFR.3b**	✓	**NFR.4**	✓	**NFR.5**	**X**	**NFR.6**	✓
NFR.7	✓	**NFR.8**	✓	**NFR.9**	**TBD**	**NFR.10.1**	✓	**NFR.10.2**	✓	**NFR.10.3**	✓	**NFR.10.4**	**X**
NFR.10.5	✓	**NFR.10.6**	✓	**NFR.10.7**	✓	**NFR.10.8**	✓	**NFR.10.9**	**TBD**	**NFR.10.10**	✓	**NFR.10.11**	✓
NFR.10.12	✓	**NFR.10.13**	✓	**NFR.10.14**	✓	**NFR.10.15**	✓	**NFR.10.16**	✓	**NFR.11**	✓		
MISSION REQUIREMENTS AND CONNSTRAINS													
MR.1	✓	**MR.2**	✓	**MR.3**	✓	**MR.4**	✓	**MR.5**	✓	**MR.6**	✓	**MR.7**	✓
MR.8	✓	**MR.9**	✓	**MR.10**	✓	**MR.11**	**TBD**	**MR.12**	**X**				
CONSTRAINS ON DEVELOPMENT													
COD.1	**X**	**COD.2**	✓	**COD.3**	✓								

20

Conclusion

This report has outlined the detailed design process and results of a sustainable future rotorcraft solution for short range missions in 2020. The coaxial helicopter configuration powered by hydrogen fuel cell propulsion technology has been selected as a feasible solution to achieve the goal of developing a environment friendly future personal air transport vehicle.

Starting from a clear project definition phase including a project need statement, mission analysis, vehicle requirements and market analysis, the suggested design concept was stated. This concept selection has served as an input to a vehicle subsystem design phase in which the coaxial rotor, propulsion, hub, stabilizers, fuselage and cockpit subsystems have been designed in detail.

From the aerodynamic rotor design point of view, it can be concluded that the fundamental problem in designing a coaxial rotor system is to account for the complex interference of the upper rotor wake on the lower rotor, assumptions made in this area often serving as an explanation of possible design result inaccuracies.

The main challenge for the propulsion subsystem design is, as for any transportation vehicle, the design approach towards a lightweight sustainable engine which is hard to realize with current technology. The sizing of a hydrogen fuel cell propulsion system described in the report is the result of an investigation of all feasible engine technologies and energy sources prior to the sizing process. The main conclusions to be drawn for this subsystem are that it turned out to be 15 kg heavier than previously expected, that the challenges involved in the design of the cooling system with respect to weight were underestimated and that the tank design incorporating aerospace design standards with respect to safety factors turned out to be lighter than expected.

From the gearbox-motor combination, it can be concluded that its resulting power to weight ratio seems reasonable and that the total weight setup including the motor, gearbox and motor controller was found to be heavier than specified in most reference data. This difference is most likely due to the rough weight estimation methods used in the hub design process for sizing the different parts.

The main aim of the stability and control discipline in the design process was to size the horizontal and vertical tail of the vehicle to ensure flight stability by predicting dynamic vehicle behaviour. It has been investigated and concluded that coaxial rotorcraft without horizontal and vertical tailplanes are always unstable. The horizontal tail to provide the trim condition for longitudinal stability was therefore sized, keeping in mind that maintaining a positive M_w stability derivative is crucial. A controller gain to ensure overall design stability, chosen based on EASA regulations, was also selected.

The final subsystems from which conclusions are drawn are the fuselage and cockpit. For the sizing of the skids, calculations were performed using 3-D statics theory from which numerical force distribution values were obtained. These skid sizing results were then implemented into Inventor, a program which performs structural load calculations. It can be concluded that the manual results matched accurately with the values obtained using Inventor, the only differences most likely due to the fact that Inventor also uses gravity forces of the structural components in the calculations. Based on this procedure, Inventor was validated for practical usage purposes. The fuselage has been sized using a packaging approach, using the pilot seats and remaining required components as inputs to design the most weight-efficient fuselage around them. The joysticks and controls in the digital cockpit were selected off-the-shelf. Lastly, the large amount of glass the fuselage is made of ensures high pilot visibility.

Regarding the final design, it can be concluded that innovative characteristics have been proposed such as a novel engine-hub integration in which two engines are used to independently drive the rotors. Furthermore, no swash plate has been used in the design for controlling the H2Copter. It has been replaced by servo flaps on the rotor blades, used as a control method. The total cost of the final design is estimated to be 14% higher than the value obtained in the MTR. From the life cycle assessment of the final design, it can be concluded that the H2Copter is 65% more sustainable than a conventional helicopter using a fossil fuel based engine sized for the same mission. Finally, from the requirements compliance matrix it can be concluded that not all initially set requirements have been met. However, most of them have successfully been achieved in the final design.

Part IV

Recommendations

21

PROJECT DESIGN AND DEVELOPMENT LOGIC

This chapter will describe the steps taken in the design of the H2Copter and the steps that will need to be taken to further realize the production of the H2Copter. The design phases as described in figure 21.1 are followed.

This project is between the point where the configuration is frozen and authorization to proceed.

21.1. PROJECT PHASES

In this section the project phases are explained. The Market analysis, conceptual design and preliminary design are further explained respectively.

Market analysis

In the beginning of the project a detailed market analysis was made. This market analysis has given the project the needed extra requirements to define the project need statement. Although this was at the beginning of the designing phase, the market analysis must be kept up to date to possibly integrate small changes to be more fit in the market.

Conceptual design

For the conceptual design, the project need statement was the leading requirement for choosing the concepts worth to investigate. It resulted in a mission need statement and project statement.

Preliminary design

The preliminary design consist of elaborating in smaller groups on work packages. Each group had a specific task. It resulted in a preliminary design for the H2Copter.

A flowchart of the several phases is provided in figure 21.2.

21.2. POST-PROJECT PHASES

In this section of the report, the duration of the following tasks are estimated. This is done with references from within the helicopter business.

In figure 21.3 the highest order of Gantt chart is shown. In the following subsection this Gantt chart is divided into smaller work packages.

Preliminary design: After reviewing the final report, minor adjustments in the design should be made. This should not take longer than one week from the point this report is handed in.

Detailed design: (*9 months*) In the detailed design phase the overall detail of the H2Copter should be increased. The detailed design phase consist of better weight estimation, better sizing, more detailed structural design, more detailed materials description, aerodynamics, controller electric system, hub design and powertrain design.

Testing: (*9 months*) After the detailed designs, the physical and computational testing must be done. This must be done in detail to ensure the safety of the product designed. The possible disadvantage of all delivered products may be catastrophic for financial and market reasons. This testing is without testing for the certification because that will be done in the time for certification.

Production preparation: (*15 months*) Production preparation must be considered as a time consuming part of the total process of production. The need of suppliers for respectively advanced technological parts may take more time than original planned.

Certification: (*57 months*) The certification process of the Robinson R44 which took 53 months.The estimation has been made that the certification process of the H2Copter will take 3 months longer because of the new implementations of many new technologies in aviation.

Production: (*48 months*) The production set up of a H2Copter will take an estimated 2 years for the first pro-

duction model. After this, the first H2Copter in the production line will follow.

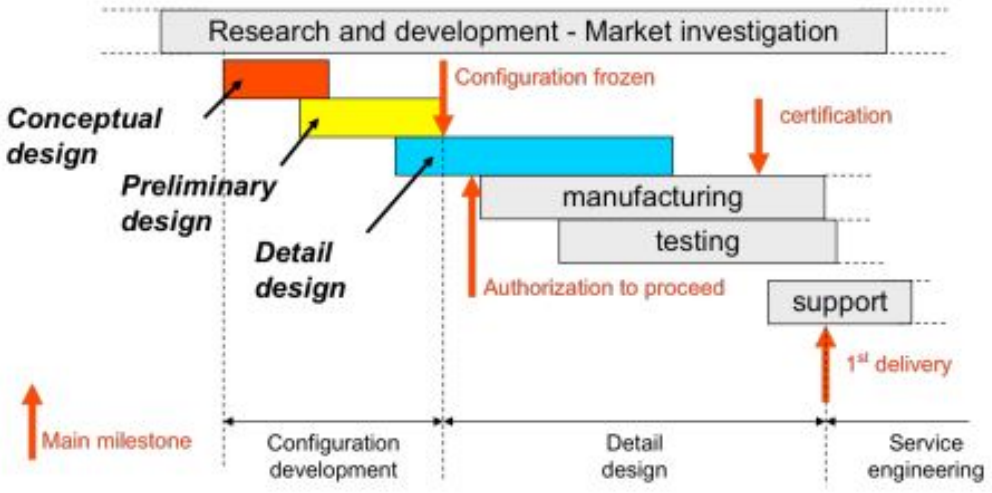

Figure 21.1: Systems Engineering Diagram [107]

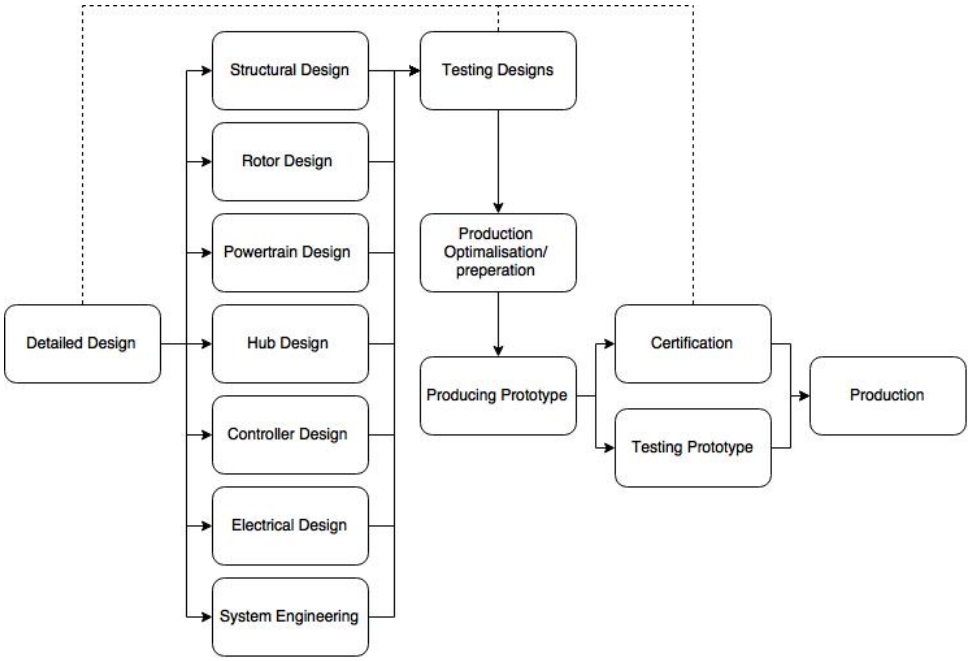

Figure 21.2: PD&DL Diagram

	Naam	Duur	Aanvang	Voltooiing
1	**Preliminary Design**	**40d**	**08/05/2015**	**02/07/2015**
2	**Detail Design**	**204d**	**08/06/2015**	**17/03/2016**
3	**Testing**	**208d**	**09/10/2015**	**26/07/2016**
4	**Production Preperation**	**320d**	**24/06/2016**	**14/09/2017**
5	**Certification**	**628d**	**05/12/2016**	**01/05/2019**
6	**Production**	**501d**	**25/06/2018**	**25/05/2020**

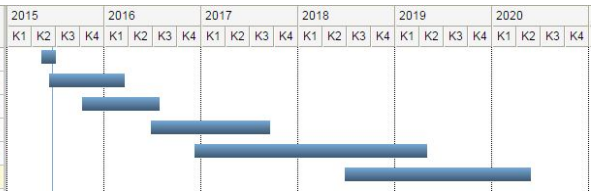

Figure 21.3: Gantt Chart of the post-project phases

	Naam	Duur	Aanvang	Voltooiing
1	**Preliminary Design**	**40d**	**08/05/2015**	**02/07/2015**
2	**Detail Design**	**204d**	**08/06/2015**	**17/03/2016**
3	Structural Design	85d	09/06/2015	05/10/2015
4	Powertrain Design	97d	09/06/2015	21/10/2015
5	Hub Design	91d	09/06/2015	13/10/2015
6	Controller Design	115d	04/08/2015	11/01/2016
7	Rotor Design	108d	18/08/2015	14/01/2016
8	Electric System Design	98d	16/10/2015	01/03/2016
9	Systems Engineering	71d	21/12/2015	28/03/2016
10	**Testing**	**208d**	**09/10/2015**	**26/07/2016**
11	Structural testing	91d	09/10/2015	12/02/2016
12	Hub testing	73d	16/10/2015	26/01/2016
13	Powertrain testing	100d	23/10/2015	10/03/2016
14	Controller testing	64d	11/01/2016	07/04/2016
15	Rotor testing	82d	15/01/2016	09/05/2016
16	Electric system testing	91d	03/03/2016	07/07/2016

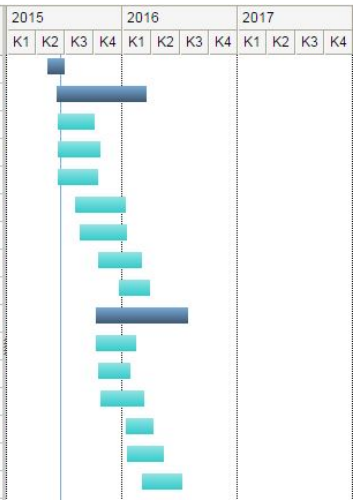

Figure 21.4: Gantt Chart of the post-project phases with Detail Design in detail

	Naam	Duur	Aanvang	Voltooiing
17	**Production Preperation**	**320d**	**24/06/2016**	**14/09/2017**
18	Design optimisation	49d	20/06/2016	25/08/2016
19	Tooling Equiment	43d	27/07/2016	23/09/2016
20	Contacting suppliers	85d	27/07/2016	22/11/2016
21	Supplier parts	127d	10/08/2016	02/02/2017
22	Supplier logistics	112d	01/09/2016	03/02/2017
23	Location Production	67d	31/10/2016	31/01/2017
24	Prototype	157d	06/02/2017	12/09/2017
25	**Certification**	**628d**	**05/12/2016**	**01/05/2019**
26	Numerical testing	172d	07/12/2016	03/08/2017
27	Physical testing	169d	03/08/2017	27/03/2018
28	Power reliability testing	205d	30/03/2018	10/01/2019
29	Noise testing	79d	15/01/2019	03/05/2019
30	**Production**	**501d**	**25/06/2018**	**25/05/2020**

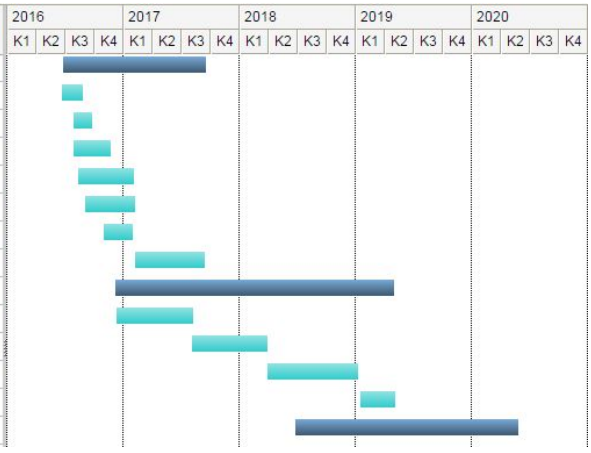

Figure 21.5: Gantt Chart of the post-project phases in detail

22

RECOMMENDATIONS

With a first design iteration performed, a long list of recommendations on improvements and ideas has been shaped. This chapter highlights the main recommendations for future design iterations on similar or derived design concepts.

One of the most distinct features of the H2Copter is the hydrogen electric powertrain. After a more detailed research on performance and structure of the fuel cell system many values seem to deviate from resources found. Based on that the climb rate requirement of the helicopter can not be achieved unmitigated. Using the new performance data derived will result in a more realistic class 2 weight estimation and thus more sophisticated iteration.

As the design needs to perform after a successful technical certification and test, an improved infrastructure on hydrogen supply needs to be realized. Since the use of hydrogen powertrains is limited at the moment, most hydrogen fuel stations can be found in industrial areas. An increase in use of hydrogen powertrains can lower the cost of hydrogen supply and production as well as driving developments on local hydrogen generation by means of electrolyse, driven by solar or wind energy.

A lot of potential can still be gained by a more advanced body-chassis integration. Once all components in size and weight as well as their position is determined, research can be done on a design which increases the functionality of the body with regards to aerodynamic and load carrying functions. This also includes a computational fluid dynamics analysis on the body and external components to get a better estimate on what has been derived based on statistical data until now.

The servo flap design as described is based on many simplifications and dimensions set to self-defined values to keep the work load to an acceptable level. Research has to be done on the effect of the servo control on the blade dynamics. Research performed by Airbus Helicopters shows a decrease in noise and vibration for the use of servo controls.

For the rotor design the wake in forward flight is assumed to be linear, while for hover it is assumed that the lower rotor is in the fully developed slipstream of the upper rotor. A better aerodynamic model of the wake can be implemented that holds for all flight velocities, for a more realistic result. Due to time constraints, only a few flight phases are evaluated. The aerodynamic model can however be used to calculate more flight phases with minor adjustments. The structure of the blade can be designed in more detail, with less assumptions made, for a more realistic result for the final weight and weight per unit span.

The hub design shows a redefinition of the conventional setup. Further improvements can be done on the overall drag reduction by decreasing the diameter of the shaft between the motors and by improving the shape from cylindrical to airfoil-like.

Concluding the stated improvements and recommendations, many fields do require more time to be designed in more detail. During the process new technologies got added and functions of different components got defined in a new way. We are certain that the recommendations as well as the technique described in this report form a solid base for following developments and designs on future electric rotorcraft.

BIBLIOGRAPHY

[1] M. D. Pavel, *Project Guide* (TU Delft Aerospace Engineering, 2015).

[2] F. Buysschaert, P. Hendrick, and S. Newman, *Conventional Helicopters and their Adaptiveness for More Electric and Alternative Transmission Technologies,* in *Proceedings of the 36th European Rotorcraft Forum* (2010).

[3] V. T. Nagaraj and I. Chopra, *Explorations of Novel Powerplant Architectures for Hybrid Electric Helicopters,* in *Proceedings of the 70th Annual Forum and Technology Display* (2014).

[4] T. van Holten and J. Melkert, *Helicopter Performance, Stability and Control* (Faculty of Aerospace Engineering, Delft University of Technology, 2002).

[5] M. Langer, *The Deadman's Curve,* http://www.aneclecticmind.com/2008/04/27/the-deadmans-curve/ (2008), accessed June 2, 2015.

[6] Federal Aviation Regulations, *Minimum safe altitudes: General,* http://quietskiescoalition.org/MINIMUM_ALTITUDES.html (2006), accessed April 22, 2015.

[7] Advisory Council for Aviation Research and Innovation in Europe, *A new beginning for European Aviation Research,* http://www.acare4europe.com/about-acare (2015), accessed April 29, 2015.

[8] DSE Group 11, *Electric Helicopter Mid-term review* (Delft University of Technology, 2015).

[9] R. W. Prouty, *Helicopter Performance, Stability, and Control* (Robert E. Krieger Publishing Company, 1990).

[10] DSE Group 11, *Electric Helicopter Baseline Report* (Delft University of Technology, 2015).

[11] Darden School of Business, *Tesla Strategic Analysis,* http://www.slideshare.net/joseangeldf/darden-school-of-business-tesla-strategic-analysis (2008), accessed June 18, 2015.

[12] D. Chaika and J. Davison, *How Tesla Motors can manage the extreme competition from large and premium manufactures,* http://www.academia.edu/7563935/tesla_motors_startegic_analysis (2008), accessed June 18, 2015.

[13] Tutors India, guidance for research, *MBA Marketing Assignments,* http://www.tutorsindia.com/mba-marketing-assignments/ (2015), accessed June 22, 2015.

[14] W. Kania, W. Stalewski, and B. Zwierzchowska, *Design of the modern family of helicopter airfoils*, Tech. Rep. (Institute of Aviation, 2008).

[15] Airfoil Tools, *Boeing-vertol VR-12 airfoil,* http://airfoiltools.com/airfoil/details?airfoil=vr12-il (2015).

[16] L. Leihon, *Structural design of composite rotor blades*, Tech. Rep. (Georgia Institute of Technology, 2008).

[17] DOW chemical company, *Technical data sheet, Compaxx 700-X Structural Foam,* http://www.dow.com/en-us/markets-and-solutions/products/compaxx/compaxx700xstructuralfoam/ (2015).

[18] J. G. Leishman and S. Ananthan, *Aerodynamic optimization of a coaxial proprotor*, Tech. Rep. (Aerospace Engineering, Glenn L. Martin Institute of Technology, Maryland, 2006).

[19] J. G. Leishman and S. Ananthan, *Contributions to the aerodynamic optimization of a coaxial rotor system,* Tech. Rep. (Aerospace Engineering, M. Syal Department of Aerospace Engineering, University of Maryland, 2008).

[20] J. G. Leishman, *Principles of helicopter aerodynamics*, Cambridge aerospace series (Cambridge University Press, Cambridge, New York, 2000).

[21] J. Seddon, *Helicopter aerodynamics* (British Library, Oxford, London, Edinburgh, 1990).

[22] Wikipedia, *Kamov Ka-15,* https://en.wikipedia.org/wiki/Kamov_Ka-15 (2015), accessed June 29, 2015.

[23] H. W. Kim and R. E. Brown, *A comparison of coaxial and conventional rotor performance,* Journal of the american helicopter society **55**, 1 (2010).

[24] YASA Motors, *YASA 400,* http://www.yasamotors.com/products/yasa-400/ (2008), accessed June 4, 2015.

[25] YASA Motors, *YASA 750,* http://www.yasamotors.com/products/yasa-750/ (2008), accessed June 4, 2015.

[26] YASA Motors, *YASA 250,* http://www.yasamotors.com/products/yasa-250/ (2008), accessed June 4, 2015.

[27] US Hybrid, *Medium Duty Integrated Electric Drive Unit EDU200,* http://www.ushybrid.com/index.php/products (2008), accessed June 4, 2015.

[28] US Hybrid, *Integrated Generator Control Unit GCU100,* http://www.ushybrid.com/index.php/products (2008), accessed June 4, 2015.

[29] *Manual for EMRAX motors*, ENSTROJ electric motor innovation (2014).

[30] GKN Driveline, *Axial Flux Electric Motor AF,* http://www.gkn.com/driveline/our-solutions/edrive-systems/eMachines/Pages/default.aspx (2008), accessed June 4, 2015.

[31] Protean Electric, *Protean Drive Specifications,* http://www.proteanelectric.com/en/specifications/ (2008), accessed June 4, 2015.

[32] J. Popovic, *Et3051tu electronic power conversion (lecture slides),* Delft University of Technology (2014).

[33] W. group, *The abc's of synchronous motors,* http://ecatalog.weg.net/files/wegnet/WEG-the-abcs-of-synchronous-motors-usaem200syn42-brochure-english.pdf, accessed June 8, 2015.

[34] Sevcon, *Gen4,* http://www.sevcon.com/ac-controllers/gen4-size-10.aspx (2008), accessed June 5, 2015.

[35] *Manual for Digital Battery-Motor-Controller BAMOCAR-D3*, Unitek Industrie Electronik GmbH, 7th ed.

[36] W. J. A. Datta, *Powerplant design and performance analysis of a manned all-electric helicopter,* Journal of Propulsion and Power **30**, 490 (2014).

[37] Q. Yan, H. Toghiani, and H. Causey, *Steady state and dynamic performance of proton exchange membrane fuel cells (pemfcs) under various operating conditions and load changes,* Journal of Power Sources **161**, 492 (2006).

[38] S. S. J.P van Buijtenen, W.P.J. Visser and F. Montella, *Gas Turbines, Propulsion and Power, AE2–203* (Faculty of Aerospace Engineering, Delft University of Technology, 2001).

[39] *Compressor OA3150*, Autorortot Opcon AB (2008).

[40] *FES MOTOR MANUAL Type: FES-LAK-M100*, LZ design, 1st ed. (2013).

[41] *Digital Battery Drive BAMO-D3.2 for EC Servo Motors and AC Motors*, Unitek Industrie Electronik GmbH, 2nd ed.

[42] *Military COTS DC-DC Bus Converters*, SynQor (2015).

[43] J. Hesselgreaves, *Compact Heat Exchangers: Selection, Design and Operation* (Pergamon, 2001).

[44] Davies Craig Pty. Ltd., *Davies Craig Electric Water Pump EWP,* http://daviescraig.com.au/electric-water-pumps (2008), accessed June 22, 2015.

[45] Perma Cool, *Automotive Electric Fan 8ẍ 2 1/4 ẗ2400 CFM,* http://shop.perma-cool.com/19128-Std-Electric-Fan-8-2400-CFM-19128.htm (2008), accessed June 22, 2015.

[46] Parker Industrial Hose, *Industrial Hose Products Catalog,* http://www.safehose.com/ParkerProducts.asp?catID=668 (2015).

[47] T. H. et al., *Technical Assessment of Compressed Hydrogen Storage Tank Systems for Automotive Applications*, Tech. Rep. (Argonne National Labaratory, 2010).

[48] Quantum Technologies, *High Pressure Lightweight Type IV H2 Cylinders – 34L/40L,* http://www.qtww.com/assets/u/TankBrochure34L40L.pdf (2008), accessed May 29, 2015.

[49] A. Datta, W. Johnson, *Requirements for a hydrogen powered all-electric manned Helicopter*, Tech. Rep. (NASA, 2012).

[50] L. Zhou, *Progress and problems in hydrogen storage methods,* Renewable and Sustainable Energy Reviews **9**, 395 (2005).

[51] N. Bimbo, *Integrating novel adsorbent materials in hydrogen cylinders for improved storage efficiency and safety,* in *11th International Hydrogen & Fuel Cell Conference* (2015).

[52] M. Schlichtenmayer, B. Streppel, M. Hirscher, *Hydrogen physisorption in high ssa microporous materials - a comparison between ax-2133 and mof-177 at cryogenic conditions,* International Journal of Hydrogen Energy **36**, 586 (2011).

[53] A. Züttel, P. Wenger, S. Rentsch, P. Sudan, Ph. Mauron, Ch. Emmenegger, *Libh4 a new hydrogen storage material,* Jounal of Power Sourcesy **118**, 1 (2003).

[54] K. J. Gross, E. Majzoub, G.J. Thomas, and G. Sandrock, *HYDRIDE DEVELOPMENT FOR HYDROGEN STORAGE,* in *Proceedings of the 2002 U.S. DOE Hydrogen Program Review* (2002).

[55] T. Kim, *Nabh4 (sodium borohydride) hydrogen generator with a volume-exchange fuel tank for small unmanned aerial vehicles powered by a pem (proton exchange membrane) fuel cell,* Energy **69**, 721 (2014).

[56] Ying Wu, *Hydrogen Storage via Sodium Borohydride,* in *GCEP – Stanford University* (2003).

[57] V.V. Vasiliev , A.A. Krikanov, A.F. Razin, *New generation of filament-wound composite pressure vessels for commercial applications,* Composite structures **62**, 449 (2003).

[58] A.C. Pipkin, R.S. Rivlin, *Minimum-weight design for pressure vessels reinforced with inextensible fibers,* Journal of Applied Mechanics **62**, 103 (1963).

[59] J. Stewart, *Calculus, Early Transcendals* (Brooks/Cole cengage Learning, 2012).

[60] E.W. Lemmon, M.L. Huber, *Revised standardized equation for hydrogen gas densities for fuel consumption applications,* Journal of Research of the National Institute of Standards and Technology **113**, 341 (2008).

[61] Torayca, *T1000G data sheet,* http://www.toraycfa.com/intermediatemodulus.html (2008), accessed June 1, 2015.

[62] J. Wong, *CNG & Hydrogen Tank Safety, R&D, and Testing,* http://www.tutorsindia.com/mba-marketing-assignments/ (2015), accessed June 22, 2015.

[63] A.R. Hassan, *Contact Stress Analysis of Spur Gear Teeth Pair*, Tech. Rep. (World Academy of Science, Engineering and Technology, 2009).

[64] P.Jaenker, *Piezo active vibration and noise control in helicopters*, Tech. Rep. (ICAS, 2008).

[65] J. Kursu, *Static and Dynamic Rollover* (The Finnish Border Guard, 2013).

[66] Aviastar, *Hughes 600X, 1981-project,* .

[67] EASA, *Certification Specifications for Small Rotorcraft CS27,* http://easa.europa.eu/system/files/dfu/CS-27%20Amdt%202%20final.pdf (2008), accessed June 10, 2015.

[68] EASA, *EASA.IM.E.027,* https://easa.europa.eu/documents/type-certificates/engine-cs-e/easaime027 (2011).

[69] B. Haqi, *WELCOME TO CLASS AJD 21603 ROTORCRAFT SYSTEM, MAINTENANCE AND ROLE EQUIPMENT, Course Code: AJD21603, Faculty of Aerospace Engineering, Malaysian institute of aviation technology, 2014,* Malaysian institue of aviation technology (2014), Accessed May 30, 2015.

[70] ASM, *Elements of metallurgy and Engineering alloys,* http://www.asminternational.org/documents/10192/1849770/05224G_Chapter14.pdf (2008), accessed May 29, 2015.

[71] Fischer+Entwicklungen, *Leightsweight Construction,* http://www.fischer-seats.com/unternehmen/technologie-innovation/leichtbauweise.html (2007), accessed June 18, 2015.

[72] H3R Aviation, *MODEL A344T - Halon 1211 Fire Extinguisher,* http://www.h3raviation.com/halon_1211_a344t.htm (2008), accessed June 18, 2015.

[73] Infinity Aerospace, *Military Style Stick Grips (HOS),* http://infinityaerospace.com/product/featured/military-style-stick-grips/#pricing (2015), accessed July 29, 2015.

[74] UAV Vision, *CM202 Multi-sensor Gimbal,* http://uavvision.com/product/cm202-3/ (2008), accessed June 19, 2015.

[75] Whelen Engineering Co., *MicroBurst™ Series Lighting,* https://www.aircraftspruce.com/catalog/pdf/microburst23.pdf (2009), accessed June 18, 2015.

[76] Garmin, *Garmin Helicopters,* http://sites.garmin.com/en-US/helicopters/#HSVT (2008), accessed June 19, 2015.

[77] Honeywell , *Honeywell Air Data Module,* https://aerospace.honeywell.com/~/media/Products/Air%20Data%20Products/Air%20Data%20Modules.ashx (2008), accessed June 19, 2015.

[78] M.D. Pavel, *SIX DEGREES OF FREEDOM L1NEAR MODEL FOR HELICOPTER TRIM AND STABILITY CALCULATION,* (1996).

[79] G. D. Padfield, *Helicopter Flight Dynamics, 2nd Edition* (Blackwell, 2008).

[80] M. Sadraey, *Aircraft Design: A Systems Engineering Approach* (Wiley, 2012).

[81] Politie, *Welke specificaties hebben de toestellen?* https://www.politie.nl/themas/helikopter-boven-mijn-huis.html (2008), accessed June 22, 2015.

[82] ATC the Netherlands, *INTEGRATED AERONAUTICAL INFORMATION PACKAGE,* http://www.ais-netherlands.nl/aim/index.html (2008), accessed June 22, 2015.

[83] M. P. M. Melaina, *Hydrogen Station Cost Estimates, Comparing Hydrogen Station Cost Calculator Results with other Recent Estimates*, Tech. Rep. (NREL, 2013).

[84] T. Ramsden, *An Evaluation of the Total Cost of Ownership of Fuel Cell-Powered Material Handling Equipment*, Tech. Rep. (NREL, 2013).

[85] K. M. Spencer, C. A. Martin, *Investigation of Potential Fuel Cell Use in Aircraft*, Tech. Rep. (Institute for Defense Analyses, 2013).

[86] Keith Wipke, Cory Welch, Holly Thomas, Sam Sprik, Sigmund Gronich, John Garbak, *Controlled hydrogen fleet and infrastructure demonstration and validation project initial fuel cell efficiency and durability results,* World Electric Vehicle Journal **1**, 1 (2006).

[87] Michael W. Ellis, Michael R. Von Spakovsky, Douglas J. Nelson, *Fuel Cell Systems: Efficient, Flexible Energy Conversion for the 21st Century,* in *Proceedings of the IEEE* (2001).

[88] A. Johanning, D. Scholz, *A first step towards the integration of life cycle assessment into conceptual aircraft design,* in *Deutscher Luft- und Raumfahrtkongress* (2013).

[89] M. Goedkoop, R. Heijungs, M. Huijbregts, A. de Schrijver, J. Struijs, R. van Zelm, *ReCiPe 2008*, Tech. Rep. (Ministerie van Volkshuisvesting, Ruimtelijke Ordening en Milieubeheer, 2013).

[90] M. Goedkoop, R. Heijungs, M. Huijbregts, A. de Schrijver, J. Struijs, R. van Zelm, *ReCiPe Mid/Endpoint method - Characterisation factors, version 1.11,* http://www.lcia-recipe.net/file-cabinet (2013), accessed June 12, 2015.

[91] M. Pehnt, *Life-cycle assessment of fuel cell stacks,* International Journal of Hydrogen Energy **26**, 91 (2001).

[92] M. Granovskii, I. Dincer, M.A. Rosen, *Life cycle assessment of hydrogen fuel cell and gasoline vehicles,* International Journal of Hydrogen Energy **31**, 337 (2006).

[93] C. Koroneos, A. Dompros, G. Roumbas, N. Moussiopoulos, *Life cycle assessment of hydrogen fuel cell production process,* International Journal of Hydrogen Energy **29**, 1443 (2004).

[94] International Civil Aviation Organization, *Environmental protection (Annex 16, volume 1)* (2011).

[95] T. F. Brooks, J. R. Jolly, M. A. Marcolini, *Helicopter main-rotor noise*, Tech. Rep. (NASA, 1988).

[96] O. Rand and V. Khromov, *Helicopter sizing by statistics,* in *American Helicopter Society 58th Annual Forum* (2004).

[97] H.W. Kim, *A comparison of coaxial and conventional rotor performance,* Journal of the American Helicopter Society **55** (2010).

[98] Reddick, Jr., H. K., *ARMY HELICOPTER COST DRIVERS*, Tech. Rep. (National technical Information Service, 1975).

[99] K. Hartley, *The Economics of Defence Policy, A new perspective* (Routledge, 2011).

[100] Perma Cool, *Board Governers of the federal Reserve System,* http://www.federalreserve.gov/releases/h15/update/ (2015), accessed June 22, 2015.

[101] J. J. Dougherty and L. D. Barrett, *RESEARCH REQUIREMENTS TO IMPROVE RELIABiLITY OF CIVIL HELICOPTERS*, Tech. Rep. (NASA, 1978).

[102] *R22 Maintenance Manual and Instructions for Continued Airworthiness*, Robinson Helicopter Company (2014).

[103] *R44 Maintenance Manual and Instructions for Continued Airworthiness*, Robinson Helicopter Company (2014).

[104] *R44 Raven II & R44 Clipper II 2015 Estimated Operating Costs,* Robinson Helicopter Company (2015).

[105] *IEA Energy Technology Essentials*, Tech. Rep. (International Energy Agency, 2007).

[106] J. Wong, P.Eng, *RCNG & Hydrogen Tank Safety, R&D, and Testing*, Powertech Labs Inc. (2009).

[107] D. I. R. Vos and I. B. Zandbergen, *Systems engineering,* Delft University of Technology (2014).